

Geobarometry, phase relations and elasticity of eclogite under conditions of Earth's upper mantle

Dissertation

zur Erlangung des Doktorgrades der Naturwissenschaften

Dr. rer. nat.

an der Bayreuther Graduiertenschule für Mathematik und Naturwissenschaften

vorgelegt von:

Christopher Beyer, M. Sc.

aus Hamm (Westf.)

Bayreuth, 2015

Die vorliegende Arbeit wurde in der Zeit von 10/2011 bis 03/2015 in Bayreuth am Bayerischen Geoinstitut unter Betreuung von Herrn Professor Dr. Daniel J. Frost angefertigt.

Vollständiger Abdruck der von der Bayreuther Graduiertenschule für Mathematik und Naturwissenschaften (BayNAT) der Universität Bayreuth genehmigten Dissertation zur Erlangung des akademischen Grades eines Doktors der Naturwissenschaften (Dr. rer. nat.).

Dissertation eingereicht am: 01.04.2015

Zulassung durch das Leitungsgremium: 15.04.2015

Wissenschaftliches Kolloquium: 14.07.2015

Amtierender Direktor: Prof. Dr. Franz Xaver Schmid

Prüfungsausschuss:

Prof. Dr. Daniel J. Frost (Erstgutachter)

Prof. Dr. Alan Woodland (Zweitgutachter)

Prof. Dr. David Rubie (Vorsitzender)

Dr. Hauke Marquardt

Acknowledgments

I would like to thank Dan Frost for his trust in my work and his motivation even in the moments where I was not able to see the benefit of experiments which failed to my mind. He taught me to think twice and not to be satisfied with the low-hanging fruits. I highly appreciate that he gave me the opportunity to gather so many different experiences in my time at the BGI.

I want to express my gratitude to Tiziana Boffa Ballaran for her extraordinary optimism. I am thankful for her support with X-ray diffraction measurements and her help to formulate my results more positively. I am grateful for the countless nights Alexander Kurnosov spent to perform high-temperature XRD measurements. Many thanks go to Nobuyoshi Miyajima for the operation of the TEM and his assistance with EELS data processing.

I would like to thank the whole support staff of the BGI, especially Sven Linhardt for his help with the heated DAC and with all the stuff which broke during numerous experiments, preferentially during the night. I am indebted to Hubert Schulze and Raphael Njul for their outstanding work polishing my samples. Also I would like to thank Detlef Krause for his help with the microprobe.

I am indebted to Stephan Klemme who persuaded me to pursue experimental petrology and who suggested to me to apply for a position at the BGI.

I thank for financial support by Grant no. 227893 "DEEP" funded through the EU 7th Framework Programme and funding through the DFG.

Ganz besonders möchte ich meiner Frau Sara danken, die mit mir nach Bayreuth gekommen ist und immer hinter mir stand und steht. Vielen Dank, dass du da bist!

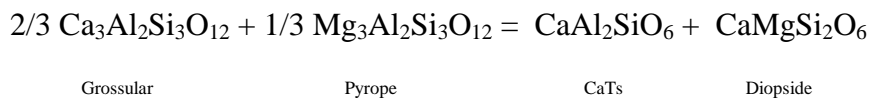
Table of Contents

Abstract	1
Zusammenfassung	6
1. Introduction	
1.1. Role and occurrence of eclogites	10
1.1.1. Mineralogy and phase relations	13
1.1.2. Role as diamond host	16
1.2. Thermodynamic principles	
1.2.1. Geothermobarometry	18
1.2.2. Basic principles of multi component mixing	21
1.3. Elasticity of silicate solid solutions	25
1.4. Fluorine in eclogite	29
2. Aims of the study	31
3. Methods	
3.1. Generating Earth's mantle pressures within the laboratory	33
3.1.1. Piston cylinder	34
3.1.2. Multi-anvil apparatus	35
3.1.3. Diamond anvil cell and heated diamond anvil cell	39
3.2. Single-crystal X-ray diffraction measurements	41
3.2.1. Equation of state	44
3.2.2. Pressure determination in the DAC	49
3.3. Analytical methods	
3.3.1. Scanning electron microscopy	52
3.3.2. Electron microprobe	53
3.3.3. Electron energy-loss spectroscopy	53
3.3.4. SHRIMP	54
4. Experimental calibration of a garnet-clinopyroxene geobarometer for mantle eclogites	
4.1. Introduction	56
4.2. Experimental methods	
4.2.1. Rationale	58
4.2.2. Starting material	59
4.2.3. High pressure experimental procedure	60
4.2.4. Analytical methods	63
4.3. Experimental results	
4.3.1. Textures and phase relations	63
4.3.2. Mineral chemical compositions	66
4.3.3. Melt analyses	73
4.3.4. Attainment of equilibrium	74
4.3.5. Thermodynamic model	76
4.4. Discussion	
4.4.1. Model uncertainties	85
4.4.2. Comparison with previous studies	87
4.4.3. Geobarometry of mantle eclogites	90
4.4.4. Summary	95
5. Experimental calibration of a geobarometer for majoritic garnets from the lowermost upper mantle and transition zone	
5.1. Introduction	97
5.2. Methods	100
5.3. Results and discussion	103

5.4. Comparison with other barometers	117
5.5. Application to natural majoritic inclusions in diamonds	119
5.6. Further applications to trace geological processes	122
5.7. Conclusions	126
6. P-V-T of complex garnet solid solutions up to 16 GPa and 800 K: Implications on the bulk modulus in aluminous garnet solid solution series	
6.1. Introduction	128
6.2. Methods	
6.2.1. Experimental rationale	131
6.2.2. Static compression experiments	132
6.3. Results and discussions	
6.3.1. Room temperature compression experiments	133
6.3.2. High temperature compression experiments	143
6.4. Conclusions and implications	146
7. Fluorine partitioning between eclogitic garnet, clinopyroxene, and melt at upper mantle conditions	
7.1. Introduction	150
7.2. Methods	152
7.3. Analytical methods	154
7.4. Results	154
7.5. Discussion	158
7.6. Geological implications	167
8. Final conclusions and outlook	173
Appendices	177
References	200
Erklärung	217

Abstract

Eclogite rocks, composed mainly of garnet and clinopyroxene, form principally as a metamorphic product of oceanic crust as it undergoes subduction. The equilibrium between garnet and clinopyroxene is sensitive to temperature and pressure, therefore eclogitic outcrops and xenoliths can reveal important information on the chemical and mineralogical processes occurring during such episodes. This is particularly the case for lithospheric eclogitic xenoliths from Archean cratons, which can potential reveal information on ancient (> 1 Ga) subduction events. To obtain information on the depth of origin of eclogitic xenoliths the first project of this thesis was designed to establish a thermodynamically grounded geobarometer, which is based on the incorporation of tetrahedrally coordinated aluminum in clinopyroxene coexisting with garnet:



The reaction was calibrated against high-pressure and high-temperature experiments carried out in the multi-anvil and piston-cylinder apparatus between pressures of 3 and 7 GPa and temperatures from 1200 to 1550 °C. Starting materials were hydrous and anhydrous synthetic mixtures of basaltic bulk compositions that yielded homogeneous biminerally garnet-clinopyroxene phase assemblages. The experimental data set was expanded by employing results from previous experimental studies conducted in eclogitic systems, which widened the range of applicable conditions and compositions. The calibration reproduces experimental pressures of biminerally eclogite assemblages, in addition to SiO₂-saturated and kyanite-bearing eclogites, to within 0.4 GPa at the 95 % confidence interval. The barometer was then used to examine equilibration pressures recorded by natural mantle eclogites from various xenolith locations covering a wide

pressure, temperature, and compositional range. The results seem to indicate that many eclogite xenoliths fall towards the hotter side of the range of geothermal temperatures displayed by peridotitic xenoliths from the same localities.

The second project calibrates the composition of majoritic garnets, which contain excess silicon substituted onto the octahedrally coordinated garnet site, coexisting with clinopyroxene as a function of pressure, temperature and bulk composition. Majorite substitution for a given bulk composition increases with pressure, and its proportion can in principle be used as a geobarometer. Single majoritic garnet crystals are found as inclusions in diamonds, which are generally used to support a sublithospheric origin in the deeper upper mantle or transition zone. The chemical compositions of such inclusions indicate that they have formed from a number of different lithologies, including mafic, ultramafic and pyroxenitic. These inclusions give important insight into the environment where diamonds crystallize and the evolution of deep subducted crustal material. The empirical barometer studied here is based on the three major majoritic substitutions: $2\text{Al}^{3+} \rightarrow \text{Mg}^{2+} + \text{Si}^{4+}$ (Mj), $\text{Mg}^{2+} + \text{Al}^{3+} \rightarrow \text{Na}^{1+} + \text{Si}^{4+}$ (NaSi), $\text{Mg}^{2+} + \text{Al}^{3+} = \text{Na}^{1+} + \text{Ti}^{4+}$ (NaTi), and the secondary effect of chromium on the stability of Mj. The barometer was calibrated against experiments conducted in the multi-anvil apparatus between pressures of 6 and 16 GPa and temperatures of 1000 to 1400 °C. In order to expand the applicability to a wide range of compositions experiments were performed in three different mafic compositions and in one pyroxenitic composition. Moreover, existing experimental data in mafic and ultramafic systems, including mid-ocean ridge basalts, kimberlite, komatiite and peridotite bulk compositions were included in the calibration covering pressures from 6 to 20 GPa and temperatures from 900 to 2200 °C. Applying the geobarometer to natural majoritic diamond inclusions reveals clearly that eclogitic and pyroxenitic inclusions form dominantly at conditions near the top of the transition zone (300-400 km). Peridotitic

inclusions, however, have formed generally at shallower depths ~200 km within the Earth's upper mantle. This may reflect the differences expected for the oxygen fugacity between peridotitic and eclogitic/pyroxenitic rocks. If diamonds form through the reduction of carbonate or CO₂ bearing melts then most peridotitic rocks would be already within the diamond stability field by depths of 200 km. At greater pressures carbon would remain immobilized as diamond and there is no mechanism by which new diamonds can form. Eclogitic rocks formed by the subduction of oceanic crust, however, should form an intrinsically more oxidized environment that remains within the carbonate stability field to much higher pressures. The diamond stability field would be eventually reached, however, due to either the effect of pressure on controlling Fe³⁺/Fe²⁺ equilibria or due to partial melting, which would preferentially remove ferric iron and lower the Fe³⁺/ΣFe of the residue, on which the oxygen fugacity is mainly dependent. In fact deep partial melting as slabs heat up may be the mechanism by which both the local oxygen fugacity is lowered, carbon is mobilized and pyroxenite rocks are formed, with the latter occurring through reaction with the surrounding peridotite.

The third project was focused on the elasticity of garnet solid solutions formed from eclogitic compositions. Garnet is an important mineral because it is a major phase in the upper mantle and dominates mafic rocks at these conditions. The elastic behavior of garnet solid solutions plays a role in the interpretation of seismic data and is important for estimating the density contrast between subducting slabs and the surrounding mantle. High-precision single-crystal X-ray diffraction measurements at high pressure have been conducted on three different ternary garnet solid solutions with varying chemical composition in order to examine possible non-ideal contributions to the volume and compressibility of garnet solid solutions. Furthermore one experiment has been conducted at high pressures and high temperatures to examine the effect of temperature on the

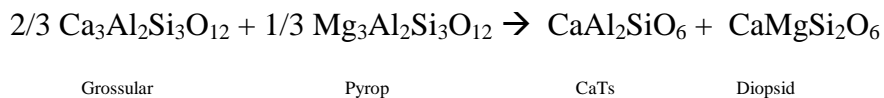
elasticity of complex garnet solid solutions. Experimental results reveal that the concentration of the almandine ($\text{Fe}_3\text{Al}_2\text{Si}_3\text{O}_{12}$) component has a significant effect on the elasticity, whereby 10 – 20 mole% of almandine is sufficient to overprint the previously reported minima of the bulk modulus along the pyrope-grossular join. It has also been shown that minor compositional variations of Ca and Mg within the Mg-Fe-Ca garnet ternary are not resolvable within the analytical errors. Therefore, the two eclogitic samples have similar bulk moduli within the analytical uncertainties. In contrast to previous studies, no evidence was found that garnets have a K' significantly different from 4. The high-temperature experiment revealed that the relatively small fraction of almandine in a solid solution increased the softening of garnet with temperature. Finally, the experimental volumes and calculated densities have been compared to the self-consistent thermodynamic model of Stixrude and Lithgow-Bertelloni (2005, 2011). The comparison clearly reveals that volume and elastic properties cannot be linearly interpolated as a function of composition. Moreover, it has been shown that the excess properties vary not only as a function of composition and pressure, but also as a function of temperature.

The final project is focused on the partitioning of fluorine (F) between garnet, clinopyroxene, and silicate melt within eclogitic compositions. Fluorine is the most abundant halogen on Earth and plays an important role in the formation of ultrapotassic lithologies, i.e. lamproites that contain several wt.% F, in contrast to the average lithospheric mantle that contains only tens of $\mu\text{g/g}$ F. The cycling and partitioning behavior of fluorine in the Earth's mantle are not well understood. High-pressure experiments have been conducted in the multi-anvil apparatus to obtain mineral-melt partition coefficients between garnet, clinopyroxene, and coexisting silicate melt of fluorine in a mafic system under conditions of the Earth's upper mantle. The results show that mafic crust can host significantly more fluorine than the surrounding ultramafic mantle, due to the much higher

proportion of clinopyroxene and its high fluorine partition coefficient of $D_F^{clinopyroxene/melt} = 0.057 - 0.074$. Combining the fluorine partitioning data with water partitioning data yields a plausible process to generate lamproitic magmas with a high F/H₂O ratio. The enrichment of fluorine relative to H₂O is triggered by multiple episodes of small degree melting which deplete the residual more in H₂O than in fluorine, caused by the approximately three times smaller mineral-melt partition coefficients of H₂O.

Zusammenfassung

Die vorliegende Arbeit befasst sich mit aus Granat und Klinopyroxen bestehenden Eklogiten, die als metamorphe Hochdrucksteine der ozeanischen Kruste subduziert werden. Eklogite-Aufschlüsse und Mantelxenolithe liefern wertvolle Informationen über die chemischen und mineralogischen Prozesse, die während der Subduktion ablaufen. Lithosphärische Eklogite aus Xenolithen von Archaischen Kratonen haben teilweise ein Alter von mehr als 1 Ga und liefern damit Informationen über Subduktionsprozesse der frühen Erde. Um den Druck und die Tiefe für die Entstehung von Eklogiten bestimmen zu können, wurde im ersten Kapitel ein Geobarometer entwickelt, welches auf thermodynamischen Parametern beruht, die den Einbau von vierfach koordiniertem Aluminium in Klinopyroxen im Gleichgewicht mit Granat beschreiben:



Die Kalibrierung des Barometers basiert auf Hochdruckexperimenten, die bei Drücken zwischen 3 und 7 GPa und Temperaturen von 1200 bis 1550 °C in Vielstempel- und Stempelzylinder-Pressen durchgeführt wurden. Die Startzusammensetzungen waren synthetische wasserhaltige und wasserfreie basaltische Gläser, die zu einer homogenen Mischung aus Granat und Klinopyroxen kristallisierten. Der Datensatz wurde mit Literaturdaten erweitert, um die Anwendung so universell wie möglich zu machen. Die Kalibrierung reproduziert experimentelle Drücke von bimineralischen Eklogiten mit 0.4 GPa innerhalb des 95 % Konfidenzintervalls. Das Barometer wurde bei natürlichen Eklogit-Xenolithen von verschiedenen Lokalitäten angewendet. Die Ergebnisse zeigen, dass viele Eklogit-Xenolithe bei höheren geothermischen Temperaturen equilibriert sind als Peridotit-Xenolithe von der gleichen Lokalität.

Im zweiten Kapitel wurde die Änderung der Zusammensetzung von majoritischen Granaten kalibriert, welche häufig als Einschlüsse in Diamanten aus großen Tiefen zu finden sind. Majoritische Granate sind anhand des überschüssigen Silikons zu erkennen, welches sechsfach koordiniert ist. Es gibt prinzipiell drei majoritische Phasentransformationen: $\text{Al}^{3+} = \text{Mg}^{2+} + \text{Si}^{4+}$ (Mj), $\text{Mg}^{2+} + \text{Al}^{3+} = \text{Na}^{1+} + \text{Si}^{4+}$ (NaSi), $\text{Mg}^{2+} + \text{Al}^{3+} = \text{Na}^{1+} + \text{Ti}^{4+}$ (NaTi) und zusätzlich den sekundären Einfluss von Chrom auf die Stabilität der Mj-Komponente. Diese majoritischen Substitutionen sind druckabhängig und lassen sich somit als potentiell Geobarometer nutzen. Ein Geobarometer kann Aufschluss über die Entstehungstiefe von Diamanten geben und inwiefern diese einen sublithosphärischen Ursprung im tieferen Erdmantel und der Übergangszone haben. Das Barometer wurde mit einer Vielzahl von Hochdruckexperimenten in unterschiedlichen mafischen Zusammensetzungen bei Drücken zwischen 6 und 16 GPa und Temperaturen zwischen 1000 und 1400 °C kalibriert. Der Datensatz wurde mit existierenden Experimenten in ultramafischen und mafischen Systemen erweitert. Die Kalibrierung wurde auf eklogitische, pyroxenitische und peridotische Granat-Einschlüsse in Diamanten angewandt und deren Druck zu bestimmen. Das Barometer zeigt eine bimodale Verteilung der Einschlüsse: Eklogitische und pyroxenitische Einschlüsse sind bei Drücken, die einer Tiefe von 300 - 500 km entsprechen, entstanden. Peridotitische Diamanten hingegen entstanden bei deutlich geringeren Drücken, die einer Tiefe von ungefähr 200 km entsprechen. Dies könnte ein Indiz für die unterschiedliche intrinsische Sauerstoff fugazität zwischen eklogitischen und peridotitischen Gesteinen sein. Falls Diamanten durch die Reduktion von Karbonat oder einem CO₂-führenden Fluid entstanden wären, wären Peridotite bereits bei einer Tiefe von 200 km innerhalb des Diamantstabilitätsfeldes entstanden. In größeren Tiefen ist Kohlenstoff in Form von Diamanten stabil und es gibt keinen bekannten weiteren Mechanismus durch den weitere Diamanten entstehen könnten.

Eklogitische Gesteine, als Produkte der metamorphen Umwandlung von ozeanischer Kruste, entstehen wahrscheinlich in einer Umgebung mit höherer Sauerstoffugazität was dazu führt, dass diese Gesteine das Diamantstabilitätsfeld erst bei höheren Drücken erreichen. Sie könnten das Diamantstabilitätsfeld erreichen, indem entweder durch den Druckeffekt das $\text{Fe}^{3+}/\text{Fe}^{2+}$ -Verhältnis geändert wird, oder indem durch partielles Aufschmelzen dreiwertiges Eisen bevorzugt in die Schmelze geht und somit das verbleibende Gestein reduziert wird. Das Aufheizen tief subduzierten Gesteins und das dadurch ausgelöste partielle Aufschmelzen könnte der Mechanismus sein, welcher die lokale Sauerstoffugazität verringert und Kohlenstoff mobilisiert. Der Kohlenstoff könnte somit durch Reaktion mit dem umgebenden peridotitischen Mantel pyroxenitische Lithologien formen.

Das dritte Kapitel behandelt die Elastizität von Granat-Mischkristallen mit komplexen Zusammensetzungen. Granate sind die wichtigste aluminiumführende Phase in mafischen Gesteinen des Erdmantels und spielen eine wichtige Rolle in der Analyse von seismischen Daten und der Interpretation von Dichtekontrasten zwischen subduzierten Platten und dem umgebenden Mantel. Zur Bestimmung des Kompressionsmoduls wurden hochpräzise Einkristall-Röntgenmessungen an komplexen Granat-Mischkristallen in der Diamantstempelzelle bei hohen Drücken und Temperaturen zur Bestimmung des Volumens und der Kompressibilität durchgeführt. Die Messungen zeigen, dass das eisenreiche Granat-Endglied Almandin ($\text{Fe}_3\text{Al}_2\text{Si}_3\text{O}_{12}$) einen starken Einfluss auf das Kompressionsmodul (K_{T0}) des Mischkristalls hat. Schon kleinere Mengen Almandin erhöhen das Kompressionsmodul des Mischkristalls erheblich. Im Widerspruch zu einigen anderen Studien, zeigte keiner der gemessenen Granate einen K'_{T0} deutlich größer als 4. Die Ergebnisse aus dem Hochtemperatur-Experiment zeigten, dass schon ein geringer Anteil an Almandin einen deutlichen Einfluss auf die Verringerung des

Kompressionsmoduls mit steigender Temperatur hat. Die experimentellen Ergebnisse wurden mit dem thermoelastischen Modell von Stixrude und Lithgow-Bertelloni (2005, 2011) verglichen. Dabei zeigte sich, dass in dem Modell nicht berücksichtigte Exzess-Volumina zur Kalkulation von falschen Volumina der Mischkristalle und deren Dichten führen. Darüber hinaus wurde festgestellt, dass Exzess-Volumina nicht nur eine Funktion von Druck und Zusammensetzung sind, sondern auch von der Temperatur abhängig. Daher ist es wichtig, dass Exzess-Volumina berücksichtigt werden, um anhand thermoelastischer Modelle Rückschlüsse aus seismischen Daten über die Zusammensetzung des Erdmantels zu ziehen.

Im letzten Kapitel wurde die Verteilung von Fluor (F) zwischen Granat, Klinopyroxen und silikatischer Schmelze bei hohem Druck bestimmt. Fluor ist das am häufigsten vorkommende Halogen im Erdmantel und spielt vermutlich eine wichtige Rolle bei der Entstehung von kaliumreichen Gesteinen, wie Kimberliten und Lamproiten, die mehrere Gewichtsprozent F enthalten können. Jedoch gibt es bisher nur wenige Studien, die sich mit dem Verteilungsverhalten und möglichen Reservoirs von F im Erdmantel beschäftigen. Die Ergebnisse zeigen, dass Klinopyroxen von den nominell fluorfreien Phasen den höchsten Verteilungskoeffizient hat und damit potentiell auch am meisten F speichern kann. Daher kann basaltische, subduzierte Kruste, welche reich an Klinopyroxen ist, relativ zum umgebenden ultramafischen Mantel, mehr Fluor transportieren. Durch die Kombination der F-Verteilungskoeffizienten mit Wasser-Verteilungskoeffizienten ist es möglich, durch wiederholtes partielles aufschmelzen von mafischen Fragmenten, F/H₂O-Verhältnisse zu generieren, die denen von Lamproiten entsprechen. Der Grund hierfür ist, dass der F-Verteilungskoeffizient für mafische Gesteine ca. dreimal höher ist als der entsprechende Wasser-Verteilungskoeffizient. Daher wird Wasser stärker im Residuum verarmt als Fluor.

1. Introduction

1.1. Role and occurrence of eclogites

A profound knowledge of subduction zone processes is crucial to understand the evolution, the past, and the present state of the Earth's interior. Since eclogites are considered as mafic oceanic crustal rocks they may be used to trace subduction zone processes (Helmstaedt and Doig, 1975; Jacob, 2004; MacGregor and Manton, 1986). Furthermore, eclogites are regarded as record of the evolution of cratonic lithosphere (Griffin et al., 2003; Rapp et al., 1991; Shirey et al., 2001). This record can be recovered by studying eclogitic xenoliths found in kimberlites which are interpreted as recycled subducted oceanic crust. Intriguingly, radiometric dating techniques reveal some eclogites to be Archean in age, providing the unique possibility to study subduction processes which were active during the early stages of Earth's history (Jacob et al., 1994). There is ample evidence that these eclogites are formed as high-grade metamorphic rocks developed by the continuous reaction of a basaltic precursor via amphibolite to eclogite within the subducting oceanic crust (Hacker, 1996; Helmstaedt and Doig, 1975; MacGregor and Manton, 1986).

There are several hypothesis on how eclogites are formed. Eclogite rocks are formed either from mafic protoliths (i.e. basaltic magmas on mid-ocean ridges), within high grade metamorphic belts (i.e. Weißenstein eclogite in the Münchberg gneiss complex, Germany), and in ultra-high pressure terrains (i.e. Dora-Maira Massif, Alps) where their presence indicates pressures of at least 1 GPa (Liou et al., 2009), or are formed as mantle xenoliths in kimberlites erupted within the cratonic lithosphere, in which the occasional presence of diamonds indicates equilibration pressures of at least 4 GPa i.e. greater than 120 km depth (Jacob, 2004; Schulze, 1989). It has also been suggested that cold subducting slabs, especially their upper eclogitic layers, are denser than the surrounding mantle, and can

therefore penetrate into the transition zone due to their density larger than the surrounding peridotitic material, and are incorporated into the source of ocean island basalt (OIB) (Hofmann and White, 1982; Sobolev et al., 2005) (Fig. 1.1.1). From a geophysical point of view, it is assumed that eclogites are an important contributor to the density distribution observed in the Earth's upper mantle and the adjacent transition zone (Irifune and Ringwood, 1993; Kesson et al., 1994).

However, it has also been proposed that at least some eclogite xenoliths are magmatic rocks formed as deep seated cumulates (Hatton and Gurney, 1987; O'Hara, 1969; O'Hara et al., 1975; Smyth et al., 1989; Taylor and Neal, 1989). This hypothesis requires that eclogites crystallized from cumulates of primary melts with garnet and clinopyroxene as the first phases forming from the cooling melt. But the problem with the "mantle hypothesis" is that these phases are together at the liquidus at relatively high pressures (2.5 GPa), only. For that reason, melt derived eclogite could only originate deeper in the mantle and not from olivine tholeiites which form around 1.5 – 1.7 GPa from the partial melting of peridotite as it was argued by Jacob (2004). An example for this mechanism is the Zero eclogite of the Kuruman group, South Africa which may have been formed from cumulates of picritic melts (Schmickler et al., 2004).

Eclogites can be seen as "messengers" probing the Earth's mantle and are exceptionally important for our understanding of processes in the deeper Earth. Due to their potentially central role in the formation and evolution of the cratonic lithosphere it is important to be able to reconstruct the pressure and temperature conditions at which eclogitic xenoliths last equilibrated.

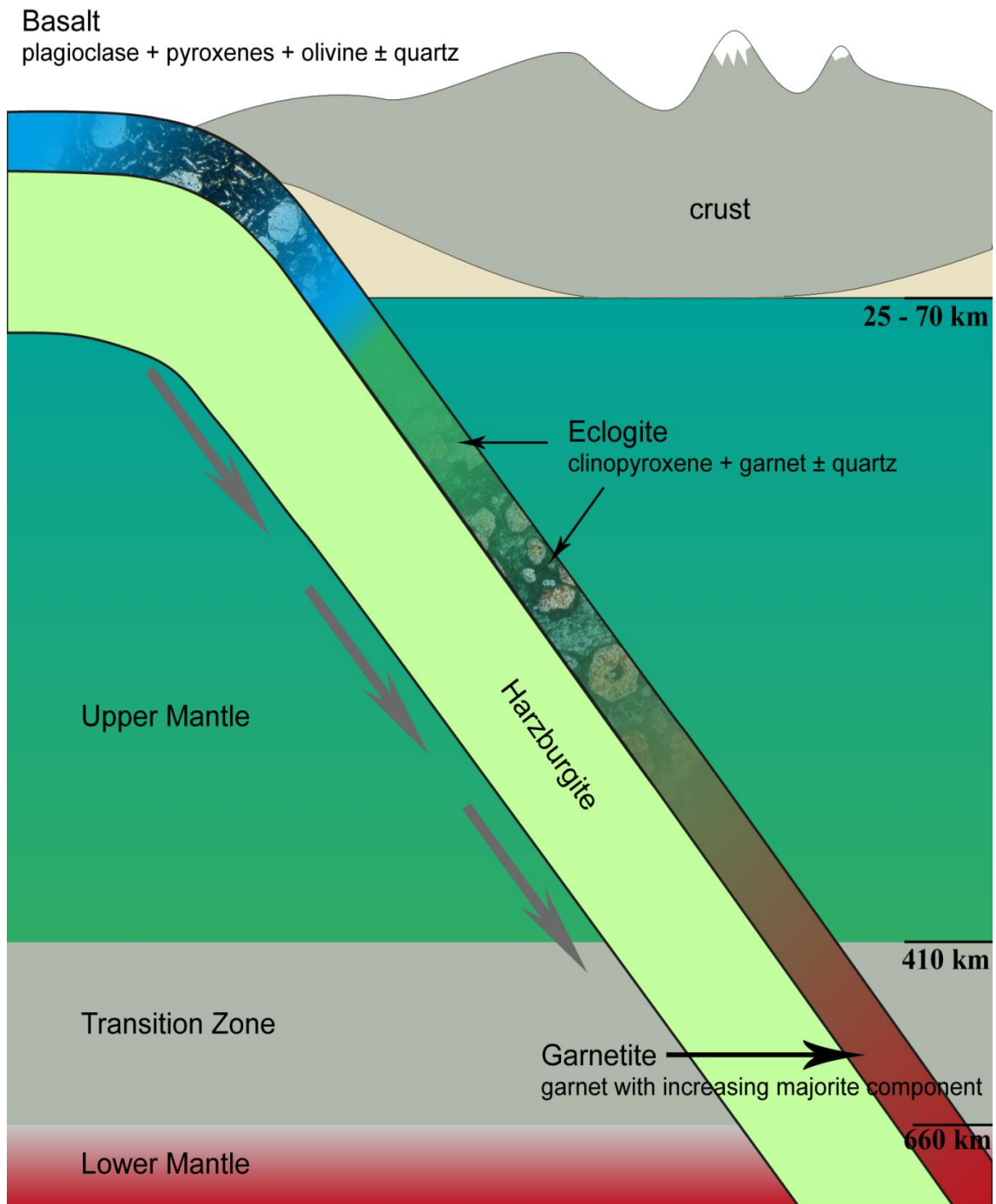


Fig.1.1.1 Schematic section through a generic subduction zone showing the basalt to eclogite to garnetite transformation. The scale is exaggerated for the purpose of illustration and is not representative.

1.1.1. Mineralogy and phase relations

In order to gain a comprehensive knowledge of petrological processes within the deeper Earth a thorough understanding of the effect of composition, pressure, and temperature on mineral solid solutions is essential. Since the majority of minerals form complex solid solutions, knowledge of mixing behavior is necessary to construct models which can be used to extrapolate laboratory measurements conducted over a restricted range of pressures, temperature, and compositions of the Earth's interior.

In the specific case of eclogite, garnet (grt) and clinopyroxene (cpx) form extensive solid solution series. These solid solutions comprise a large proportion of the subducted oceanic lithosphere in the Earth's mantle (Anderson, 1979; Lin-Gun, 1980; Rapp et al., 2003). During subduction of the oceanic crust the basaltic precursor, basically consisting of olivine, pyroxene, and plagioclase is transformed into eclogite, mainly composed of garnet and clinopyroxene (Coleman et al., 1965; Green and Ringwood, 1967) (Fig. 1.1.1.1). At pressures above ~5 GPa the MgSiO_3 and FeSiO_3 pyroxene components start to dissolve as majoritic components into the garnet transforming the garnet in a silica-rich garnet (Akaogi and Akimoto, 1977; Irifune, 1987; Irifune, 1993; Irifune et al., 1986). This transformation is approximately completed at mid-transition zone conditions of about 15 GPa (Irifune, 1987). Below the TZ majoritic garnet decomposes into calcium perovskite from its Ca component and magnesium perovskite from its Mg-Fe component (Harte, 2010). Remaining elements such as sodium and aluminum are incorporated into the calcium-ferrite phase (cf) and new aluminum-rich phase (NAL) (Hirose et al., 1999; Hirose et al., 2005; Perrillat et al., 2006). The mafic layer of subducted oceanic lithosphere is therefore comprised of Ca-rich, Cr-poor garnet and omphacitic pyroxene between approximately 60 and 450 km depth, gradually transformed into garnetite with increasing majorite content down to 660 km depth (i.e. Irifune et al., 1986). In this depth interval major changes in

chemistry and phase proportions happen which affect the density and as a consequence the buoyancy of the subducted material (Aoki and Takahashi, 2004; Irifune et al., 2008; Irifune and Ringwood, 1993). The compositional change with pressure and temperature in basaltic systems has been studied intensively over the last few decades (Aoki and Takahashi, 2004; Irifune, 1993; Okamoto and Maruyama, 1998, 2004; Ono et al., 2001; Ono and Yasuda, 1996; Yasuda et al., 1994). However, little attention has been paid on fractional changes in bulk composition and on their effect on majorite phase transformation and phase proportions.



Fig. 1.1.1.1 Typical bimineralic eclogite from the Mariánzke Lázně complex in the Czech Republic, Kelee Collection (Ian Geoffrey Stimpson @ flickr.com). Reddish crystals are garnets whereas green crystals are clinopyroxenes.

A number of studies have identified natural majoritic garnets with estimated pressures of equilibration ranging up to 400 km (12-13 GPa) (Haggerty and Sautter, 1990). However such pressure estimates are based on very little experimental data applicable to only a limited range of compositions. Irifune et al. (1986) for example has performed an experimental study on the eclogite to garnetite transformation at 1200°C in a simplified system. Subsequently, Aoki and Takahashi (2004) expanded this study to a wider temperature range from 1200 to 1700 °C. The key phase transformation in a basaltic regime is the gradual solution of clinopyroxene in majoritic garnet that shifts the modal composition to garnetite (Anderson, 1979; Irifune et al., 1986; Sekine et al., 1986) (Fig. 1.1.1.2).

Okamoto and Maruyama (2004) conducted experiments in the MORB + H₂O system at 10–19 GPa and found that significant amounts of water are stored in all nominally anhydrous silicates. They identified three different types of formerly proposed majorite substitution mechanism in garnet, which are Na + Ti = Ca + Al (Ringwood and Lovering, 1970), Na + Si = Ca + Al (Ringwood and Major, 1971; Sobolev and Lavrent'ev, 1971) and Na + Si = Mg + Al (Gasparik, 1989).

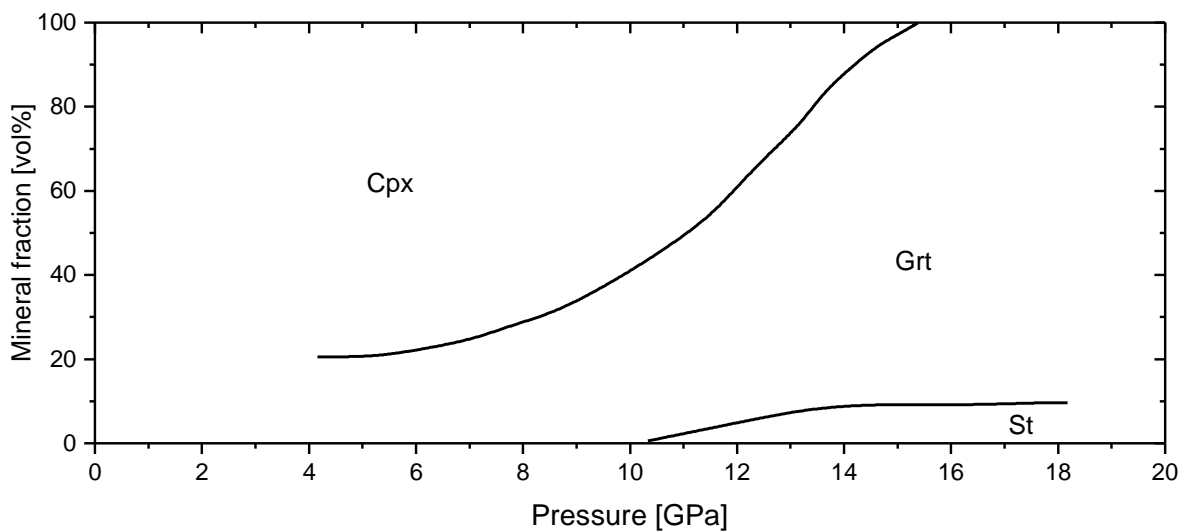


Fig. 1.1.1.2 Change of modal composition with pressure in an olivine tholeiite composition (after Irifune et al. 1986). Cpx = clinopyroxene, Grt = garnet, St = stishovite

In Chapter 5 the bulk chemical effect on the different majorite substitutions will be discussed and as well as the implications this has on the onset of the clinopyroxene to garnet transformation and its applicability to geobarometry. The effect of mixing on the volume of aluminous garnet solid solutions will be investigated in Chapter 6.

1.1.2. Role as diamond host

Eclogitic xenoliths are of economic interest due to their higher yield of diamonds relative to peridotitic xenoliths (Cartigny, 2005; Stachel and Harris, 2008). Eclogitic rocks account for only a small percentage of mantle xenoliths (Schulze, 1989; Sobolev, 1977), but their significance outweighs their abundance for several reasons. Schulze (1989) concluded, based on heavy mineral concentrates extracted from kimberlites, that eclogite probably represents less than 1% of the upper 200 km subcontinental mantle. This is in contrast with the analysis of 2844 inclusion in diamonds where the relative abundance of eclogitic inclusions is 33% (Fig. 1.1.2.1).

Also, it is intriguing that some eclogites contain both diamond and graphite, suggesting conditions close to the graphite-diamond phase boundary (Hatton and Gurney, 1979; Robinson, 1979).

Inclusions in diamonds with a metabasic/eclogitic origin are predominately formed from depth around 300 – 500 km whereas inclusions in diamonds from greater depth are mostly peridotitic (Harte, 2010). This contradicts the findings of Haggerty (1986) who proposed that in a cratonic environment eclogitic diamonds were formed under higher pressure than peridotitic diamonds. The nature of this distribution is unclear and needs clarification (Stachel and Harris, 2008; 2009). Hence, to understand the above described discrepancies between observed and calculated abundances of diamond-bearing eclogites, precise determination of the last equilibration conditions is necessary. Geobarometry may shed light on the evolution and emplacement of diamonds and the cycle of carbon in the Earth's mantle. In addition, a barometer applicable to mineral inclusions in diamonds might be a useful tool for the economic prospection and evaluation of diamond deposits. In the upcoming Chapters two different approaches will be presented to obtain the depth of

formation of xenoliths hosting diamonds in the upper mantle (Chapter 4), and of mineral inclusions in diamonds from the lowermost upper mantle and transition zone (Chapter 5).

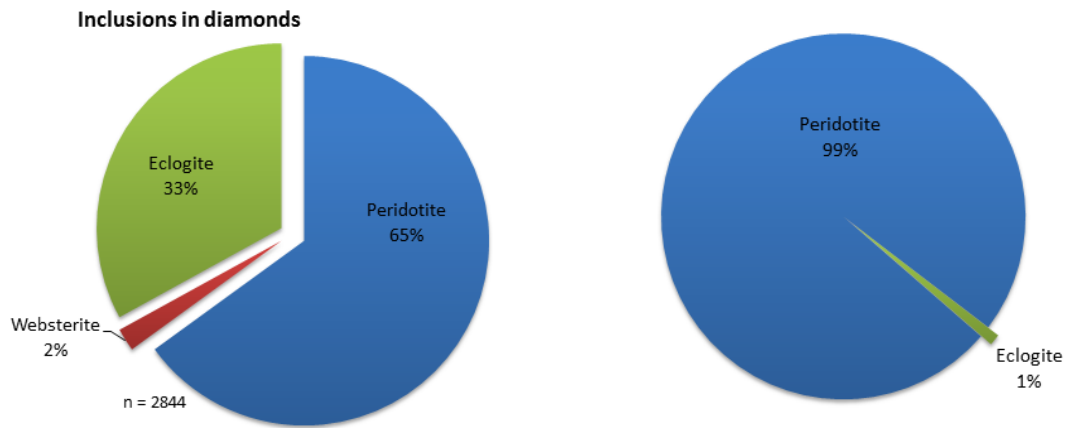


Fig. 1.1.2.1 The left diagram shows the result of the analysis of 2844 inclusions in diamonds from Stachel and Harris (2009). The right diagram represents the calculated amount of eclogite within the upper 200 km of the subcontinental mantle (Schulze, 1989). The discrepancy between the amount of diamonds from eclogitic environments and the amount of eclogite present in the upper mantle is evident.

1.2. Thermodynamic principles

1.2.1. Geothermobarometry

In petrology, geothermobarometry is routinely used to gain knowledge on the pressure and temperature of last equilibration of metamorphic mineral assemblages. To obtain a geothermobarometer either equilibrium thermodynamics is applied to a clearly defined mineral reaction or a large set of experimental data is used to obtain an empirical calibration. This study makes use of both techniques. In Chapter 4 a self-consistent thermodynamic formulation has been derived to obtain the pressure of formation of eclogites in the upper mantle, whereas, in Chapter 5 an empirical calibration has been used to calculate pressures of majoritic garnets from the lowermost upper mantle and transition zone. Hereafter, the principles of the underlying thermodynamics of the former barometer will be introduced.

A good geobarometer usually is based on reactions which involve a large change in volume and therefore is very sensitive to changes in pressure (Fig 1.2.1.1). In order to setup a reaction-based thermodynamic geobarometer the following parameters are required:

- Reaction with a significant change in volume
- Thermodynamic data of all phases involved in the chosen reaction
- Chemical components of the system
- Mixing properties of possible solid solutions.

A number of studies have been performed to understand the formation conditions of eclogitic outcrops and xenoliths. Ellis and Green (1979) and Krogh (1988) calibrated Fe-Mg exchange between clinopyroxene and garnet in order to use it as a geothermometer; however this calibration does not take into account the large jadeite component in mantle eclogites and moreover it is calibrated at relatively low pressures. A more recent empirical

thermometer takes into account a large number of chemical parameters which enhances the applicability to more complex systems, and a wider range of pressure and temperature (Nakamura, 2009).

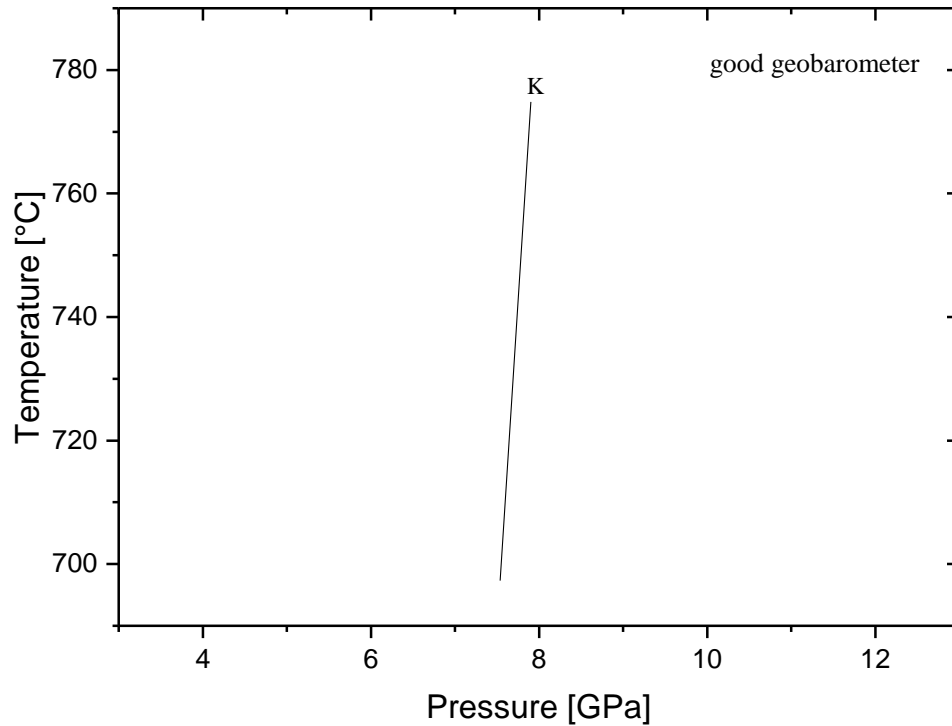
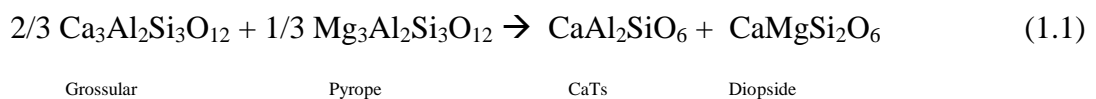
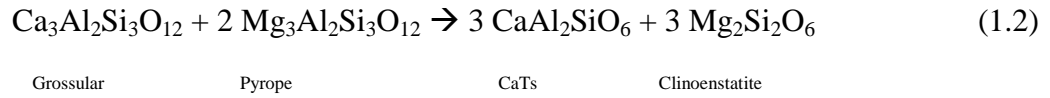


Fig. 1.2.1.1 The line represents the equilibrium constant K of an ideal geobarometer plotted in the P-T space. The reaction is mostly dependent on pressure rather than on temperature. An ideal geothermometer would be depicted as a perpendicular line in P-T space.

Furthermore, there are several barometers using the garnet-clinopyroxene assemblage and Al-bearing pyroxene end-members to estimate the pressure of mafic and ultramafic rocks (Brey et al., 1990; Mukhopadhyay, 1991; Simakov, 2008; Simakov and Taylor, 2000). The most promising candidate geobarometer based on Ca-Tschermaks in clinopyroxene (CaTs) coexisting with garnet was introduced by Mukhopadhyay (1991):



and modified by Simakov and Taylor (2000) using the reaction:



Unfortunately, most of the thermodynamic parameters for clinopyroxene are not well known and have to be inferred from other end-members. A detailed discussion on how these parameters have been derived in the present study is given in Chapter 4.

To use the above described equation the following conditions at the P and T of equilibrium must be fulfilled:

$$\Delta G_{P,T}^0 = -RT \ln K \quad (1.3)$$

with

$$\Delta G_{P,T}^0 = \Delta H + \int Cp \, dT - T \left(\Delta S + \frac{\int dCp}{TdT} \right) + (P - 1) \Delta V^0 \quad (1.4)$$

where Cp being the heat capacity, T the temperature in K, ΔH the enthalpy, ΔV^0 the volume change of the reaction at reference conditions.

Rearranging equation (1.3) and substituting and integrating equation (1.4) gives the following expression for pressure:

$$P = [-\Delta G_{T,1bar}^0 + RT \ln K] / \Delta V_r \quad (1.5)$$

where K is the product of the ideal contribution of molar mixing K_x and the non-ideal contribution K_y , and ΔV_r is the volume change of the reaction. $\Delta G_{T,1bar}^0$ is based on a regression of standard state end-member data over a suitable P-T range for the upper mantle.

The ΔV_r of the reaction has been inferred from the average volume change based over a pressure/temperature range corresponding to the P-T limits of the barometer. The same procedure has been applied for the calculation of $\Delta G_{T,1bar}$. Although this seems a rather severe simplification, it can predict experimental conditions quite well within the given P-T range under the assumption, that the effects of pressure and temperature on the volume change basically cancel each other out.

Nimis and Taylor (2000) calibrated the Cr-in-cpx barometer and an enstatite-in-cpx thermometer in the CMS and CMAS-Cr system as an alternative to the Al-in-cpx thermobarometers. Its application to eclogites is rather limited, due to the very small amount of Cr in basaltic systems. The clinopyroxene solid solution in particular is complex in composition and a description with simple binary or ternary thermodynamic models (Berman and Koziol, 1991; Cheng and Ganguly, 1994; Gwanmesia et al., 2000) is far from applicable to the multicomponent solid solutions found in the Earth, because the existing data sets are not sufficient to describe the large number of mixing parameters in natural systems (Geiger, 2000; Mukhopadhyay et al., 1993). For this reason developing thermometers and geobarometers that can be used on eclogitic rocks over natural ranges of composition has been elusive.

1.2.2. Basic principles of multi component mixing

As already highlighted in Section 1.1, minerals form a wide range of solid solutions, depending on pressures, temperature, and bulk composition. In particular, garnet and

clinopyroxene show a high thermodynamic variance, because they can incorporate the majority of common divalent (Mg, Fe, Mn, Ca) and trivalent (Fe, Al, Cr) cations. The majority of solid solutions do not mix ideally, i.e. their properties cannot be described by a simple linear combination of the end-member properties. For that reason, formulations have been employed to describe the non-ideal contribution as excess properties. The excess properties in volume, enthalpy, and entropy all contribute to the total excess energy, usually expressed as excess Gibbs free energy. In this study excess mixing parameters of clinopyroxene solid solutions have been refined based on a large number of experimental data to better account for complex mixing behavior (Chapter 4). In Chapter 6 the concept of excess properties has been applied to the excess volume of mixing of aluminous garnets. The volumes are based on high precision single-crystal X-ray diffraction compression data as given in Chapter 6 (Table 6.5 and 6.6). In this Chapter the basic principles of multi-component mixing is briefly described. Since, basically all silicate minerals form non-ideal solid solutions (Wood and Fraser, 1978) it is necessary to introduce formulations which describe the activity relationship within a certain composition:

$$a_i^j = X_i^j \gamma_i^j \quad (1.6)$$

X_i describes simple mixing based on the mole fraction X of compound i . γ_i is the activity coefficient describing the deviation from the ideality. If the activity coefficient equals one the requirements for ideal mixing are fulfilled. The thermodynamic description of ideal mixing of pure phases can be expressed as simple mixing of the molar proportions of each phase:

$$G_{mix} = nRT(X_A \ln X_A + X_B \ln X_B) \quad (1.7)$$

where G_{mix} is the Gibbs free energy of mixing, R is the gas constant, T is the temperature in K, n is the number of moles, and X_A/X_B is the fraction of the A and B components.

In case of non-ideal mixing where the phases are not pure and consist of solid solutions the non-idealities described as excess properties have to be added to the above expression according to:

$$G_{mix} = nRT(X_A \ln X_A + X_B \ln X_B) + nX_A X_B W_G \quad (1.8)$$

The first part describes the ideal contribution based on mole fractions of each compound (X_A/X_B) equal to Eq. 1.7. The second part represents the excess contribution (G_{xs}) to the Gibbs free energy of mixing given as activity coefficients. The term W_G is the Margules interaction parameter, accounting for effects of non-ideal mixing between components of the solid solution. For example, the activity coefficient in a symmetric binary solution is given by:

$$RT \ln \gamma_A = W_G (1 - X_A)^2 = W_G X_B^2 \quad (1.9)$$

The excess Gibbs energy G_{xs} , is then a symmetric parabola (1.2.2.1).

$$G_{xs}(sym) = W_G X_A (1 - X_A) \quad (1.10)$$

where W_G describes the interaction energy between A and B. However, mixing can also be asymmetric, e.g. in the pyrope-grossular binary where the magnitude of deviation from ideality of the excess volume and excess heat of mixing is shifted towards the Ca-rich site (Berman, 1990). In this case it is necessary to treat the solid solution with a more

sophisticated formulation where two W terms (W_{AB} and W_{BA}) can account for asymmetry in the system. The formulation for an asymmetric binary solid solution is therefore:

$$RT\ln\gamma_A = X_B^2(W_{AB} + 2X_A(W_{BA} - W_{AB})) \quad (1.11)$$

Expressed in terms of G_{xs} , Eq. 1.11 yields an oblique parabola:

$$G_{xs}(asym) = X_A X_B (W_{AB} X_B + W_{BA} X_A) \quad (1.12)$$

shown in Fig. 1.2.2.1. This approach will be applied to garnet and clinopyroxene solid solutions and extended to ternary and quaternary cases. A detailed description of the applied formulations is given in Chapter 4.

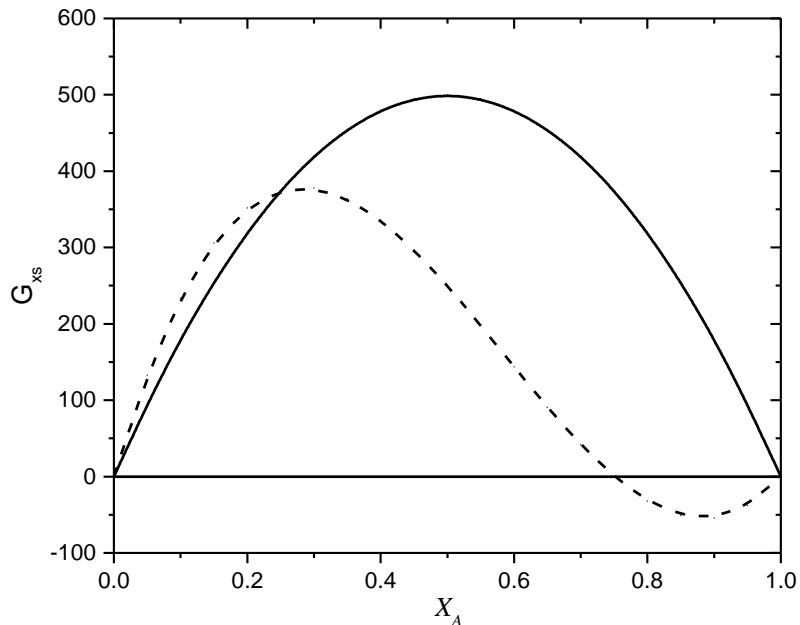


Fig. 1.2.2.1 The excess contribution in joules to G shown as a function of composition. The solid lines represents symmetric mixing with its maximum at $X = 0.5$ and $W_G = 2000$ J. The dashed line depicts a asymmetric solid solution with $W_{AB} = 3000$ J and $W_{BA} = -100$ J.

1.3. Elasticity of silicate solid solutions

Elastic properties are a key to the deeper understanding of Earth's hidden interior. Since seismic waves are the only direct observation of the physical properties of the deeper Earth, a thorough understanding of the elastic properties (i.e. bulk modulus K , and shear modulus μ), which can be related directly to the seismic wave speeds V_P (Eq. 1.13) and V_S (Eq. 1.14), are mandatory to improve the interpretation of seismic models and to reveal the structure of the Earth's mantle.

$$V_P = \sqrt{\frac{(K_S + \frac{4}{3}\mu)}{\rho}} \quad (1.13)$$

$$V_S = \sqrt{\frac{\mu}{\rho}} \quad (1.14)$$

with the adiabatic bulk modulus K_S , the shear modulus μ , and the density ρ . Aggregate sound velocities of eclogites are calculated to be 2 to 6% faster than the surrounding peridotite, depending on the amount of high pressure silica polymorphs present and on the degree of hydration (Connolly and Kerrick, 2002; Helffrich et al., 1989). Furthermore, eclogitic minerals, omphacite (3.2 – 3.4 g/cm³) and garnet (3.6 – 4.0 g/cm³) have a significantly higher combined density than basalt (2.9 g/cm³) in the uppermost part of the mantle (Carmichael, 1989).

However, the difference in sound velocities between subducted oceanic lithosphere and the asthenosphere appears to be mainly accounted by the thermal difference between cold subducting slabs and hotter surrounding mantle (Helffrich et al., 1989). To assign variations

in velocities either to thermal differences or to phase transitions a comprehensive understanding of the excess contributions from solid solutions to the latter is required.

End-member elastic properties have been studied in great detail for the last fifty years, and the understanding of the elasticity and density of garnet and clinopyroxene solid solution have been improved step-by-step over the last decades (Berman and Koziol, 1991; Conrad et al., 1999; Ganguly et al., 1996; Ganguly and Saxena, 1984; Geiger, 1999; Isaak and Graham, 1976; McCormick et al., 1989; Nishihara et al., 2003; O'Neill et al., 1989; Pavese et al., 2000; Pavese et al., 2001b). As a first approximation, the bulk modulus (K) of aluminous garnet solid solution can be described by the weighted sum of the end-member moduli expressed in terms of grossular, almandine, spessartine, and pyrope (O'Neill et al., 1989):

$$M_{SS} = \sum f_i M_i \quad (1.15)$$

where f_i is a weighing factor, i.e. volume or molar fraction, and M_i the end-member property of compound i . Although Bass (1989) found that some garnet solid solutions can be recalculated from end-member elasticity within 3%, he pointed out that a linear modulus relationship is not appropriate for all silicate garnets.

Sinogeikin and Bass (2002) found that the commonly used high-temperature pyrope-rich garnet elastic properties of Suzuki and Anderson (1983) are clearly different from pure pyrope, suggesting that although the fraction of almandine is only 16% it has an unusual large effect on the high-temperature softening of garnet solid solutions.

To date, there is a clear discrepancy between different studies for similar compositions in terms of K and K' , which are required to calculate sound velocities (Fig 1.3.1). For

example, the values of the isothermal bulk modulus (K_{T0}) for pure almandine vary between 185(3) GPa (Zhang et al., 1999) and 168(5) GPa (Takahashi and Liu, 1970). In addition, different measurement techniques are not consistent with each other. In particular the values of K'_{T0} derived from ultrasonic studies are larger than those obtained from X-ray diffraction or Brillouin spectroscopy measurements. Good examples for the discrepancy on garnet end-member in K'_{T0} are almandine and grossular. In case of grossular, ignoring the studies with fixed K'_{T0} , the majority of studies reproduce a value of $K'_{T0} \sim 6$, besides the study of Jiang et al. (2004) which reports $K'_{T0} = 3.9(2)$. Even more diverse are the reported values for almandine, for which the values of K'_{T0} range between 4.2(3) and 6.2(5) depending on the chosen measurement method. Beside different methods, also the pressure calibrant used may play a role on the discrepancies observed. In a study of Zha et al. (1998) the difference in pressure determination between the ruby scale and the absolute pressure obtained from Brillouin spectroscopy is 1.6%. It is of great importance therefore to understand the influence of the measurement technique, pressure transmitting medium, pressure gauge, and pressure range on the obtained elastic parameters.

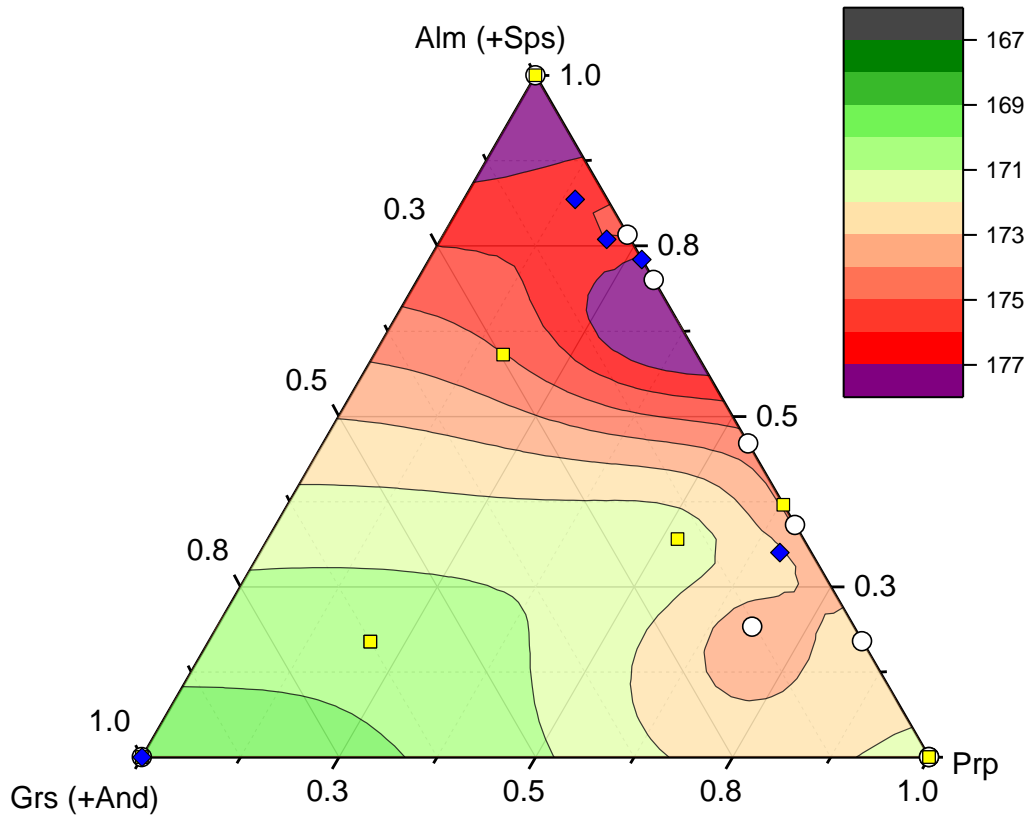


Fig. 1.3.1 Ternary diagram of aluminous garnet end members. The contouring depicts K_{T0} whereas the axes represent mole fractions of garnet end members. Symbols mark K_{T0} measured in previous studies by P-V fitting using compression data obtained with high-pressure X-ray diffraction (white circle) (Duba and Olinger, 1972; Hazen et al., 1994; Pavese et al., 2001b; Takahashi and Liu, 1970; Zhang et al., 1998; Zhang et al., 1999) or Brillouin spectroscopy (yellow square) (Chai et al., 1997; Conrad et al., 1999; Jiang et al., 2004; O'Neill et al., 1989; Webb, 1989), and single crystal ultrasonic measurements (blue diamonds) (Babuška et al., 1978; Chen et al., 1997; Isaak and Graham, 1976; Verma, 1960; Wang and Huang, 1975; Wang and Simmons, 1974). There is an apparent lack of data within the ternary to fully describe mixing and a discrepancy between the measurement methods. Therefore, the contouring is an interpolation representing the mean of all experiments.

A non-linear elastic behaviour of a mineral with pressure and temperature also may have implications for the complex structure and stiffness of subducted slabs and the density contrast between eclogite and the surrounding ultramafic mantle, which would directly influence the type of subduction. Elasticity of orthopyroxene (opx) is a good example, while opx has a lower bulk modulus, in the uppermost upper mantle, it becomes faster than olivine at depth of around 200 km as a result of its lower bulk modulus (Bina and Helffrich, 2014; Flesch et al., 1998).

Non-ideal effects of elastic properties could give a different interpretation of seismic measurements and our understanding of the chemical composition of the deeper Earth.

1.4. Fluorine in eclogite

Fluorine (F) is the most abundant element among the halogens (F, Cl, Br, I), and it is one of the most common volatiles in the Earth and in planetary systems (Palme and O'Neill, 2003). Halogens, and in particular fluorine, have a noticeable influence on magmatic processes (Filiberto et al., 2012; Luth, 1988) and behave similar to hydroxyl (OH⁻), because both have the same charge and very similar ionic radii, 1.33 Å vs 1.37 Å for 6-fold coordination (Shannon, 1976). Hence, it is likely that fluorine is also cycled from the surface into the mantle and back again in the same manner as water (Hofmann and White, 1982; Ito et al., 1983).

Over the last couple of years there has been renewed interest in the fate and cycling of fluorine and in its partitioning behavior in nominally fluorine free minerals (NFFMs). It has been shown that NFFMs are suitable to account Earth's F budget without invoking fluorine-bearing phases such as phosphates, humite-group minerals, and micas (Beyer et al., 2012; Dalou et al., 2012). Although recent studies shed light on the role of fluorine in Earth's upper mantle it is still not thoroughly understood how and to what extent fluorine is incorporated into the subducted oceanic crust and its major phases. Moreover, the partitioning behavior of fluorine under high pressure and high temperature has not been studied, yet. Due to their high modal abundance and wide range of stability, fluorine concentrations in major rock forming minerals phases like olivine and pyroxenes are sufficient to explain Earth's fluorine budget. Though, the fate of fluorine when the subducting slab is entering Earth's transition zone and its role in high-pressure phase transitions is yet unknown. The elevated fluorine concentrations in ocean island basalt,

kimberlites and lamproites (Aoki et al., 1981) yield evidence that fluorine is possibly enriched in a deep mantle reservoirs where these magma types pass or originate. Hence, the partitioning of fluorine between garnet, clinopyroxene, and silicate melt at conditions of the upper mantle will be discussed in Chapter 7.

Fluorine concentrations were analyzed using Sensitive High Resolutions Ion Microprobe (SHRIMP) to obtain precise and accurate fluorine concentrations.

2. Aims of the study

This study is aimed at the investigation of chemical and elastic properties of complex natural-like garnet and clinopyroxene in a mafic environment under upper mantle and transition zone conditions. In Chapter 4 and 5 two barometers are set up to precisely determine the last pressure of equilibration of xenoliths from the upper mantle and transition zone. These barometers may help to identify the origins of mantle xenoliths and inclusions in diamonds, hence revealing the state and evolution of their source regions. The static compression data at high P/T on complex garnet solid solution presented in Chapter 6 addresses the issue of contradicting experimental results on K_0 and K_0' of aluminous garnets found in the literature. The influence of non-ideal mixing on the recalculation of solid solution from end-member based thermodynamic models is discussed. Chapter 7 covers the partitioning behavior of the most abundant halogen fluorine between garnet, clinopyroxene, and melt at conditions of the upper mantle. The fluorine partitioning data are combined with water partitioning data from the literature to explain how fluorine-rich ultrapotassic lithologies may have been formed and where fluorine in mafic material resides.

- The first part of the thesis deals with the calibration of a geobarometer for application on natural biminerally eclogites, solely based on garnet and clinopyroxene. High pressure experiments between 3 and 7 GPa with various MORB bulk compositions were conducted to set up a thermodynamic self-consistent geobarometer based on end-member properties obtained from thermochemical data sets and newly derived excess mixing terms from high-pressure experiments and existing studies.

- The next step is to set up a geobarometer applicable to the lowermost upper mantle and transition zone, where the majoritic end-members become dominant in garnet solid-solutions. An empirical barometer is described, which is on phase equilibrium data from experiments conducted up to pressures of 16 GPa and temperatures between 1000 and 1400 °C with different mafic starting compositions. By using high pressure experimental data from previous studies the barometer is extended to peridotitic and pyroxenitic bulk compositions. The empirical calibration will be solely based on the chemistry of majoritic garnet, which makes it applicable to majoritic inclusions in diamond.
- In Chapter 6 accurate determinations of thermodynamic properties on complex garnet solid solutions is used to examine how the properties of the end-members are linked to this multicomponent system. Large single crystals of garnet recovered from experiments with different bulk compositions are examined in the diamond anvil cell to determine compression behavior as a function of pressure, temperature and chemical composition. High-pressure, high-temperature compression experiments will be performed to approximately 16 GPa and 550 °C.
- In the last Chapter element partitioning coefficients of fluorine between garnet, clinopyroxene and coexisting hydrous silicate melt are determined to understand the role of halogens during the subduction of eclogitic material. This part is aimed to reveal the fate of F during the descent into Earth's mantle and its possible influence on magmatic processes. Moreover, partition coefficients are used to quantify possible storage capacities of F in deep subducted eclogites and the recycling into plume environments such as OIBs, kimberlites, and lamproites.

3. Methods

3.1. Generating Earth's mantle pressures within the laboratory

The generation of high pressures and high temperatures corresponding to the conditions of the Earth's deep interior have a rather short history in geosciences. In the late 1950s and early 1960s, several efforts have been made to develop high pressure apparatuses which overcome the limitations of uniaxial piston cylinder-like devices (Bundy, 1962; Hall, 1958, 1960; Weir et al., 1959). The piston cylinder apparatus was the first high-pressure device to reach conditions of the Earth upper mantle with pressures up to 7 GPa and temperatures up to 2000 °C (i.e. Boyd and England, 1960) with sample volumes as large as 500 mm³ depending on the pressure of interest. In order to reach higher pressures, two very distinct types of techniques: the multi-anvil apparatus (MA) with several stages of anvils and the diamond anvil cell (DAC) with two opposing diamonds for pressure generation (Fig. 3.1.1) have been developed. These devices have different applications.

The MA is basically used to produce relatively large samples in the cubic millimetre range, and to conduct high pressure deformation experiments (Cordier and Rubie, 2001); however pressures are limited to ~26 GPa using WC anvils (Frost et al., 2004; Rubie, 1999) but can reach up to 60 GPa using sintered diamond anvils (Ito et al., 2005; Ohtani et al., 1989; Tange et al., 2008). Due to the installation of MAs at 3rd generation synchrotron facilities (Spring 8, ESRF, APS, Petra III, Australian Synchrotron) it has become possible to use in situ X-ray methods and MA together, opening up new possibilities to study larger sample volumes *in-situ*.

The DAC is mainly used to reach pressures up to several hundred Mbar, temperatures more than 5000 K and to conduct in-situ observations using X-ray, neutron or optical methods (Mao and Mao, 2007). By reaching these extreme conditions it is possible to study materials under conditions of Earth's inner core (Ruoff et al., 1990; Tateno et al., 2010).

Recent innovations in DAC designs pushed the limit in pressure even further, up to 640 GPa, by using micro-ball nanodiamond anvils (Dubrovinsky et al., 2012). The major limitations of the DAC techniques are the very small sample volume, normally smaller than a few cubic millimetres, and the difficult recovery of the sample for further characterisations.

In the next Sections the methods used in this study will be briefly described and advantages and limitations will be discussed.

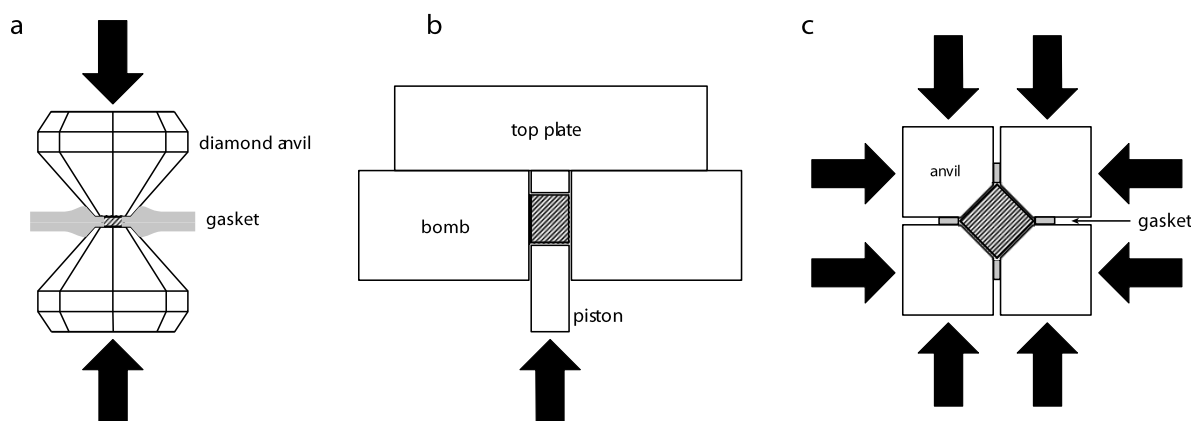


Fig. 3.1.1 showing the principal of three high pressure techniques: a) diamond anvil cell, b) piston cylinder, c) multi anvil apparatus. Image © Andreas Audetát from Keppeler and Frost (2005). Arrows mark the direction of force.

3.1.1. Piston cylinder

In order to obtain very large crystals experiments for the synthesis of crystals for subsequent single crystal X-ray diffraction (Chapter 6) have been conducted in the piston cylinder (PC) apparatus. In Chapter 4 the PC has been used to conduct experiments at lower pressures around 3 GPa because using the PC over MA at this low pressure is economically more efficient.

The piston cylinder is a very simple device where the sample is compressed by a tungsten carbide (WC) piston pushed into an outer cylinder made of several layers of WC and hardened tool steel (Fig. 3.1.1). The sample itself is surrounded by solid pressure media in

form of sleeves of talc-pyrex and pyrophyllite to reduce the inherent friction between the sample and the cylinder and to ensure hydrostatic conditions. The advantage of the piston cylinder is that it has a larger sample volume (up to 5 x 10 mm) than multi anvil devices and can be kept at stable temperatures for days to weeks.

The capsules for piston cylinder experiments conducted in this study were either made from high-purity graphite or Re-foil. The graphite capsules were sealed with a tight-fitting graphite lid. The Re-capsules were folded and sealed with Re-discs on both ends. The capsules containing the starting material powder were placed into an outer Pt-capsule which has been welded shut on both ends. Due to the larger volume, two inner capsules were loaded into one Pt-capsule. One capsule was a graphite capsule and the other capsule was made from Re-foil.

Temperatures were monitored using an axially inserted D-type thermocouple consisting of W_3Re_{97} - $W_{25}Re_{75}$ alloy wires. The tension between the two different wires is a function of the difference in temperatures between the contact point and the reference temperature measured outside the press. D-type thermocouple is suitable for temperatures up to 2300 °C. The uncertainty on the temperature at the thermocouple junction is 1%. No correction for a pressure effect on the thermocouple emf was applied. Piston cylinder runs are listed in Chapter 4, the analyses are given in Appendix 1.

3.1.2. Multi-anvil apparatus

Over the last few decades several different setups have been developed to perform high pressure experiments with large sample volumes. In this study, two different configurations of the classical 6/8 multi anvil of Kawai (Kawai and Endo, 1970; Walker et al., 1990) were used. The 1000 tonne and 5000 tonne press installed at the BGI are designed as split-sphere

apparatus (Frost et al., 2004), whereas, the 500 tonne press is equipped with a Walker-module (Fig. 3.1.2.1).

As described in Chapters 4, 5 and 7, MAs syntheses have been performed to obtain an equilibrium phase assemblage at upper mantle to transition zone conditions. Some of the large crystals obtained during these syntheses have been used in the compressibility study described in Chapter 6, Table 6.2.1.1. In all experiments the standard BGI 18/11 assemblage consisting of a MgO-octahedron doped with 5 wt.% Cr₂O₃ (18 mm octahedral edge length / 11 mm truncated edge length) was used. This assemblage is suitable to cover a pressure range up to 16 GPa in combination with a large sample volume of more than 10 mm³ (capsule outer dimensions: 3.5 x 2 mm). Pyrophyllite gaskets were used to seal the assemblage from pressure leakage (blowout). A stepped graphite resistance heater has been used for temperatures up to ~1400 °C and pressures up to 16 GPa. Above these conditions graphite transforms into diamond and the resistance rises to infinity. Therefore, a stepped LaCrO₃ was used at higher P and T. The temperature was measured as described for PC in Chapter 3, Section 3.3.1.



Fig. 3.1.2.1 Multi-anvil devices used in this thesis from left to right: Zwick 5000 tonne press, Hymag 1000 tonne press, and the Voggenreiter 500 tonne press. In the images of the Zwick and Hymag press the lower guide block have been pulled out. In the Voggenreiter press the pressure plate has been removed.

The hydraulic pressure of the press is transferred to the sample by two sets of anvils. Eight second stage anvils are made of tungsten-carbide (WC) cubes with a truncated edge. Cubes with a face length of 32 mm have been used for the 1000 tonne and 500 tonne press, whereas cubes with a face length of 54 mm have been used for the 5000 tonne press to hydrostatically compress the octahedron containing the sample capsules.

The WC cubes, representing the inner anvils, are compressed by two first stage anvils, so called guide blocks, made of hardened tool steel. The 500 tonne press instead uses a Walker-module which consists of six cylindrical wedges, which are confined into a steel cylinder and driven via a pressure plate by a single piston. The wedges are not fixed to the outer support ring. The “free” floating of the wedges ensures quasi-hydrostatic compression (Walker et al., 1990).

To relate the applied load to the pressure recorded by the sample, calibration experiments have been conducted with several calibrants over a wide P/T range. The experimental pressure was previously calibrated against the quartz – coesite, fayalite (Fe_2SiO_4) – ringwoodite, garnet / CaGeO_3 – perovskite, rutile – TiO_2 II, and coesite – stishovite phase transformations (Keppler and Frost, 2005). In the present study previous calibrations have been verified using the olivine (α) to ringwoodite (γ) transition (Fig. 3.1.2.2). The results show that, for pressures above 10 GPa the calculated two phase stability field of olivine and ringwoodite was overestimated by ~ 1 GPa when using the 1000 tonne press. Therefore, the pressures had to be corrected by this offset. For larger pressures the calibration could be reproduced within 0.5 GPa up to 16 GPa when using the 5000 tonne press. Therefore, the majority of high pressures experiments between 12 and 16 GPa, as discussed in Chapter 5 and given in Table 5.3, have been conducted in the 5000 tonne press.

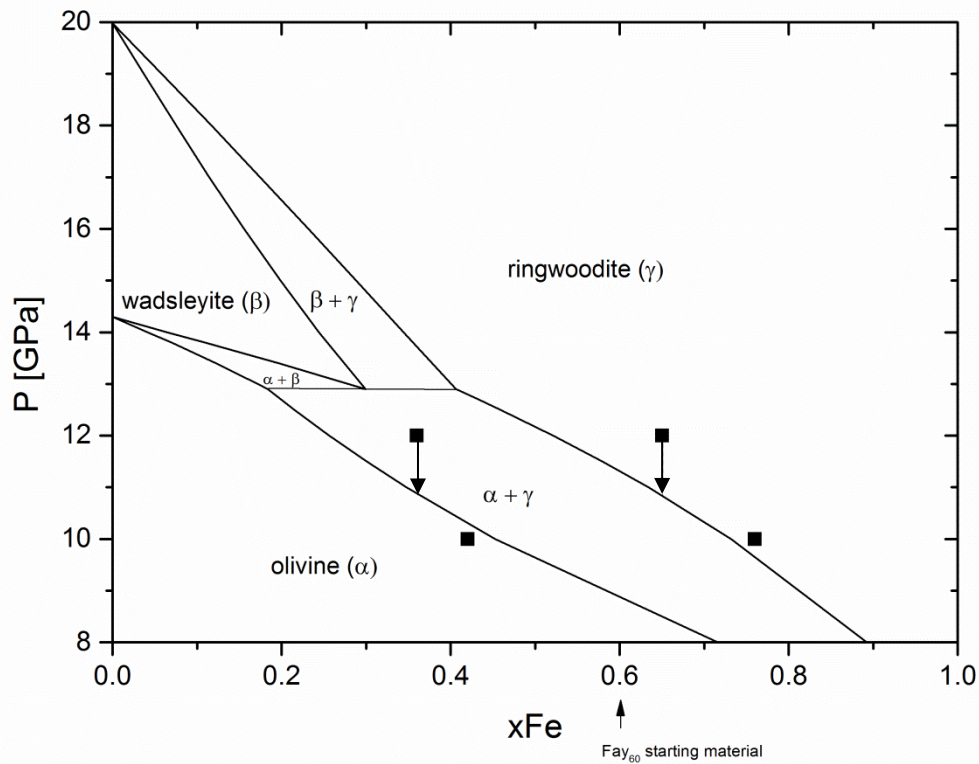


Fig. 3.1.2.2 Phase diagram of the high pressure polymorphs of olivine from a calibration experiment conducted in the 1000 tonne MA. Black squares are measured compositions at a given pressure. Towards higher pressure an adjustment of pressure by ~ -1 GPa is necessary. Phase boundaries are calculated according to Frost and Dolejš (2007). xFe represents the fraction of Fe-bearing olivine compound within the binary Mg-Fe olivine solid solution series.

The starting materials used to synthesize the samples studied in Chapter 4, Table 4.1 have been enclosed either into a single graphite capsule or wrapped in 25 μm thick Re-foil. These inner capsules were placed in an outer Pt-capsule which has been welded shut. One sample described in Chapter 4 has been contained into an AuPd-alloy capsule which has been also welded shut using an arc-welder.

To perform multiple experiments under the same P/T conditions multi-chambers capsules have been employed. Five 250 μm holes have been drilled into a 1 x 2 mm Re (Chapter 4) or AuPd-disc (Chapter 5) cut from a solid rod (Fig. 3.1.2.3) by means of spark erosion. This has been proven to be extremely useful for the phase relation equilibrium experiments

discussed in Chapter 5, where four different starting materials were loaded into the same disc. All charges were exposed to the same P/T conditions which made a direct comparison of the recovered samples possible. The disadvantage of this method is that the discs cannot be welded shut, and the sample volume is smaller than the single capsule technique. Therefore this technique has not been used to grow crystals for single crystal X-ray diffraction experiments (Chapter 6) or phase assemblages large enough for SHRIMP measurements (Chapter 7).

All capsules were inserted at the center of the octahedral pressure assembly surrounded by a MgO sleeve, a heater, and a ZrO₂ insulation sleeve. Remaining cavities around the capsule were filled with dried MgO powder.

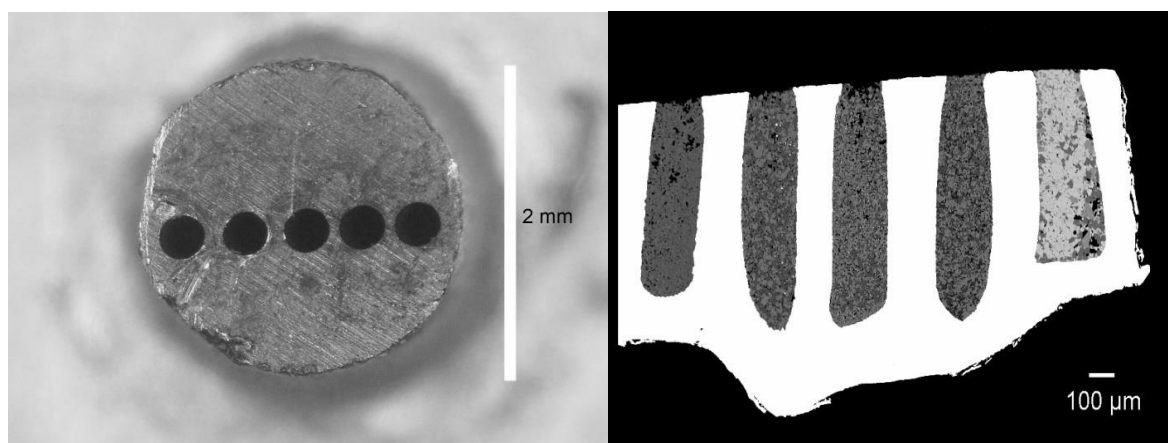


Fig 3.1.2.3 a) AuPd disc with 5 spark-eroded holes each with a diameter of 250 μm. b) BSE cross-section of a recovered multi-chamber experiment.

3.1.3. Diamond anvil cell and heated diamond anvil cell

All P-V and P-V-T measurements reported in Chapter 6 have been carried out in piston cylinder BX90 DAC (Kantor et al., 2012) with type Ia Bohler-Almax design diamond anvils, 16-sided, 80°, (100)-oriented and a culet of 500 μm placed in conical WC-seats (Boehler and De Hantsetters, 2004) (Fig. 3.1.3.1). This particular diamond anvils have a

very wide aperture ($\alpha_x = 80^\circ$), which allows X-ray measurements at higher 2Θ diffraction angles. Higher 2Θ angles enable a better fitting of the $K\alpha_1/\alpha_2$ reflections obtained from the BGI single crystal diffractometers, resulting in higher analytical resolution.

Re-metal has been chosen as gasket material because of its hardness and its chemical inertness. The gasket was pre-indented to 50 – 70 μm . With a spark erosion tool a 150 μm diameter hole was drilled into the center of the indentation. Subsequently, the garnet crystals were loaded to ~ 0.7 GPa with neon as pressure-transmitting medium together with a chip of Sm:YAG and ruby as pressure standards using the gas-loading device installed at the BGI (Kurnosov et al., 2008). Neon behaves hydrostatically within the experimental pressure range between ambient pressure and 16 GPa (Klotz et al., 2009). The room pressure unit-cell volume (V_0) was measured with the crystals inside the DAC before it was loaded with Ne.

For high P/T measurements the cell was equipped with an external resistance heater enabling to heat the experiment up to ~ 900 K. The heater is made from a special high temperature ceramic (7 mm height, 2 mm thick, 17 mm inner radius) wrapped with 0.5 mm Pt-wire (Fig 3.1.3.1). The heater has been cemented to one side of the DAC. The heating wire was not touching the DAC-housing to prevent a short circuit.

The temperature within the cell was monitored with one or two PtRh S-type thermocouples positioned as close as possible to the gasket hole. The wires were fixed with cement to make sure that the TC did not move during goniometer motion. Insulation tubes inhibited a short circuit between the heater and the thermocouple wires.

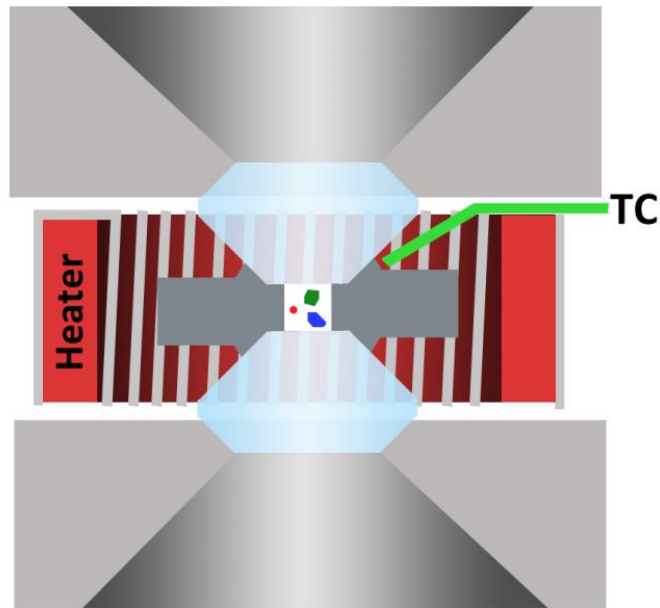


Fig. 3.1.3.1 Schematic cross section of the heating setup, with Boehler Almax Ia shaped diamonds (blue), matching WC-sits (light grey), Re-gasket (dark grey), Pt-wire loop heater (red), and thermocouple (green).

3.2. Single-crystal X-ray diffraction measurements

In order to obtain precise and reproducible compressibility data, single-crystal X-ray diffraction (SC-XRD) has been applied to a number of gem-quality garnet single-crystals synthesized as described in the previous sections to obtain unit cell dimensions (Chapter 6, Table 6.4 and Table 6.6). Based on Bragg's law:

$$n\lambda = 2d\sin\theta \quad (3.1)$$

the distance d between the lattice planes is determined. Experiments were performed using two Huber 4-circle diffractometer which are designed as Eulerian cradles. Room

temperature compression experiments H3605 and B834 were carried out on a Huber SMC9000 4-circle Eulerian-cradle single crystal diffractometers equipped with a Mo K α X-ray tube with wavelength of 0.709316 Å and 0.713606 Å, and an intensity ratio K α 1/K α 2 of 0.53. The X-ray tube was powered with 40 mA and 50 kV. The room temperature compression experiment of crystal A719-JB1 was carried out on a SMC9300 Huber 4-circle Eulerian-cradle single crystal diffractometer equipped with an ultra-high intensity Rigaku FR-E⁺ SuperBright rotating anode X-ray source, emitting unfiltered Mo K α radiation, focused with a multilayer VaryMax focusing optics. The advantage of the second setup is a 25 times higher intensity compared to a standard x-ray tube, and a better signal-to-noise ratio (Trots et al., 2011). The rotating anode was powered with 55 mA and 45 kV.

To minimize the experimental errors on the volume the specimen were measured in 4- and 8-position centering mode for the high-temperatures and the room temperature experiments, respectively. In the 8-position centering mode the errors in alignment, diffractometer aberrations, goniometer imperfection, and crystal offset are corrected by measuring each reflection in all 8 possible equivalent positions (Angel, 2000; King and Finger, 1979). The 4-position centering has been applied in high T experiments because the outer cell for the gas flow and the capillaries for the membrane limit the degrees of freedom of the goniometer. The *Single* software package (Angel and Finger, 2011) was used to center the reflections and to calculate the unit-cell parameters. To ensure precise and accurate measurements the difference between 8- and 4-position centering modes in terms of $\Delta d/d$ has been tested. The deviation is within the precision of the experimental setup. Especially at higher 2θ diffraction angles there is virtually no difference between the two centering procedures, whereas the 2-position centering shows a slightly lower precision (Fig. 3.2.1).

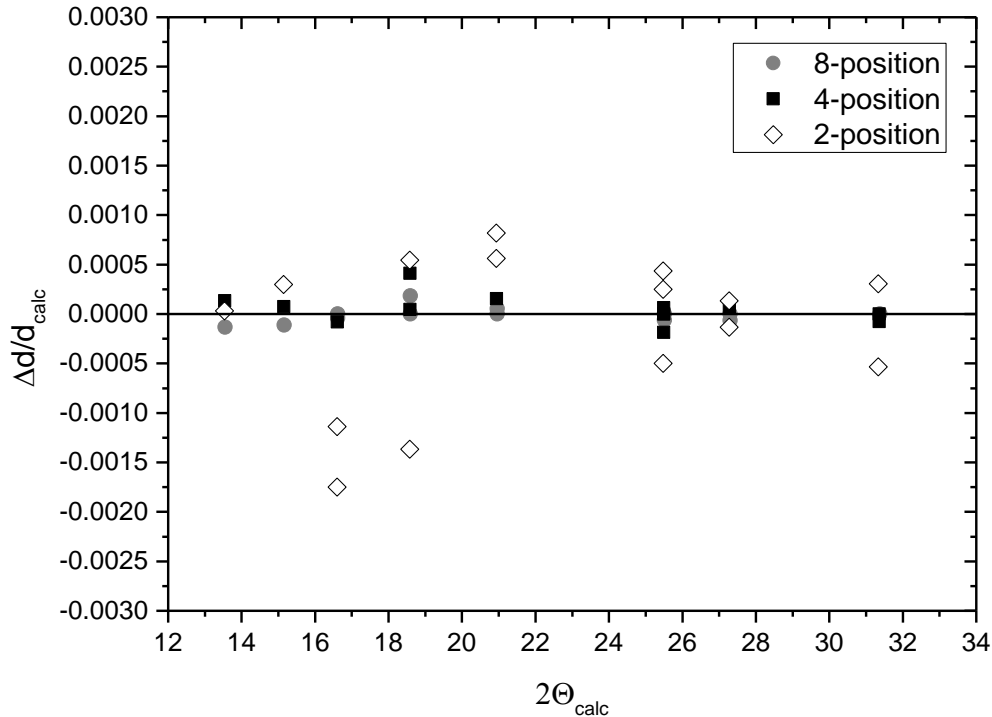


Fig. 3.2.1 Comparison between 2-, 4-, and 8-position centering as a function of 2Θ . 4-, and 8-position centering yields smaller scatter and higher precision.

For P-V measurements no special setup was required. The pressure was manually changed using four screws. All P-V experiments were performed in 8-position centering mode. The pressure was measured before and after each experiment using the pressure dependent shift of the ruby R_1 luminescent line (Mao et al., 1986). A good indicator for equilibration was a difference between the pressure values measured before and after the experiment P_{before} and P_{after} of <0.05 GPa, this value is practically the uncertainty of the ruby calibration.

The P-V-T experiments reported in Chapter 6 were conducted with the heated DAC described in Section 3.3.3. During the experiments voltage and current of a DC power supply were kept constant to prevent any fluctuation in temperature. Initial equilibration of temperature took up to 12 h.

To prevent the Re-gasket and the diamond-anvils from oxidizing at temperatures above 450 °C the cell was flushed with a continuous Ar₉₉H₁ gas flow. Another benefit of the gas flow was a more homogeneous temperature distribution within the cell (cross-checked with two thermocouples in different positions). The nozzle of the gas flow system was attached to a custom made housing encapsulating the whole DAC.

The pressure within the cell was regulated either manually with four screws or semi-automatically with a gas membrane to guarantee almost equal pressure steps. The membrane has the advantage than manual handling of the cell is not required, which simplifies and speeds up the alignment process for each pressure step. Adjusting the pressure with the screws using a key influenced the temperature, increasing the amount of time for equilibration of each data point.

3.2.1. Equation of state

The variation of the density of any material with P and T is described using an equation of state (EoS). In particular the variation of volume with P is quantified through the bulk modulus $K = -V\partial P/\partial V$ and its first derivative $K' = \partial K/\partial P$. One of the most common formulations to obtain the bulk modulus for geomaterials is the isothermal Birch-Murnaghan EoS (BM-EoS) which is based on the finite strain theory (Birch 1947). Specifically, the BM-EoS is based on the Eulerian strain $f_E = -\epsilon = [(V_0/V)^{2/3} - 1]/2$. This EoS has been developed on the assumption that the Helmholtz free energy can be described as a Taylor-expansion in the strain. Truncating such expansion at the 3rd order and differentiating it with respect to volume one obtains the following expression for P:

$$P = 3K_0 f_E (1 + 2f_E)^{\frac{5}{2}} (1 + \frac{3}{2}(K' - 4)f_E) \quad (3.2)$$

If K' has an implied value of $s = 4$ the BM-EoS can be truncated at the 2nd order term, leaving V_0 and K_0 as the only fitting parameters. For most garnets (i.e. pyrope, almandine) this is a fair assumption since K' is close to 4 within the given analytical errors (e.g. Zhang et al., 1999).

An handy tool to decide whether higher order terms of the Helmholtz free energy are required to describe a specific material is represented by the f - F plot (Fig. 3.2.1.1) (Angel, 2000). By plotting normalized stress (F_E):

$$F_E = P/3f_E(1 + 2f_E)^{5/2} \quad (3.3)$$

over finite strain (f_E) it is possible to visualize whether the experimental data is approaching a horizontal limit, i.e. the BM-EoS can be truncated after the second term with K' equals 4. In order to get a measurement for the precision on the plot, experimental uncertainties must be taken into account. Following the approach of Heinz and Jeanloz (1984) modified by Angel (2000) these uncertainties are:

$$\sigma_f = \frac{1}{3}\eta^{-5/3}\sigma_\eta \quad (3.4)$$

$$\sigma_F = F_E \sqrt{\left(\frac{\sigma_P}{P}\right)^2 + (\sigma')^2} \quad (3.5)$$

With

$$\sigma' = (7\eta^{-2/3} - 5)\sigma_\eta/3(1 - \eta^{-2/3}) \quad (3.6)$$

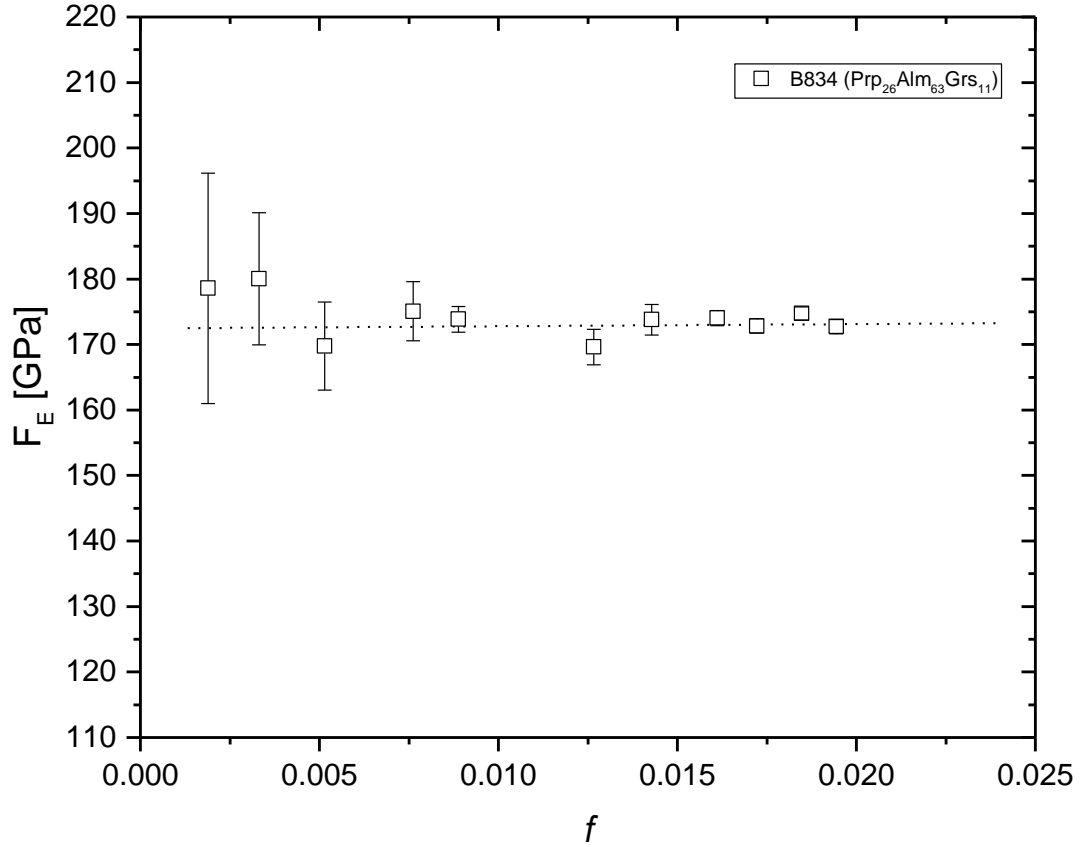


Fig. 3.2.1.1 Example of the f - F plot calculated for an almandine-rich garnet, showing that a 2nd order BM-EoS is sufficient to obtain the bulk modulus K_{T0} .

A thermal equations of state requires an additional parameter, the thermal expansion coefficient $\alpha(T)$, for calculating the temperature contribution to the bulk modulus. In Chapter 6 the equation for thermal pressure as introduced by Holland and Powell (2011) has been used to calculate the thermal expansion of the garnet solid solutions and the Sm:YAG. $P(V,T)$ at pressure and temperature has been calculated by adding the thermal pressure P_{th} to the pressure at ambient temperature P_0 (calculated from Eq. 3.2):

$$P(V,T) = P_0 + \Delta P_{th} \quad (3.7)$$

with

$$\Delta P_{th} = \alpha_0 K_{T0} \left(\frac{\Theta_E}{\xi_0} \right) \left(\frac{1}{\exp(\Theta_E/T) - 1} - \frac{1}{\exp(\Theta_E/T_0) - 1} \right) \quad (3.8)$$

and Θ_E representing the Einstein temperature:

$$\Theta_E = \frac{h\nu_E}{2\pi k_B} \quad (3.9)$$

h being the Planck constant, k_B being the Boltzmann constant, and ν_E the Einstein frequency. Since Θ_E cannot be measured directly, Holland and Powell (2011) provide an empirical approximation:

$$\Theta_E = \frac{10636}{S/n+6.44} \quad (3.10)$$

with S representing the molar entropy of the phase, and n being the number of atoms per formula unit. Θ_E needs only to be approximated because it only significantly effects low temperature thermal expansion (Holland and Powell, 2011). The factor ξ_0 is given by Kroll et al. (2012):

$$\xi_0 = \frac{(\Theta_E/T_0)^2 \exp(\Theta_E/T_0)}{(\exp(\Theta_E/T_0)-1)^2} \quad (3.11)$$

Θ_E has been calculated using Eq. 3.10. To approximate Θ_E , S has been calculated by adding up the entropy of formation S^0 of the garnet end-members and the configurational entropy of mixing S_{mix} of the garnet solid solution.

$$S = \sum_i X_i S^0 + S_{mix} \quad (3.12)$$

S^0 for garnet end-member has been taken from the tabulated values given in Holland and Powell (2011) and S^0 for YAG from Fabrichnaya et al. (2001). To obtain S_{mix} for the garnet solid solution of aluminous garnets random mixing only at the X-site with no mixing on the Y-site and tetrahedral site has been assumed, giving the following expression:

$$S_{mix} = -\Phi R \sum_i X_i \ln X_i \quad (3.13)$$

where Φ is the number of atoms per formula unit available for randomly mixing on the crystallographic site and X_i being the fraction of the mixing components (Ganguly, 2008; Wood and Fraser, 1978). In the case of an aluminous garnet solid solution $\Phi = 3$. R is the gas constant.

Another formulation for the thermal pressure also has been used at the end of Chapter 6 in order to compare the results on the thermal elastic properties of this study with the thermodynamically self-consistent model of Stixrude and Lithgow-Bertelloni (2011). In this model the thermal contribution to the pressures has been calculated using the Mie-Grüneisen-Debye EoS (MGD) (Jackson and Rigden, 1996):

$$P(V, T) = P_0 + \Delta P_{th} \quad (3.14)$$

where

$$\Delta P_{th} = \frac{\gamma(V)}{V} [E_{th}(V, T) - E_{th}(V, T_0)] \quad (3.16)$$

The thermal free energy E_{th} is calculated according to the Debye-model (Debye, 1912):

$$E_{th} = \frac{9nRT}{(\Theta/T)^3} \int_0^{\Theta/T} \frac{(\Theta/T)^3 d(\Theta/T)}{e^{(\Theta/T)} - 1} \quad (3.17)$$

$$\Theta = \Theta_0 \exp \left[\frac{\gamma_0 - \gamma}{q} \right] \quad (3.18)$$

$$\gamma = \gamma_0 \left(\frac{V}{V_0} \right)^3 \quad (3.19)$$

where Θ is the Debye temperature, n is the number of atoms per formula unit, R is the gas constant, γ_0 is the Grüneisen parameter at V_0 , Θ_0 is the Debye temperature at V_0 , and $q = (\partial \ln \gamma / \partial \ln V)$.

3.2.2. Pressure determination in the DAC

Pressure for the P-V experiments was obtained by measuring the pressure dependent shift of the ruby R_1 luminescent line (Mao et al., 1986) using the modified parameters from Jacobsen et al. (2008):

$$P(\text{GPa}) = \frac{A}{B} \left(\left[1 + \frac{\Delta\lambda}{\lambda_0} \right]^B - 1 \right) \quad (3.20)$$

with $A = 1904$ and $B = 10.32$, λ_0 is the reference wavelength of the ruby R_1 line measured at ambient conditions, and $\Delta\lambda$ is the difference between the measured wavelength at pressure and λ_0 . The two ruby peaks were fitted by using Lorentzian functions.

Since during the P-V-T experiments described in Chapter 6 it was not possible to measure the fluorescence shift of ruby, another approach for obtaining temperature and pressure during the measurements had to be applied, namely the volume of a Sm:YAG crystal loaded together with the single-crystal of garnet has been measured as internal standard. The EoS and thermal expansion of Sm:YAG are well known (Trots et al., 2013). In particular, the thermal expansion curve of Trots et al. (2013) has been refined in this study using the following expression for the volume at room pressure $V_0(T)$, to obtain parameters consistent with later calculations in Chapter 6 based on the formalism introduced by Holland and Powell (2011):

$$V_0(T) = V_0(T_0) \left[-K'_{T_0}(T_0) + [1 + K'_{T_0}(T_0)]1 - \left(\frac{K'_{T_0}(T_0)[2 + K'_{T_0}(T_0)]}{1 + K'_{T_0}(T_0)} A \right)^B \right] \quad (3.21)$$

with

$$A = \alpha_0(T_0) \left(\frac{\Theta_E}{\xi_0} \right) \left(\frac{1}{\exp(\Theta_E/T) - 1} - \frac{1}{\exp(\Theta_E/T_0) - 1} \right) \quad (3.22)$$

$$B = -1/K'_{T_0}(T_0)[2 + K'_{T_0}(T_0)] \quad (3.23)$$

with Θ_E from Eq. 3.10, and ξ_0 from Eq. 3.11. As mentioned all relevant parameters K_{T0} , K'_{T0} , Θ_E , and α_0 are well known (Trots et al. 2013), therefore pressure and temperature of each data point has been solely calculated from the V_0 and V_T of the Sm:YAG measured together with the specimen of garnet.

In the P-V experiments the largest uncertainties come from the pressure calculation, due to the intrinsic uncertainty of the ruby scale, whereas in the high-temperature experiments, large uncertainties are associated to the fact that temperature estimations is solely based on the Sm:YAG thermal expansion. During the course of the measurements the temperature varied by a few degrees. Moreover, during P-V-T experiments, the pressure increased in some experiments by ~ 0.1 GPa during the measurement. All these uncertainties have to be taken into account in order to obtain meaningful elastic parameters.

3.3. Analytical methods

3.3.1. Scanning electron microscopy

Scanning electron microscopy (SEM) is one of the most common techniques to analyse recovered solid samples from high pressure experiments in geosciences (Reed, 2005). By accelerating electrons on to the sample surface with several kV, secondary processes within the uppermost part of the sample are excited (Fig. 3.3.1).

The secondary electrons are used to obtain a topographical image of the sample surface. The backscattered electrons are scattered depending on the atomic mass of the targeted area, giving rise to contrasts helpful to distinguish between chemically different phases. With an energy-dispersive X-ray detector (EDX) attached to the system it is also possible to detect X-rays to identify phases and their chemical compositions from the characteristic X-ray absorption lines.

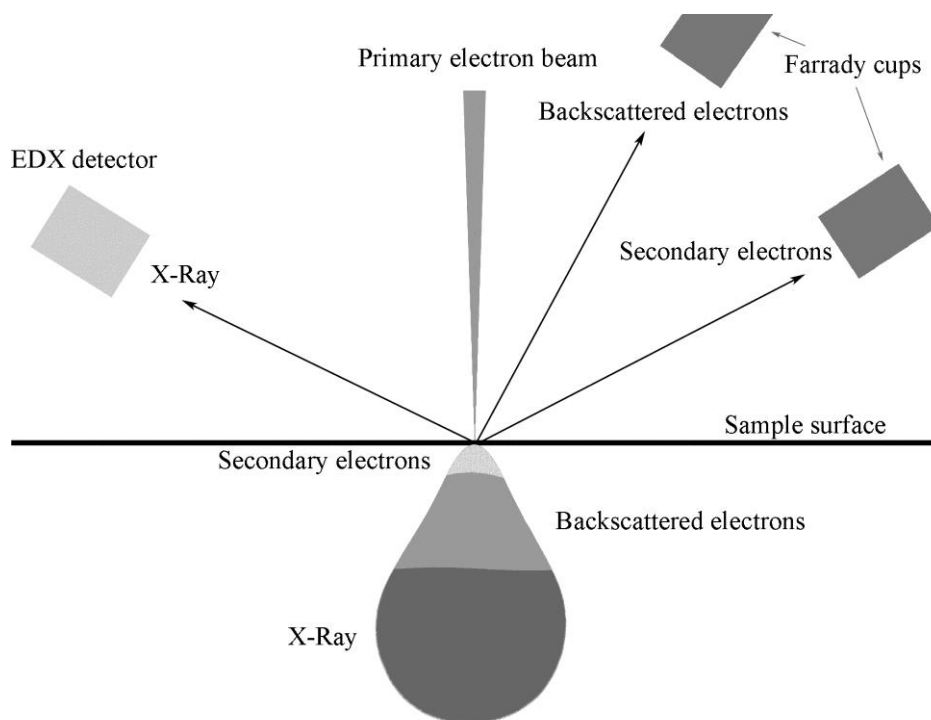


Fig. 3.3.1 Principal sketch of relevant interactions between incident electron beam, sample surface and sample volume.

In the course of this study a Zeiss Gemini 1530 SEM equipped with a field emission gun (FEG) has been used to determine qualitatively the phase assemblage and to check for chemical zonations using BSE-images and 2-D mapping using the Oxford Instruments Inca™ EDX software package. In this way it was possible to assess whether a sample contained all relevant phases for the garnet-clinopyroxene barometer as outlined in Chapter 4. Moreover, the BSE-images were used to identify inhomogeneity, i.e. zonations.

3.3.2. Electron microprobe

The electron microprobe is a standard technique to obtain precise chemical compositions using wavelength-disperse X-rays (WDX). A detailed description on the principals is given by Reed (2005) . Analyses have been performed using a JEOL JXA-8200 microprobe equipped with a tungsten cathode, five WDX spectrometers, and an additional EDX system. The cathode was powered with 15 kV and 15 nA. All crystalline phases were

analyzed with a focused beam. Counting times were 15 s on the peak and 5 s on the background and 20 s and 10 s on the samples. The following matrix-matched calibration standards were used: jadeite (Na), wollastonite (Ca), enstatite (Mg), pyrope (Al), diopside (Si), rutile (Ti), Fe-metal (Fe), MnTiO₃ (Mn), Ir-metal (Ir), and Re-metal (Re). The internal reproducibility was better than 0.5 % for all elements. Mineral analyses which varied by more than 1.5 wt.% from 100 wt.% totals were neglected. The choice of standard materials was of great importance for tracing the onset of Ca-Tschermaks in clinopyroxene and majorite in garnet. For example, using pure SiO₂ as a standard for Si biased significantly the resulting values for Si amount in garnet. Additional care was taken for analysing glassy melts with high fractions of volatile elements such as K, Na, H, and F. In this case the measurement setup was varied by using a wider beam diameter (10 µm), and shorter counting time (10 s peak, 5 s background) duration to limit volatile loss.

Measuring F in quenched glasses as described in Chapter 7 required a different method due to the interference of iron (Witter and Kuehner, 2004). The acceleration voltage was 10 kV with 30 nA beam current. Peaks were measured for 60 s and background for 20 s. An in-software overlap correction has been applied to account for the interference between the fluorine and iron peak. With the relatively high concentration of F in the glass, the peak located on the Fe K α shoulder was easily distinguishable and the background subtraction was trivial.

3.3.3. Electron energy-loss spectroscopy

To evaluate the ferric/ferrous iron ratio in garnet and clinopyroxene (Chapter 4) a sample from a graphite/Pt capsule experiment (H3605x) and one from a Re capsule experiment (V772) were examined with a 200 kV Philips CM-20FEG analytical transmission electron microscope (ATEM) equipped with a parallel electron energy-loss spectrometer (PEELS

Gatan 666). The ferric iron over total iron ratio was obtained from the Fe $L_{2,3}$ edge electron energy-loss near-edge structure (ELNES) following the method of (van Aken and Liebscher (2002); van Aken et al. (1998)) using the Matlab™ based software EELSA 1.0 created by C. Prescher. Sample H3605x was ground to a fine powder and placed upon a TEM Cu-grid coated with lacey carbon film. Sample V772 was double polished into a thin section of less than 30 μm thickness, which was glued to a 100 mesh Mo-grid. The sample was subsequently thinned to electron transparency by Ar ion milling. A stationary unfocused electron beam with a spot size between 250 – 500 nm was used for EDXS and PEELS. ELNES spectra were collected in diffraction mode with convergence and collection semi-angles of $\alpha = 4$ mrad and $\beta = 2.7$ mrad for sample V772 and $\alpha = 4$ mrad and $\beta = 4.3$ mrad for sample and H3605x, an energy dispersion of 0.1 eV per channel and 20 – 40 sec integration time per read-out. The energy resolution was between 0.8 and 0.9 eV, measured as the full width at half maximum (FWHM) of the zero-loss peak. No oxidation by beam damage was observed, which would have caused a shift in the $\text{Fe}^{3+}/\Sigma\text{Fe}$ ratio during EELS measurements.

3.3.4. SHRIMP

Fluorine analyses in garnet and clinopyroxene were performed on the SHRIMP SI ion microprobe at the Research School of Earth Sciences (RSES), Canberra. Energy filtering was applied to reduce molecular interferences. Detection limits for a pit 20 μm across and a few micrometers deep were in the order of 0.05 ppm. Prior to analysis samples were polished, cleaned with ethanol, and coated with a thin Al film to provide electrical conductivity. A 3.5 nA beam of mass-filtered ^{133}Cs accelerated to a nominal 9 kV, which was focused to a 15–30 mm diameter spot has been used. Negative secondary ions were accelerated to 9.3 keV, thus leading to total primary ion impact energy of 15 keV. Mass

resolution was adjusted to $\sim 2300 \text{ M}/\Delta\text{M}$ so as to eliminate all significant isobaric interferences. Secondary ion intensities were normalized to the ^{28}Si count rate. Peak counting times were set at 4 s for ^{19}F and 2 s for ^{28}Si , resulting in a measurement period of approximately 15 min for a single analysis.

A synthetic F-saturated forsterite single crystal as matrix matched reference materials for calibrating ion has been used similar to Beyer et al. (2012).

4. Experimental calibration of a garnet-clinopyroxene geobarometer for mantle eclogites

4.1. Introduction

Geobarometry measurements are essential for understanding the thickness, thermal structure and tectonic evolution of the lithosphere in addition to providing vital information on the depth of magmatic and metasomatic processes evident in mantle xenoliths (Rudnick et al. 1998; Griffin et al. 2003; Kopylova et al. 2004).

Over the last decades several efforts have been made to calibrate geobarometers suitable for the determination of the depth at which eclogite rocks have equilibrated (e.g. Ashchepkov et al., 2010; Nimis and Ulmer, 1998; Simakov, 2008). Most of the experimental calibrations, however, have been limited to a relatively narrow range of pressure, temperature and bulk composition and many of the reactions investigated employ accessory phases, such as olivine, cordierite, quartz, kyanite, orthopyroxene and mica that are not always present in eclogite rocks (Brey and Köhler, 1990; Coleman et al., 1965; Newton and Perkins, 1982; Nickel and Green, 1985; Nikitina, 2000; Nimis and Taylor, 2000). In order to compare equilibration conditions of eclogites world-wide it is important to be able to employ a geobarometer that is based only on garnet and clinopyroxene (cpx) that are present in all eclogites. This has proved difficult, however, (Koons, 1984; Mukhopadhyay, 1991; Newton, 1986), and has been proposed to be also complicated by metasomatic overprinting (Liu et al., 2009; Smart et al., 2009; Tappe et al., 2011). Only a few such studies exist and these are either limited in their application by the chemical system (e.g. CMAS, Cr-content), the narrow compositional range of the calibration or by the reliance on data from non-eclogitic assemblages (Brey et al., 1986; Mukhopadhyay,

1991; Nimis and Taylor, 2000; Simakov and Taylor, 2000). The significant jadeite (Jd) component in eclogitic clinopyroxenes has also been ignored in some studies.

It has long been recognized that Al incorporation in clinopyroxene coexisting with garnet is pressure dependent (Herzberg, 1978; Brey et al., 1986; Mukhopadhyay, 1991). In eclogitic clinopyroxene Al is incorporated through the jadeite ($\text{NaAlSi}_2\text{O}_6$), Ca-Tschermaks ($\text{CaAlAlSi}_2\text{O}_6$) and Ca-Eskola ($\text{Ca}_{0.5}\square_{0.5}\text{AlSi}_2\text{O}_6$) components. While Ca-Eskola is a minor component in the majority of eclogites (Simakov, 2008), Ca-Tschermaks is common, with concentrations of up to 25 mole% (Dawson and Carswell, 1990) and the jadeite component can range up to 70 mole% in kyanite- or corundum-bearing eclogites (O'Reilly and Griffin, 1995). As the proportion of the Ca-Tschermak (CaTs) component had been shown to decrease with pressure (Boyd 1970), Mukhopadhyay (1991) proposed the following equilibrium as a potential geobarometer:



This geobarometer was applied successfully to garnet clinopyroxenites (Mukhopadhyay 1991), however, the calibration presented is less suitable for eclogitic clinopyroxenes with high jadeite contents. Simakov (2008) also presented a thermodynamic calibration for this equilibrium over a wider range of pressure and temperature. However, very little of the data used in this calibration were applicable to natural eclogite compositions, with a significant portion of the employed data being either from very simple systems (Gasparik, 1996), peridotitic systems (Walter, 1998) or from experiments at more extreme conditions (Ono and Yasuda, 1996) than those associated with mantle xenoliths.

Here we present a new thermodynamic calibration for equilibrium (4.1), which takes explicit account of the clinopyroxene jadeite component and is based on the results of high pressure eclogite equilibration experiments. The barometer is, therefore, applicable to natural eclogitic bulk compositions including those that resemble normal mid ocean ridge basalt (N-MORB). The experimental calibration extends to conditions applicable to eclogite xenoliths from depths of up to 250 km. H₂O was employed as a flux in the experiments to promote equilibrium and most eclogitic assemblages coexisted with large portions of hydrous silicate melt. The barometer calibration is made more rigorous by the inclusion of additional experimental data sets from previous studies. Finally, the calibration has been applied to several natural suits of eclogitic xenoliths and to some eclogitic diamond inclusions to determine equilibration pressures. The results are also compared with two other geobarometers.

4.2. Experimental methods

4.2.1. Rationale

In order to calibrate the compositional evolution of bimineralic eclogites as a function of pressure, experiments were conducted in multi-anvil and piston cylinder devices at pressures between 3 and 7 GPa and temperatures of 1200 to 1550°C. The starting material was a synthetic average “wet” N-MORB composition containing ~2 wt.% H₂O. The bulk composition was simplified by the exclusion of minor elements such as K, P and Cr, but in some experiments 2 wt.% fluorine was also added. In order to ensure chemical equilibrium experiments were performed in the presence of hydrous melt and initially raised by 50° C above the final run temperature. This generally ensured complete recrystallisation of the solid assemblage, indicated by a lack of chemical zonation. The objective was to obtain chemical equilibrium by performing experiments at temperatures generally higher than

those at which many natural eclogitic assemblages equilibrated. These experiments were then used to calibrate parameters in a thermodynamic model that could be reliably extrapolated to lower temperatures. When fitting the thermodynamic model, well constrained parameters were taken from previous studies (Ganguly et al., 1996; Holland and Powell, 2011). The experimental data were only used to derive non-ideal mixing terms for the clinopyroxene solid solution, for which cation interaction terms on the different sites are poorly constrained, particularly in eclogitic compositions.

4.2.2. Starting material

The principal eclogitic starting material (OC1/2, Table 4.2.3.1), which was an average N-MORB composition (Lehnert et al., 2000), was fabricated from a synthetic mixture of analytical grade oxides and carbonates, which were dried to remove surface water and ground in an agate mortar under acetone. The initial composition was made with a deficit of Al_2O_3 such that it could be added in a final stage as $\text{Al}(\text{OH})_3$ in order to add H_2O to the starting composition. Subsequently, the mix was decarbonated in air by heating it to 1000 °C for 3 hours. The powder was then fused in a Fe saturated platinum crucible at 1600 °C in order to obtain a homogenous glass that was reground in an agate mortar under acetone to a fine powder. Iron, originally added to the starting mixture as Fe_2O_3 , was reduced by pressing the powder into a pellet and suspending it in a gas-mixing furnace at 800 °C with a 50:50 CO_2 - H_2 gas mix for 15 hours at an f_{O_2} of approximately 2 log units below the fayalite magnetite quartz (FMQ) oxygen buffer. $\text{Al}(\text{OH})_3$, and in some cases CaF_2 , were added to the mixture to provide sources of H_2O and fluorine. 1 wt.% of IrO_2 was added to the mixture and acted as a redox sensor (Woodland and O'Neill, 1997). After additional grinding to homogenize the mixture it was dried and denitrified in a drying oven at 140 °C. A series of 5 more anhydrous bulk compositions (Omph/Opx_{ss}1-5, Table 4.2.3.1) were

synthesized following the same procedure but with varying Fe/Mg ratios, as reported in Table 4.3.2.1. The compositions were based on clinopyroxene analyses reported by Yaxley and Brey (2004) from 1200°C and were designed to crystallize a significant proportion of clinopyroxene coexisting with a smaller amount of orthopyroxene or garnet. The results were used to specifically extract clinopyroxene Fe-Mg activity-composition terms.

4.2.3. High pressure experimental procedure

Experiments at pressures between 4 and 7 GPa were performed in a 1000 ton Kawai-type multi-anvil apparatus and in a 500 ton press equipped with a Walker-type module. An 18/11 (octahedral edge length in mm / anvil corner truncation edge length in mm) octahedral assembly was used as a pressure medium for all experiments. The octahedron was comprised of MgO doped with 5wt.% Cr₂O₃. It was compressed using 8 tungsten carbide anvils of 32 mm edge length.

The OC1/2 starting material was either filled into a graphite capsule with a tight fitting graphite lid or placed into a folded Re-foil capsule. These inner capsules were then placed inside an outer platinum tubing capsule (2.0 x 3.5 mm OD), which was welded closed on both sides with an arc-welder. Some experiments were also performed using a single Au₈₀Pd₂₀ capsule (1.2 mm OD/ 0.9 mm ID or 2.0mm OD/ 1.5 mm ID). The different capsule types were employed to examine the influence of variable oxygen fugacity on the calibration.

The variable Fe/Mg starting materials (Omph/Op_{x_{ss}}1-5, Table 4.2.3.1) were loaded into 5 sample chambers each approximately 0.25 mm in diameter produced in a single Re metal cylinder of 2 mm diameter, by spark erosion. A piece of Re foil was placed over the 5 holes to chemically isolate the samples from the assembly. Using such multi-chamber capsules

cpx-garnet Fe-Mg partitioning could be studied as a function of Fe/(Fe+Mg) ratio in a single experiment.

All capsule types were placed at the center of a hole drilled inside the octahedral pressure assembly, surrounded by an MgO sleeve, a stepped graphite heater, and a ZrO₂ insulation sleeve. Remaining cavities around the capsule were filled with dried MgO powder. The temperature was monitored using D-type thermocouple (W₃Re-W₂₅Re) axially inserted inside an alumina thermocouple tube, with the junction in contact with the top of the sample capsule.

Table 4.2.3.1 Starting compositions

oxide	OC1/2	Omph/Opx _{ss} 1	Omph/Opx _{ss} 2	Omph/Opx _{ss} 3	Omph/Opx _{ss} 4	Omph/Opx _{ss} 5
SiO ₂	46.5	50.2	49.7	51.2	52.8	54.7
TiO ₂	1.0		-	-	-	-
Al ₂ O ₃	15.0	6.9	6.9	6.8	6.8	6.7
FeO*	8.8	27.5	29.6	24.1	17.8	10.8
MnO	0.13		-	-	-	-
MgO	8.2	6.0	4.4	8.6	13.3	18.6
CaO	13.6	7.1	7.1	7.0	7.0	6.9
Na ₂ O	2.5	2.3	2.3	2.3	2.3	2.3
H ₂ O	2		-	-	-	-
F	2		-	-	-	-
total	99.7	100	100	100	100	100

*all Fe given as FeO.

A Re-disc was inserted between the Pt-capsule and the thermocouple to prevent the soft capsule material from being extruded into the thermocouple holes of the alumina tubing, which can cause misleading temperature measurements. No correction for a pressure effect on the thermocouple emf was applied. The experimental pressure was previously calibrated against the quartz – coesite, fayalite (Fe₂SiO₄) – ringwoodite, garnet (CaGeO₃) – perovskite, rutile – TiO₂ II, and coesite – stishovite phase transformations (Keppler and Frost, 2005).

Experiments were pressurized for between 1½-3 hours, depending on the final pressure, at room temperature. The run temperature was then raised at ~ 150 °C/min to approximately 50 °C above the final run temperature. After holding this temperature for 15 minutes, the sample was cooled to the desired run temperature with a ramp of 2 – 7 °C/min. The final temperature was held for between 1 and 24 hours, depending on the temperature. Some experiments were directly heated to the final temperature (Table 4.2.3.2). The superheating and slow cooling was designed to promote the growth of large homogeneous crystals with a reasonable size for further analytical procedures. The experiments were quenched by switching off the power to the furnace, which caused the temperature to drop to <120 °C in approximately 2 seconds.

Experiments at lower pressure (3 GPa) were conducted using an end loaded piston cylinder apparatus. A 1/2" talc-pyrex tubular pressure medium was employed, containing a tapered graphite heater and Al₂O₃-spacers. A 5.0x7.0 mm Pt-capsule was used with two different inner sample containers. One container was made from graphite, while the second was made from folded Re-foil. Both capsules were loaded with the same starting material, but should have experienced different oxygen fugacities. The temperature was monitored with a D-type thermocouple.

Recovered capsules from all experiments were embedded in epoxy resin, then cut and polished with diamond paste. Some capsules were impregnated with epoxy resin under vacuum to fill cavities.

Table 4.2.3.2: Experimental run conditions and recovered phases

#	P [GPa]	T _{final} [°C]	T _{start} [°C]	cooling rate [°C/min]	runtime [h,min]	starting material	capsule	phases present ¹
A571	3	1430	1500	2	3	OC1/2	graphite	grt, cpx, glass
H3547	4	1485	1520	7	3h 30	OC1/2	graphite	grt, cpx, glass
H3543	4	1460	1500	5	1h 30	OC1/2	graphite	grt, cpx
V772-5	4	1200	1200	-	24h	Omph/Op _{x_{ss}}	Re	grt, cpx, glass (not in #5), opx(#5)
V780**	6	1200	1200	-	24h	Omph/Op _{x_{ss}}	Re	grt, cpx, qx (not in #5)
V792**	4	1050	1050	-	24h	Omph/Op _{x_{ss}}	Re	grt, cpx
H3639	5	1445	1490	4	1h 20 min	OC1/2	Au ₈₀ Pd ₂₀	grt, cpx, glass
H3540	6	1480	1520	5	1h 30 min	OC1/2	Re	grt, cpx, glass, qx
H3483	6	1549*	1549	-	3h	OC1/2	graphite	grt, cpx, glass, qx
H3602	6	1518*	1518	-	1h	OC1/2	graphite	grt, cpx, glass
H3510	6	1430	1480	5	2h 8 min	OC1/2	graphite	grt, cpx, coesite
H3605x	7	1480	1480	-	1h 30 min	OC1/2	graphite	grt, cpx

A571 is a piston cylinder experiment, all others are multi-anvil experiments. *estimated from the electrical power to the heater

¹grt: garnet, cpx: clinopyroxene, opx: orthopyroxene, qx: quench crystals; ** only used for obtaining W_{FeMg}^{M1CPX}

4.2.4. Analytical methods

Run products were examined qualitatively using a Zeiss Gemini 1530 scanning electron microscope (SEM) equipped with a field emission gun and an energy-dispersive X-ray spectrometer (EDXS). Major element concentrations were determined with a 5-spectrometer JEOL JXA-8200 microprobe using an acceleration voltage of 15 kV and a 15 nA beam current. A detailed description is given in Chapter 3, Section 3.3.1 for the SEM technique and in Section 3.3.2 for the microprobe technique. The determination of the valence of iron is described in chapter 3.3.3.

4.3. Experimental results

4.3.1. Textures and phase relations

Multi-anvil experimental charges from runs employing the hydrous bulk composition OC1/2 (Table 4.2.3.1) yielded euhedral to subhedral garnet and clinopyroxene crystals. Garnet, clinopyroxene and melt were present in varying proportions in all samples

depending on pressure and temperature. Clinopyroxene generally occupies interstitial regions within a relatively coarse grained garnet matrix. Some samples displayed a layered sequence of minerals and melt between the bottom and the top of the capsule. Depending on temperature and pressure, melt is present as either pale-to-brownish homogeneous glass or as quenched crystals.

Mineral phases are generally transparent. Garnets have a pinkish to yellowish tint, while clinopyroxenes have a greenish tint. The size of the garnets varies between 10 μm and 500 μm . Clinopyroxenes are elongated and generally smaller, although in some instances were up to 80 μm in the longest dimension. Garnets often contain inclusions of submicron Ir-nuggets. Care was taken, while analyzing these garnets because large Ir-nuggets alloyed with iron can bias the analytical result. Images of typical recovered samples are shown in Fig. 4.3.1.1.

The anhydrous experiments (V772, V780, V792) performed in multi-chamber Re capsules to study Fe-Mg partitioning between 1050 and 1200°C yielded garnet and clinopyroxene and in some chambers also quenched melt. In addition orthopyroxene was found in the most Fe-poor capsule chamber. Euhedral garnets are smaller than in the hydrous experiments with sizes not exceeding 20 μm . Clinopyroxenes are subhedral and are up to ~80 μm in the longest dimension. All charges are clearly dominated by clinopyroxene accompanied by less than 5% garnet. Quenched melt formed at the bottom of the sample chambers and did not exceeding 10% of the chamber volume.

In anhydrous runs where melt was absent garnets contain slightly iron-enriched cores, whereas these concentric zonations are scarcely observed in experiments where melt was present. Garnet rim analyses were employed in these experiments. Zonations were not observed in clinopyroxenes regardless of whether melt was present and even when very large 80 μm crystals were produced. Quenched melt regions were also observed to be

homogeneous throughout the capsules. In all experiments doped with Ir, Ir-Fe-alloy was present as small nuggets with a size typically <1-3 μm . Nuggets were generally evenly distributed throughout the capsules, although the bottom and rim of the capsules showed slight accumulations. In Re capsules Re was additionally present in some alloys.

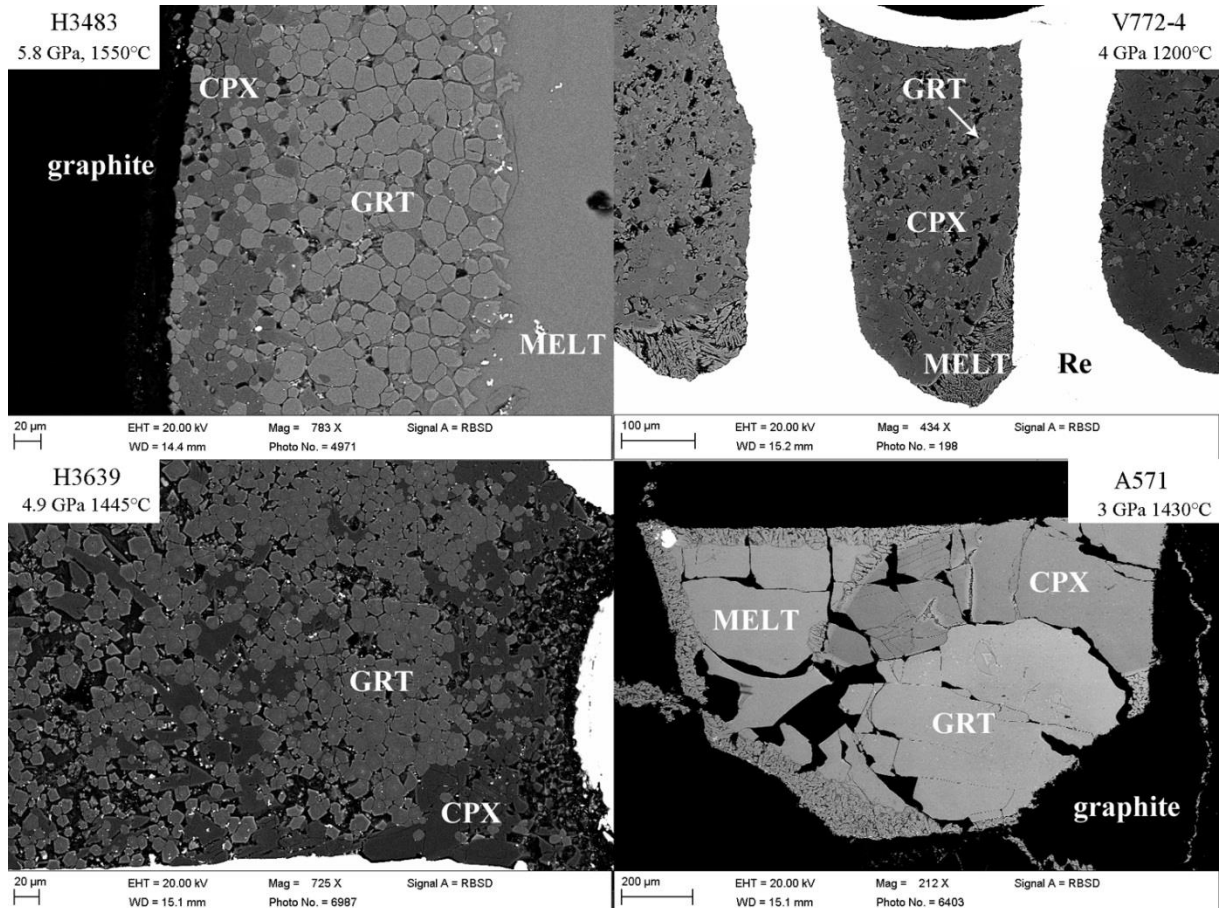


Fig. 4.3.1.1 Representative backscattered electron images of run products from each capsule type (see Table 4.2.3.2 for more details). Experiment H3483 (top left) shows vertical banding of cpx-rich material, followed by a garnet-rich band and then glass on going from left to right. The black material on the far left is the graphite capsule. Experiment V772-4 (top right) the multi-chamber capsule shows small euhedral garnet grains within a matrix of larger cpx. Quenched melt can be seen at the base of the chamber. Run H3639 (bottom left) shows vertical bands of cpx within garnet and plucked quenched melt on the right hand side. Piston-cylinder experiment A571 (bottom right) contains a large garnet crystal at the base with a large (darker) cpx crystal above; the top left quadrant is occupied by glass. On the capsule rim the melt formed quench crystals instead of glass.

Run products from piston cylinder experiments generally resembled those from multi-anvil experiments but some twinned clinopyroxenes were produced in addition to some that showed slight zonation. The zoned crystals were treated the same way as described above for the garnets. Generally, the crystalline phases reached significantly larger sizes compared to crystals recovered from multianvil experiments, with some crystals growing up to 1 mm in the longest dimension. The crystals are inclusion-free except for small Ir-Fe nuggets.

4.3.2. Mineral chemical compositions

Mineral chemical analyses are presented in Appendix 1. In melt bearing experiments mineral grains were chemically homogeneous and minerals within a single capsule showed very little variation in composition.

Garnet

Garnets are generally dominated by pyrope and grossular components, though in most experiments all three major end members are present in sub-equal quantities. Garnet grains obtained from the bulk starting material OC1/2, for example, are solid solutions containing between 30 and 34 mole% grossular ($\text{Ca}_3\text{Al}_2\text{Si}_3\text{O}_{12}$), 37 to 48 mole% pyrope ($\text{Mg}_3\text{Al}_2\text{Si}_3\text{O}_{12}$) and 17 to 28 mole% almandine ($\text{Fe}_3\text{Al}_2\text{Si}_3\text{O}_{12}$). Minor components of spessartine ($\text{Mn}_3\text{Al}_2\text{Si}_3\text{O}_{12}$; 3 - 7 mole%), andradite ($\text{Ca}_3\text{Fe}^{3+}_2\text{Si}_3\text{O}_{12}$; up to 5 mole%), majorite ($\text{Mg}_4\text{Si}_4\text{O}_{12}$; up to 5 mole%), and NaTi-garnet ($\text{Na}_2\text{CaTi}_2\text{Si}_3\text{O}_{12}$; ~ 2 mole%) are also present. Garnets recovered from the anhydrous and more iron-rich bulk compositions (Omph/Op_{x_{ss}}2-5) contain 30 to 77 mole% almandine, 11 to 60 mole% pyrope and 9 to 13 mole% grossular. NaTi-garnet and majorite component concentrations both show clear positive pressure dependences.

Garnet grains from a graphite capsule experiment (H3605x) performed at 7 GPa and 1480°C have $\text{Fe}^{3+}/\Sigma\text{Fe}$ ratios of approximately 0.16 (4). Fe^{2+} may have been oxidised by H_2O in these experiments, with the presence of graphite providing an upper limit to the level of oxidation. This limit depends, however, on the activity of CO_2 in the melt phase, which was not determined. The determined $\text{Fe}^{3+}/\Sigma\text{Fe}$ ratio is similar to recent measurements reported by Purwin et al. (2013) for eclogitic garnets equilibrated in graphite capsules from 3 GPa and 1300°C. Purwin et al. (2013) reported garnet $\text{Fe}^{3+}/\Sigma\text{Fe}$ ratios to increase with temperature above 1100°C at 3 GPa and reach 0.15 at 1300°C, however, as the presence of graphite does not, on its own, buffer the oxygen fugacity, no direct comparison can be made between the two studies other than noting the qualitative similarity of the measurements.

Garnets analyzed from the anhydrous experiment performed in a Re capsule (V772) at 4 GPa and 1200°C have lower $\text{Fe}^{3+}/\Sigma\text{Fe}$ ratios of 0.08 (2). This is slightly lower than the value reported by Purwin et al. (2013) at 3 GPa and 1200°C in a graphite capsule but reflects more reducing conditions resulting from the absence of an oxygen source such as H_2O or ReO_2 in the experiments. Since, the starting material was reduced at FMQ -2 in the gas mixing furnace and there was no oxygen source, the oxygen fugacity likely remained at a similar level.

The obtained $\text{Fe}^{3+}/\Sigma\text{Fe}$ ratios have been used in Appendix 1 to calculate cation proportions of both ferric and ferrous iron in garnet, with the ratios assumed to be identical in all samples employing the same type of capsule. However, in the following discussion and in all thermodynamic calculations garnet end members have been calculated by assuming all Fe analyzed is Fe^{2+} to allow applicability to datasets with unknown Fe^{3+} concentrations. The proportion of the grossular component in garnet is, therefore, defined as the Ca mole fraction on the dodecahedral site i.e.,

$$X_{Ca} = [Ca/(Ca+Mg+Fe^{total})] \quad (4.2)$$

with similar expressions for X_{Mg} and X_{Fe} . Mixing on the Al and Si sites in garnet were neglected in modelling.

Clinopyroxene

The eclogitic clinopyroxenes can be considered to be multisite solid solutions with the general formula $(Fe,Ca,Na,Mg)^{M2}(Fe,Mg,Al,\square)^{M1}(Si,Al)^{IV}Si^{IV}O_6$ (Mukhopadhyay 1991; Simakov 2008). Clinopyroxenes analyzed from a hydrous experiment (H3605x) performed in a graphite capsule at 7 GPa and 1480°C yielded $Fe^{3+}/\Sigma Fe$ ratios of 0.19(3) (Fig. 4.3.2.1), although the absolute uncertainty on the measurement is in the range 15 - 30% due to the low total Fe concentration, which is close to the resolution limit of the EELS system. This ratio is similar to values reported for eclogitic clinopyroxenes formed in graphite capsules by Purwin et al. (2013) at 3 GPa but only at temperatures below 1200°C. At higher temperatures Purwin et al. (2013) report a steep drop in clinopyroxene $Fe^{3+}/\Sigma Fe$ ratios. Clinopyroxenes from Re capsule experiments at 4 GPa and 1200°C yielded $Fe^{3+}/\Sigma Fe$ ratios of 0.06 (1), which are much lower than the measurements of Purwin et al. (2013) from the same temperature.

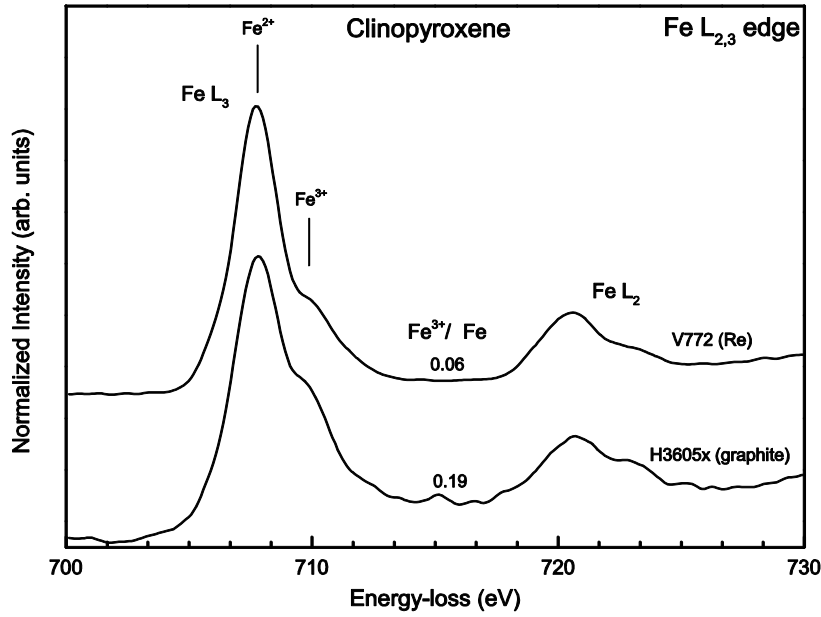


Fig. 4.3.2.1 Normalized and deconvoluted EELS spectra of clinopyroxenes from sample H3605x (graphite capsule) and V772 (Re capsule). The $\text{Fe}^{3+}/\Sigma\text{Fe}$ ratios were determined following the method of van Aken et al. (1998).

To calculate the proportion of cpx end members the method of Zhao et al. (2011) has been applied, and the following end members considered: jadeite ($\text{NaAlSi}_2\text{O}_6$), diopside/hedenbergite ($\text{Ca}[\text{Mg,Fe}]\text{Si}_2\text{O}_6$), enstatite/ferrosilite ($[\text{Mg,Fe}]_2\text{Si}_2\text{O}_6$), Ca-Tschermaks (CaAlAlSiO_6), and Ca-Eskola ($\text{Ca}_{0.5}\square_{0.5}\text{AlSi}_2\text{O}_6$). Ferric iron could be assigned to either an acmite ($\text{NaFeSi}_2\text{O}_6$) or a CaFeAlSiO_6 component, but has been ignored in modelling of the barometer for the same reasons as described above for garnet. Furthermore as the total amount of Fe^{3+} , as shown in Appendix 1, is small it most likely has no major effect on equilibrium 4.1. The following site assignments are made, starting with the determination of the proportion of tetrahedrally coordinated Al, which also defines the proportion of the Ca-Tschermaks (CaTs) component:

$$Al^{IV} = 2 - Si \quad (4.3)$$

Where Si is, for example, the number of Si atoms per 6 oxygen formula units. The remaining Al is assigned to the M1-site,

$$Al^{M1} = Al - Al^{IV} \quad (4.4)$$

A portion of this remaining Al is then assigned to jadeite i.e.

$$\text{Jadeite (NaAlSi}_2\text{O}_6) = \text{Na} \quad (4.5)$$

Although not important for the barometry calculations described later, any remaining Al is assumed to form the Ca-Eskola component, determined from,

$$\text{Ca Eskola} = \text{Al} - 2\text{Al}^{IV} - \text{Na}. \quad (4.6)$$

Ca, Na and Mn are assigned to the M2 site. Mg, Fe and Ti are assigned to M1 until the site occupancy is 1, upon which the residual Mg + Fe is assigned to M2. The Fe/(Fe + Mg) ratio in both M1 and M2 sites is constrained to be the same. Fe³⁺ contents in the cpx M1 site are shown in Appendix 1, calculated by assuming Fe³⁺/ΣFe ratios are the same for each capsule type as in the two representative samples examined. As stated previously, however, all Fe is considered to be Fe²⁺ in the barometer refinement. Although this does influence the calculated proportion of Ca-Eskola, the mixing of Ca-Eskola associated vacancies on M2 is anyway ignored in the thermodynamic modelling so this should have no implications.

These site assignments result in clinopyroxene compositions for starting material OC1/2 with 17 – 38 mole% jadeite, 27 – 37 mole% diopside/hedenbergite, 7 – 13 mole% (clino-)enstatite/ferrosilite, 7 – 20 mole% Ca-Tschermaks, and 0 – 10 mole% Ca-Eskola.

The anhydrous starting materials Omph/Opx_{ss} yielded clinopyroxenes with 17 – 19 mole% jadeite, 30 – 38 mole% diopside/hedenbergite, 44 – 51 mole% (clino-)enstatite/ferrosilite, 2 – 3 mole% Ca-Tschermaks, and < 1 mole% Ca-Eskola.

An alternative procedure for clinopyroxene component assignment is to first determine the proportion of Ca-Eskola from the deficit in the total number of cations compared to the 4 cations in the formula (Pertermann and Hirschmann, 2003). Further components are then assigned in the reverse order to those used in this study. The different procedures result in quite different assignments, particularly for Ca-Eskola, in some instances. These differences arise because the techniques are sensitive to different uncertainties in the microprobe measurements. The method employed here results in a smaller uncertainty in the Al^{IV} content, which is then not influenced by the error in the $Fe^{3+}/\sum Fe$ ratio and uncertainties over the proportion of ferric iron components. When employing clinopyroxene data from previous studies component assignments have been redetermined, where necessary, to be consistent with the method used here.

Fig. 4.3.2.2 shows how the clinopyroxene Al^{IV} component decreases with pressure between 3 and 7 GPa in line with previous studies (Kiseeva et al., 2012; Klemme et al., 2002; Pertermann and Hirschmann, 2003). The Na, i.e. jadeite component, on the other hand increases with pressure. This reflects an exchange of Al between the tetrahedrally coordinated Si site and octahedrally coordinated M1 site, which leaves the total clinopyroxene Al content relatively constant with pressure at a given temperature. The Al^{IV} content also increases with temperature (Fig. 4.3.2.3) while the proportion of the jadeite component, decreases with temperature. The combined effect is an increase in the total cpx Al content with temperature, as reported by Kiseeva et al. (2012). In comparison to the study of Kiseeva et al. (2012), however, cpx Al^{IV} contents measured at a similar pressure and temperature in this study are systematically lower, as will be discussed later. The cpx

Ca-content increases with temperature and decreases with pressure. This is matched by a corresponding increase in the garnet Ca content with pressure.

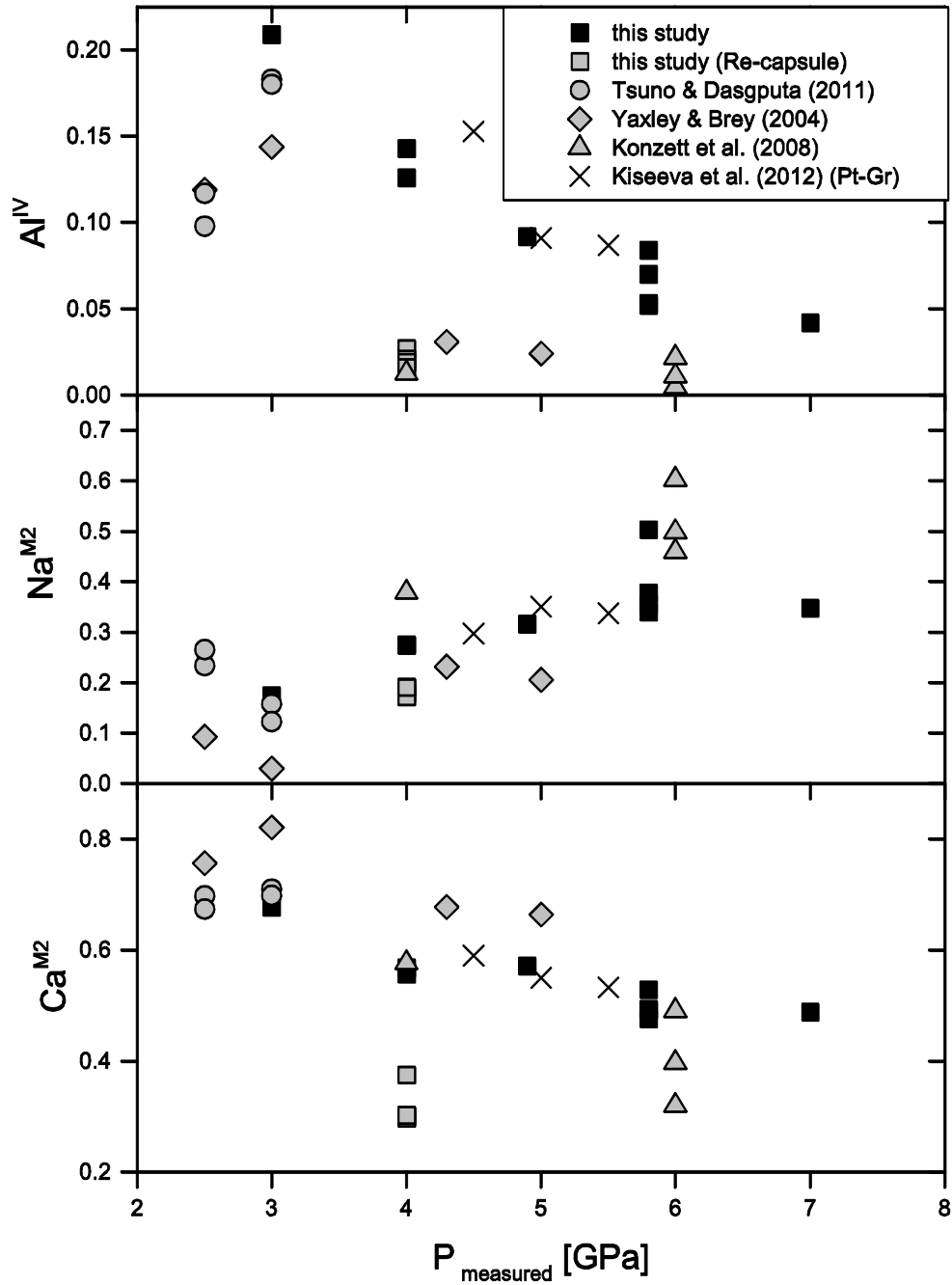


Fig. 4.1.2.2 Clinopyroxene cation contents, in terms of a 6 oxygen formula unit, plotted as a function of pressure. The data are from various temperatures, which causes the main variation other than pressure. Re capsule experiments from this study were performed at 1200°C, while the other experiments from this study were performed in the range 1377-1550°C. For clarity only the results of Kiseeva et al. (2012) collected at 1250°C are shown.

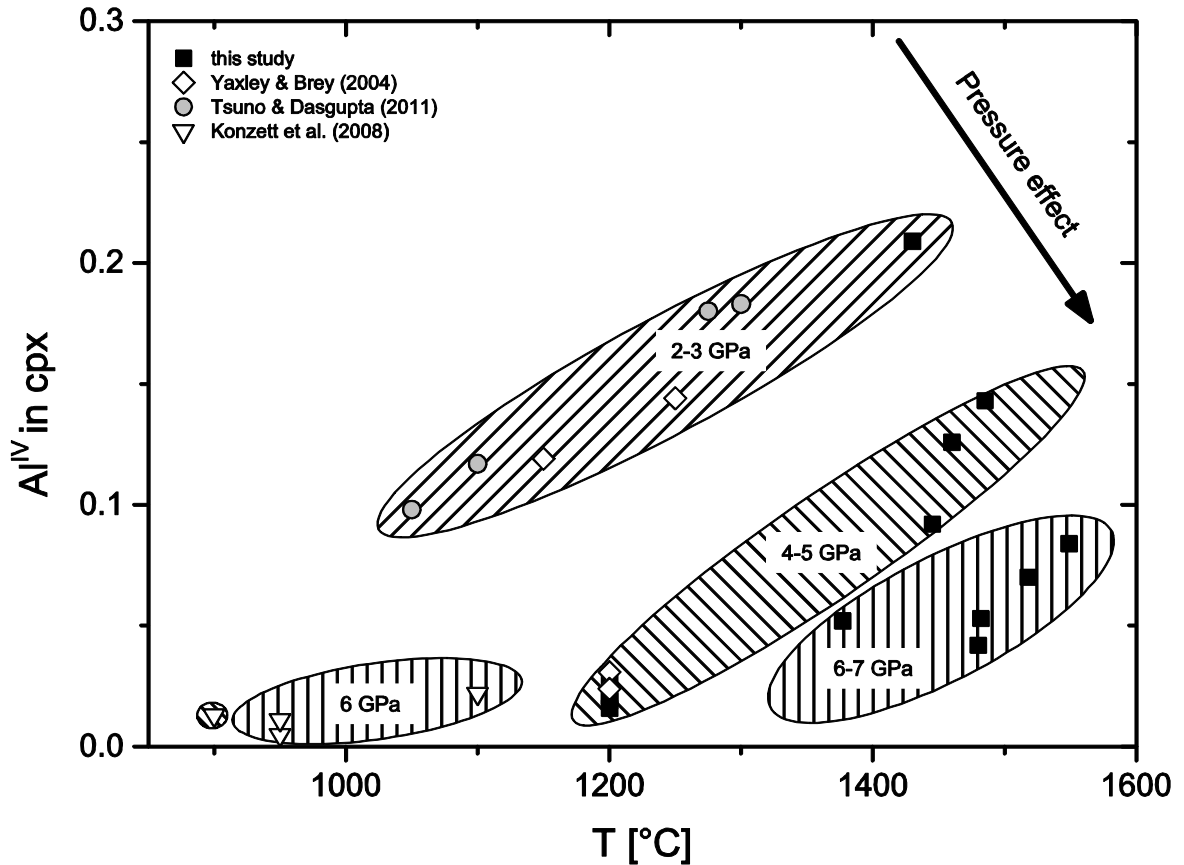


Fig. 4.3.2.3 Variation with temperature of the clinopyroxene tetrahedral Al concentration (Al^{IV}) in formula units. Pressures are indicated by the banded areas.

4.3.3. Melt analyses

The melt phase is present either as homogeneous glass or as small quenched dendritic crystals. When both glass and dendrites are present the quench crystals preferentially crystallized on the contact between sample and capsule material. When a large fraction of melt is present ($> \sim 20$ vol.%) the melt tends to form a glass, whereas smaller melt fractions crystallize as dendritic quench crystals. The amount of quenched melt increased with increasing temperature at the expense of clinopyroxene. At higher pressures the proportion of melt decreases at a given temperature. The chemical composition of the glass and the quench crystals is virtually identical throughout the samples with variations only in SiO_2 , which appears to be 2-4 wt.% higher in the quenched crystals. The glass/quench crystals of

starting material OC1/2 are basaltic melts with 46 - 50 wt.% SiO₂ and 1.4 - 3.5 wt.% Na₂O. The analytical sums were generally below 98 wt.% indicating high contents of volatile components, i.e. F and H₂O. Measurements of F in the glass gave F concentrations between 1 and 3.9 wt.%, depending on the melt fraction.

Quenched melts recovered from the anhydrous experiment V772 (Omph/Opx_{ss}2-4) are also basaltic with SiO₂ concentrations of 49 to 53 wt.% and Na₂O concentrations of 2.4 to 3.3 wt.%. The melt FeO content varies strongly, from 9 to 35 wt.%, due to the significantly different bulk FeO/MgO ratios of the starting materials. The fraction of melt decreases with decreasing bulk FeO content in the samples, and melt is absent in the chamber with the lowest bulk FeO content (V772-5).

4.3.4. Attainment of equilibrium

The attainment of equilibrium is critical to the accuracy of the geobarometer calibration because it relies on the cpx Al concentration, which can be strongly zoned if equilibrium is not obtained. In the current experiments the presence of a significant proportion of hydrous silicate melt acted as a flux from which mineral grains were crystallized. This was aided by initially raising the temperature by 50°C in the first 15 min of the experiment, then cooling to the run temperature. Crystals that grow from the melt show very little chemical zonation and crystals throughout the charge have a homogeneous composition, even though some are up to 0.3 mm in diameter, which is good evidence for the attainment of equilibrium.

A further method for assessing the state of equilibrium is to obtain an independent estimate for the temperature of the experiments using the Ellis and Green (1979) and Nakamura (2009) garnet-clinopyroxene geothermometer, which is a sensitive function of the Fe-Mg exchange between the mineral phases. Such estimates are compared with the thermocouple

temperature in Fig. 4.3.4.1. Given the likely thermal gradient throughout the charge (~50°C), the uncertainty of ± 50 °C for both geothermometers and accounting for the uncertainty in the electron microprobe analyses, acceptable levels of equilibrium should give temperatures within 100 °C of the thermocouple temperature. The majority of samples plot within a mean deviation of ± 32 °C. Experiments that fell outside of the ± 100 °C range were excluded.

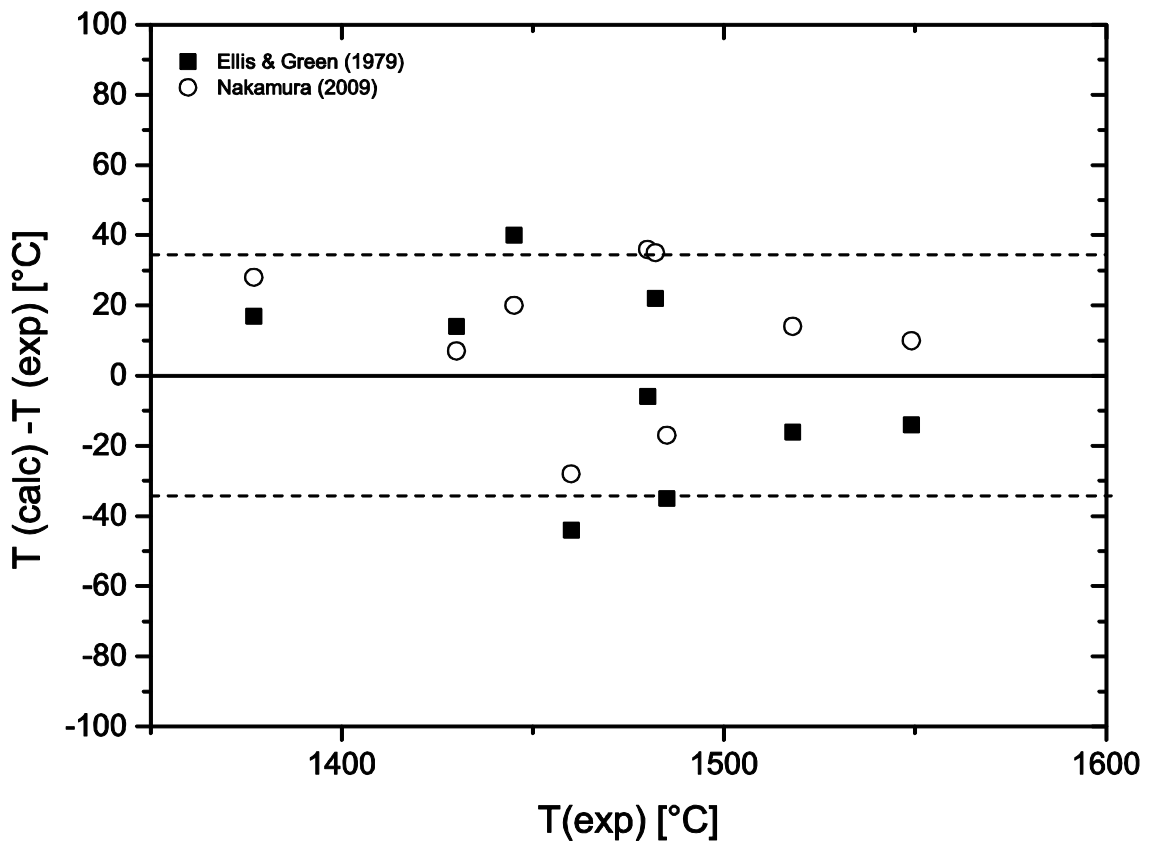


Fig. 4.3.4.1 The difference between experimental thermocouple temperatures and the temperature calculated with the Ellis and Green (1979) and Nakamura (2009) geothermometers for experiments performed in this study.

4.3.5. Thermodynamic model

Equilibrium (4.1) describes the distribution of Al_2O_3 between garnet and clinopyroxene. If pressure and temperature influences on the volume are ignored, then at equilibrium pressure can be determined from the expression,

$$P = -\left[\Delta G_{T,1bar}^0 + RT \ln K_{(1)}\right] / \Delta V_r \quad (4.7)$$

where R is the gas constant and $\Delta G_{T,1bar}^0$, ΔV_r and $K_{(1)}$ are the standard state Gibbs free energy change, (with the standard state being the pure phases at 1 bar and the temperature of interest), molar volume change of the pure phases and the equilibrium constant of reaction (4.1) respectively. $\Delta G_{T,1bar}^0$ and ΔV_r can be calculated from end-member thermodynamic data (Holland and Powell 2011) and over the range of plausible eclogite equilibration conditions i.e., 2-7 GPa and 700 to 1400 °C, the calculated values can be fitted by the simple expression,

$$\Delta G_{T,1bar}^0 = 16500 - 23.50 * T \quad (4.8)$$

with

$$\Delta V_r = 0.719 \text{ J/bar} \quad (4.9)$$

being a suitable average value applicable over the range of conditions. The equilibrium constant for equilibrium (4.1) is

$$K_{(1)} = \frac{a_{Di}^{Cpx} a_{CaTs}^{Cpx}}{[a_{Gr}^{Gt}]^{2/3} [a_{Py}^{Gt}]^{1/3}} = \frac{X_{Di}^{Cpx} X_{CaTs}^{Cpx}}{[X_{Gr}^{Gt}]^{2/3} [X_{Py}^{Gt}]^{1/3}} \cdot \frac{\gamma_{Di}^{Cpx} \gamma_{CaTs}^{Cpx}}{[\gamma_{Gr}^{Gt}]^{2/3} [\gamma_{Py}^{Gt}]^{1/3}} \quad (4.10)$$

Where a , X and γ refer to the activity, molecular fraction and activity coefficient of the mineral components. Rearranging equation (4.7) gives an expression for $\Delta G_{T,P}^0$ the standard state Gibbs free energy at the pressure and temperature of interest i.e.

$$\Delta G_{T,1\text{ bar}}^0 + P\Delta V_r = -RT \ln K_{(1)} \quad (4.11)$$

The barometer is calibrated by minimizing the difference between both sides of this equation for each experimental data point. To do this most of the required thermodynamic data has been taken from the literature and in particular from studies that have determined thermodynamic parameters using large experimental data sets (e.g. Ganguly et al. 1996; Holland and Powell 2011). Only the less well constrained activity composition relations for clinopyroxene have been refined using the experimental results and some results from previous studies. $K_{(1)}$ is determined from the mineral compositions using equation (4.10) as follows. For garnet, mixing is considered only on the dodecahedral site, with the molecular fractions of the garnet components defined as,

$$X_{Gr}^{Gt} = (X_{Ca})^3 \quad (4.12)$$

And

$$X_{Py}^{Gt} = (X_{Mg})^3 \quad (4.13)$$

The activity coefficients are described using an asymmetric Margules model,

$$\begin{aligned}
 & RT \ln \gamma_{Gr}^{Gt} \\
 &= 0.5 W_{CaMg} X_{Mg} [1 - X_{Ca} + X_{Mg} + 2X_{Ca}(X_{Ca} - X_{Mg} - 1)] \\
 &+ 0.5 W_{MgCa} X_{Mg} [1 - X_{Ca} - X_{Mg} - 2X_{Ca}(X_{Ca} - X_{Mg} - 1)] \\
 &+ 0.5 W_{CaFe} X_{Fe} [1 - X_{Ca} + X_{Fe} + 2X_{Ca}(X_{Ca} - X_{Fe} - 1)] \\
 &+ 0.5 W_{FeCa} X_{Fe} [1 - X_{Ca} - X_{Fe} - 2X_{Ca}(X_{Ca} - X_{Fe} - 1)] \\
 &+ W_{MgFe} X_{Mg} X_{Fe} (X_{Mg} - X_{Fe} - 0.5) \\
 &+ W_{FeMg} X_{Fe} X_{Mg} (X_{Fe} - X_{Mg} - 0.5) \\
 &+ W_{CaMgFe} X_{Mg} X_{Fe} (1 - 2X_{Ca})
 \end{aligned} \tag{4.14}$$

$$\begin{aligned}
 & RT \ln \gamma_{Py}^{Gt} \\
 &= 0.5 W_{MgCa} X_{Ca} [1 - X_{Mg} + X_{Ca} + 2X_{Mg}(X_{Mg} - X_{Ca} - 1)] \\
 &+ 0.5 W_{CaMg} X_{Mg} [1 - X_{Mg} - X_{Ca} - 2X_{Mg}(X_{Ca} - X_{Mg} - 1)] \\
 &+ 0.5 W_{MgFe} X_{Fe} [1 - X_{Mg} + X_{Fe} + 2X_{Mg}(X_{Mg} - X_{Fe} - 1)] \\
 &+ 0.5 W_{FeMg} X_{Mg} [1 - X_{Mg} - X_{Fe} - 2X_{Mg}(X_{Mg} - X_{Fe} - 1)] \\
 &+ W_{CaFe} X_{Ca} X_{Fe} (X_{Ca} - X_{Fe} - 0.5) \\
 &+ W_{FeCa} X_{Fe} X_{Ca} (X_{Fe} - X_{Ca} - 0.5) \\
 &+ W_{CaMgFe} X_{Ca} X_{Fe} (1 - 2X_{Mg})
 \end{aligned} \tag{4.15}$$

Garnet Margules parameters (W) are well constrained over wide ranges of composition by a large number of previous experimental data. To take advantage of this, values were taken from the model derived by Ganguly et al. (1996). The relatively small pressure dependent terms arising from the excess volumes of mixing were neglected to avoid the necessity to iterate the barometer equation (4.7) in terms of pressure. Garnet Margules parameters are

given in Table 4.3.5.1 on a single site basis i.e. equations (4.14) and (4.15) must be multiplied by 3.

For clinopyroxene mixing occurs on 4 sites (Simakov, 2008; Wood and Banno, 1973) with thermodynamic molecular fractions employed in equation (4.10) defined by,

$$X_{Di}^{Cpx} = X_{Ca}^{M2} X_{Mg}^{M1} (X_{Si}^{IV})^2 \quad (4.16)$$

$$X_{CaTs}^{Cpx} = 4X_{Ca}^{M2} X_{Al}^{M1} X_{Al}^{IV} X_{Si}^{IV} \quad (4.17)$$

Where $X_{Al}^{IV} = Al^{IV} / 2$, Al^{IV} is as defined in equation (4.3) and $X_{Si}^{IV} = Si / 2$. The remaining site mole fractions are determined as described in the previous section. Activity coefficients were calculated assuming a ternary symmetric mixing model for the M1 site and a quaternary symmetric mixing model for the M2 site. For the tetrahedral site a simple binary mixing model is introduced to account for Al^{IV} -Si interaction. This gives the following activity models for clinopyroxene:

$$\begin{aligned} & RT \ln \gamma_{Di} \\ &= [W_{MgAl} X_{Al}^2 + W_{MgFe} X_{Fe}^2 + X_{Fe} X_{Al} (W_{MgFe} + W_{MgAl} - W_{FeAl})]^{[M1]} \\ &+ [W_{CaMg} X_{Mg}^2 + W_{CaNa} X_{Na}^2 + W_{CaFe} X_{Fe}^2 + X_{Mg} X_{Fe} (W_{CaMg} + W_{CaFe} - W_{MgFe}) \\ &+ X_{Mg} X_{Na} (W_{CaMg} + W_{CaNa} - W_{MgNa}) + X_{Na} X_{Fe} (W_{CaNa} + W_{CaFe} - W_{NaFe})]^{[M2]} \\ &+ (W_{AlSi} X_{Al}^2)^{[IV]} \end{aligned} \quad (4.18)$$

$$\begin{aligned} & RT \ln \gamma_{CaTs} \\ &= [W_{MgAl} X_{Mg}^2 + W_{FeAl} X_{Fe}^2 + X_{Mg} X_{Fe} (W_{MgAl} + W_{FeAl} - W_{MgFe})]^{[M1]} \end{aligned}$$

$$\begin{aligned}
 &+ [W_{CaMg}X_{Mg}^2 + W_{CaNa}X_{Na}^2 + W_{CaFe}X_{Fe}^2 + X_{Mg}X_{Fe}(W_{CaMg} + W_{CaFe} - W_{MgFe}) \\
 &+ X_{Mg}X_{Na}(W_{CaMg} + W_{CaNa} - W_{MgNa}) + X_{Na}X_{Fe}(W_{CaNa} + W_{CaFe} - W_{NaFe})]^{[M2]} \\
 &+ (W_{AlSi}X_{Si}^2)^{[IV]}
 \end{aligned} \tag{4.19}$$

To account for the interaction between cations from different sites, the following reciprocal equilibria were examined (Mukhopadhyay, 1991; Simakov, 2008; Wood and Nicholls, 1978):



With the following Gibbs free energies, $\Delta G_I^0 = -21 \text{ kJ}$, $\Delta G_{II}^0 = -4.68 \text{ kJ}$, $\Delta G_{III}^0 = -5.01 \text{ kJ}$ (Mukhopadhyay, 1991). The following reciprocal terms should then be added to the activity composition formulations of diopside and CaTs:

$$RT \ln \gamma_{CaTs}(Recip) = (1 - X_{Al}^{M1})(X_{Fe}^{M2} \Delta G_I^0) - X_{Fe}^{M1}(X_{Fe}^{M2} \Delta G_{II}^0 + X_{Mg}^{M2} \Delta G_{III}^0) \tag{4.20}$$

$$RT \ln \gamma_{Di}(Recip) = -X_{Al}^{M1}(X_{Fe}^{M2} \Delta G_I^0) - X_{Fe}^{M1}(X_{Fe}^{M2} \Delta G_{II}^0 + X_{Mg}^{M2} \Delta G_{III}^0) \tag{4.21}$$

For the experimental eclogite data tested, however, these expressions make contributions to the total free energy that are generally <1 kJ, which makes them trivial in comparison to the interaction terms of the individual clinopyroxene sites (Table 4.3.5.1). The magnitude

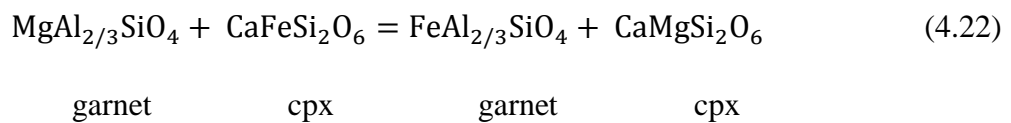
of these terms increases mainly with the Mg and Fe proportion on the M2 site, however, as most experimental and natural samples have < 0.2 formula units of Mg + Fe on M2 these terms can be safely neglected.

Table 4.3.5.1 Interaction parameters for garnet and clinopyroxene

Parameter (W_{ij})	Garnet	Clinopyroxene		
	X^*	M1	M2	T
W_{CaMg}	21.6-0.00578T		24.9	
W_{MgCa}	9.8-0.00578T			
W_{CaFe}	0.87-0.00169T		-49.3	
W_{FeCa}	6.8-0.00169T			
W_{MgFe}	2.1			
W_{FeMg}	0.7	0	0	
W_{MgAl}		4.9		
W_{FeAl}		3.6		
W_{CaNa}			11.6	
W_{MgNa}			-35.9	
W_{FeNa}			59.3	
W_{AlSi}				7.0

All values reported on a single site bases and in kJ/mol. T in K. * data compiled by Ganguly et al. (1996), P-dependent terms set to zero. The ternary interaction term is calculated from $W_{CaMgFe} = [(W_{MgCa} - W_{CaMg}) + (W_{CaFe} - W_{FeCa}) + (W_{FeMg} - W_{MgFe})]/2$

Using the results of experiments V772, V780 and V792 (Appendix 1), which employed multi-chamber capsules and each contained a range of starting materials with different Fe/Mg ratios, it was possible to obtain an estimate of the W_{MgFe}^{Cpx} interaction term that is independent from the rest of the experimental data. The 5 bulk starting materials in each capsule covered Mg/Fe ratios from ~ 0.2 to ~ 0.8. The Mg-Fe exchange between garnet and clinopyroxene can be described with the following equilibrium on a single site basis:



from this, the following distribution coefficient K_D is obtained:

$$K_D = \frac{X_{Mg}^{Cpx} X_{Fe}^{Gt}}{X_{Mg}^{Gt} X_{Fe}^{Cpx}} \quad (4.23)$$

To calculate the interaction term describing Mg-Fe mixing in clinopyroxene i.e. W_{MgFe}^{Cpx} , both garnet and cpx sites are considered to be symmetric solid solutions, which results in the following expression for K_D :

$$RT \ln K_D = -\Delta G^0 + W_{FeMg}^{Gt} (2X_{Fe}^{Gt} - 1) + W_{FeMg}^{Cpx} (1 - 2X_{Fe}^{Cpx}) \quad (4.24)$$

This expression was then fitted to the experimental data using a least squares routine where ΔG^0 and W_{FeMg}^{Cpx} were refined parameters and the term W_{FeMg}^{Gt} , which has been well studied, was calculated from the model of Ganguly et al. (1996) at the appropriate garnet Ca concentration. A comparison between the fitted terms in equation (4.24) and the experimental K_D for each experiment is shown in Fig. 4.3.5.1. The resulting value for W_{FeMg}^{Cpx} is -360 J/mol with an average deviation from the fit of less than 1 kJ. Although this fitting procedure assumes single site mixing for Fe and Mg in cpx, as the interaction parameter obtained is essentially zero, Fe-Mg mixing terms on both M1 and M2 are assumed to be zero in the following model. Each experimental data point was then used to calculate the difference across equation (11), and these differences were minimized using a least squares procedure, by refining the clinopyroxene Margules terms in equations (4.18) and (4.19). Two terms for the clinopyroxene M1 site were refined, five for M2 and one describing Si-Al interaction. To expand the range of conditions and compositions covered in this refinement further literature studies were employed. A criterion for the use of previous studies was that they employed eclogitic bulk compositions, covered conditions

where a detectable clinopyroxene CaTs component was present and that high quality mineral chemical analyses were provided with small analytical standard deviations.

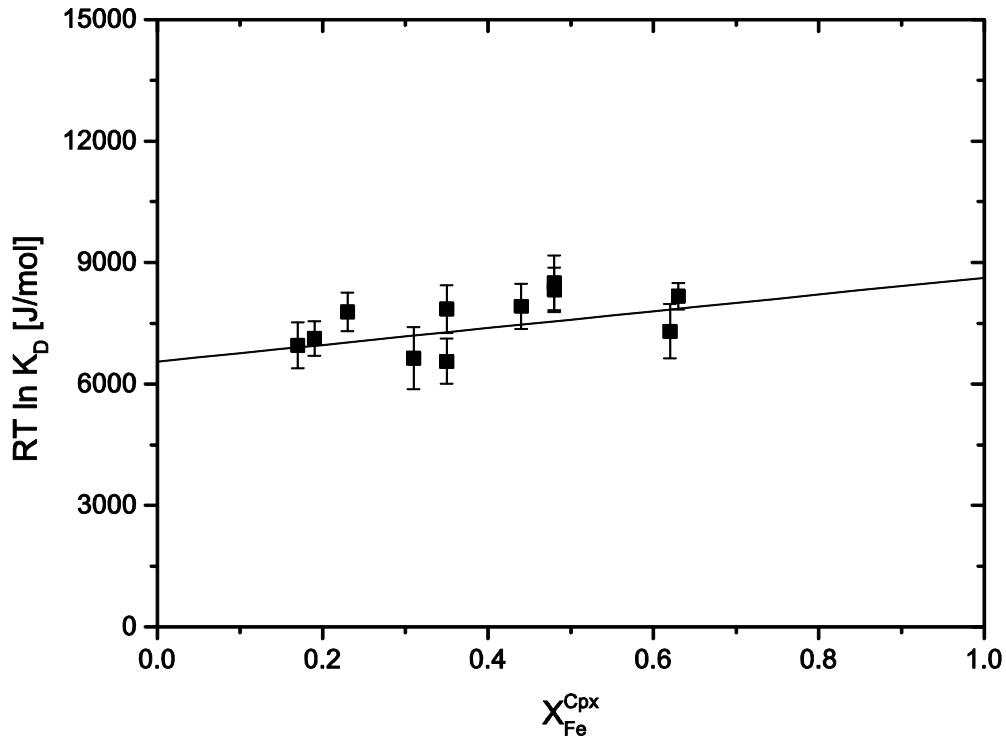


Fig. 4.3.5.1 $RT \ln(K_D)$, where K_D is the Fe-Mg exchange coefficient between garnet and clinopyroxene (equation 23), R is the gas constant and T is temperature, versus the mole fraction of Fe in clinopyroxene. The solid line shows the fit of equation (24) to the experimental data in order to determine the Fe-Mg Margules interaction parameter for clinopyroxene (see text). K_D 's are extracted from 3 multi-chamber capsule experiments containing a total of 11 individual sample chambers. The error bars indicate 1 standard error propagated from the microprobe analyses.

Experiments where heterogeneous mineral compositions led to large Al and Si standard deviations were neglected. In addition all data were tested using the Ellis and Green (1979) and Nakamura (2009) garnet-clinopyroxene geothermometer and any data that failed to reproduce the experimental temperatures within 100°C were excluded. Of the previous studies examined those of Tsuno and Dasgupta (2011), Yaxley and Brey (2004), Konzett et al. (2008) and Pertermann and Hirschmann (2003), met these criterion and resulted in a refined model consistent with the experimental data from this study. Several other studies

(Kiseeva et al. 2011; Spandler et al. 2008; Hammouda et al. 2009) that met the initial criteria but provided a poor fit to this model are discussed later, along with some possible explanations.

The combined data set comprises 46 experimental points between 2 and 7 GPa, and temperatures from 900 to 1550 °C. The resulting parameters are given in Table 4.3.5.1 with the residuals for each experimental point, i.e. the difference in free energy across equation (4.11), plotted as a function of Al^{IV} in Fig. 4.3.5.2(a). These residuals are in general less than 2 kJ with some values around 3 kJ. Most importantly the residuals show no correlation with Al^{IV} or in fact any other chemical component. Expressed as ΔP between the calculated and experimental pressure as shown in Fig. 4.3.5.2(b) the average deviation is ~0.2 GPa.

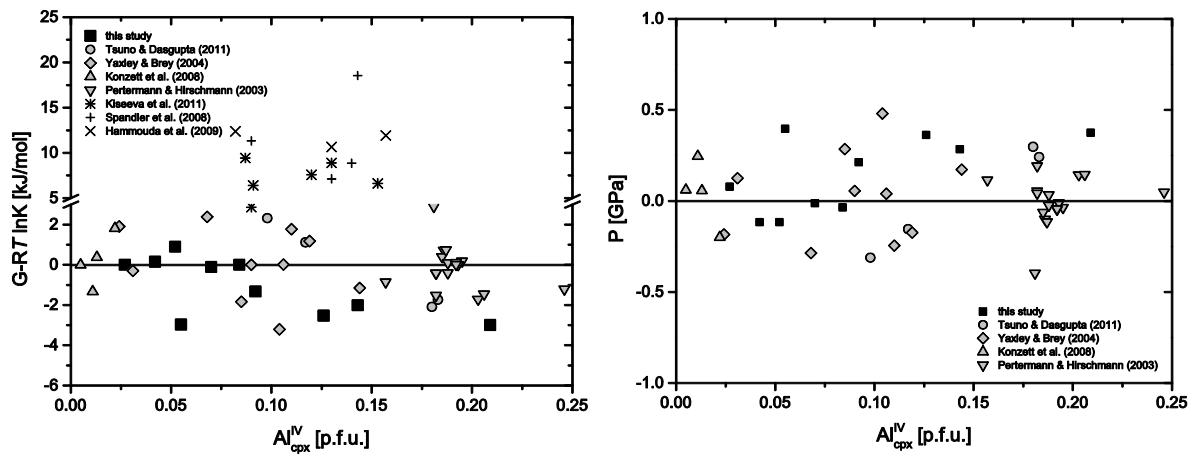


Fig. 4.3.5.2 (a) Residuals from the minimisation of the Gibbs free energy change of equation (4.11) at the pressure and temperature of interest, plotted against the proportion of the CaTs component (i.e. cpx Al^{IV}). The experiments used in the refinement show a deviation which is generally within +/- 2 kJ/mole. Several further studies show much greater residuals and were not included in the refinement. Possible reasons for this discrepancy are discussed in the text. **(b)** $P_{calc} - P_{exp}$ of experimental run products as a function of the CaTs component. As in **(a)** no systematic variation with CaTs can be observed.

4.4. Discussion

4.4.1. Model uncertainties

The quality of the clinopyroxene chemical analyses causes the main source of uncertainty in the calculated pressure. The contributions to the activity term in equation (4.11) are approximately 40 % CaTs, 15 % diopside, 10 % pyrope and 35 % grossular. Accordingly, uncertainties in the determination of the CaTs fraction have the largest impact on the calculated pressure, with uncertainties in SiO₂ analyses having by far the largest influence. When cpx Si concentrations remain below 1.985 formula units, then a 1 % uncertainty on the SiO₂ analyses propagates to a maximum uncertainty of ~ 10 % in pressure. A 5 % uncertainty on any of the other major oxides propagates to an absolute pressure uncertainty that remains below 0.1 GPa. However, once silica contents rise above 1.985 formula units pressure uncertainties rise quickly and reach for example 25 % at ~ 1.995 formula units of Si. A Si content of around 1.985 formula units, i.e. 1.5 mole% CaTs content, is therefore, a practical limit to the use of the barometer. This can be also expressed as a simple exponential function for the percentage error on the calculated pressure i.e.,

$$\%err = 1.94 * 10^{-8} e^{10.18398 * [Si]} \quad (4.25)$$

where [Si] is the number of Si cations in the cpx formula. An uncertainty in temperature of 100 °C corresponds to an uncertainty in the pressure of ~ 0.5 GPa. However, for most compositions temperature variations will move pressure determinations along a slope that is approximately parallel to a calculated cratonic geotherm. Incorrect temperature estimates will lead to incorrect depth determinations but should not strongly influence the geotherm along which the sample lies.

The Fe^{3+} content of the mineral phases can potentially influence the determination of pressure using the barometer, primarily as it influences the determination of cation mole fractions on each site but also potentially due to non-ideal cation interactions with Fe^{3+} . Because analyses of natural samples rarely include accurate Fe^{3+} determinations and only a limited number of $\text{Fe}^{3+}/\Sigma\text{Fe}$ measurements were made in the current study, all Fe is treated as Fe^{2+} in the barometer calibration and both of these influences are ignored. An estimate of at least the primary influence of Fe^{3+} on pressure determinations can be made however. Measurements (Cosca and Peacor, 1987; Luth and Canil, 1993) and reasoning imply that Fe^{3+} partitions preferentially onto the cpx M1 site and the octahedral (Al) site of garnet. As such the most significant consequence for the barometer of unknown $\text{Fe}^{3+}/\Sigma\text{Fe}$ ratios is on the mole fraction of Mg on the cpx M1 site and the mole fractions of Ca and Mg on the garnet dodecahedral site. Using measurements of mineral $\text{Fe}^{3+}/\Sigma\text{Fe}$ ratios measured in this study, i.e. 0.16 for garnet and 0.2 for cpx, the apparent effect on the barometer resulting from a drop in the Fe^{3+} contents of both minerals to zero, i.e. a hypothetical more reduced condition, would be an increase in the pressure by up to 0.15 GPa. As this is relatively trivial, $\text{Fe}^{3+}/\Sigma\text{Fe}$ ratios of natural samples (Sobolev et al. 1999), which in most instances appear to be similar or lower than those measured in this study, can be safely assumed to be zero without major consequences. If, on the other hand, garnet that $\text{Fe}^{3+}/\Sigma\text{Fe}$ ratios are higher than those determined in the experiments then in comparison to the case where all Fe is treated as Fe^{2+} , the activities of Mg and Ca in the dodecahedral site will in reality increase, but the Al activity, which is assumed to be 1 in the current study, would in effect decrease. These effects will tend to cancel out and unless strong non-ideal interactions take place, the uncertainties introduced by assuming all Fe is Fe^{2+} will be trivial. The effect on cpx is even smaller. In summary, as the experiments were performed in equilibrium with graphite and lithospheric oxygen fugacities are typically also in the range of graphite or

diamond stability (Stagno et al. 2013), the barometer can likely be applied to a wide range of mantle rocks while assuming all measured Fe is Fe²⁺. The same argument most likely holds for diamond inclusions.

4.4.2. Comparison with previous studies

As described previously the studies of Tsuno and Dasgupta (2011), Yaxley and Brey (2004), Konzett et al. (2008) and Pertermann and Hirschmann (2003) can be consistently fitted along with the current study into a refinement of the geobarometer parameters. Some data from these studies were excluded from the refinement, either because of large reported uncertainties on the chemical analyses, in particular the Al₂O₃ and SiO₂ analyses, or because the experimental temperature was not reproduced by the application of the Ellis and Green (1979) and Nakamura (2009) geothermometers by better than 100 °C. As shown in Fig. 4.4.2.1 the barometer reproduces the reported experimental pressures within these 5 studies to better than 0.2 GPa at the 1 σ level. The experimental data are only from eclogitic bulk compositions, but in addition to biminerally assemblages these also include silica saturated and kyanite-bearing run products (e.g. Konzett et al. 2008; Pertermann and Hirschmann 2003), for which pressures are well reproduced. The barometer has not been calibrated using samples containing orthopyroxene or olivine, however, for which other barometers are likely more suitable.

A number of further experimental studies, which were not used in the calibration, also report eclogitic mineral compositions that are consistent with the barometer (Klemme et al. 2002; Green et al. 2000; Kessel et al. 2005; Kogiso and Hirschmann 2006). Several other studies, however, that passed the tests imposed to filter out disequilibrium experiments result in significant differences when experimental and calculated pressures are compared (Kiseeva, et al. 2012; Spandler, et al. 2008; Hammouda, et al. 2009). These differences are

consistently in the same direction and arise from higher CaTs contents, generally ~0.05 formula units, in these experiments compared to those used in the refinement at similar pressures and temperatures. This leads to an underestimation in the calculated pressure compared to the experimental pressure (Fig. 4.8). The extent of the underestimate increases with pressure from -0.1 GPa at around 3 GPa to -2 GPa at 6 GPa. The exact cause of this discrepancy is hard to determine, though the increase of the mismatch with pressure might point at an issue in pressure calibration at high pressures. The bulk compositions employed are similar across all studies, to the extent that they mainly crystallize a bimineralec assemblage of garnet and cpx.

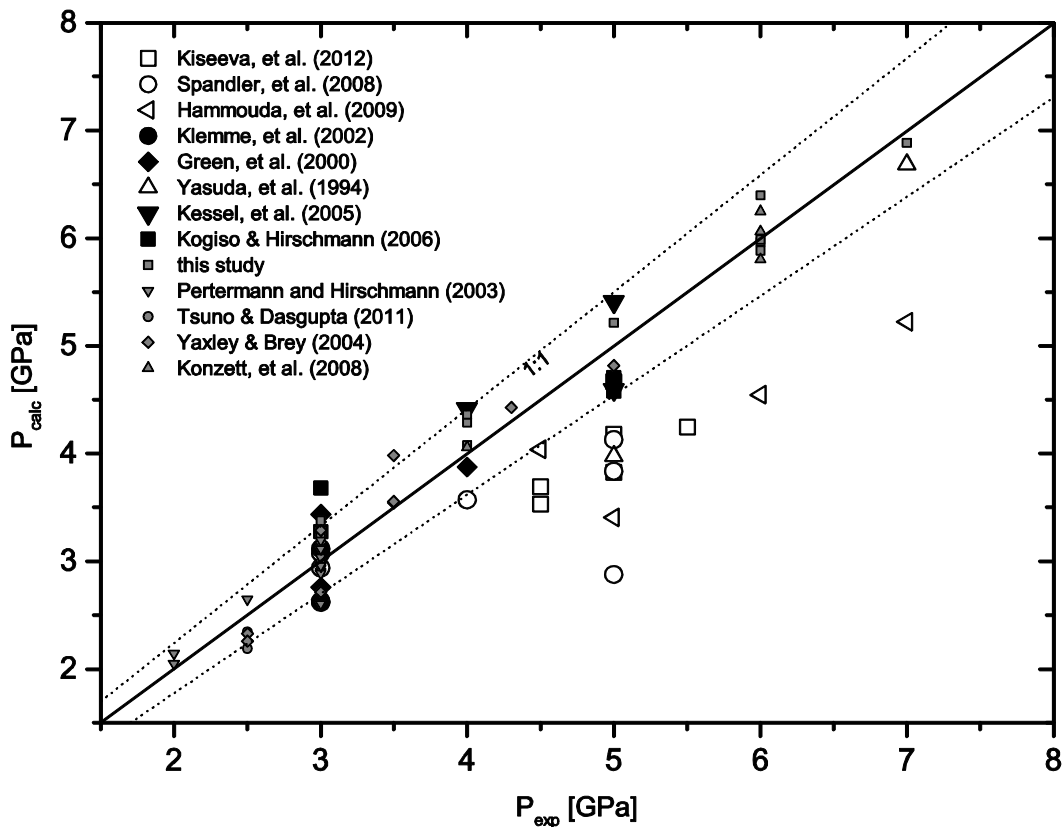


Fig. 4.4.2.1 Comparison between calculated and estimated pressure for a number of experimental studies conducted in eclogitic systems. Those data used in the refinement of the geobarometer are indicated by small grey symbols. The dotted lines represent the 10% uncertainty as discussed in the text.

The main variation is in the addition of volatiles, with the current study containing H₂O and F and the discrepant studies mainly performed in the presence of CO₂. However, the studies of Tsuno and Dasgupta (2011), Yaxley and Brey (2004) were also anhydrous and contained CO₂ and are in good agreement with this study. Another possibility would be differences in the Fe³⁺/ΣFe ratios in phases between the two groups of studies. However, there is no reason, based on the experimental procedures, to expect large differences in oxygen fugacity between the studies and, as explained in the previous section, such differences would not be expected to have a significant effect on calculated pressures.

One explanation would be a difference in the calibrated pressure between the two groups of studies. Some indication that this is indeed an issue can be obtained by also examining the garnet majorite content, which is also a function of pressure. In this study garnet Si contents start to rise above 3 cations per formula unit at pressures above 4 GPa and reach values of 3.05 i.e. 5 mole % majorite, by 7 GPa. This is consistent with recent thermodynamic calculations that incorporate many experimental data sets (Stixrude and Lithgow-Bertelloni, 2011). The studies of Hammouda et al. (2009) and Kiseeva, et al. (2012) show in general lower garnet majorite contents at comparable conditions, which would be consistent with the inferred difference in pressure between the two sets of studies based on the cpx CaTs content.

In Fig. 4.4.2.2 the barometer calibration is compared with a similar calibration made by Simakov (2008). Pressures for experiments performed in this study and that of Petermann and Hirschmann (2003) are calculated and compared. Both barometers are in good agreement at pressures up to 3 GPa, but at higher pressures the Simakov (2008) geobarometer predicts pressures that are systematically high compared to this study. We

note that at high pressures the experimental data set used by Simakov (2008) employs many assemblages which are not formed from eclogitic bulk compositions.

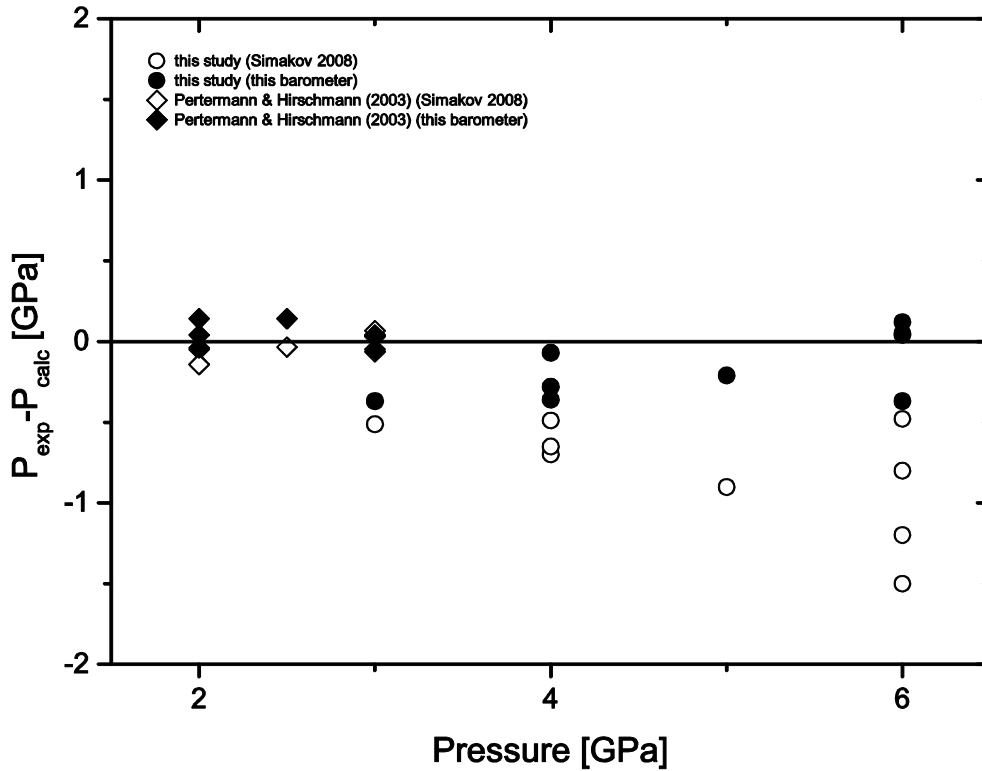


Fig. 4.4.2.2 Differences between experimental pressures and those calculated using the barometer refined in this study and the barometer of Simakov (2008) are shown using the experiments performed in this study and those performed at lower pressures by Petermann and Hirschmann (2003).

4.4.3. Geobarometry of mantle eclogites

The geobarometer has been used to calculate apparent equilibration pressures for a range of eclogitic mantle xenolith assemblages selected from cratonic kimberlites from various localities (Table 4.4.3.1). Analyses were selected for samples where clinopyroxenes contained sufficient CaTs in clinopyroxene. Furthermore, mostly pristine samples were selected that lacked significant overprinting by metamorphic events, based on the described textural observations and exsolution lamellae in clinopyroxene. The temperature for each garnet-clinopyroxene pair was determined with the Ellis and Green (1979) garnet-

clinopyroxene geothermometer and cross-checked using the geothermometers of Krogh (1988) and Nakamura (2009). The pressure and temperature calculated for each assemblage is shown in Fig. 4.4.3.1 where the values are compared with conductive geotherms for cratonic lithosphere calculated for heat flows between 40 and 45 mWm^{-2} . Three sets of samples, representative of different conditions, are plotted with error bars calculated using equation (25). For clarity the errors on other sample sets are not shown. Error bars reflect the uncertainties in the CaTs component, which increase with pressure and temperature as the component decreases.

The lowest pressure samples investigated are from the Zero kimberlite in the Kuruman group, which come from a locality close to the edge of the Kaapvaal craton (Schmickler et al. 2004). The bimineralec eclogites indicate conditions slightly hotter than a 45 mWm^{-2} geotherm, which probably reflects their origin at the margin of the craton where the lithosphere is thinner. Orthopyroxene bearing rocks from the same suite are also shown in Fig. 4.4.3.1 with pressures determined from the Al-in orthopyroxene geobarometer of Brey et al. (1990). These also plot on or slightly above the 45 mWm^{-2} geotherm and are in reasonable agreement, particularly when errors on both barometers are considered. The bimineralec and orthopyroxene bearing samples indicate a slightly hotter geotherm compared to that estimated from peridotitic xenoliths from the same locality (Shee et al., 1989) but this difference is again similar to the uncertainties in the pressure determinations.

A suit of eclogites from the Nunatak-1390 kimberlite boulders, West Greenland (Tappe, et al. 2011) are shown in Fig. 4.4.3.1 revealing a relatively narrow pressure range averaging at approximately 3 GPa. The samples plot along a hotter geotherm compared to projections of the North Atlantic cratonic geotherm of Sand et al. (2009) determined from peridotite xenoliths. Based on clinopyroxene trace element concentrations both pristine and metasomatically overprinted assemblages can be identified within this group with the latter

showing strong incompatible element enrichments (Tappe, et al. 2011). Although, the calculated pressures for the over printed assemblages have a slightly larger spread than the pristine samples, average pressures determined for both suites, 2.9 ± 0.1 GPa (pristine) and 3.0 ± 0.3 GPa (overprinted), are practically identical.

Eclogitic xenoliths from the Kaapvaal craton (Jagersfontein, Roberts Victor, Bellsbank) follow geotherms between $38\text{--}45 \text{ mWm}^{-2}$, with some of the deepest eclogites in accord with the lowest geotherm. Pressures are found to penetrate well into the diamond stability field (Roberts Victor and Jagersfontein), consistent with the diamondiferous nature of some xenoliths from these localities.

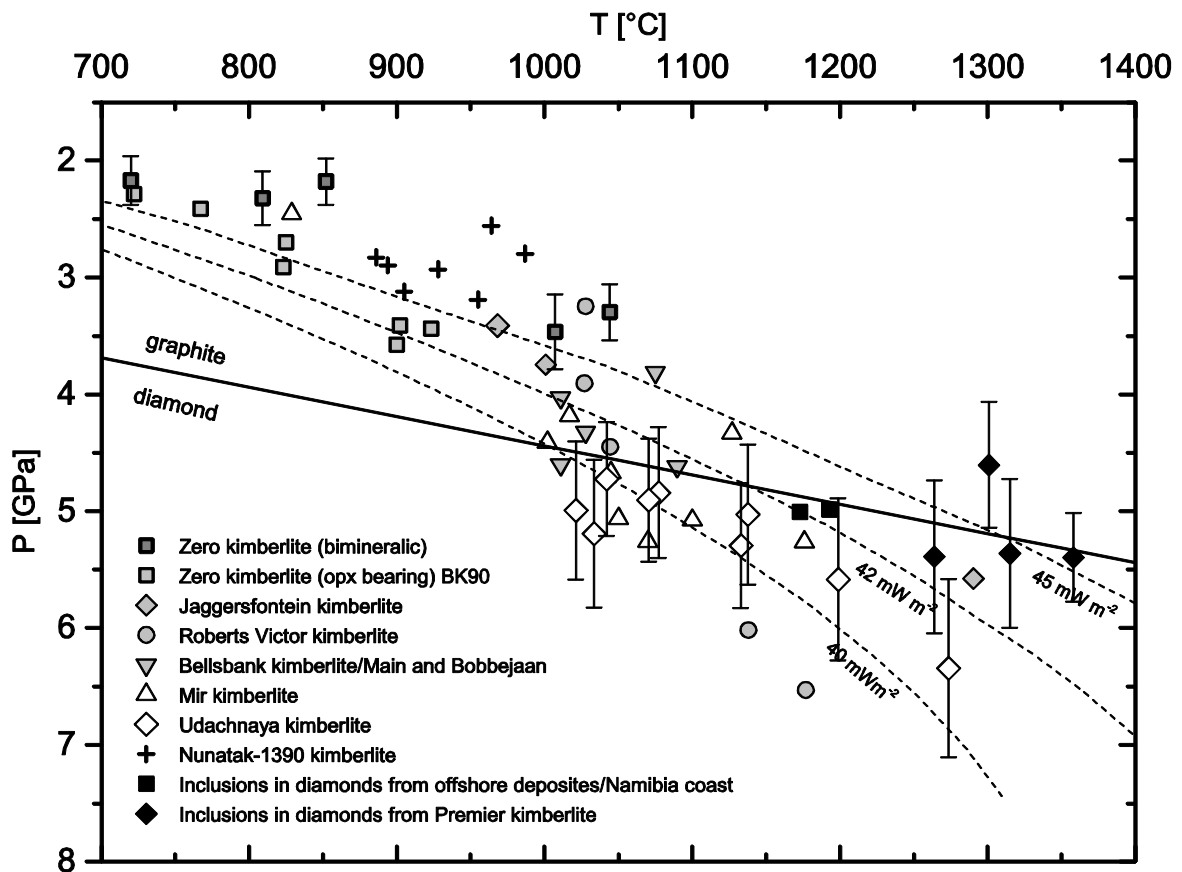


Fig. 4.4.3.1 Pressure-temperature calculations for natural eclogite xenoliths from several kimberlites and eclogitic diamond inclusions. The graphite-diamond transition is taken from Kennedy and Kennedy (1976). The geotherms are calculated according to (Pollack and Chapman (1977)). References for each sample suite are given in Table 4.4.3.1. Uncertainties are shown for just 3 representative sample sets for clarity, calculated using equation (4.25).

Eclogitic xenoliths from the Mir and Udachnaya kimberlites from the Siberian craton give pressures that penetrate the diamond stability field and follow a conductive mantle geotherm between 40 and 42 mWm⁻². This is slightly higher than that commonly assumed for the Siberian craton of around 35 - 40 mWm⁻² based on peridotitic samples and geophysical observations (Beard et al., 1996; Kuskov et al., 2011). These observations are, however, in reasonable agreement with those made by Ashchepkov et al. (2010) on Siberian kimberlite xenocrysts using monomineralic thermobarometry.

Table 4.4.3.1 P-T calculations for various eclogite xenoliths from cratonic localities.

Sample No.	T [°C] ¹	P [GPa]	comment	Reference ²
Zero eclogite, Kuruman group, Kaapvaal craton, South Africa				
Z184	1007	3.5		1
Z323	1044	3.3		1
Z257	852	2.2		1
Z298	809	2.3		1
Z239	720	2.2		1
Kaalvallei Group II kimberlite, South Africa				
295	1201	6.2		2
384	1121	6.0		2
385	1041	6.4		2
394	1152	7.8		2
413	1141	7.0		2
415	1160	6.1		2
Mir kimberlite, Yakutia, Russia				
M-432	1070	5.3	high Ca-group	3
M-69	1100	5.1	high Ca-group	3
M-54	1050	5.1	high Ca-group	3
M-60/1214	1127	4.3	intermediate Ca-group	3
M-53/1164	829	2.5	intermediate Ca-group	3
M-53	1002	4.4	intermediate Ca-group	3
M-2385	1176	5.3	low Ca-group	3
M-704	1045	4.7	low Ca-group	3
M-180	1017	4.2	low Ca-group	3
Bellsbank kimberlite, Main and Bobbejaan fissure, South Africa				
CK22/3	1075	3.8		4
CK22/7	1028	4.3		4
CK27/3	1011	4.5		4
CK27/4	1090	4.6		4

Experimental calibration of a garnet – clinopyroxene geobarometer for mantle eclogites

Sample No.	T [°C] ¹	P [GPa]	comment	Reference ²
Ck27/7	1011	4.0		4
Roberts Victor kimberlite, South Africa				
HRV247A	1027	3.9		5
HRV247B	1028	3.2		6
HRV247F	1044	4.4		6
RV9A	1138	6.0		4
RV9B	1177	6.5		4
Nunatak-1390 kimberlite, West Greenland				
488585C	886	2.8	pristine	7
592572E	894	2.9	pristine	7
592572G	928	2.9	pristine	7
488585B	831	3.1	metasomatically overprinted	7
592572A	964	2.6	metasomatically overprinted	7
592572C	905	3.1	metasomatically overprinted	7
592572DA	955	3.2	metasomatically overprinted	7
592572DB	987	2.8	metasomatically overprinted	7
Eclogitic inclusions in diamonds, Namibia coast				
Nam-89	1193	5.0		8
Nam-203	1173	5.0		8
Eclogitic inclusions in diamonds, Premiere Mine, South Africa				
AP101	1301	4.6		9
AP102	1315	5.4		9
AP106	1358	5.4		9
AP108	1264	5.4		9
Eclogite xenoliths, Udachnaya kimberlite, Yakutia, Russia				
56/2	1138	5.0		10
112/3	1042	4.7		10
58/2	1273	6.3		10
55/2	1077	4.8		10
27a/1	1034	5.2		10
37/1	1071	4.9		10
50/2	1021	5.0		10
100/2	1199	5.6		10
107/2	1133	5.3		10

¹Temperatures calculated with the Ellis and Green (1979) thermometer, *Temperatures calculated with the Krogh (1988) geothermometer. ²References: 1 Schmickler et al. (2004), 2 Viljoen et al. (2005), 3 Beard et al. (1996), 4 Carswell et al. (1981), 5 Luth et al. (1990), 6 O'Reilly and Griffin (1995), 7 Tappe, et al. (2011), 8 Stachel, et al. (2004), 9 Viljoen et al. (2010), 10 Jerde et al. (1993)

The geobarometer has also been used to determine the equilibration pressure of some eclogitic diamond inclusions. In Fig. 4.4.3.1 pressures for paired inclusions are determined for diamonds from the Premier kimberlite (Viljoen et al., 2010) and for placer diamonds from the coast of Namibia (Stachel et al., 2004). The inclusions from both locations give

pressures which are within the diamond stability field. Only the inclusion AP101 from the Premier mine has calculated pressures outside of the diamond stability field when errors are included (1301 °C, 4.6 GPa).

4.4.4. Summary

The garnet-clinopyroxene geobarometer has been calibrated based on the pressure dependence of Ca-Tschermaks substitution in clinopyroxene. Experimental data on biminerally eclogites used in the calibration were supplemented by literature data to obtain analyses in the range of 2 - 7 GPa, 900 - 1550°C. The barometer can be used with limited uncertainty if mineral $\text{Fe}^{3+}/\Sigma\text{Fe}$ ratios remain below 0.2, which is consistent with values obtained in equilibrium with graphite or diamond.

The barometer calculations are inconsistent with some previous studies (Hammouda et al., 2009; Kiseeva et al., 2012; Spandler et al., 2008) although the discrepancies in pressure calculated are to some extent consistent with generally lower garnet majorite components in these studies. This may indicate that pressures have been overestimated in these previous studies. Other experimental studies in eclogitic systems which were not included in the calibration are in good agreement with the barometer and reproduce the experimental pressures within 2σ (Green et al., 2000; Kessel et al., 2005; Klemme et al., 2002; Kogiso and Hirschmann, 2006). The barometer reproduces experimental pressures down to conditions of 2 GPa and 900°C and up to approximately 7 GPa and 1500°C. Due to the use of a thermodynamically consistent model these ranges can likely be extended at least in temperature down to 700°C, although the lack of well equilibrated experimental data at these conditions means the results should be viewed more critically. Furthermore, the phase transition in omphacite from P2/n to C2/c at approximately 865°C at 1.5 - 1.8 GPa, which is not accounted for in the barometer, may also influence its use at low temperatures and

pressures (Carpenter, 1982). Limits to the use of the barometer at lower temperatures and high pressures are set by the diminishing mole fraction of the Ca-Tschermaks component. The barometer should be suitable for calculating pressures of equilibration of deep crustal and upper mantle eclogite xenoliths and paired garnet-clinopyroxene diamond inclusions. Furthermore, the barometer can be applied to quartz and kyanite-bearing eclogitic samples. Other barometers can most likely be more reliably applied to orthopyroxene bearing assemblages.

This Chapter has been published in Contributions to Mineralogy and Petrology as C. Beyer, D.J. Frost, N. Miyajima (2015), Experimental calibration of a garnet-clinopyroxene geobarometer for mantle eclogites. Contrib Mineral. Petrol. 169(2), 1 – 21.

5. Experimental calibration of a geobarometer for majoritic garnets from the lowermost upper mantle and transition zone

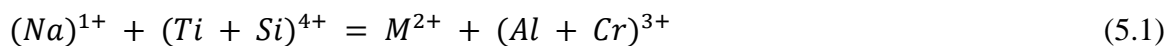
5.1. Introduction

Under conditions of the Earth's deeper upper mantle and the transition zone garnet becomes more majoritic (Mj) ($M_4Si_4O_{12}$) as a result of Si, Mg and Fe substituting for Al on the octahedrally coordinated site (Akaogi and Akimoto, 1977). In addition, in sodium and/or titanium rich bulk compositions (i.e. mafic bulk compositions) Al is preferentially replaced by either Si or Ti with charge balance provided by the replacement of divalent cations by Na, which forms either the NaSi-majorite $Na_2MSi_5O_{12}$, or NaTi-majorite $Na_2MTi_2Si_3O_{12}$ components (Gasparik, 1989; Ringwood and Major, 1971; Sobolev and Lavrent'ev, 1971). These majoritic components start to increase in garnet-bearing assemblages at pressures above 4 GPa as a result of the breakdown of orthopyroxene and clinopyroxene. By 20 GPa the majorite component in garnet normally reaches a limit due to the exhaustion of pyroxenes. The proportions of the different majorite components depends on both pressure and bulk composition. The absence of orthopyroxene in mafic compositions, for example, results in lower proportions of the $M_4Si_4O_{12}$ majorite component compared to ultramafic compositions but mafic compositions generally have raised Na and Ti contents. Naturally occurring majoritic garnets are found as mineral inclusions in diamonds and are therefore an important source of information both on the conditions of formation of ultra-deep diamonds and the chemical composition of deep upper mantle and transition zone lithologies (Collerson et al., 2000; Haggerty and Sautter, 1990; Stachel et al., 2005). In addition to majoritic garnets of clear ultramafic and mafic heritage, Kiseeva et al. (2013) recently proposed that some inclusions originated from an intermediate pyroxenitic source

that may be a hybrid between mafic and ultramafic sources. As a consequence these inclusions may reveal information on mantle mixing and homogenization processes.

The strongly pressure dependent incorporation of majoritic components in garnet (Akaogi and Akimoto, 1977; Irifune et al., 1986) opens up the possibility of using their concentration as a geobarometer for determining the depth of origin of ultra-deep xenoliths and mineral inclusions and also for estimating pressures of meteorite shock events. Ultra-deep xenoliths samples recovered from the Jagersfontein kimberlite, South Africa have been identified based on garnet majorite contents and are estimated to have originated from depths of approximately 400 km (Haggerty and Sautter, 1990). The estimated pressure is based on a comparison with experimental data on the formation of Mj-majorite in the simple $Mg_4Si_4O_{12} - Mg_3Al_2Si_3O_{12}$ and $Fe_4Si_4O_{12} - Fe_3Al_2Si_3O_{12}$ systems (Akaogi and Akimoto, 1977). However, these pressures are somewhat uncertain due to the likely bulk compositional effects of Cr, Na and Ti on the stability of majorite in more complex natural systems (Haggerty and Sautter, 1990) in addition to the consequences of the absence of orthopyroxene in mafic bulk compositions.

Collerson et al. (2010) (C10) calibrated a semi-empirical formulation based on the coupled substitution of



to calculate the depth of formation of majoritic garnets. In Eq. 5.1 the Mj substitution with $2Al^{3+} = M^{2+} + Si^4$ and the NaSi and NaTi substitutions with $M^{2+} + Al^{3+} = Na^{1+} + Si^{4+}$ have been combined. The C10 barometer is based on two formulations to specify the cation

substitution. One equation accounts for the excess silicon and titanium on the octahedral lattice position:

$$X^{cat}Mj_1 = [^{IV,VI}(Si + Ti) - 3 + ^{VIII}Na] \quad (5.2)$$

The second equation is based on the depletion of Al + Cr on the octahedral site:

$$X^{cat}Mj_2 = [1 - 0.5 * ^{VI}(Al + Cr)] + ^{VIII}(Na * 1.25)] \quad (5.3)$$

The factor 1.25 has been obtained from the substitution vector of divalent + trivalent cations versus tetravalent + monovalent cations as shown in Fig. 5.1.1. The final C10 calibration is based on the average of Eq. 5.2 and Eq. 5.3 yielding a linear expression for majoritic substitutions with pressure.

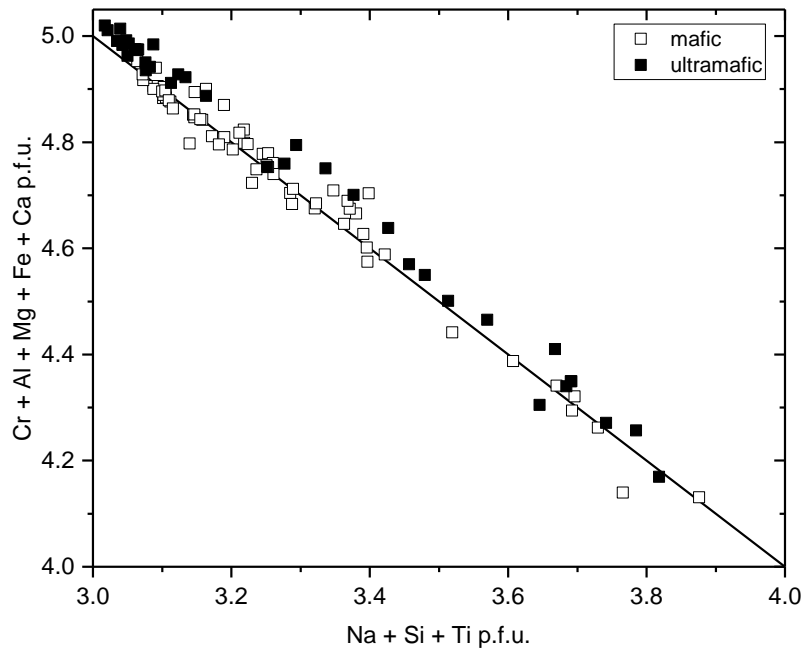


Fig. 5.1.1 Divalent + trivalent cations plotted against tetravalent and monovalent cations based on the experimental samples used in the empirical calibration. The plot is modified after Collerson et al. (2010).

However, applying the barometer to experimental data with mafic compositions reveals inconsistencies in the determined pressure that cannot be explained by the commonly recognized incorporation mechanisms for majoritic components. This deviation probably results from the influence of the bulk composition on majorite substitution mechanisms, which have not in the past been specifically examined for any component other than Cr in simple systems (Zou and Irifune, 2012; Sirotkina et al. 2015). Moreover, unknown amounts of Fe^{3+} may influence the cation recalculation and therefore affect Eq. 5.3. Another reason for the high uncertainties is that mafic compositions are underrepresented in the C10 calibration data set, which is therefore biased towards ultramafic samples. Less than 10 % of the experimental samples used for the C10 barometer represent mafic compositions; all other compositions are ultramafic.

In this Chapter, an empirical geobarometer that uses the variation in majoritic garnet components with pressure has been calibrated using the results of experiments that cover a wide range of mafic bulk compositions, pressure and temperature. In order to make the calibration rigorous and applicable to the widest possible range of chemical bulk compositions, additional high-pressure studies conducted in mafic and ultramafic systems have been included in the calibration. Finally, the calibration has been compared with the C10 barometer and used to examine the pressure of origin of majoritic inclusions in diamonds.

5.2. Methods

Starting materials were chosen to cover a wide range of mafic lithologies. Three of the four bulk compositions were basaltic whereas composition Mix1G was pyroxenitic. OC1/2 and NMORB4 are mid-ocean ridge basalts representing an average oceanic crust with the main

difference being a raised Ti content in the latter. Composition JB1 is similar to the Japanese reference alkali basalt described in Terashima et al. (1998). Mix1G is a silica-deficient pyroxenite as used by Hirschmann et al. (2003). In Fig. 5.2.1 the starting compositions of this study are shown together with the garnet inclusions in diamonds as reported in Kiseeva et al. (2013). The dark regions indicate bulk compositions of pyroxenitic and eclogitic rocks on the left and right hand side of the En-CaTs tie-line respectively. The colors of the garnet inclusions indicate whether they originated from a pyroxenite or eclogite bulk compositions, following the arguments of Kiseeva et al. (2013). Other than proposed pyroxenitic garnets extending to more normative enstatite compositions, however, there appears to be no grounds to differentiate these garnet compositions on the basis of this diagram. Fig 5.2.1 shows that the pyroxenitic Mix1G starting material lies to the left of the En-CaTs tie-line.

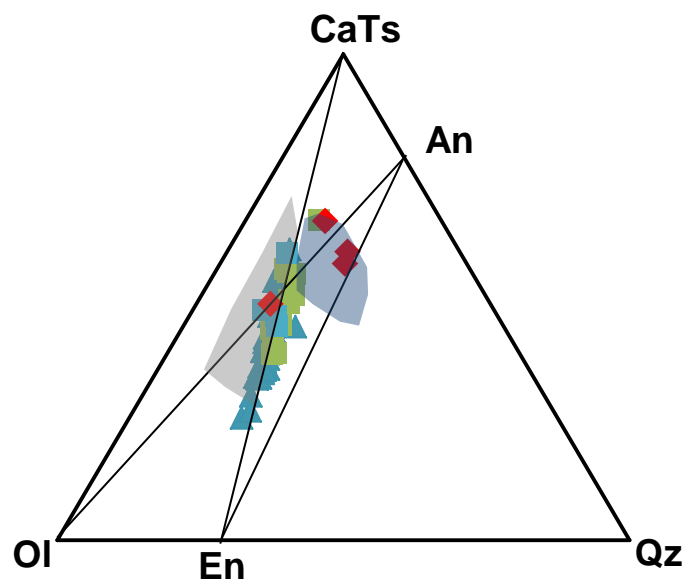


Fig. 5.2.1 Starting compositions shown on a pseudo-ternary Mg_2SiO_4 (Ol) - $CaAl_2Si_2O_6$ (CaTs) - SiO_2 (Qz) section projected from $CaMgSi_2O_6$ diopside. Red diamonds show starting compositions, green squares and blue triangles are garnet inclusions from diamonds proposed to be from eclogites and pyroxenites respectively (Kiseeva et al. 2013). A shaded field showing the extent of natural eclogite compositions is shown to the right of the En-CaTs tie line whilst to the left is a field of pyroxenites.

Water was added as hydroxides to all compositions to promote crystal growth and to aid the attainment of equilibrium. Starting materials were synthesized and hydrated according to the procedure described in Chapter 4.2. Bulk compositions are given in Table 5.2.1. All experiments were conducted using five hole, spark-eroded multi-chamber AuPd capsules, as described in Chapter 3, 18/11 octahedral pressure media and either a 500 (V), 1000 (H) or 5000 tonne (Z) MA. To cross-check the pressure calibration a pressure standard consisting of a Fe_2SiO_4 - Mg_2SiO_4 mixture was filled into one sample chamber in each experiment.

Table 5.2.1 Bulk starting materials based on weight in.

	OC1/2	NMORB4	JB1	Mix1G
SiO₂	46.53	50.50	53.25	45.56
TiO₂	1.02	2.76	1.37	0.9
Al₂O₃	15.00	13.64	14.83	15.19
FeO*	8.76	9.67	8.36	7.77
MnO	0.13		0.17	0.15
MgO	8.18	6.06	7.89	16.67
CaO	13.62	11.89	9.48	11.48
Na₂O	2.46	2.88	2.85	1.44
K₂O		0.41	1.46	0.04
OH**	2	3	2	2
F**	2			
total	99.7	101.6	101.6	101.2

The Fe/(Fe+Mg) ratio of this mixture was chosen to fall within the range of the two phase binary field of olivine and ringwoodite as described in Section 3.1.2 and shown in Fig. 3.1.2.2. A stepped graphite heater was employed. The temperature was monitored with a D-type thermocouple axially inserted into the octahedron, with the junction in contact with the top of the multi-chamber capsule. The sample chambers were cold sealed with 2 discs of Re-foil. Cavities around the thermocouple were filled with dried MgO powder. Experiments were terminated by shutting down the electrical power to the furnace, causing

the samples to quench in less than 2 seconds to ~100°C. Run conditions were between 6 and 16 GPa at three different temperatures 1000, 1200, and 1400 °C. The experimental conditions are reported in Table 5.2.2.

Table 5.2.2 Experimental conditions

run#	P [GPa]	T [°C]	duration [h]	capsule
V860	8	1200	144	5-hole AuPd
V861	6	1200	48	5-hole AuPd
V867	6	1000	24	5-hole AuPd
V868	10	1000	23	5-hole AuPd
H3951	6	1400	1 2/3	5-hole AuPd
H3953	10	1400	3	5-hole AuPd
H3955	12	1400	4 1/2	5-hole AuPd
H3966	10	1200	49	5-hole AuPd
H3967	12	1200	48	5-hole AuPd
Z1113	16	1400	3 2/3	5-hole AuPd
Z1132	16	1200	23	5-hole AuPd
Z1136	16	1000	23	5-hole AuPd
Z1138	14	1400	23	5-hole AuPd

Run products were cut in half and embedded into epoxy resin for further analysis. The capsule disc was cut perpendicular so that all chambers were exposed. A capsule-disc is depicted in Fig 3.1.2.3 in Chapter 3. Samples were analyzed using a Jeol JXA-8200 microprobe using the same methods as described in Section 4.2.

5.3. Results and discussion

Run products crystallized euhedral to subhedral mineral grains, which suggests that the samples approached equilibrium conditions. Garnets are generally larger with crystal diameters of up to 30 µm. Clinopyroxenes are smaller and ~20 µm in the longest dimension. At lower temperatures and higher pressures the crystals become smaller yielding grain sizes between 5 and 15 µm. In Fig. 5.3.1 two cross-sections of a

multi-chamber capsule at high and low temperature are shown to illustrate the grain size distribution with temperature and pressure.

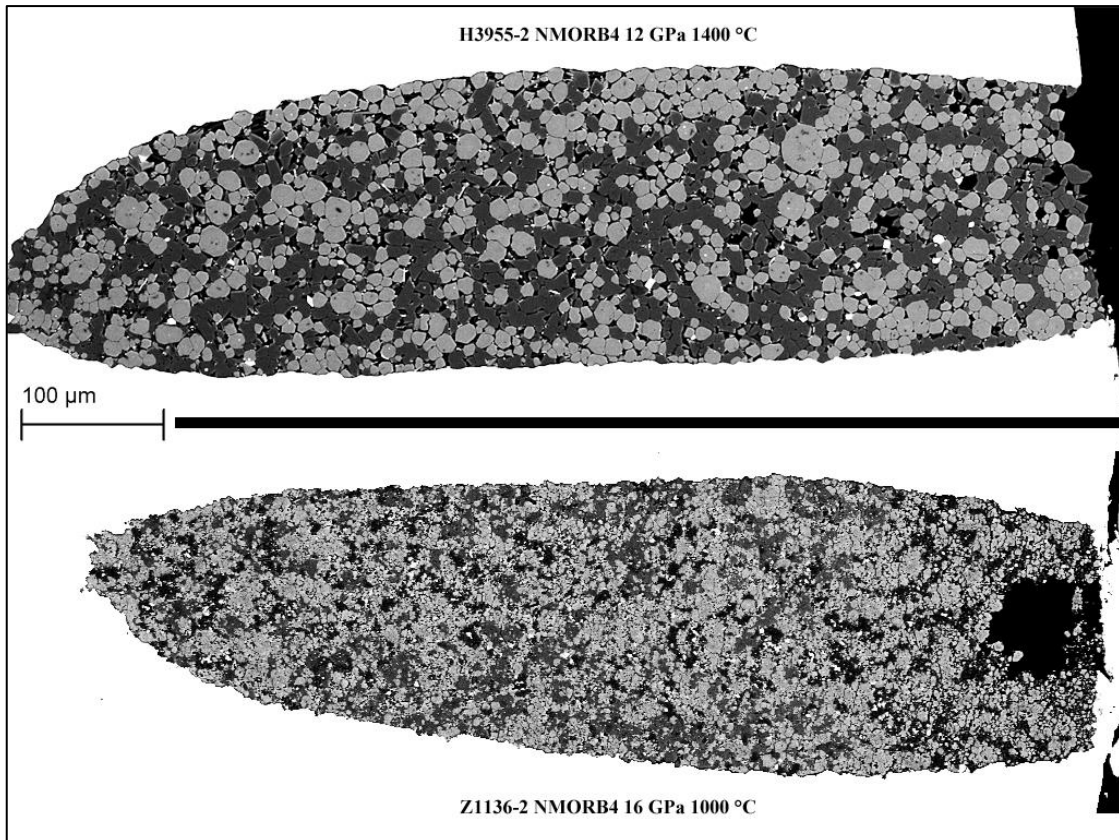


Fig. 5.3.1 BSE images of two recovered capsules. Images have been scaled to match each other dimensions for comparison.

The majority of runs yielded homogenous phase assemblages consisting of garnet + clinopyroxene \pm coesite/stishovite \pm rutile \pm glass/quenched melt. The silica-undersaturated starting material (Mix1G) crystallized to a biminerally eclogite containing varying proportions of garnet and clinopyroxene and trace amounts of olivine in runs V861, V867, H3953, H3967, and Z1113. Within the chosen compositional range clinopyroxene was present up to 16 GPa. Minor amounts of rutile were found in some run products from the Ti-rich bulk composition NMORB4. SiO₂-polymorphs were either present as coesite until

~9 GPa and above ~9 GPa as stishovite in the majority of basaltic run products (Table 5.3.1). Chemical analyses for all experiments are given in Appendix 2.

Table 5.3.1 Phases of the run products

run#	P [GPa]	T [°C]	Phases			
			OC1/2	NMORB4	JB1	Mix1G
V860	8	1200	grt,cpx,gl	grt,cpx	grt,cpx,coe,gl	grt
V861	6	1200	grt,cpx	grt,cpx	grt,cpx	grt,cpx,ol
V867	6	1000	grt,cpx	grt,cpx,coe	grt,cpx,coe	grt,cpx,ol
V868	10	1000	grt,cpx,stish	grt,cpx,stish,rt	grt,cpx,stish,rt	grt,cpx
H3951	6	1400	grt,cpx,gl	grt,cpx,gl,qm	grt,cpx,gl	cpx
H3953	10	1400	grt,cpx	grt,cpx,stish	grt,cpx	grt,cpx,ol,gl
H3955	12	1400	grt,cpx	grt,cpx	grt,cpx	grt,cpx
H3966	10	1200	grt,cpx,stish	grt,cpx,stish	grt,cpx,stish	grt,cpx
H3967	12	1200	grt,cpx,stish	grt,cpx	grt,cpx,stish	grt,cpx,ol
Z1113	16	1400	grt,cpx	grt,cpx,stish	grt,cpx	grt,cpx,ol
Z1132	16	1200	grt,cpx,stish,qm	grt,cpx,stish,rt	grt,cpx,stish	grt,cpx
Z1136	16	1000	grt,cpx,stish	grt,cpx,stish,rt	grt,cpx,stish,	grt,cpx
Z1138	14	1400	grt,cpx,stish	grt,cpxstish,qm	grt,cpx,stish,qm	grt,cpx

grt: garnet, cpx: clinopyroxene, coe: coesite, stish: stishovite, rt: rutile, ol:olivine, gl:glass, qm: quenched melt. Rutile was only present as tracers.

Mass balance calculations on a basaltic (OC1/2) and the pyroxenitic (Mix1G) bulk composition at isothermal conditions show how mineral fractions change with pressure (Fig. 5.3.2), which are comparable to what has been observed in previous studies (Irifune, 1987; Okamoto and Maruyama, 2004). The garnet fraction increased continuously with pressure by incorporating majoritic components at the expense of clinopyroxene. As a result all garnets in all bulk compositions showed excess silica, i.e. >3 Si p.f.u. on a 12 oxygens basis. In contrast to the previous studies Na and Si are present in lower concentrations when compared at the same pressure. Above 14 GPa the majoritic garnets coexisting with clinopyroxenes in the study of Okamoto and Maruyama (2004) contain more excess silica (>3.28 Si p.f.u.) than all garnets recovered from this study, which have Si <3.23 p.f.u at 16 GPa pressure. Compared to the work of Irifune et al. (1986), who observed the disappearance of clinopyroxene at 15 GPa, in this study clinopyroxene is still

stable at 16 GPa in all bulk starting compositions. These differences demonstrate how subtle variations in bulk composition influence the garnet majorite contents.

At 1000 °C and high pressures (12 – 16 GPa) several phases showed evidence that equilibrium may not have been obtained, i.e. core to rim zonations and very small xenomorphic crystals. A likely explanation is that at 1000 °C the system was not able to reach equilibrium within the given duration of the experiment. These experiments were either neglected in the case of very strong zonations or only the rim compositions have been used for further calculations, as it is assumed the rims are in equilibrium with the adjacent phases. Where garnet cores were formed they were mostly enriched in Ca and Ti.

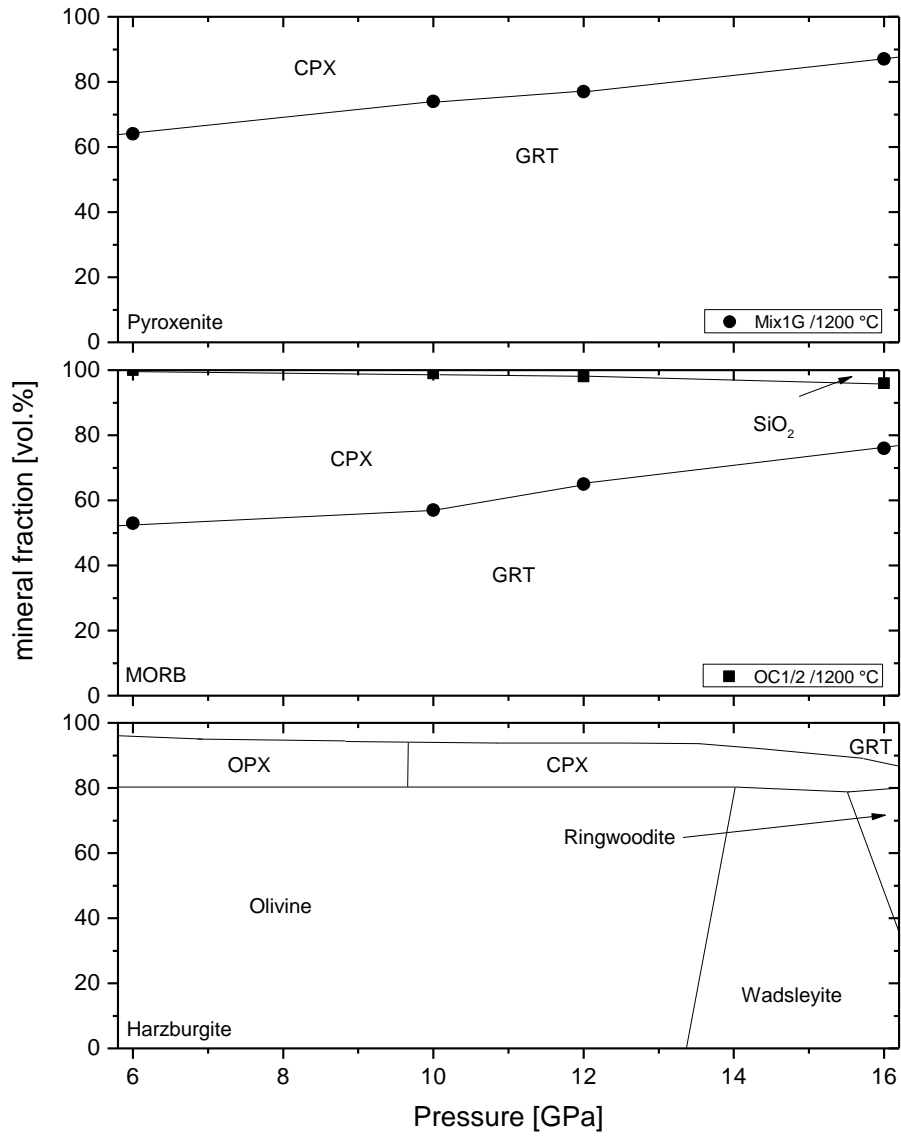


Fig. 5.3.2 Mineral fraction as a function of pressure of the basaltic starting material OC1/2 and the pyroxenitic starting material Mix1G compared with a typical harzburgite modified after Irifune and Ringwood (1987).

Chemical variations of the majorite end-members with pressure are shown in Fig. 5.3.3. The proportions of the end-members were calculated following the procedure of Okamoto and Maruyama (2004), where:

$$M_j = (Si - 3 - Na)/2 \quad (5.4)$$

$$NaTi = Ti/2 \quad (5.5)$$

$$NaSi = (Na - Ti)/2 \quad (5.6)$$

with cation contents expressed as atoms per 12 oxygen formula unit. The resulting majorite end-members are specified below:

- Normal majorite (Mj): $Mg_3MgSiSi_3O_{12}$
- NaSi-majorite: $Na_2MgSi_5O_{12}$
- NaTi-majorite: $Na_2MgTi_2Si_3O_{12}$

where, Mg can be substituted with Fe and Ca. In garnets crystallized from the basaltic starting compositions the two Na-majorite substitution mechanisms dominate (Fig. 5.3.3), whereas, garnets from the pyroxenitic bulk starting material Mix1G are dominated by Mj-majorite ($Mg_3MgSiSi_3O_{12}$) substitution. Around 15 GPa the NaSi-majorite fraction starts to increase more significantly with pressure but still at a lower rate than observed by Okamoto and Maruyama (2004). Only the Ti-rich starting material (NMORB4) is dominated by NaTi-majorite. In all other bulk compositions, NaTi is the smallest majorite component, which is clearly controlled by the amount of Ti in the bulk composition. NaTi-majorite showed the weakest correlation with pressure compared to the other two substitution mechanisms. Within the temperature range of this study no systematic variation with temperature has been observed.

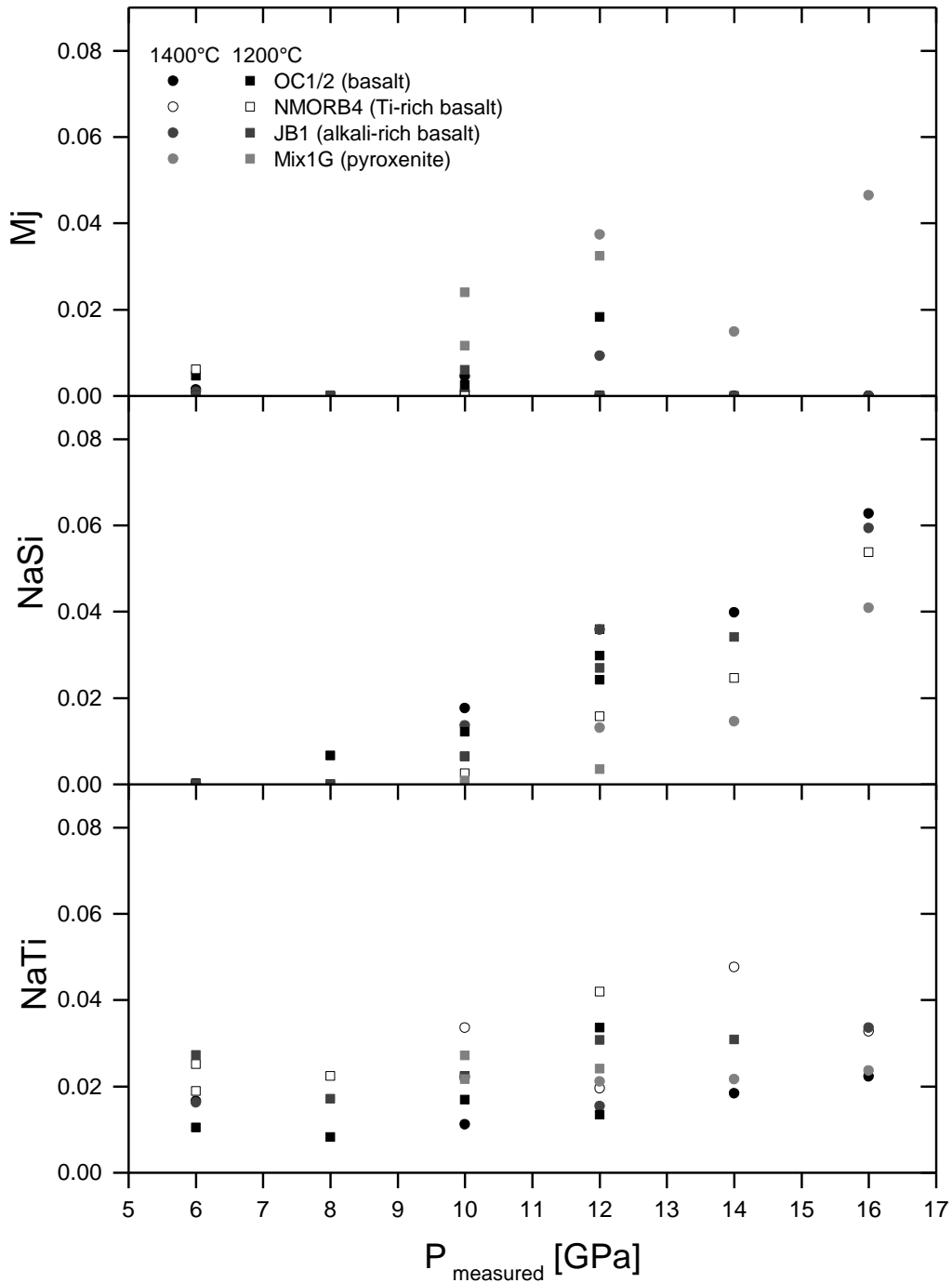


Fig 5.3.3 Variation of the three principal garnet substitution mechanism with pressure at 1200 and 1400 °C.

Clinopyroxenes become increasingly jadeitic with pressure, compensated by a decrease in CaTs and diopside/hedenbergite (Fig. 5.3.4). There is no distinct variation with temperature, although, based on the results of Chapter 4, CaTs concentrations should also be temperature dependent. The difference between run products from the pyroxenitic

starting material (Mix1G) can be solely explained by a different Na/Ca ratio in the bulk starting material. The differences in the nominally basaltic bulk compositions have no pronounced effect on clinopyroxene chemistry. Mg and Fe follow the trend of Ca due to the coupled substitution forming either diopside (Mg) or hedenbergite (Fe). Neither Ti nor Mn show any systematic variation with P or T. Potassium concentrations were generally close to the detection limit with less than 0.1 wt% K₂O. Only clinopyroxenes from the K-rich starting material JB1 show a weak increase of K with pressure (0.1 to 0.5 wt%). Clinopyroxenes from experiments performed at 1000°C were often zoned and not very well equilibrated, and are therefore not shown in Fig. 5.3.4.

Taking a closer look at the clinopyroxene Ca-Eskola component ($\text{Ca}_{0.5}\square_{0.5}\text{AlSi}_2\text{O}_6$) the data of this study support the results of Knapp et al. (2013) and Woodland et al. (2013) in that Ca-Eskola is observed to decrease continuously with pressure starting from 4 GPa. In the data presented covering the pressure interval between 6 and 16 GPa a general decrease with pressure appears to be followed by all three mafic compositions: JB1, OC1/2, and NMORB4 (Fig. 5.3.4). Around 12 GPa Ca-Eskola completely disappeared from the clinopyroxene solid solution. It has been proposed that a sharp decrease in the proportion of Ca-Eskola could cause stishovite to form over a small depth interval and that the resulting change in elastic properties could be responsible for the X seismic discontinuity observed at ~ 300 km depth, i.e. ~ 9 GPa (Williams and Revenaugh (2005)). However, the drop in the Ca-Eskola component of clinopyroxene in an eclogitic system is found not to be particularly sharp and does not result in a sharp exsolution of SiO₂-polymorphs (~9 GPa) (Knapp et al., 2013). As suggested by Woodland et al. (2013) one possible mechanism for the formation of a sufficient proportion of excess silica from an eclogitic residue may be by melting at pressures around 5 GPa. The Ca-Eskola component is calculated as described in Chapter 4, Eq. 4.6.

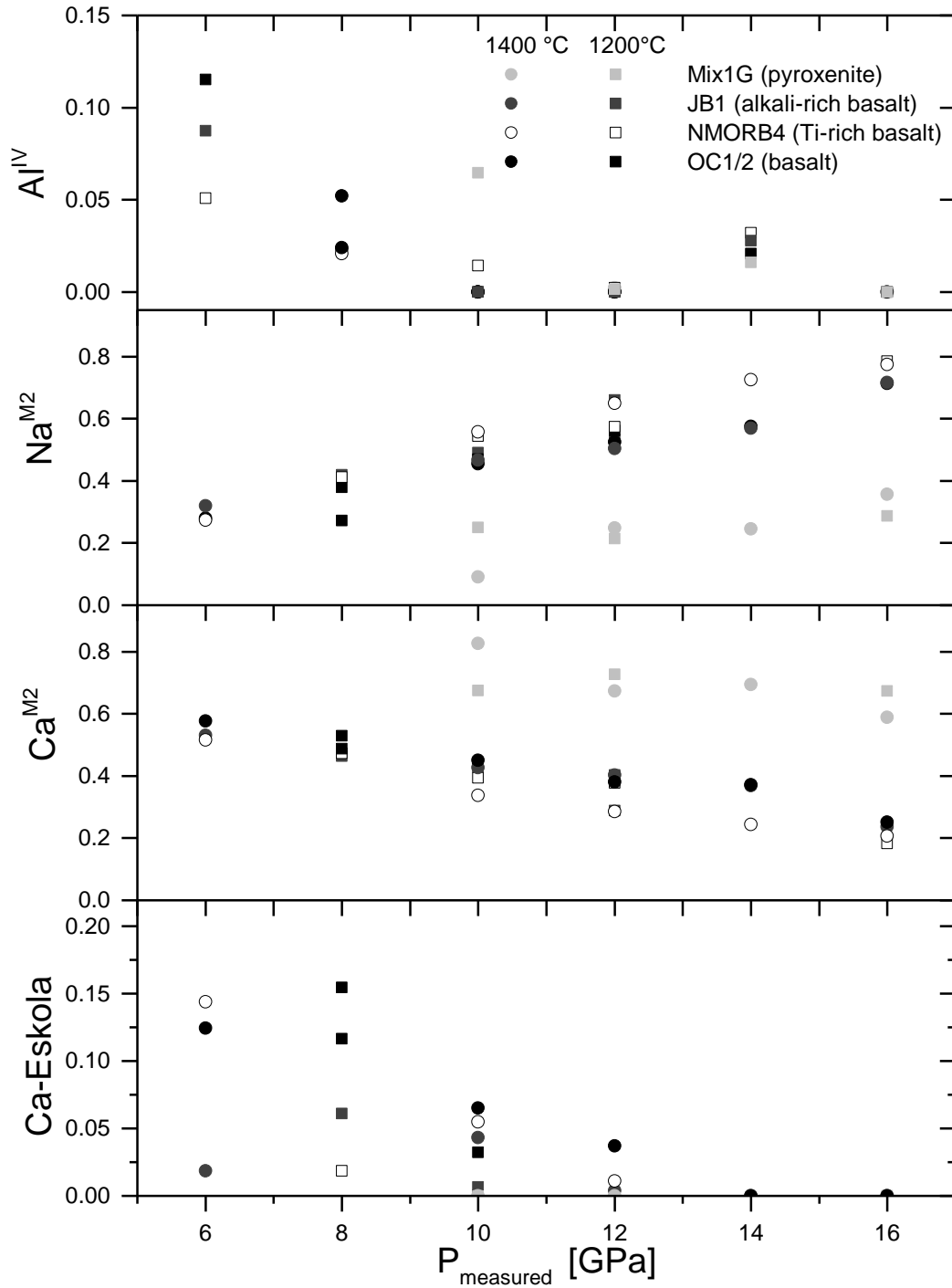


Fig. 5.3.4 Chemical variation of clinopyroxene composition with pressure. Cations given as a.p.f.u. based on 6 oxygens.

Compared with additional high pressure experiments on basalts (Okamoto and Maruyama, 2004; Ono and Yasuda, 1996; Yasuda et al., 1994), peridotites (Herzberg and Zhang, 1996; Wang and Takahashi, 2000), pyrolite (Walter, 1998), group II kimberlite (Ulmer and

Sweeney, 2002), and Al-depleted komatiite (Nishihara and Takahashi, 2001) two distinct trends are striking (Fig. 5.3.5a/b). Peridotitic and komatiitic bulk compositions experience a strong increase of M_{jg} with pressure, that is basically independent of temperature. The NaSi and NaTi fractions in garnet is also dependent on pressure but to a lesser extent (Fig. 5.3.5b).

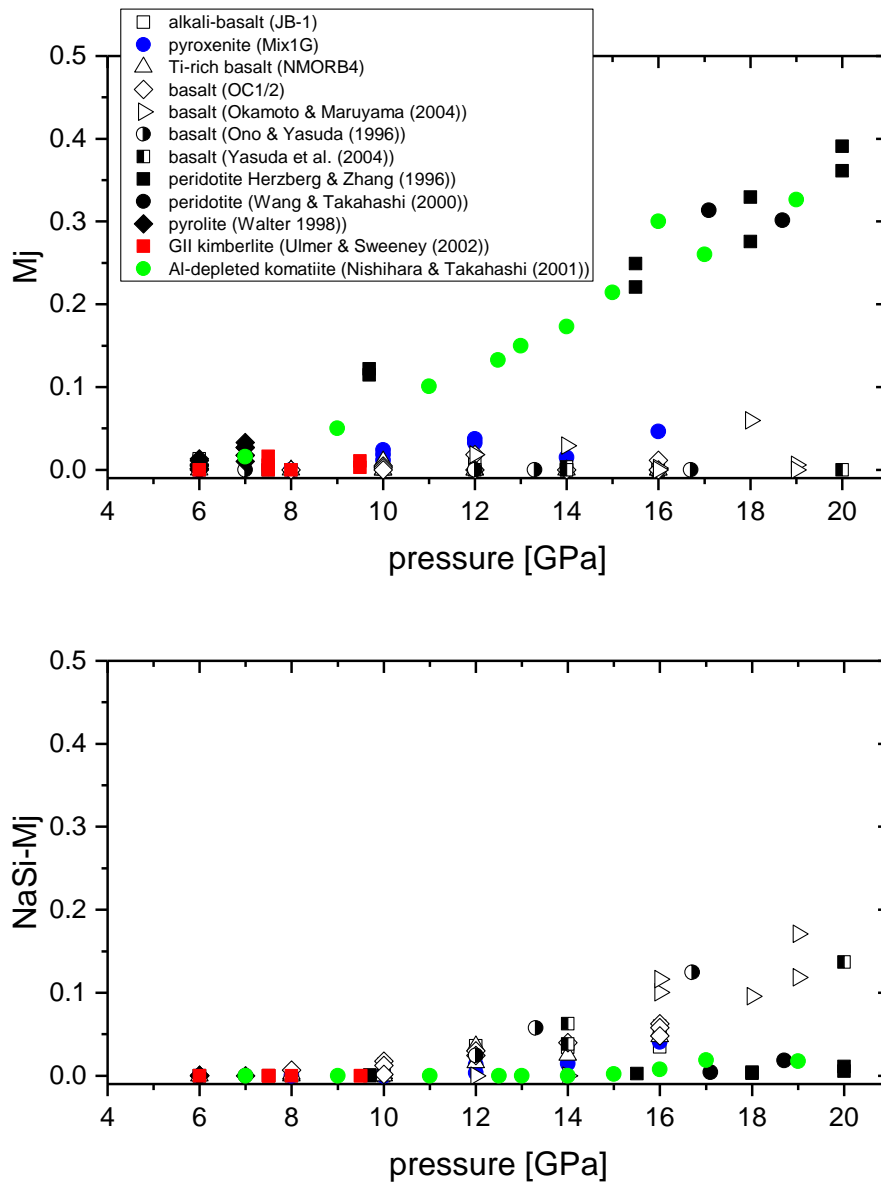


Fig. 5.3.5 a) The upper figure shows the pressure dependent incorporation of M_{jg} -majorite. b) The lower image shows the NaSi-majorite substitution with pressure.

If the two major substitution trends for NaSi and NaTi are compared to the Mj substitution as depicted in Fig. 5.3.6 (Kiseeva et al. 2013) the difference between experimental and natural majoritic garnets from eclogitic and peridotitic bulk compositions is less pronounced. Experimental data from this study do not fall onto the 2:1 ratio line expected for NaSi or NaTi-majorite substitution. The vast majority of eclogitic compositions demonstrate sub-equal levels of both the Mj-substitution and the sodium substitutions, whereas, in peridotitic compositions the substitution is still dominated by the Mj-substitution. Some inclusions, classified as eclogitic inclusions, for example the Al-24 inclusions from the Monastery kimberlite (Moore and Gurney, 1985), follow the Mj-substitution trend. Kiseeva et al. (2013) argued that garnet inclusions formed from eclogitic bulk compositions would follow the Na-substitution trend in Fig. 5.3.6, while peridotites should fall along the Mj-substitution trend. They proposed, however, that garnets formed from hybrid pyroxenitic compositions in the mantle would also follow the Mj trend. The results from this study show clearly that garnets formed from eclogite compositions do not necessarily lie along the Na-substitution trend, which is therefore not an inclusive criteria for defining majoritic garnets with an eclogitic origin. The results do confirm, however, that even orthopyroxene free pyroxenite bulk compositions produce garnets that lie along the Mj substitution trend.

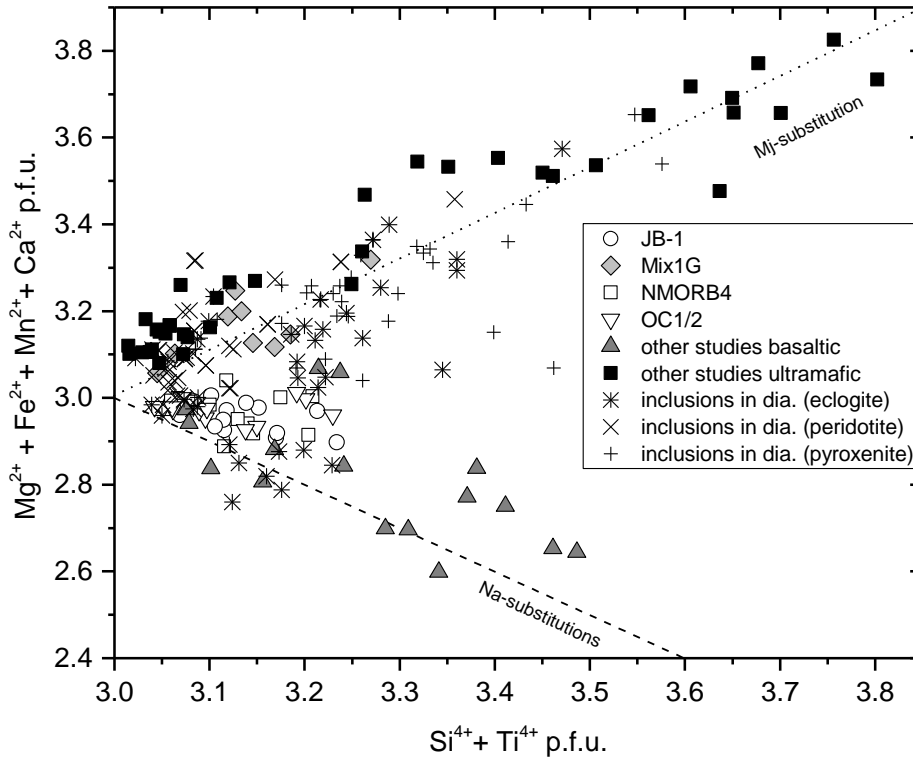


Fig. 5.3.6 Experimental data of this study and previous studies compared to natural majoritic inclusions in diamonds. References for all inclusion data are given in Fig 5.5.2, whereas references for the experimental data are given in Section 5.3.

These trends are key for obtaining a sensitive majorite barometer for the large variety of garnets from lithologies of the upper mantle and transition zone since relatively small changes in the NaSi and NaTi fraction correspond to quite large changes in pressure. Nevertheless, although the uncertainties will be larger for mafic compositions, as long as they are taken into account a parameterization of these results can still be useful, particularly for estimating pressures of garnet inclusions within diamonds from the deeper upper mantle and transition zone, where the NaSi component reaches its highest levels. Here data from this study and previous studies from the literature have been combined in a single empirical parameterization designed to describe the minimum pressure at which single garnet grains equilibrated based on their majorite (i.e. Mj, NaSi and NaTi) content. By combining sufficient data on a range of bulk compositions, pressures can be determined for garnets that originally formed within mafic to ultramafic assemblages.

As Collerson et al. (2010) noted, the upper limit for a majorite barometer is the onset of Ca-perovskite exsolution from garnet at ~20 GPa, at which point the majorite component of garnet starts to decrease. As the majorite concentration decreases, the pressure estimated for the sample based on this concentration becomes ambiguous, as similar concentrations are also reached at lower pressures. For this reason and because it is also possible that pyroxenes were absent in the particular bulk composition, the majorite content can only be used to estimate a minimum pressure based on the composition of a single garnet inclusion. The onset of the exsolution of the sodium and aluminum-rich NAL-phase from garnet, which occurs at ~23 GPa, (Gasparik et al., 2000; Irifune and Ringwood, 1993; Miura et al., 2000; Miyajima et al., 2001) will also mark a similar limit for the increase in NaSi and NaTi-majorite components with pressure. For these reasons experimental data from the literature collected above 20 GPa were excluded as they cannot be distinguished from results at lower pressures. All 94 experiments together cover pressures from 6 to 20 GPa and temperatures from 900 to 2200 °C and roughly equal proportions of mafic (n = 56) and ultramafic (n = 38) samples. The barometer is based on the empirical equation,

$$P(\text{GPa}) = 13.917 + 15.871B - 10.751A - 0.1193A^2 \quad (5.7)$$

with

$$A = -38.74 - 18.19Mj * [Al/(Al + Cr)] - 118.45NaTi - 57.26NaSi \quad (5.8)$$

$$B = -15.54 + 0.77(Si - 3) + 1.93Na - 1.01Ti \quad (5.9)$$

Mj, NaSi and NaTi were calculated as described above with the cation proportions reported as a.p.f.u.. The average deviation from a least squares refinement of the experimental data is $\sigma = 0.86$ GPa with $\Delta_{\max} = 2.4$ GPa. The addition of further cations, such as Fe, Mg, and Ca or the element ratios Fe/Mg did not significantly improve the fit. The residuals show no systematic correlation with pressure (Fig. 5.3.6) or any major element. The apparent scatter is evenly distributed and likely reflects experimental errors in both pressure and compositional determination. Particularly accurate microprobe analyses are required for experiments performed below 6 GPa, where the onset of the majorite substitutions occurs. Even small uncertainties in the microprobe analyses at these conditions, in particular Si and Al, strongly influence the calculation of pressure.

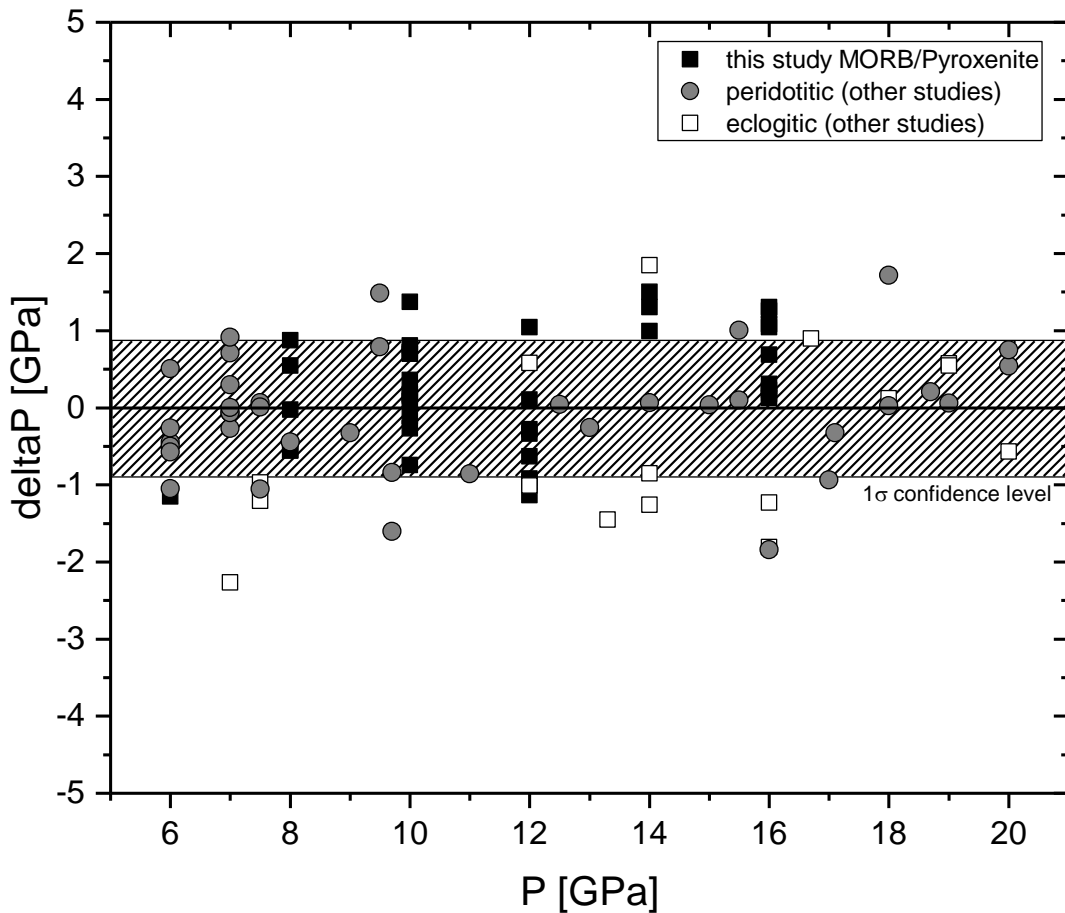


Fig 5.3.6 Residuals of the fitting in terms of ΔP . The banded area depicts the 1σ confidence interval.

By means of standard error propagation an error of 1 % within the microprobe analyses for all elements has been applied to the barometric formulation. Independent of pressure the 1σ uncertainty between 6 and 16 GPa is ~ 0.27 GPa. Below 6 GPa the majorite fraction is on the order of the precision of the microprobe analyses with values below 3.010 Si p.f.u. corresponding to 0.2% error on the Si analyses. Hence, pressures between 4 and 6 GPa are not distinguishable.

Compared to the intrinsic uncertainties of the pressure calibration of the multi-anvil presses of ~ 0.5 GPa and the uncertainty in the barometer fitting of 0.86 GPa, the uncertainties on the chemical analyses have a minor influence on the pressure determination for pressures above 6 GPa. Uncertainties in the chemical analyses become the major source of error if they exceed 4 %, which equates to a uncertainty in the SiO_2 content of garnet of ± 1.6 wt.%. By using internal garnet standards, however, it should be possible to ensure that absolute errors remain at or below the 1 % level.

5.4. Comparison with other barometers

The empirical barometer of this study has been compared with the majorite barometer of Collerson et al (2010). Applying the C10 barometer, which has been described in Section 5.1, to the experimental data results in a mismatch between the calculated and observed pressure (Fig 5.4.1) that increases with pressure and reaches levels of 6 GPa. In addition to the systematic bias shown in Fig 5.4.1, the C10 barometer has a generally poorer fit to the experimental data, $\sigma_{\text{C10}} = 1.8$ GPa compared to the empirical barometer presented in this study, $\sigma_{\text{this study}} = 0.86$ GPa. The scatter in the data seems to be not sufficiently described by the formulation of Collerson et al. (2010). Reasons for that could be that the NaSi and NaTi-substitution trends are poorly described (Fig. 5.3.5a/b) because mafic compositions are underrepresented in the data set of Collerson et al. (2010) as already described in

5.5. Application to natural majoritic inclusions in diamonds

To test the empirical barometer derived in this study the eclogitic and peridotitic majorite inclusions in diamonds reported in Collerson et al. (2010) and Kiseeva et al. (2013) have been used (Appendix 3). The samples cover localities across the major cratons collected from kimberlites and placer deposits in Africa, Siberia, South America, China, and North America. The exact localities and chemical analyses are given in Appendix 3.

Applying the empirical barometer and the C10 barometer to natural eclogitic inclusions in diamonds (Fig 5.5.1), yields a similar pressure curve as already observed in Fig. 5.4.1 with the experimental data. The C10 barometer underestimates pressures of eclogitic samples which have presumably originated from high pressures. Though, pressures obtained for pyroxenitic inclusions are in general in good agreement within 1.5 GPa. The highest deviation in pressure between the barometers (C10 - this study) is $\Delta P = -5.1$ GPa and corresponds to a sample with low Ca and Ti compared to samples from the same suite of inclusions in the Kankan diamonds from Guinea (Stachel et al., 2000). This particular low-Ca majoritic garnet inclusion (KK-5) has the highest Na content (0.195 Na p.f.u.) among all described samples, which is accompanied by a high silicon concentration (3.165 Si p.f.u.). Based on the experimental observations of this study and previous investigations of i.e. Irifune (1993), the high Na and Si contents are consistent with very high pressures. Therefore the calculated pressure of 17.5 GPa, using the barometer derived in this study, seems to be more consistent with the available experimental data.

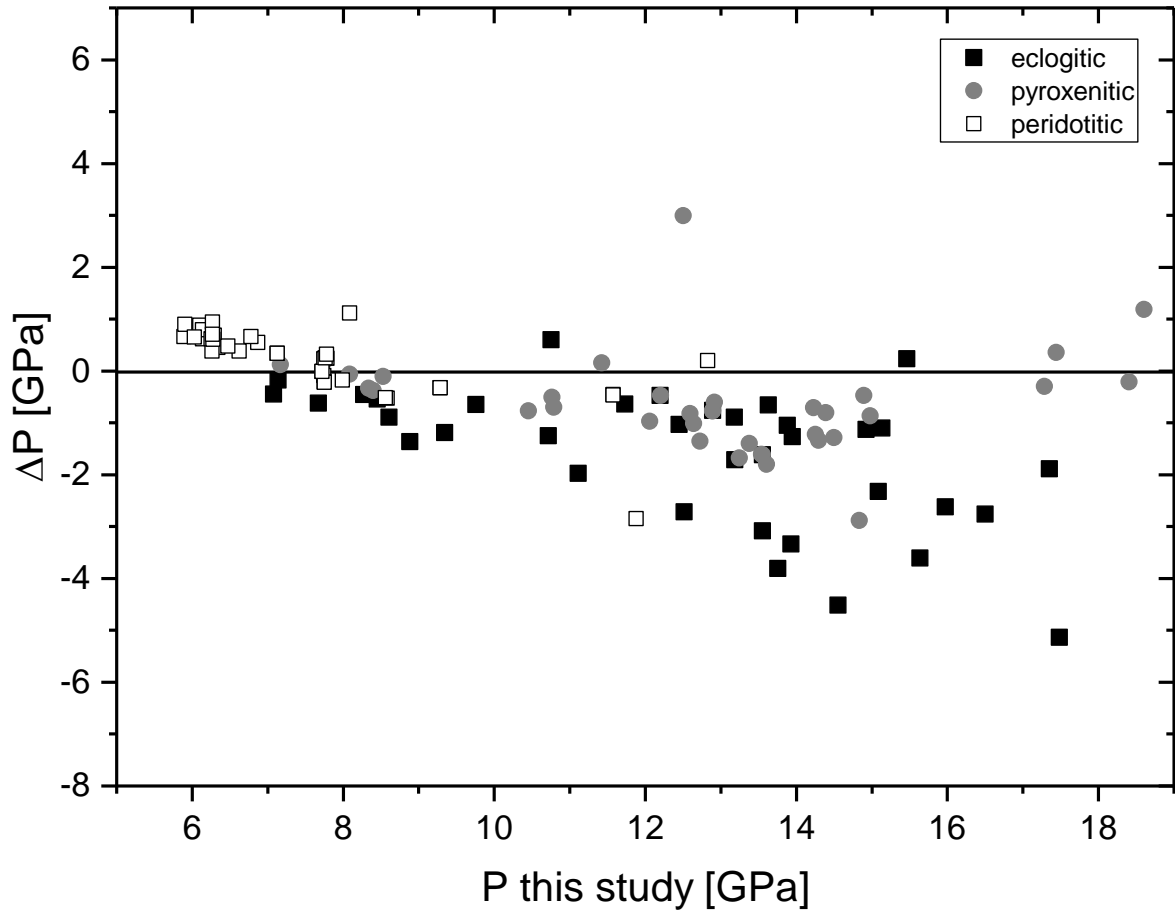


Fig. 5.5.1 Pressure for diamond inclusions calculated with the barometer of this study compared with the ΔP between the Collerson et al. (2010) barometer and this barometer. The compilation of inclusion in diamonds was adopted from Collerson et al. (2010) and Kiseeva et al. (2013) using the data from references therein (Bulanova et al., 2010; Davies et al., 2000; Davies et al., 2004; Harte and Cayzer, 2007; Kaminsky et al., 2001; Meyer and Mahin, 1986; Meyer and Svisero, 1975; Moore and Gurney, 1989; Moore and Gurney, 1985; Moore et al., 1991; Pokhilenko et al., 2004; Sobolev et al., 1997; Stachel et al., 2000; Stachel and Harris, 1997; Tsai et al., 1979; Wang et al., 2000; Wilding, 1990).

The secondary effect of the garnet chromium concentration on the stability of majorite can be examined independently by comparing phase equilibria data from Gasparik (1989) in the MAS system with recent experimental data on the Cr-MS system by Sirotkina et al. (2015). At a given pressure, Cr-bearing garnet contains more silicon than Cr-free majorites, i.e. at 14 GPa it is 3.576 (Cr-MS) vs. 3.336 (MAS) Si p.f.u.. Both garnets are in equilibrium with pyroxenes. Cr therefore appears to stabilize the majorite component in garnet at a given pressure. The effect on the majorite stability is likely caused by the different ionic radii of

Al ($r = 0.535 \text{ \AA}$) and C ($r = 0.615 \text{ \AA}$). Since, Cr is larger than Al it is easier to substitute $\text{Mg}^{2+} + \text{Si}^{4+}$ for Cr into the lattice of Cr-rich garnet. Specific account of this effect has been included in the parameterization of this study by allowing the Mj coefficient in equation 5.8 to be a function of the Al/(Al+Cr) ratio. Figure 5.5.2 shows the difference in predicted pressures between the current calibration and that of C10 for Cr-bearing natural majoritic garnet inclusions. The C10 calibration predicts high Cr garnets, with high majorite components to originate from high pressure. However the more inclusive parameterization performed in this study accounts for the fact that Cr stabilizes the majorite component to some degree and therefore predicts slightly lower pressures for these samples.

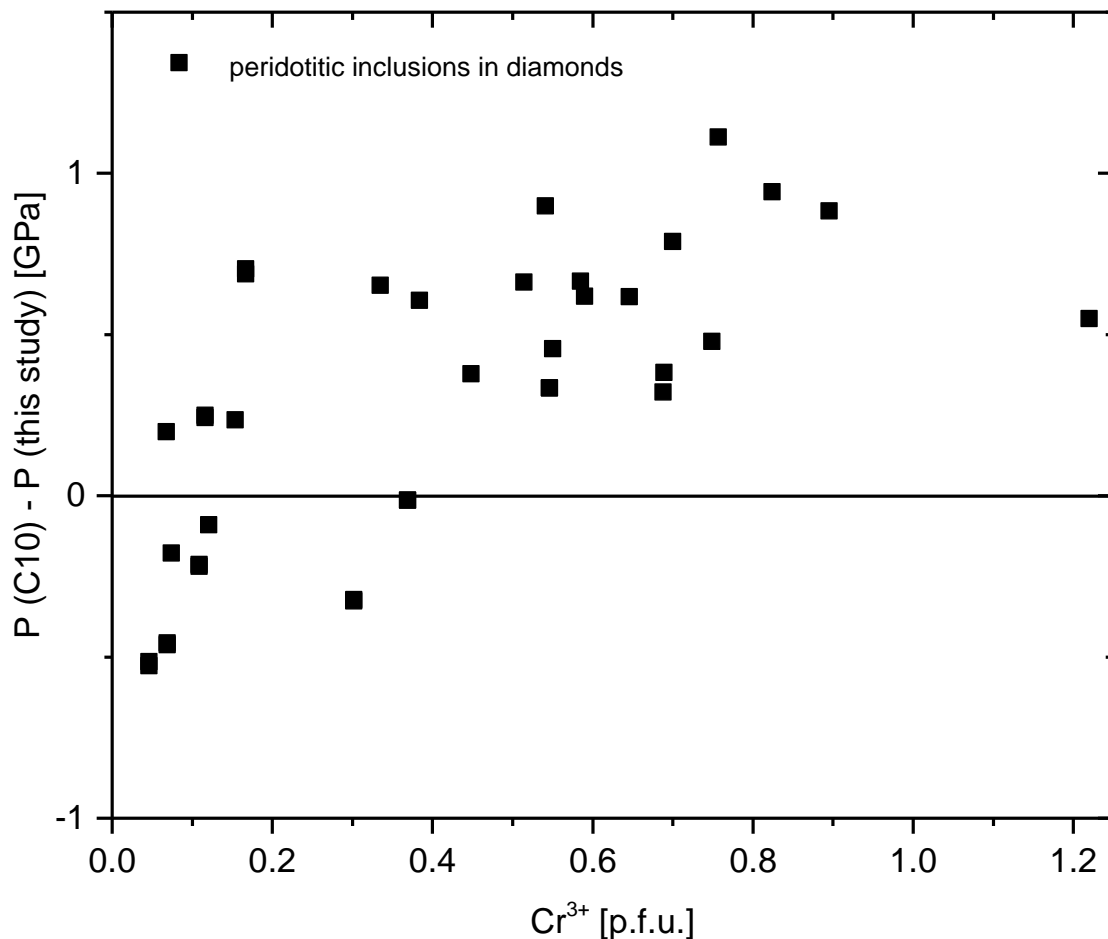


Fig. 5.5.2 Difference in pressure of peridotitic inclusion in diamonds obtained with the C10 and the empirical barometer. References are given in the Fig. 5.5.1 caption.

The C10 barometer yields similar pressures for all tested peridotitic mineral inclusions in diamonds, although, the variable concentrations of excess Si rather suggest differences in pressure. This emphasizes that future studies should investigate the effect of high Cr-concentrations in complex natural bulk compositions on the stability of Mj. Until now, the effect of Cr has only been studied for simple binaries which are not representative of natural samples (Sirotkina et al., 2015; Zou and Irifune, 2012).

Logically, because of equal charge and similar ionic radius ($^{VI}\text{Fe}^{3+} = 0.645 \text{ \AA}$), one could argue that Fe^{3+} has a comparable effect to Cr and has to be taken into account. Unfortunately, analyses on high-pressure experimental data on majoritic garnets are currently lacking information on the $\text{Fe}^{3+}/\Sigma\text{Fe}$ ratio.

5.6. Further applications to trace geological processes

The empirical barometer can also be used to determine the depth of geological processes responsible for the formation of diamonds. Applying the empirical barometer to majoritic inclusions in diamonds ($n = 103$) revealed significantly different depth of last equilibration for peridotitic and eclogitic/pyroxenitic samples (Fig. 5.6.1). Eclogitic majorites ($n = 37$) show a normal distribution with pressure with a median pressure around 13 GPa equivalent to a depth of ~400 km, close to the 410 km discontinuity and marks the upper boundary of the transition zone. Pyroxenitic inclusions ($n = 35$) show a very similar distribution. Accordingly, majoritic garnet inclusions from eclogitic and pyroxenitic source lithologies formed under similar conditions. These inclusions have been lastly equilibrated at conditions of the lowermost upper mantle just above the transition zone. In contrast, peridotitic samples ($n = 31$) generally fall in a shallower depth interval corresponding to depths between 150 and 300 km. These results support the findings of Haggerty (1986)

who argued that in a cratonic environment eclogitic diamond inclusions are formed under higher pressure than peridotitic inclusions. These observations raise several issues:

Firstly, the obtained pressures appear to provide evidence that kimberlites sample regions of the lowermost upper mantle down to the transition zone and that their origin, and certainly the origin of the diamonds, is closely related to mafic lithologies. Alternatively, it could be argued that the diamond inclusions formed initially at these great depths but were then assimilated into the cratonic lithosphere at shallower depths i.e. < 250 km, as a result of convective upwelling in the solid state. As the inclusions are majoritic, however, such a pathway of initial slow decompression should cause pyroxene to exsolve from the garnet, as long as the pressure in the inclusion remains the same as the pressure of the surrounding mantle. This is now a quite pressing issue particularly since the discovery of a ringwoodite inclusion in diamond (Pearson et al. 2014). Does the preservation of high pressure mineral structures imply that they were rapidly brought to the surface by kimberlites originating at least at the same depth? Or could slower mantle convection processes raise these diamonds to shallower depths at the base of the lithosphere, while the strong diamond lattice retains a higher internal pressure than the surrounding mantle. This question can probably only be addressed through measurements of the creep strength of diamond at deep mantle conditions.

Secondly, while the corresponding depths of eclogitic/pyroxenitic inclusions fall within the depth interval of 250 - 500 km, peridotitic inclusions seem to be much rarer in the deeper mantle. The eclogitic diamond inclusions are likely associated with deeply subducting slabs, which may even tend to accumulate in the transition zone (i.e. Fukao et al., 2009). A likely explanation is the availability of carbon within the different lithologies. Carbon bearing liquids may be more prevalent in eclogitic systems than peridotitic at these depths. This is unlikely to be a result of the melting temperatures of carbon bearing systems, which

are in general lower in mafic compared to ultramafic systems (Dasgupta et al., 2004; Stagno et al., 2015; Yaxley and Brey, 2004). It might, however, be related to the difference in the oxygen fugacity of diamond formation from carbonate liquids between the different lithologies. While Stagno et al. (2013) showed that due to the effect of pressure on ferric/ferrous iron equilibria down welling carbonate peridotite will tend to enter the diamond stability field by 200-300 km, recent work on carbonated-eclogites indicates that much greater depths may be necessary before the ambient oxygen fugacity passes into the diamond stability field (Stagno et al. 2015). This is particularly the case if the eclogitic rocks contain a high initial carbonate contents.

Pressures obtained with the C10 barometer are much more widespread and do not yield a maximum around 13 GPa for eclogitic inclusions. Taking into account the poor pressure estimates for experimentally produce mafic garnet samples using C10, the empirical barometer derived in this study appears to be more robust and makes predictions that may be also consistent with the oxygen fugacity of diamond formation expected for the different rock types.

In the chosen set of inclusions those containing Ca-perovskite have been ignored due to the ambiguity in the pressure determined from the majorite content once this phase forms. According to Harte (2010), however, Ca-perovskite bearing inclusions show a predominantly peridotitic signature. This seems not to fit with the arguments made above and a further mechanism would be required to explain the origin of these deeper diamond inclusions.

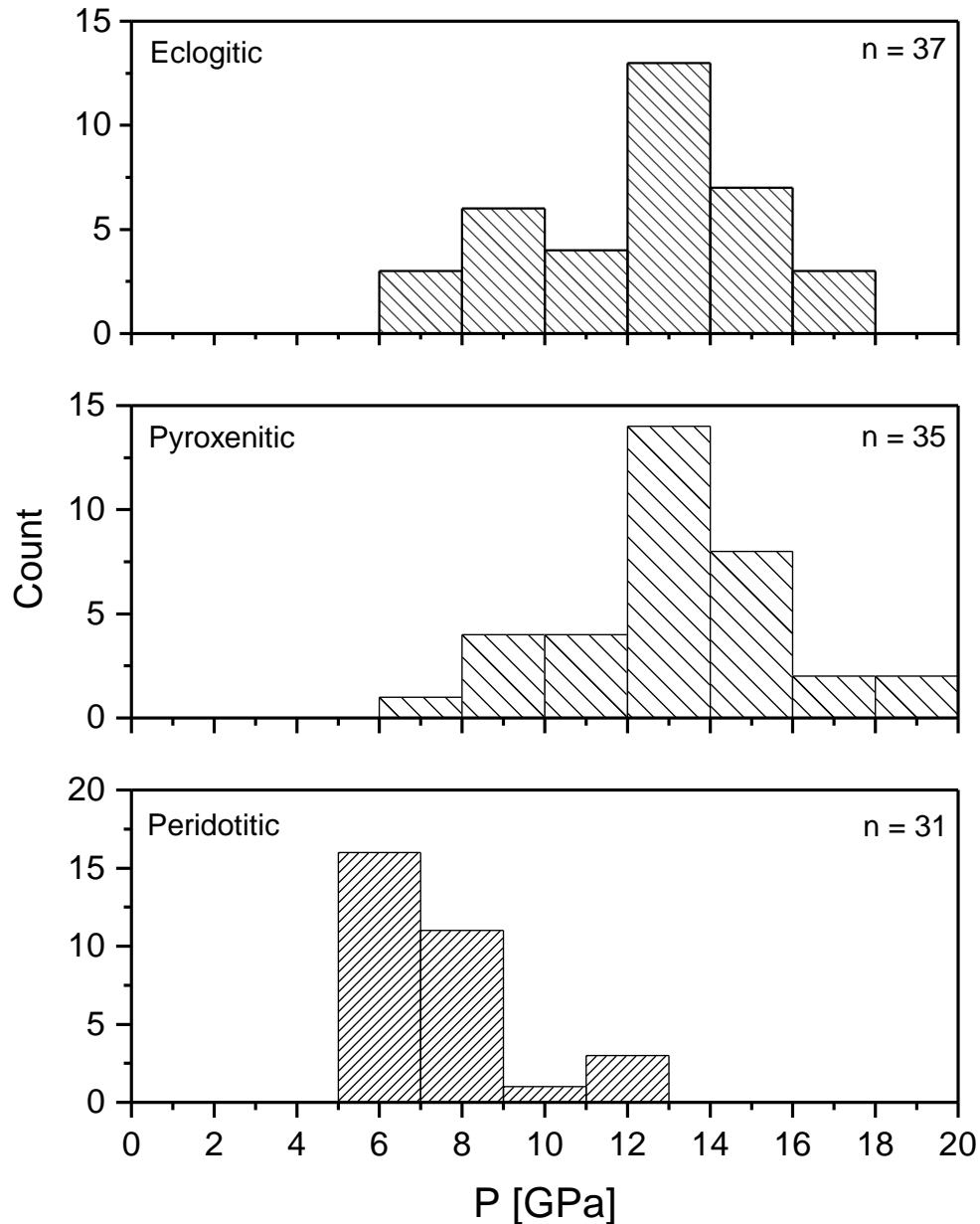


Fig. 5.6.1 Depth distribution of three chemically distinct sets of majoritic inclusions in diamonds. Majorites with a pyroxenitic and eclogitic signature seem to originate from the same depth interval, whereas, peridotitic samples generally form at shallower depths. Data and references are listed in Appendix 3.

Lastly, the results of this study support the presence of pyroxenitic material in the transition zone as proposed by Kiseeva et al. (2013). The authors suggest that melts or fluids released from an eclogitic source at these depths may react with the surrounding peridotite to form intermediate, i.e. pyroxenitic lithologies. The pressures obtained for

pyroxenites using the barometer determined in this study are quite consistent with this scenario.

5.7. Conclusions

The geobarometer derived in this study is able to reproduce pressures of formation of experimentally produced majoritic garnets formed in eclogitic, peridotitic, and kimberlitic bulk compositions within 0.86 GPa between 6 and 20 GPa and 900 to 2200 °C. The empirically formulated barometer takes far better account of chemical variations in majorite-bearing garnets formed from mafic compositions compared to the barometer of Collerson et al. (2010). The advantage of the new formulation is that pressures of inclusions with a mafic origin are calculated with higher precision.

The barometer has been used to determine the pressure of origin of ~100 garnet diamond inclusions with a majorite component from different apparent lithologies. The results indicate that there is a peak in formation pressure for eclogitic and pyroxenitic garnets at pressures of ~13 GPa, i.e. the base of the upper mantle. Most peridotitic majorite garnet inclusions, however, record pressures that peak at ~6 GPa i.e. at the base of the cratonic lithosphere. These observations may be consistent with recent studies on the stability of carbonate-bearing melts in peridotite and eclogite lithologies with respect to diamond. Diamonds can presumably only form at conditions where melts containing a carbonate component are stable. Stagno et al. (2013) proposed that the redox state of peridotite lithologies becomes increasingly reduced with depth, such that the diamond stability field would be reached for average peridotite compositions by ~6 GPa and carbonate-bearing melts would no longer be stable at greater depths. A complementary study on eclogitic rocks indicated that carbonate-bearing melts would remain stable to much greater depths

(Stagno et al. 2015), possibly explaining why deeper mantle diamonds are found associated with such lithologies. These arguments of course ignore the possibility that diamonds could also form through the oxidation of CH₄ bearing fluids, for which the current results appear to have no obvious bearing.

Additional high-pressure experiments with different bulk compositions are required to shed light on bulk compositional effects on the majorite stability. Particular attention should be paid to Cr- and Fe³⁺-rich systems. Ultimately, future studies should aim at setting up a self-consistent thermodynamic barometer which is applicable to majoritic garnets independent of their chemical origin. Therefore a profound knowledge of the interaction between the different substitution mechanisms will be very important.

6. P-V-T of complex garnet solid solutions up to 16 GPa and 800 K: Implications on the bulk modulus in aluminous garnet solid solution series

6.1. Introduction

Garnet is volumetrically the most important Al-bearing phase in the Earth's upper mantle and transition zone. Solid solutions of end-members grossular, almandine, pyrope, and spessartine form the majority of garnet in the shallow upper mantle. With increasing depth majorite-type end-members become increasingly important (Irifune et al., 1986). Given the abundance of garnet, seismic velocities of the Earth's upper mantle are expected to depend strongly on the elastic properties of garnet end-members. Thorough understanding of the effect of mixing behavior of elastic properties at pressure and temperature is, therefore, very important for interpreting seismic data. Although, end-member properties and binary systems of aluminous garnet have been studied in great detail (Bass, 1989; Huang and Chen, 2014; Isaak and Graham, 1976; Jiang et al., 2004; Pavese et al., 2001b; Takahashi and Liu, 1970; Weaver et al., 1976) (Table 6.1.1), only a few studies have examined the elasticity of more complex solid solutions (Babuška et al., 1978; Chai et al., 1997; Duba and Olinger, 1972; Jiang et al., 2004; O'Neill et al., 1989), such as those representative of naturally occurring garnets found in mantle xenoliths. Moreover, no study has examined the compressibility of garnets expected to form from mafic, i.e. eclogitic bulk compositions in the mantle. Babuška et al. (1978) point out that garnet solid solutions can be described using a linear addition law by weighting the end-member's elastic moduli using their mole fraction. However, this relationship has not been proven at high temperatures and with ternary solid solutions containing nearly equimolar proportions of pyrope, grossular and almandine, representative of eclogitic upper mantle garnets. Studies on the excess contributions, i.e. excess volumes of mixing (Berman and Koziol, 1991; Ganguly et al., 1993) contradict the assumption that volume dependent properties (i.e. bulk modulus) are

linear functions of end-members. The results reported so far show large discrepancies among the absolute values of K_0 and especially K'_0 (Wang and Ji, 2001; Zhang et al., 1999) reported for different garnet endmembers. It is still an open question whether these differences are real, or arise from differences in experimental techniques, pressure transmitting media, pressure ranges, or whether the almandine component has a non-linear effect on the compressibility of garnets. Accordingly, a careful determination of the effect of mixing is required to describe the elasticity of the whole compositional range of aluminous garnet solid solutions. The accurate determination of the bulk modulus and its first pressure derivative is a first step to shed light on the elastic behavior of eclogitic garnet and on the interpretation of densities obtained from seismic observations.

Table 6.1.1 Compilation of K_{T0} and K'_{T0} of garnet end-members and some solid solutions.

Composition	K_{T0}	K'_{T0}	P range	ptm	Method	Reference
End-members						
Prp ₁₀₀	171(2)	4.4(2)	33	Ne/He	SC XRD	Zhang et al. 1998
Prp ₁₀₀	175(1)	4.5(5)	5	M-E	SC XRD	Levien et al. 1979
Prp ₁₀₀	174(3)	4 (fixed)	4.7	M-E	SC XRD	Hazen et al. 1994
Prp ₁₀₀	171(3)	1.8(7)	10	M-E	PC XRD	Sato et al. 1978
Prp ₁₀₀	172.8	3.8(10)	26	NaCl	PC XRD	Leger et al. 1990
Prp ₁₀₀	169.2(2)	4.4 (fixed)	12	M-E	PC XRD	Du et al. 2015
Prp ₁₀₀	171.3	3.22	10	M-E	BS	Conrad et al. 1999
Prp ₁₀₀	169(3)	4.1(3)	0.0001		BS	Sinogeikin & Bass 2000
Prp ₁₀₀	170(1)	4.9(6)	3		US PC	Wang & Ji 2001
Alm ₁₀₀	185(3)	4.2(3)	21.3	Ne/He	SC XRD	Zhang et al. 1999
Alm ₁₀₀	168(5)	5.4 (fixed)	26	NaCl	PC XRD	Takahashi & Liu 1970
Alm ₁₀₀	175(7)	1.5(1.6)	10	M-E	PC XRD	Sato et al. 1978
Alm ₁₀₀	175.1(9)	6.2(5)	3		US PC	Wang & Ji 2001
Alm ₁₀₀	174(2)*	4.9(2)	11	M-E	BS	Jiang et al. 2004
Grs ₁₀₀	175(1)	4.4 (fixed)	11.6	Ne	SC XRD	Zhang et al. 1999
Grs ₉₇ Alm ₃	169(1)	5.9(1)	37	N ₂	PC XRD	Pavese et al. 2001b
Grs ₁₀₀	168(25)	6.1(1.5)	18.4	M-E/N ₂	PC XRD	Olijnyk et al. 1991
Grs ₁₀₀	169.7(4)	4.4 (fixed)	12	M-E	PC XRD	Du et al. 2015
Grs ₉₇ Sps ₁ Alm ₁	175(4)	4.25 (fixed)	25	NaCl	PC XRD	Weaver et al. 1976
Grs ₉₇ Sps ₁ Alm ₁	165(4)	5.45 (fixed)	25	NaCl	PC XRD	Weaver et al. 1976
Grs ₉₉ And ₁	168.4(7)		0.0001		BS	Bass 1989

Table 6.1.1 continued

Composition	K_{T0}	K'_{T0}	P range	ptm	Method	Reference
Grs ₁₀₀	166.8	5.46	10	M-E	BS	Conrad et al. 1999
Grs ₁₀₀	167(1)*	3.9(2)	11	M-E	BS	Jiang et al. 2004
Grs ₁₀₀	166(3)	5.9(5)	3		US PC	Wang & Ji 2001
Grs ₉₇ And ₂ Prp ₁	167.8(7)		0.0001		Res	Isaak et al. 1992
Binary solid solutions						
Prp ₈₀ Grs ₂₀	159.1(2)	4.4 (fixed)	12	M-E	PC XRD	Du et al. 2015
Prp ₆₀ Grs ₄₀	161.8(1)	4.4 (fixed)	12	M-E	PC XRD	Du et al. 2015
Prp ₄₀ Grs ₆₀	160.7(1)	4.4 (fixed)	12	M-E	PC XRD	Du et al. 2015
Prp ₂₀ Grs ₈₀	158.3(1)	4.4 (fixed)	12	M-E	PC XRD	Du et al. 2015
Prp ₃₀ Alm ₇₀	181(4)	4.2 (fixed)	11	SO	PC XRD	Huang & Chen 2014
Prp ₅₄ Alm ₄₆	174(2)	4.2 (fixed)	11	SO	PC XRD	Huang & Chen 2014
Prp ₈₃ Alm ₁₇	171(4)	4.2 (fixed)	11	SO	PC XRD	Huang & Chen 2014
Ternary solid solutions						
Prp ₅₂ Alm ₃₂ Grs ₁₆	169.5(7)	4.09	20	Ar	ISS	Chai et al. 1997
Prp ₅₇ Alm ₂₈ Grs ₁₅	175	5.45 (fixed)	10	NaF	PC XRD	Duba & Olinger 1972
Prp ₂₁ Alm ₇₅ Grs ₃	173(6)	5.4 (fixed)	26	NaCl	PC XRD	Takahashi & Liu 1970
Prp ₂₈ Alm ₂₃ Gr ₄₈ Sp ₁	169.3(6)		0.0001		BS	O'Neill et al. 1989
Prp ₂₀ Alm ₇₂ Sps ₃ Grs ₃ And ₂	174(2)	4.7(3)	11	M-E-W	BS	Jiang et al. 2004

M-E: methanol-ethanol (4:1); M-E-W: methanol-ethanol-water (16:3:1), SO: silicon oil ptm: pressure transmitting medium

SC XRD: single crystal x-ray diffraction; PC XRD power x-ray diffraction; BS: Brillouin; ISS: laser induced phonon spectroscopy; US PC: polycrystalline ultrasonic; Res: resonance spectroscopy.

*extrapolated value

All pressures are given in GPa. If K_0 was given as K_{S0} in the original reference the values have been transformed to K_{T0} using the relationship $K_T = K_S / (1 + \alpha\gamma T)$ with the values for the thermal expansion α and the Grüneisen parameter γ reported in Anderson and Isaak (1995).

The aim of this study is to analyze two garnet crystals with typical eclogitic compositions and varying end-member proportions, as well as one garnet with an almandine-rich composition, using high-pressure, high-temperature single-crystal X-ray diffraction in a diamond anvil cell (DAC) to obtain precise density, bulk modulus (K_0), and first pressure derivative (K'_0). In particular, the effect of cation substitution on the bulk modulus and its first pressure derivative will be studied. With high-temperature and high-pressure experiments the effect of temperature on K_0 also will be investigated.

6.2. Methods

6.2.1. Experimental rationale

The single crystals used in the static compression experiments were synthesized according to the procedure described in Chapter 4. The chemical composition and the end-member assignment of the garnet solid solutions are shown in Table 6.2.1.1.

Table 6.2.1.1 Chemical composition (wt.%) and normalized end-member calculation (%).

	H3605	A719-JB1	B834
SiO ₂	40.7(2)	39.7(1)	38.2(2)
TiO ₂	0.5(1)	0.5(1)	0.27(3)
Al ₂ O ₃	21.9(2)	23.0(4)	21.8(1)
FeO*	10.0(2)	10.0(1)	29.1(2)
MnO	0.22(3)	3.6(1)	0.02(2)
MgO	12.5(1)	14.5(3)	6.40(7)
CaO	12.6(1)	8.0(1)	3.57(5)
Na ₂ O	0.25(3)	0.07(2)	0.01(1)
Total	99.0	99.3	99.5
End-member			
Pyrope	47	55	26
Almandine	19	19	63
Grossular	31	17	11
Andradite	2.5	2.3	--
Spessartine	0.5	7.7	--

* All Fe given as FeO

High-quality single-crystals were selected based on their optical properties, chemical homogeneity and sharp diffraction profiles. The selected crystals were polished down to a thickness of 16 – 20 μm . Chips of these crystal sections with a maximum edge length of 80 μm have been loaded into a piston cylinder-type BX90 DAC equipped with Boehler-Almax type Ia diamonds with a 500 μm culet. A cylindrical heater made of Pt-wire loops was added for high-temperature experiments. A detailed description of the DAC and heated DAC is given in Section 3.1.3.

6.2.2. Static compression experiments

Unit-cell parameters at each pressure for each crystal were obtained from 8-position centering (King and Finger, 1979) of at least 10 reflections, in order to correct for crystal offsets, diffractometer aberrations, and goniometer imperfections as described in Section 3.2. No significant offsets between symmetry constrained and unconstrained unit cell parameters have been observed. All crystals have been refined in the cubic system within the space group $Ia\bar{3}d$. Full-width at half maximum (FWHM) of each reflection was smaller than 0.13° in ω . To ensure equilibration of pressure and relaxation of internal stresses, samples were allowed to sit for periods of 24 h after each pressure increment before measurements were performed.

In order to obtain the elastic behavior at elevated temperatures crystals from the same batch of H3605 and B834 have been loaded together with a Sm:YAG crystal which has been used to calculate both the pressure and the temperature as described in Section 3.3.6. The experimental conditions are listed in Table 6.2.2.1. Due to limitations in space caused by the heating setup, H3605T1 and H3605T2 data were collected in 4-position centering mode, only. Also, in order to reduce the amount of time for each data point, the number of reflections was reduced to a maximum of 4 – 6. The difference between unconstrained and constrained lattice parameters was still within the uncertainties. Nevertheless, the overall precision of the high-temperature P-V-T collections is clearly lower than for the P-V collections.

Table 6.2.2.1 Experimental conditions

name	max P [GPa]	T [K]	centering	P scale	T-scale
H3605	15.7	298	8-pos.	ruby	
A719-JB1	10.5	298	8-pos.	ruby	
B834	11.5	298	8-pos.	ruby	
H3605T1	6	700	4-pos.	V-YAG	V-YAG+TC
H3605T2	10	800	4-pos.	V-YAG	V-YAG+TC

V-YAG: YAG volume, TC: thermocouple

Unfortunately, due to the collapse of the DAC during decompression of the experiment of H3605T2 it was impossible to measure precise V_{0T} of the Sm:YAG and of the garnet sample at the same conditions. Therefore, the approach using the unit cell parameters together with the well-known EoS parameters has been chosen to extrapolate the Sm:YAG compression curve measured at the given temperature to V_0 as described in Chapter 3. This extrapolation for the Sm:YAG crystal resulted in an uncertainty for V_{0T} of around 3 \AA^3 which corresponds to $\Delta T \sim 50 \text{ K}$ uncertainties in temperature. The estimated temperature in this experiment is $800 \pm 50 \text{ K}$ which agrees well with the temperature recorded by the thermocouple $T_{TC} \sim 823 \pm 20 \text{ K}$.

For run H3605T1, the volume calculations based on the averaged d-spacing of two successfully collected reflections before the cell collapsed, gave $V_{0T}(\text{Sm:YAG}) = 1752 \pm 3 \text{ \AA}^3$. This value is in good agreement with the volume that has been obtained from the extrapolation of the compressibility data and results in a temperature of $700 \pm 50 \text{ K}$ which is in within the error of the thermocouple reading, $T_{TC} \sim 663 \pm 20 \text{ K}$.

6.3. Results and Discussion

6.3.1. Room temperature compression experiments

The samples H3605, A719-JB1, and B834 have been compressed at room temperature up to 15.7, 10.5, and 11.1 GPa, respectively. The unit-cell volume data as a function of pressure at room temperature are listed in Table 6.3.1.1.

The garnet solid solutions measured in this study can be described by three major aluminous garnet substitution types: grossular ($\text{Ca}_3\text{Al}_2\text{Si}_3\text{O}_{12}$), almandine ($\text{Fe}^{2+}_3\text{Al}_2\text{Si}_3\text{O}_{12}$), and pyrope ($\text{Mg}_3\text{Al}_2\text{Si}_3\text{O}_{12}$). Minor compounds of spessartine ($\text{Mn}_3\text{Al}_2\text{Si}_3\text{O}_{12}$) and andradite ($\text{Ca}_3\text{Fe}^{3+}_2\text{Si}_3\text{O}_{12}$) have been accounted for in the end-member recalculation but have been merged with similar end-members (Table 6.2.1.1), i.e. spessartine with almandine, and

andradite with grossular, to construct a ternary diagram. Trace amounts of Na₂O (< 0.25 wt. %) and TiO₂ (< 0.5 wt. %) in H3605 and A719-JB1 have been neglected. H3605 and A719-JB1 have a typical eclogitic composition, whereas B834 is strongly enriched in the almandine compound. This Fe²⁺ enriched composition was chosen due to the fact that existing data on pure almandine and almandine rich compositions (Takahashi and Liu, 1970; Zhang et al., 1999) report contradicting values on K_{T0} and especially K'_{T0} .

Table 6.3.1.1 Room temperature static compression experiments

H3605		A719-JB1		B834	
P [GPa]	V [Å]	P [GPa]	V [Å]	P [GPa]	V [Å]
0.0001	1570.3(2)	0.0001	1555.4*	0.0001	1542.4(1)
0.43(5)	1565.2(1)	0.7(1)	1548.5(1)	1.0(1)	1533.9(1)
1.33(5)	1557.9(1)	1.36(6)	1543.5(1)	1.8(1)	1527.4(1)
1.9(1)	1553.7(1)	2.2(1)	1536.2(2)	2.7(1)	1519.1(1)
2.6(1)	1545.6(1)	3.39(6)	1525.4(1)	4.2(1)	1507(1)
3.52(7)	1538(1)	5.69(5)	1507.3(1)	4.84(5)	1502.4(1)
4.07(5)	1533.2(1)	6.86(8)	1498.4(1)	6.86(1)	1485.8(1)
5.19(5)	1526.1(1)	7.94(8)	1489.2(1)	8.0(1)	1478.8(1)
6.0(1)	1519.2(1)	9.50(6)	1479.1(1)	9.11(5)	1470.9(2)
7.2(1)	1510.3(2)	10.5(1)	1472.2(2)	9.72(5)	1466.2(2)
8.6(1)	1498.6(2)			10.60(5)	1460.9(2)
11.95(5)	1481.8(1)			11.08(5)	1456.8(3)
13.1(1)	1467.1(2)				
14.0(1)	1462.1(2)				
14.6(1)	1458.8(2)				
15.4(1)	1452.6(2)				
15.73(5)	1450.4(1)				

*inferred from intersection of the compression curve with the ordinate

P from ruby R1 line shift. 1σ error expressed as uncertainty of the last digit in parentheses

To obtain an initial estimate of the magnitude of K'_{T0} the data have been transformed into Eulerian strain f and plotted against normalized pressure F_E (Fig. 6.3.1.1). For all three garnets the f - F plot suggests values of K'_0 close to 4 in agreement with several previous studies (Jiang et al., 2004; Zhang et al., 1998; Zhang et al., 1999). However, some other studies report much higher K'_0 for aluminous garnets (Olijnyk et al., 1991; Pavese et al.,

2001b; Takahashi and Liu, 1970; Wang and Ji, 2001). Possible reasons for this discrepancy will be discussed in detail in the next Section.

All three compression data have been fitted using a 3rd order Birch-Murnaghan equation of state, BM3-EoS, (Birch, 1986), using the eosfit software package for least-squares refinement (Angel et al., 2014). The BM3-EoS formalism (6.1) is explained in detail in Section 3.3.1.

$$P_0 = 3K_{T0}f_E(1 + 2f_E)^{\frac{5}{2}} \left(1 + \frac{3}{2}(K_{T0}' - 4)f_E \right) \quad (6.1)$$

with

$$f_E = [(V_0/V)^{2/3} - 1]/2 \quad (6.2)$$

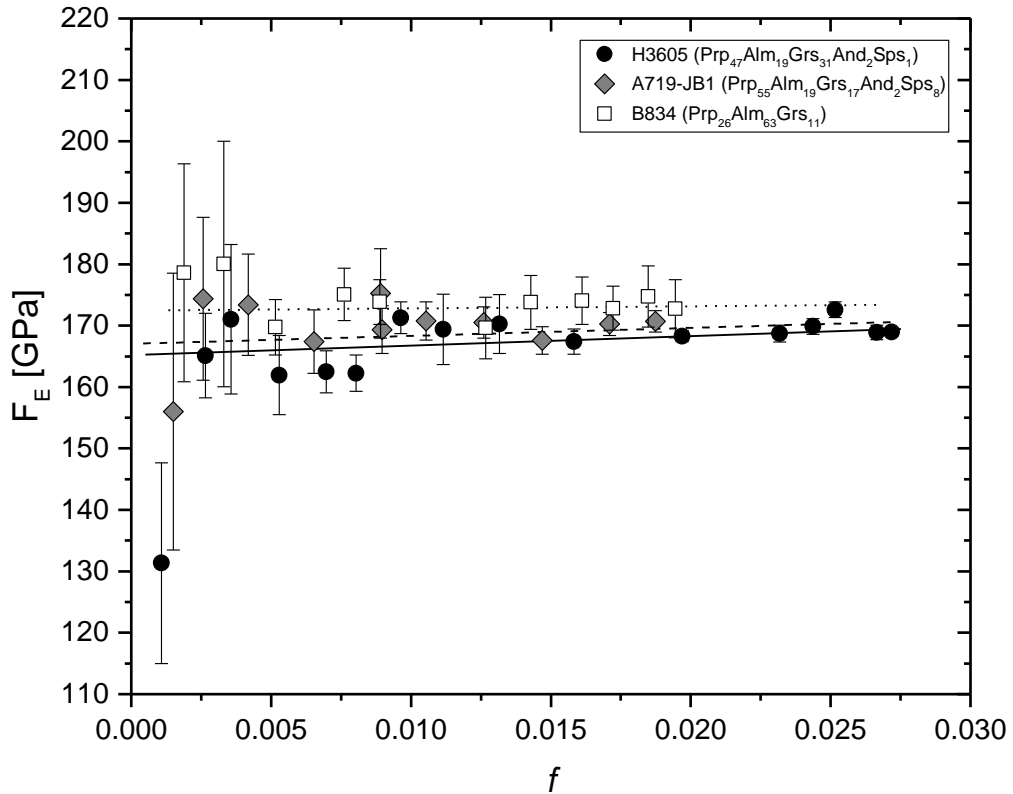


Fig. 6.3.1.1 Normalized pressure as a function of Eulerian strain for the three room pressure compression experiments. Error bars represent the 1 σ error based on propagated experimental uncertainties (Eq. 3.4 and 3.5) (Angel, 2000; Heinz and Jeanloz, 1984).

Values of the least-squares refinements are given in Table 6.3.1.2 and shown in Fig. 6.3.1.2.

Table 6.3.1.2 Results from P-V data fitting with BM3-EoS

sample	composition*	V_{T0} (\AA^3)	K_{T0} (GPa)	K'_{T0}
H3605	Prp ₄₇ Alm ₁₉ Grs ₃₁ And ₂ Sps ₁	1570.2(2)	166(2)	4.6(4)
A719-JB1	Prp ₅₅ Alm ₁₉ Grs ₁₇ And ₁ Sps ₈	1555.4(2)	168(3)	4.5(8)
B834	Prp ₂₆ Alm ₆₃ Grs ₁₁	1542.4(1)	173(3)	4.1(7)

*Na and Ti neglected (trace amounts). 1σ uncertainty expressed as the last digit in parentheses.

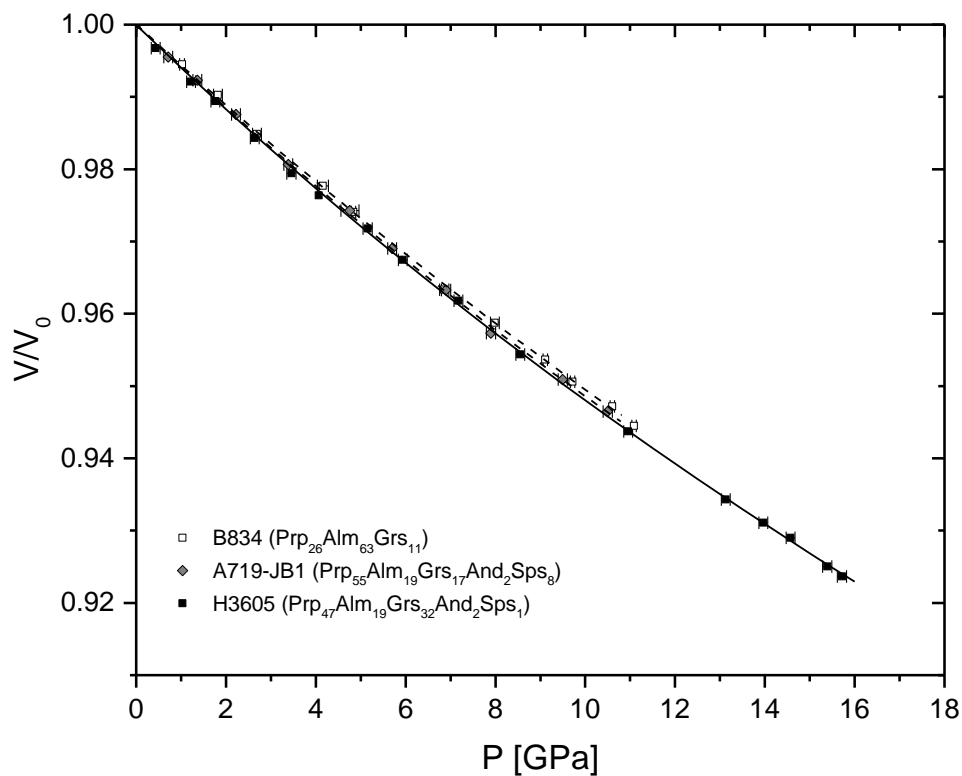


Fig. 6.3.1.2 Variation with pressure of the unit-cell volumes of the garnets investigated in this study normalized with respect to the room pressure volume V_0 . Error bars are within the symbols and represent the 1σ uncertainties of volume and pressure. The lines represent the results from BM3-EoS fitting.

As shown in Table 6.3.1.2, the K'_{T0} values are close to 4 in agreement with the f - F plots. Confidence ellipses have been constructed for all sets of K_{T0} and K'_{T0} data in order to assess the real uncertainties of the BM3 fitting procedure, and to show the strong correlation between K_{T0} and K'_{T0} (Bass et al., 1981). To construct a confidence ellipse the covariance

and variance of K_{T0} and K'_{T0} from the least-squares refinement expressed as 2x2 matrix are used:

$$\Delta = (x, y) \begin{pmatrix} V_{K.K} & V_{K.K'} \\ V_{K.K'} & V_{K'.K'} \end{pmatrix}^{-1} \begin{pmatrix} x \\ y \end{pmatrix} \quad (6.3)$$

with Δ representing the results from the chi-square distribution with two degrees of freedom for a certain confidence level of choice, i.e. for a 2σ confidence level Δ is 6.17. Under the assumption that the inverse matrix U is symmetric, meaning u_{21} equals u_{12} the equation (6.3) can be converted into a quadratic form (Angel, 2000):

$$u_{11}x^2 + 2u_{12}xy + u_{22}y^2 - \Delta = 0 \quad (6.4)$$

Solving equation (6.4) for x and y gives a group of points describing an ellipsoid around the origin of ordinates x and y representing the values of K_{T0} and K'_{T0} . The confidence ellipses depicted in Fig. 6.3.1.3 clearly show that the almandine-rich sample B834 has a larger K_{T0} and a smaller K'_{T0} than the eclogitic samples even considering the larger two dimensional uncertainties. The eclogitic garnet, instead overlap in K_{T0} - K'_{T0} space and therefore can be considered to have identical compressibility once the uncertainties are taken into account.

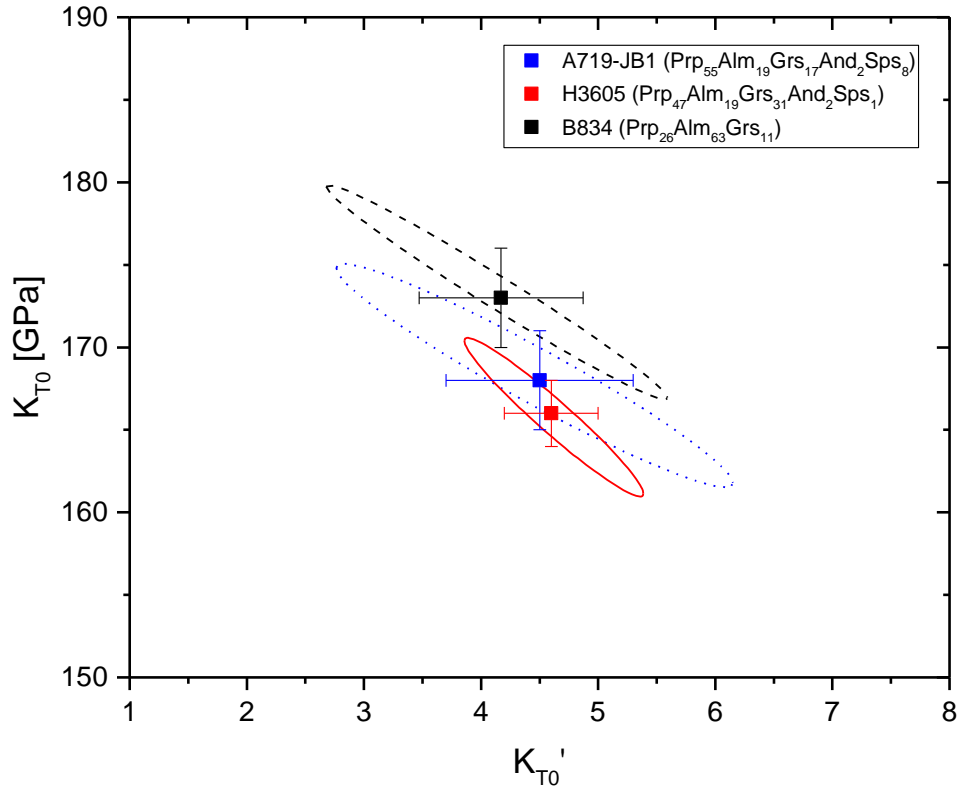


Fig. 6.3.1.3 Results of the BM3-EoS fitting shown as K_{T0} (GPa) against K'_{T0} . The confidence ellipses represent the 2σ uncertainties, whereas the error bars represent the 1σ uncertainties. Black symbols: B834; red symbols: H3605; blue symbols A719-JB1.

The bulk moduli obtained in this study are shown in the ternary diagram depicted in Fig. 6.3.1.4 and compared with the EoS parameters reported in the literature (Table 6.1.1). Since high pressure single crystal X-ray diffraction studies on complex garnets are rare, the EoS parameters obtained in this study are compared with the elastic moduli measured with different techniques and for garnet solid solution with different compositions, so that a quantitative comparison is rather difficult. The almandine-rich solid solution ($\text{Prp}_{20}\text{Alm}_{72}\text{Sp}_{83}\text{Grs}_3\text{And}_2$) of the high-pressure Brillouin measurements of Jiang et al. (2004) is similar in composition and has comparable $K_{T0} = 174(2)$ GPa and $K'_{T0} = 4.7(3)$ values to the almandine rich sample B834 of this study for which $K_{T0} = 173(2)$ GPa and $K'_{T0} = 4.1(7)$. The range of pressure on which both experimental data sets have been obtained is also very similar. The slight differences in K'_{T0} are potentially caused by non-

hydrostatic behavior above 10.5 GPa due to the glass-transition of the pressure transmitting medium (methanol-ethanol-water) used in the experiment of Jiang et al. (2004) (Klotz et al., 2009).

The results of this study together with the results of Jiang et al. (2004) suggest that the bulk modulus for pure almandine may be lower than the K_{T0} of 185 GPa reported by Zhang et al. (1999), if ideal mixing and negligible excess volume along the pyrope-almandine binary is assumed (Geiger and Feenstra, 1997). The K_{T0} from Zhang et al. and the high K_{T0} along the pyrope-almandine binary of Huang and Chen (2014) are systematically larger compared to what a linear extrapolation of the data from this study would suggest. The offset in the study of Huang and Chen might result from the pressure transmitting medium, which was silicon oil, and the relatively large uncertainty in the volumes. Above 12 GPa silicon oil shows a strong effect on the ruby R_1 line width which increases the standard deviation of the pressure calibrant up to 3 GPa at around 23 GPa (Klotz et al., 2009). The combination of large uncertainties in volume and pressure together with a small number of data points in the range of pressures covered by the study of Huang and Chen (2014) might be the explanation for the larger K_{T0} .

The only two elastic studies with a composition close to typical eclogitic garnets, which are slightly dominated by pyrope with nearly equimolar amounts of grossular and almandine, are the solid solutions studied by Chai et al. (1997) and Duba & Olinger (1972) (Table 6.1.1). The results for $K_{T0} = 169.5(7)$ and $K'_{T0} = 4.09$ of the former study are in agreement with the parameters obtained in this study for samples H3605 and A719-JB1 any variation with composition appears not resolvable within the analytical uncertainties. The values of $K_{T0} = 175$ GPa reported in the latter study is larger, however, it has to be noted that the value of K'_{T0} has been fixed arbitrarily to the value of 5.45 and the scatter on the original data is large.

Taking into account the strong excess volume of the pyrope-grossular binary (Du et al., 2015; Ganguly et al., 1993), the bulk moduli of H3605 and A719-JB1 support the findings of Du et al. (2015). Those authors report solid solutions along the pyrope-grossular binary have a smaller bulk modulus than both end-members, under the assumption of a constant K'_{T0} . The samples studied in this study clearly show the strong effect of almandine on the bulk modulus overprinting the minimum observed by Du et al. (2015). However, it cannot be ruled out completely that this minimum is also present in the presented data, but as already emphasized above, small compositional effects are not resolvable and superimposed by the large K_{T0} of almandine.

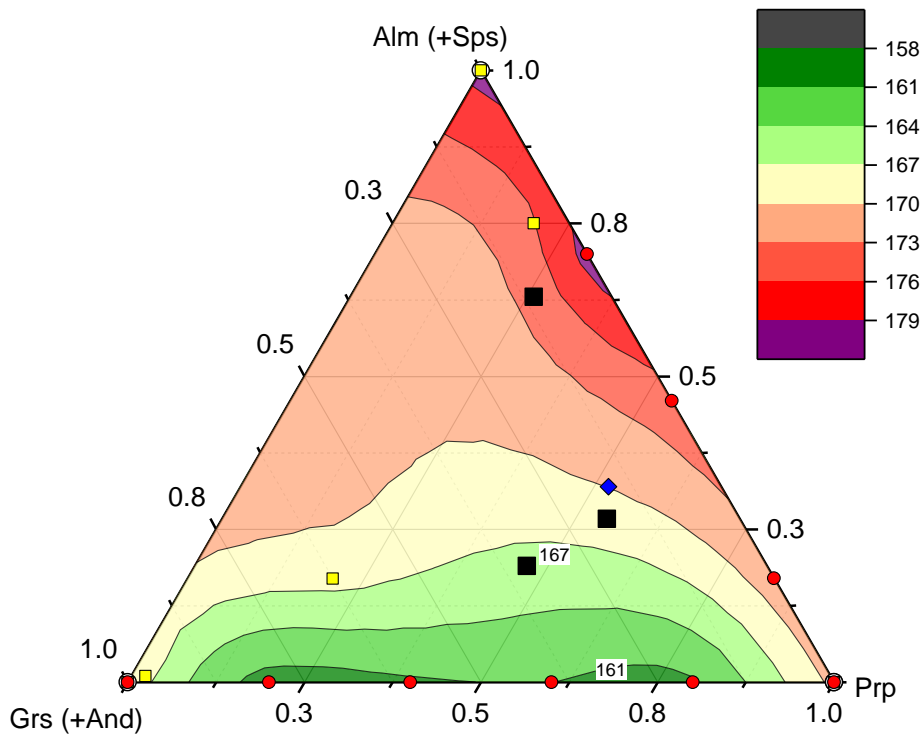


Fig. 6.3.1.4 Ternary contour diagram of the bulk modulus K_{T0} in GPa of the aluminous garnet end-members pyrope, almandine, grossular, including spessartine, and andradite. The contouring is based on the SC-XRD (white circles) of Zhang et al. (1998), Zhang et al. (1999), Hazen et al. (1994), Powder-XRD (red circles) of Huang and Chen (2014), Pavese et al. (2001b), Du et al. (2015), Brillouin data (yellow squares) of Jiang et al. (2004), O'Neill et al. (1989), Bass (1989), Sinogeikin and Bass (2000), ISS (blue diamond) of Chai et al. (1997), and SC-XRD data of this study (black squares). The underlying contouring is averaged over all reported data sets. Due to scarce data on ternary garnets the contour has been smoothed to represent a more realistic curvature. The smoothing factor was 0.05 and the number of points to interpolate was raised to 100.

One can argue whether the pressure range up to 16 GPa covered in this study is sufficient to obtain accurate values for K'_{T0} (Pavese et al., 2001b; Zhang et al., 1999). However, as already discussed above, the f - F plots of the solid solutions investigated in this study (Fig. 6.2.1.1) is in agreement with K'_{T0} values close to 4 as obtained by fitting a BM3-EoS. Pavese et al. (2001a) observed that there might be a small increase of K'_{T0} with increasing grossular fraction. The results from this study appear to follow such suggestion since sample B834 which has the smallest grossular fraction (11 %), also displays the smaller $K'_{T0} = 4.1(7)$ and sample H3605 which has the largest grossular fraction (31 %) has the largest $K'_{T0} = 4.6(4)$.

Finally, all ultrasonic studies report larger values of K'_{T0} , i.e. Wang and Ji (2001) K'_{T0} between 4.9 and 6.2. However, as summarized in Jiang et al. (2004), uncertainties may arise in the ultrasonic studies due to the polycrystalline samples or the limited pressure ranges (<3 GPa) used. It is possible that the relatively high strength of garnet allows some microscopic porosity to remain during initial pressurization, which would act to raise K'_{T0} .

Since most of the single-crystals studies present in the literature have been performed using methanol-ethanol as pressure transmitting medium, there may be the possibility that the differences in elastic parameters observed may be due to difference in hydrostaticities between the methanol-ethanol and the Ne gas used in the present study. To test such hypothesis, sample H3605 has been loaded with a 4:1 mixture of methanol-ethanol and compressed up to 10.6 GPa. A comparison between the V/V_0 values of sample H3605 obtained in neon and in methanol-ethanol is shown in Fig. 6.3.1.5. Both experiments were carried out in DACs described in Section 3.3.3 and in both experiments the ruby pressure gauge with the parameters of Jacobsen et al. (2008) has been used. Within the analytical

uncertainties of the ruby pressure scale no differences between the two pressure transmitting media up to 10.6 GPa have been observed. This observation is in good agreement with previous measurements performed with the same two pressure transmitting media (Klotz et al., 2009).

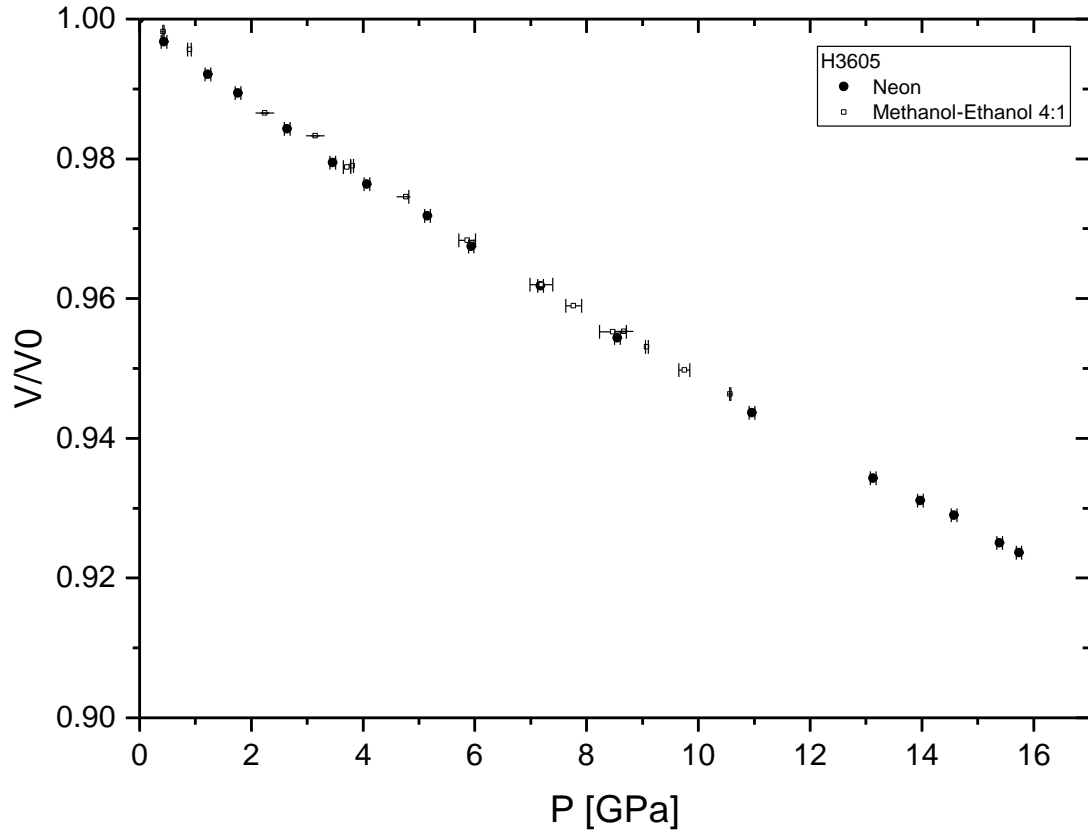


Fig. 6.3.1.5 Comparison of the unit-cell volumes V/V_0 of sample H3605 collected using neon (black diamonds) and methanol-ethanol (open square). Error bars are 1σ .

6.3.2. High-temperature compression experiments

The high-temperature compression curves for run H3605T1 and H3605T2 are listed in Table 6.3.2.1, and shown in Fig. 6.3.2.1.

Table 6.3.2.1 Compression data of the high P/T experiments.

H3605T1		H3605T2	
P [GPa]	V [\AA^3]	P [GPa]	V [\AA^3]
0.0001	1591(3)*	0.0001	1596(3)**
2.2(2)	1570.1(4)	5.5(3)	1543.7(3)
2.3(2)	1568.3(6)	8.9(5)	1516(1)
2.4(2)	1567.3(3)	9.5(5)	1511(1)
2.8(2)	1564.2(5)	10.2(5)	1505.5(8)
3.3(2)	1561.0(7)		
3.9(2)	1553.9(2)		
6.3(2)	1533(2)		

* obtained from the average d-spacing of two reflections; ** obtained from extrapolation of the Sm:YAG compression curve

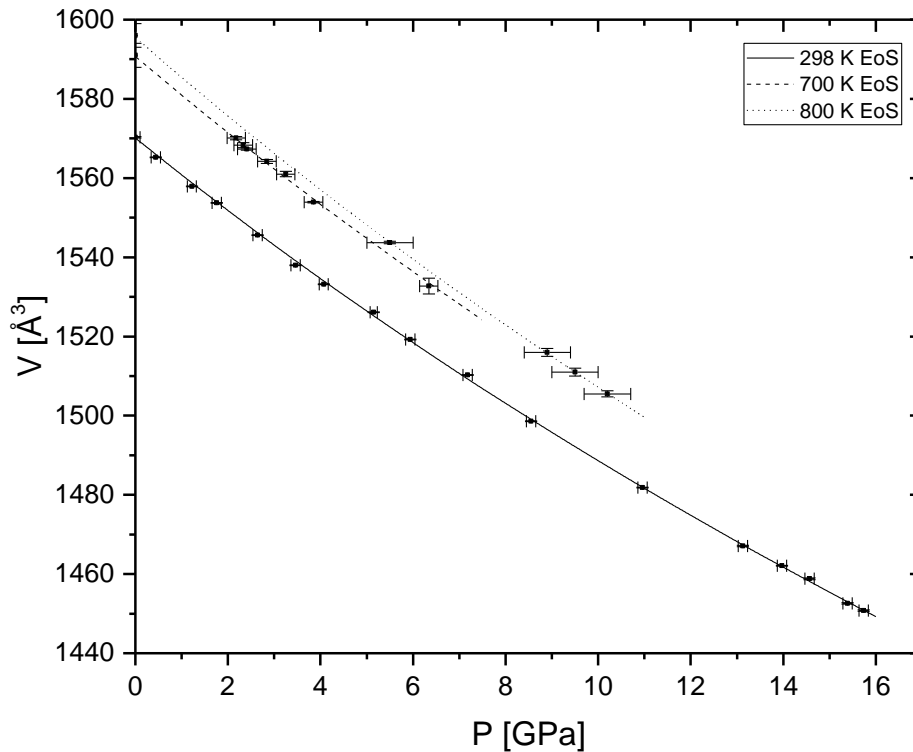


Fig. 6.3.2.1 Variations with pressure of the unit-cell volume of sample H3605 along three isotherms. Error bars represent the 1σ uncertainty.

The P-V-T EoS has been obtained following the description of Section 3.3.5 (Eqs. 3.2, 3.7, and 3.8). The value of K'_{T0} was fixed to 4.6 and the following volumes at ambient pressure

and high temperatures were used: $V_{0,700} = 1591 \pm 3 \text{ \AA}^3$, $V_{0,800} = 1596 \pm 3 \text{ \AA}^3$, resulting in the bulk moduli $K_{T,700} = 161 \pm 4 \text{ GPa}$ and $K_{T,800} = 158 \pm 5 \text{ GPa}$. Θ_E was calculated to be 456 K according to equation (3.10). In combination with K_{T0} and K'_{T0} from the room temperature experiment the thermal expansion $\alpha_0 = 2.85 \pm 0.14 \times 10^{-5} \text{ K}^{-1}$ coefficient of sample H3605 has been obtained. The results of the least-squares refinement are summarized in Table 6.3.2.2.

Table 6.3.2.2 Thermoelastic parameters of this study compared to previous studies

Composition	K_{T0} (GPa)	K'_{T0}	$(\partial K_T / \partial T)_P$	α_0 (10^{-5} K^{-1})	Method**	References ⁺
Prp ₄₇ Alm ₁₉ Grs ₃₁ And ₂ Sps ₁	166(4)	4.6*	-0.026(1)	2.85(14)	SC XRD	this study
Prp ₇₃ Alm ₁₆ And ₄ Uv ₆	169.4		-0.0256	2.36	RPR	1
Grs ₁₀₀	168.2(1.7)	4*	-0.016(3)	2.78(2)	PC XRD	2
Prp ₁₀₀	167(3)	4.1*	-0.021(1)	2.74(33)	PC XRD	3
Prp ₁₀₀	169.4(2.0)		-0.019(3)		BS	4
Alm ₈₆ Prp ₇ Sps ₇	177(2)	4*	-0.032(16)	3.1(7)	PC XRD	5

*fixed **SC XRD: single-crystal X-ray diffraction, PC XRD: powder X-ray diffraction, BS: Brillouin, RPR: Rectangular Parallelepiped Resonance

⁺ 1 Suzuki & Anderson (1983), 2 Pavese et al. (2001a), 3 Zou et al. (2012), 4 Sinogeikin & Bass (2002) 5 Fan et al. (2009)

There are very few data available on the thermal equation of state of binary garnet solid solutions (Gwanmesia et al., 2006; Isaak et al., 1992; Sumino and Nishizawa, 1978; Suzuki and Anderson, 1983). However, several studies have measured the high temperature elasticity of garnet end-members (Fan et al., 2009; Pavese et al., 2001a; Zou et al., 2012).

Due to the high uncertainties of our measurements owing to the challenging experimental conditions a quantitative determination of $(\partial K_T / \partial T)_P$ was difficult. Fitting a linear equation to the three data points of H3605 yielded $(\partial K_T / \partial T)_P = -0.026 \pm 1 \text{ GPa K}^{-1}$. The closest available solid solution (Prp₇₃Alm₁₆And₄Uv₆) measured up to 1000 K (Suzuki and Anderson, 1983) has reported values of $K_{T0} = 169.4 \text{ GPa}$ and $(\partial K_T / \partial T)_P = -0.0256 \text{ GPa K}^{-1}$ in very good agreement with the present study. A comparison with the

$(\partial K_T/\partial T)_P$ for pyrope (Zou et al., 2012), almandine (Fan et al., 2009), grossular (Pavese et al., 2001a), and $\text{Prp}_{73}\text{Alm}_{16}\text{And}_4\text{Uv}_6$ (Suzuki and Anderson, 1983) is shown in Fig. 6.3.2.2. Almandine becomes softer with increasing temperature when compared with pyrope and grossular, which have a similar and less pronounced softening. The solid solution H3605 lies below these three end-members. $(\partial K_T/\partial T)_P$ and has a very similar trend to that of pure almandine garnet, although, the fraction of almandine is smaller than the fraction of pyrope and grossular. This suggests that $(\partial K_T/\partial T)_P$ cannot be described with a simple linear combination of end-members. With the current limited amount of data available, it is rather cumbersome to derive a mixing model which describes the softening of garnet solid solutions with temperature.

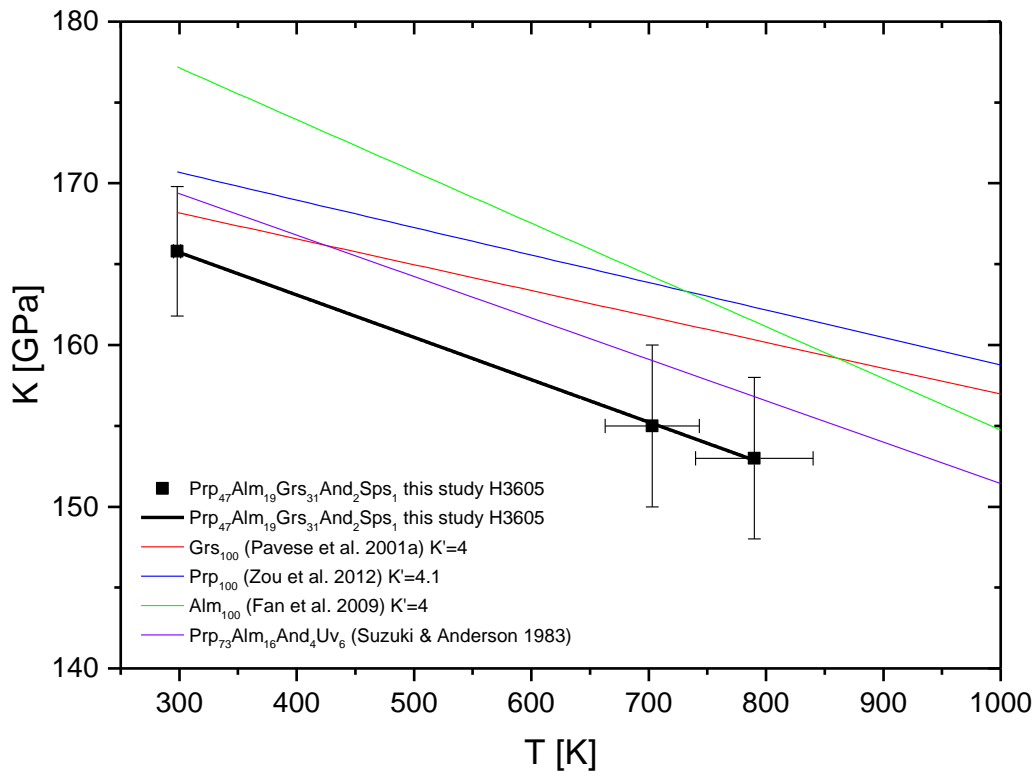


Fig. 6.3.2.2 Variation of K_T with temperature. Studies with K'_{T0} of ~ 4 have been selected to prevent potential bias. Error bars represent the 1σ uncertainties in bulk modulus and temperature as discussed in the text.

6.4. Conclusions and Implications

The compressibility data of the three garnet samples measured in this study were fitted using a BM3-EoS which yield a K'_{T0} close to 4 within the analytical uncertainties. However, there appears to be a subtle increase of K'_{T0} with increasing grossular fraction as it has been observed by Pavese et al. (2001a). The confidence ellipses from the variance-covariance matrix of K_{T0} and K'_{T0} plot show that the almandine enriched sample B834 has a larger bulk modulus and smaller K'_{T0} than the eclogitic samples H3605 and A719-JB1.

Under the assumption of ideal behavior along the pyrope-almandine binary, the K_{T0} of almandine is likely to be smaller than the value reported by Zhang et al. (1999) and in agreement with the value reported by Jiang et al. (2004) and Wang and Ji (2001). From studies on the excess volume of mixing along the pyrope-almandine binary, there is no evidence for large deviations from linearity, whereas larger values for the pure almandine bulk modulus would result in a strongly non-linear mixing behavior.

An inverse correlation of K_{T0} with excess volume and thermal expansion, resulting in a minimum for a solid solution along the pyrope-grossular binary has been observed by Du et al. (2015). The data of the present study generally agree with the results of Du et al. (2015), although samples A719-JB1 and H3605 have bulk moduli values much closer to those of the pyrope and grossular end-members. It appears therefore that minor amounts of almandine as those present in the eclogitic garnet of this study have a major effect in increasing the stiffness of the garnet structure. The presence of the almandine component also appears to have a strong effect on the value of $(\partial K_T / \partial T)_P$, this may lead to significant differences in the interpretation of seismic data for the upper mantle, where garnet can take up considerable amounts of iron. Especially in mafic environments, i.e. oceanic crust, iron

favors garnet over clinopyroxene (Chapter 4). At mantle temperatures this may result in >1% difference in density.

A logical application of the herein obtained data is their incorporation into a self-consistent thermodynamic model, as for example the model presented by Stixrude and Lithgow-Bertelloni (2011), and Stixrude and Lithgow-Bertelloni (2005). This model has been set up to extrapolate elastic properties and phase relations based on end-member data to the deep Earth's interior. However, the model is not accounting for non-idealities of mixing as those suggested in this study. Hence, an alternative approach needs to be considered to combine the ideal mixing calculated from the end-member data given in the recent tabulations of Stixrude and Lithgow-Bertelloni (2011) with the excess contributions in volume calculated from the data presented in this work. To this end, the elastic parameters for the garnet end-members have been refined in order to fit the experimental volume, considering that the “real” volume of a solid solution at pressure and temperature is made up by two contributions: the ideal volume (V_{ideal}) and the excess volume (V_{xs}):

$$V_{real} = V_{ideal} + V_{xs} \quad (6.5)$$

The ideal contribution of the volume is given by:

$$V_{ideal} = \sum_i X_i V_i \quad (6.6)$$

Where X_i is the molar fraction, and V_i is the tabulated volume of the garnet end-members at any given pressure and temperature. To calculate V_i at pressure and temperature the cold

pressure P_0 is calculated with a BM3-EoS as given in equation (6.1) and the thermal pressure is calculated using the Mie-Grüneisen-Debye EoS (MGD) (Jackson and Rigden, 1996) as described in Section 3.3.5, Eq. 3.16. The end-members volumes (V_0) at standard state are taken from the tabulation given by Stixrude and Lithgow-Bertelloni (2011), whereas the elastic parameters K_{T0} and K'_{T0} are taken from Sinogeikin and Bass (2000) for pyrope, from Jiang et al. (2004) and Zhang et al. (1999) for almandine, and from Jiang et al. (2004) for grossular (Table 6.4.1). Mole fractions X are based on the end-member recalculation reported in Table 6.2.1.1.

The excess contribution to the volume has been added using an asymmetric binary Margules formulation to calculate V_{xs} of the garnets of this study:

$$V_{xs} = X_{Ca}(X_{Mg} + X_{Fe})[W_{Ca(MgFe)}(X_{Mg} + X_{Fe}) + W_{(MgFe)Ca}X_{Ca}] \quad (6.7)$$

Where $W_{Ca(MgFe)}$ and $W_{(MgFe)Ca}$ are the asymmetric binary Margules parameters of the grossular–pyrope/almandine join, under the assumption that the pyrope-almandine binary is ideal in terms of volume, the Ca-Mg-Fe garnet ternary can be reduced to a Ca-MgFe binary. The Margules parameters were refined to reproduce the data of this study resulting in $W_{(MgFe)Ca} = 6.5 \text{ cm}^3$ and $W_{Ca(MgFe)} = 1.9 \text{ cm}^3$. Accordingly, the excess volumes were calculated to be $0.75 \text{ cm}^3\text{mol}^{-1}$ for H3605 and $0.23 \text{ cm}^3\text{mol}^{-1}$ for B834. Combining the refined Margules parameter with the fixed parameters given in Table 6.4.1 reproduced the room temperature densities better than 0.1 %.

Table 6.4.1 Parameters used for the refinement of the MGD.

	V_0	K_{T0} [GPa]	K'_{T0}	Θ_0 [K]	γ_0	q
Pyrope	113.08	169	4.1	823	1.01	1.4
Almandine	115.43	175	4.2	741	1.06	1.9
Grossular	125.12	167	3.9	823	1.05	1.5

Bold written parameters are taken from the references as described above and listed in Table 6.1.1. All other parameters are taken from Stixrude and Lithgow-Bertelloni (2011).

The results obtained in this study also indicate that the excess volume depends on temperature. The V_{xs} at high temperature was thus refined using the parameters for the MGD given in Table 6.4.1. With these parameters the excess volume for H3605 was $\sim 1.3 \text{ cm}^3 \text{ mol}^{-1}$ in the temperature range of 700-800 K. The high temperature densities were reproduced better than 0.17 % which is still an excellent result, considering the larger uncertainty on pressure and temperature of the high temperature compression data. In contrast, using the smaller value of V_{xs} obtained at room temperature to fit the high temperature data led to an overestimation in density of ~ 0.5 % at 800 K.

To accurately derive the excess terms which are required for a correct description of complex garnet solid solutions at Earth's upper mantle conditions, high temperature and high pressure studies on binaries are clearly required since as suggested in this study excess properties depends both on pressure and on temperature. Such experimental data will have the advantage of improving the interpretation of seismic models.

Future studies also would require even a better precision to resolve compositional differences, for example by reducing the largest source of uncertainty due to the pressure determination. An absolute pressure scale as used in Trots et al. (2013) may enhance the overall precision of subsequent studies on this topic. To obtain a better constraint on the bulk modulus variation with pressure (K'_{T0}) and with temperature $(\partial K_T / \partial T)_P$ experiments should also be performed over a larger pressure and temperature range.

7. Fluorine partitioning between eclogitic garnet, clinopyroxene, and melt under upper mantle conditions

7.1. Introduction

The behavior of halogens in crustal processes is well understood. In granitic rocks the halogen concentration is determined by micas, hornblendes, topaz, turmaline, fluorite, and apatite where it substitutes for OH due to the similar ionic radii ($\text{OH} = 1.35 \text{ \AA}$, $\text{F} = 1.31 \text{ \AA}$) and equal charge. The variation of F in granitic rocks and hydrous minerals formed under crustal conditions is large and can vary between a few $\mu\text{g/g}$ to several wt.% (Aoki and Kanisawa, 1979; Bailey, 1977). The average estimate for F and Cl of the continental crust are $557 \mu\text{g/g}$ and respectively $370 \mu\text{g/g}$ (Rudnick and Gao, 2003). Nominally hydrogen free minerals (NHFMs) play no role in the halogen budget of the crust.

However, there is renewed interest in halogens in the mantle over the last couple of years. Before then, only a limited number of studies have been published dealing with the role of halogens in mantle and mantle derived melts (Edgar et al., 1994; Filiberto et al., 2012; Foley, 1991; Hauri, 2002; Hazen et al., 1997; Luth, 1988; Schilling et al., 1980; Smith, 1981; Smith et al., 1981; Straub and Layne, 2003). Even fewer contributions addressed the behavior of halogens in basaltic rocks and their partitioning with experimental methods (Bromiley and Kohn, 2007; Edgar and Pizzolato, 1995; Klemme, 2004; Stalder and Ulmer, 2001).

Recently, several studies covered a wide range of questions involving halogens and in particular F. It was shown that significant amounts of halogens are stored in nominally F-free minerals such as olivine or pyroxenes (Bernini et al., 2013; Beyer et al., 2012; Bromiley and Kohn, 2007). The studies range from partitioning studies for various mantle phases between nominally halogen free minerals and melts (Beyer et al., 2012; Dalou et al., 2014; Dalou et al., 2012; Rosenthal et al., 2015), minerals and aqueous fluids (Bernini et

al., 2013; Fabbrizio et al., 2013a; Fabbrizio et al., 2013b; Wu and Koga, 2013), F-concentration in natural samples (Beyer et al., 2012; Kendrick et al., 2014; Le Voyer et al., 2014; Mosenfelder and Rossman, 2013a, b), and the incorporation mechanisms (Crépisson et al., 2014). Based on these studies important implications have been drawn for the role of fluorine in different planetary bodies, on various geologic settings, and on the Earth's fluorine cycle and budget.

The quintessence of the partitioning studies was that fluorine can be stored in substantial amounts in NHFMs with crystal-melt partition coefficients ranging from $D_F^{olivine/melt} = 0.0007 - 0.0033$, $D_F^{grt/melt} = 0.004 - 0.0123$, $D_F^{opx/melt} = 0.031 - 0.037$, up to $D_F^{cpx/melt} = 0.044 - 0.095$ (Beyer et al., 2012; Dalou et al., 2012; Hauri et al., 2006; Rosenthal et al., 2015). With respect to the high modal abundance of pyroxenes and olivine in the peridotitic mantle and oceanic lithosphere, these minerals act as major host and carrier for fluorine in the Earth. Some other studies suggest that typical fluorine bearing phases, e.g. humite-group minerals, phosphates, or serpentinites serve as potential fluorine host in subduction environments (Aoki et al., 1981; John et al., 2011; O'Reilly and Griffin, 2000; Wu and Koga, 2013).

Fluorine has a considerable effect on the liquidus temperature of basalts and supports the generation of silica-poor, alkali-rich magmas with wider implications for the generation of magmas on Earth and Mars (Filiberto et al., 2012; Luth, 1988).

Crépisson et al. (2014) found that F in the form of clumped OH/F defects in forsterite greatly enhance the water induced hydraulic weakening and propose that F and OH are closely related to each other. The authors suggest that similar defects may also be present in other NHFMs.

As part of the subducting slab this eclogite enters, along with the underlying harzburgitic oceanic lithosphere, the transition zone by convection (van der Hilst et al., 1991; van der

Hilst and Seno, 1993). Fluorine may be introduced and stored even into Earth's transition zone – similar to water (e.g. Maruyama and Okamoto, 2007). Furthermore, tomographic imaging proofed that some slabs stagnate between 400 and 1000 km depth (Fukao et al., 1992). It cannot be ruled out that very small degree partial melts form at the bottom of the upper mantle which would result in a fluorine enriched mantle reservoir. This may has implications for small degree partial melts on a regional scale and the frequently observed enriched fluorine concentration in ocean island basalts (OIBs) (Hofmann and White, 1982; Stracke et al., 2003) and in ultrapotassic rocks, i.e. lamproites (Aoki et al., 1981).

Up to now, no study has been conducted addressing the behavior of fluorine under high pressures (>4 GPa) and in an bimineralic eclogitic phase assemblage. Therefore, the present is aimed at the partitioning of fluorine between aluminous garnet, omphacitic clinopyroxene, and hydrous silicate melt in a basaltic system crystallized under upper mantle conditions between 4 and 6 GPa and 1460 to 1550 °C. These experiments are then used to estimate the fluorine budget of the subducted oceanic crust. Since oceanic crust is transformed to a clinopyroxene-rich lithology by the transformation to eclogite it can potentially host considerable amounts of fluorine.

7.2. Methods

Experiments have been conducted between 5 and 6 GPa in a 1000 tonne Kawai-type split sphere multi-anvil apparatus at the Bayerisches Geoinstitut Bayreuth, Germany. The description of the experimental setup and synthesis of the starting material have been described in chapter 4. An 18/11 octahedral assembly (18 mm length of the octahedron edge / 11 mm truncated corners of the tungsten carbide cubes) was used as a pressure medium for all experiments. The assembly was cast from Cr₂O₃-doped MgO. It was compressed with 32 mm edge length WC anvils. Experimental run conditions are listed in

Table 7.2.1. The starting material OC1/2 represents an average mid ocean-ridge basalt (MORB) (Table 7.2.1) to which water in terms of $\text{Al}(\text{OH})_3$ and fluorine in terms of CaF_2 have been added. The concentration of both volatile elements in the starting material was ~2 wt.%.

	Starting material		Experimental conditions				
	OC1/2 (20)	1 σ		P / GPa	T / °C	dur / h	SM
SiO ₂	46.53	0.09	H3483	6	1550	3	OC1/2
TiO ₂	1.0	0.1	H3522	5	1470	1	OC1/2
Al ₂ O ₃	15.0	0.1	H3601	5.4	1460	1 3/4	OC1/2
FeO**	8.76	0.07					
MnO	0.13	0.02					
MgO	8.18	0.07					
CaO	13.6	0.1					
Na ₂ O	2.46	0.07					
F*	2						
H ₂ O*	2						

P = pressure in GPa, T = temperature in °C, dur - run duration in hours, SM = starting materials used,*from initial weight; **total Fe as FeO

The starting material was filled into a graphite capsule with a tight fitting graphite lid. This inner capsule was then placed inside an outer platinum capsule (2.0 x 3.5 mm OD), which was welded shut on both sides with an arc-welder. Capsules were inserted at the center of the octahedral pressure assembly surrounded by an MgO sleeve, a stepped graphite heater, and a ZrO₂ insulation sleeve. Remaining cavities around the capsule were filled with dried MgO powder. The temperature was monitored using D-Type thermocouple (W₃Re-W₂₅Re) axially inserted inside a 4-hole alumina thermocouple tube, with the junctions in contact with the top of the sample capsule. A Re-disc was placed between the Pt-capsule and the thermocouple to prevent the soft capsule material from being indented by the thermocouple. No correction for a pressure effect on the thermocouple emf was applied. The experimental pressure was previously calibrated against the quartz – coesite, fayalite (Fe₂SiO₄) – ringwoodite, garnet / CaGeO₃ – perovskite, rutile – TiO₂ II, and coesite – stishovite phase transformations (Keppler and Frost 2005).

Experiments were pressurized for around 2 hours at room temperature. The run temperature was then raised at $\sim 150^\circ/\text{min}$ to approximately 50°C above the final run temperature. After keeping this temperature for 15 minutes, the sample was cooled to the desired run temperature. The final temperature was held for several hours. The superheating and slow cooling was designed to promote the growth of large homogeneous crystals with a reasonable size for further analytical procedures. The experiments were quenched by switching off the power to the furnace, which caused the temperature to drop $< 120^\circ\text{C}$ in a couple of seconds.

For the SHRIMP analyses samples have been mounted in a 1-inch epoxy mount and polished with a succession of diamond pastes with a grain size down to $\frac{1}{4}\ \mu\text{m}$.

7.3. Analytical methods

Run products were examined qualitatively using a Zeiss Gemini 1530 scanning electron microscope (SEM) equipped with a field emission gun and an energy-dispersive X-ray spectrometer (EDXS). Major element concentrations were determined with a 5-spectrometer JEOL JXA-8200 microprobe using an acceleration voltage of 15 kV and a 15 nA beam current. A detailed description of the reference materials and analytical method is given in chapter 3.3.1 and chapter 3.3.2. The SHRIMP measurements are briefly described in chapter 3.3.4.

7.4. Results

Mineral phases of all four run products (H3483, H3522, H3601) are very homogenous in chemical compositions and showed no evidence for zonations or inclusions (Fig. 7.4.1). All experiments contain garnet, clinopyroxene and quenched melt besides H3522 which crystallized no clinopyroxene. Garnets are basically consisting of 40 - 45 mole% pyrope

F partitioning between eclogitic garnet, clinopyroxene and melt at upper mantle conditions

($\text{Mg}_3\text{Al}_2\text{Si}_3\text{O}_{12}$), 22 - 24 mole% almandine ($\text{Fe}_3\text{Al}_2\text{Si}_3\text{O}_{12}$), and 32 - 34 mole% grossular ($\text{Ca}_3\text{Al}_2\text{Si}_3\text{O}_{12}$) and crystallized as euhedral crystals with diameters up to 500 μm . Clinopyroxene preferentially occupies the interstitials between the garnet grains, forming subhedral to euhedral crystals with sizes ranging from 10 to 120 μm . The clinopyroxene solid solutions are omphacitic and are mainly composed of ~ 27 - 36 mole% jadeite ($\text{NaAlSi}_2\text{O}_6$) and ~ 50 - 60 mole% diopside-hedenbergite ($\text{Ca}(\text{Mg,Fe})\text{Si}_2\text{O}_6$), with minor amounts of Ca-Tschermak (CaTs ; CaAlAlSiO_6) and enstatite-ferrosilite ($(\text{Mg,Fe})_2\text{Si}_2\text{O}_6$) compound.

The silicate melt is basaltic and solidified either as homogenous glass or as dendritic quench crystals close to the capsule rim. The chemical composition of each phase is shown in Table 7.4.1.

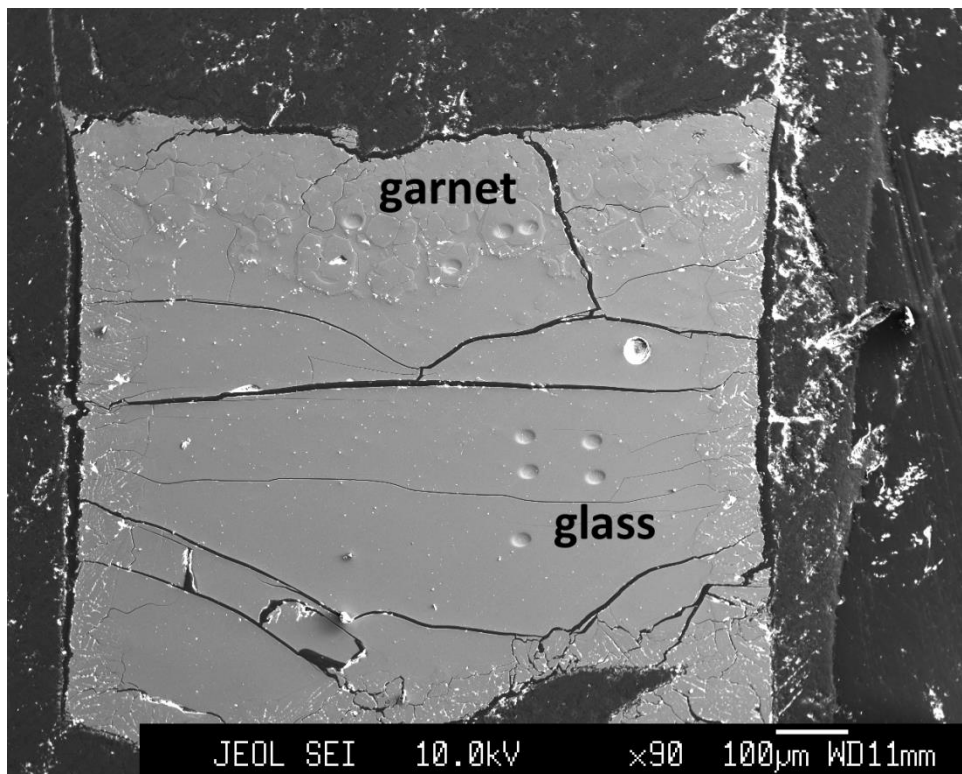


Fig. 7.4.1 SE image of run H3522 after SIMS measurement. The dark material is the graphite capsule. Cracks are from decompression.

F partition coefficients were calculated from runs H3483, H3522, and H3601. F is distributed homogeneously within each phase. The F concentration in garnet averages at 437 ± 71 $\mu\text{g/g}$, whereas, the fluorine concentration in clinopyroxene is significantly higher with an average of 1800 ± 165 $\mu\text{g/g}$. The melt contains between 2.1 and 3.3 wt.% F. The mineral/melt partition coefficient was determined using the concentrations of F in the mineral and the corresponding melt:

$$D_F^{mineral/melt} = \frac{c_F^{mineral}}{c_F^{melt}} \quad (7.1)$$

Very similar partition coefficients for garnet have been obtained in all experiments with $D_F^{grt/melt}$ between 0.015 ± 0.002 and 0.020 ± 0.002 . The partition coefficient between clinopyroxene and melt $D_F^{cpx/melt}$ is about four times higher with values of 0.057 ± 0.005 and 0.074 ± 0.001 . Based on the conducted experiments no partitioning trend with pressure or temperature for clinopyroxene has been observed but for garnet a slight decrease with pressure is recognized.

F partitioning between eclogitic garnet, clinopyroxene and melt at upper mantle conditions

7.4.1 Major element compositions

Garnet

	H3483		H3522		H3601	
n.o.a.	13	stdev	18	stdev	9	stdev
SiO ₂	40.6	0.5	40.9	0.4	40.7	0.3
TiO ₂	0.34	0.04	0.41	0.2	0.41	0.05
Al ₂ O ₃	22.1	0.2	21.9	0.6	22.2	0.1
FeO	11.6	0.2	9.7	0.3	10.7	0.2
MnO	0.24	0.02	0.22	0.03	0.23	0.03
MgO	11.7	0.2	13.1	0.7	12.2	0.4
CaO	12.1	0.2	11.8	0.8	12.6	0.4
Na ₂ O	0.29	0.04	0.25	0.06	0.16	0.02
total	98.9		98.3		99.2	

Clinopyroxene

	H3483		H3522		H3601	
n.o.a.	11	stdev		stdev	5	stdev
SiO ₂	53.4	0.2			51.9	0.7
TiO ₂	0.19	0.04			0.2	0.0
Al ₂ O ₃	13.8	0.2			11.9	0.1
FeO	4.4	0.1			4.5	0.1
MnO	0.06	0.03			0.1	0.1
MgO	8.7	0.1			10.3	0.1
CaO	12.8	0.2			16.0	0.6
Na ₂ O	5.4	0.2			3.8	0.1
total	98.8				98.8	

Glass

	H3483		H3522		H3601	
n.o.a.	10	stdev	10	stdev	10	stdev
SiO ₂	46.31	0.38	46.26	0.34	45.91	0.43
TiO ₂	1.54	0.07	1.14	0.04	1.17	0.04
Al ₂ O ₃	11.79	0.08	13.72	0.14	12.89	0.07
FeO	8.85	0.07	9.04	0.19	8.47	0.14
MnO	0.08	0.07	0.12	0.09	0.10	0.07
MgO	6.19	0.04	7.30	0.09	6.78	0.06
CaO	13.91	0.04	13.64	0.23	13.16	0.35
Na ₂ O	2.60	0.03	2.67	0.04	2.78	0.05
F	3.34	0.02	2.10	0.08	2.26	0.02
H ₂ O*	5.4		4.0		6.5	
total	100		100		100	

* H₂O by stoichiometric difference

H3522 does not contain cpx

7.5. Discussion

Fluorine partition coefficients $D_F^{cpx/melt} = 0.066 \pm 0.012$ (Table 7.5.1) for clinopyroxene are in good agreement with the D_s obtained by Hauri et al. (2006) $D_F^{cpx/melt} = 0.050 \pm 0.012$, and Rosenthal et al. (2015) $D_F^{cpx/melt} = 0.040 \pm 0.007$ and slightly smaller than the D_s from Dalou et al. (2012, 2014) $D_F^{cpx/melt} = 0.096 \pm 0.034$. Although the cpx of this study have clearly omphacitic compositions with high proportions of jadeite ($X_{jadeite} \sim 0.27 - 0.33$), the partition coefficients are very similar to the more diopside-hedenbergite dominated cpx of Dalou et al. (2012) and Hauri et al. (2006). Garnet partition coefficients with an average of $D_F^{grt/melt} = 0.017 \pm 0.002$ are similar to the single data point of Dalou et al. (2012) $D_F^{grt/melt} = 0.0123 \pm 0.0004$ and fall within the range of partition coefficients given by Hauri et al. (2006) $D_F^{grt/melt} = 0.0017 - 0.0174$ and Rosenthal et al. (2015) $D_F^{grt/melt} = 0.002 - 0.023$.

Table 7.5.1 F concentrations and partition coefficients

Run No.	Phase/D	F [$\mu\text{g/g}$]	stdev	n.o.a.
H3601	Grt	379	62	5
	Cpx	1683	24	5
	Glass*	22600	196	13
	$D_F^{grt/melt}$	0.017	0.003	
	$D_F^{cpx/melt}$	0.074	0.001	
H3522	Grt	417	46	4
	Glass*	21042	762	12
	$D_F^{grt/melt}$	0.020	0.002	
H3483	Grt	516	43	5
	Cpx	1916	170	6
	Glass*	33400	221	10
	$D_F^{grt/melt}$	0.015	0.002	
	$D_F^{cpx/melt}$	0.057	0.005	

* = glass analyses by EMPA

The garnet partitioning data obtained by Hauri et al. (2006) and Rosenthal et al. (2015) have to be seen more critically since the concentration of F in garnet is extremely low with $F < 4 \mu\text{g/g}$ respectively $< 1\mu\text{g/g}$. Very low concentration data are excluded due to their sensitivity to uncertainties in the measurement. The $D_F^{grt/melt}$ of Dalou et al. (2014) is one order of magnitude larger than all previously obtained partitioning coefficients. This outlier could have been produced due to micro fluid-inclusions. Overall, $D_F^{grt/melt}$ is virtually constant over a wide range of bulk compositions, pressures, and temperatures (Fig. 7.5.1a/b).

Accordingly, there is no distinct correlation of fluorine partitioning with garnet composition or pressure and temperature between the different studies. However, selecting the data from this study only, with a fixed bulk composition, a decrease with increasing pressure is apparent which is just outside of the uncertainties. The reason for this is unclear but results by Bernini et al. (2013) showed that F might be incorporated as defects of the hydrogarnet type, which increases the molar volume and may, therefore, be sensitive to pressure (Lager et al., 1987; Smyth et al., 1990).

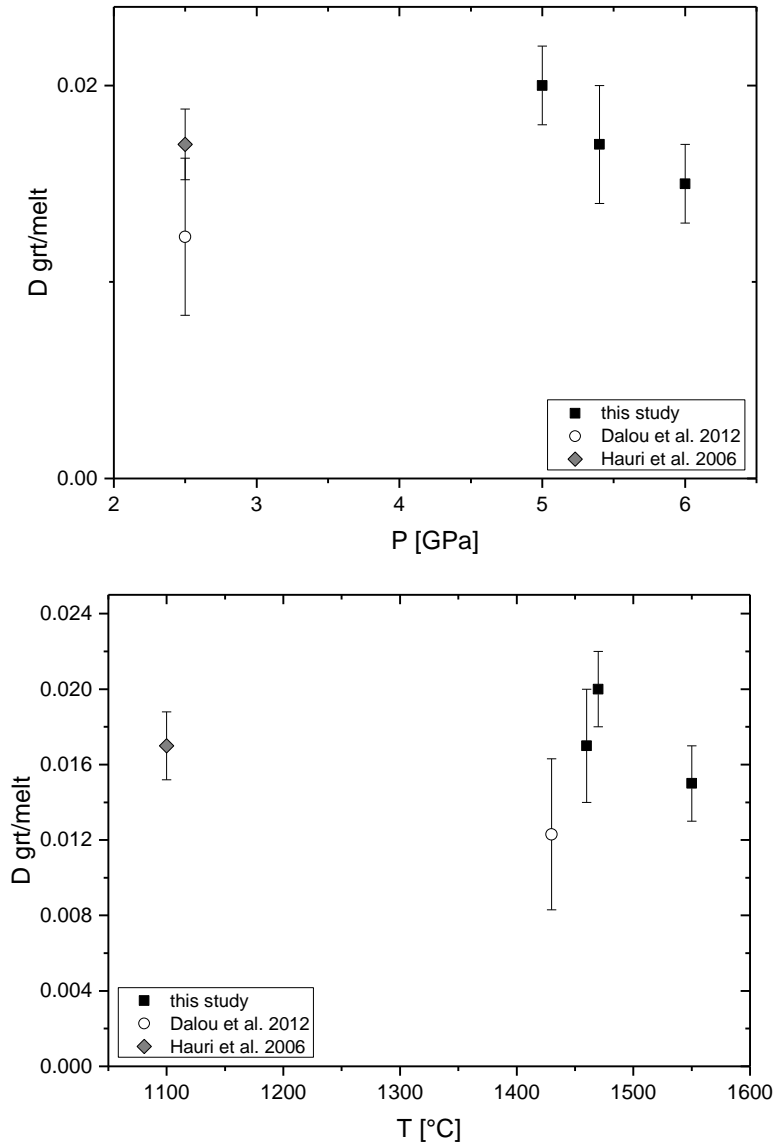


Fig. 7.5.1 a) $D_{\text{F grt}}$ against pressure. Within the data obtained in this study (black squares) there is a decrease with pressure noticeable. **b)** $D_{\text{F grt}}$ against temperature. Grt partitioning is constant over the observed temperature range. Errors are given as the 1 σ error as denoted in Table 7.5.1.

On the other hand the increase in F in garnet may be related to an increase in Na, which would relate F to an as yet unknown substitution involving the NaSi/Ti majoritic garnet component. However, the determination of the substitution process is beyond the scope of the available data.

The results can also be used to assess possible incorporation mechanisms of F into the pyroxene structure. Previous studies have observed a correlation between Al and F in orthopyroxene (Beyer et al. 2012). However, Mosenfelder and Rossman (2013b) showed in their measurements on natural samples that this may not always be the case. The authors

F partitioning between eclogitic garnet, clinopyroxene and melt at upper mantle conditions

found that F showed only a modest correlation within the augite group and that omphacites do not follow the same trend. Based on the clinopyroxene partitioning data, $D_F^{cpx/melt}$ increases slightly with $Al^{[IV]}$ and decreases with $Al^{[VI]}$ and Na (Fig. 7.5.2b/c). This would be in agreement with the observations of Mosenfelder and Rossman (2013b).

When applying this to the compositional change in clinopyroxene in eclogite with depth, the fluorine concentration should decrease with increasing pressure under the assumption that F is preferentially substituted similar to OH (Koch-Müller et al., 2004) on the O2 site with



where F is balanced by a trivalent cation on the tetrahedral site. Since this requires the presence of $Al^{[IV]}$, which is incorporated in terms of CaTs ($CaAlAlSiO_6$), this substitution mechanism is limited to ~ 200 km depth, after which the concentration of CaTs drops to very low levels (Beyer et al., 2015) for normally accepted adiabatic mantle temperatures. In Fig. 7.5.3a/b, however, it is shown that $D_F^{cpx/melt}$ remains relatively high at these conditions, while the proportion of CaTs is essentially zero. Therefore, another incorporation mechanism must be active to incorporate F into the structure at higher pressures. One possibility might be that F is balanced by the formation of vacancies on the M2-site, i.e. through formation of the Ca-Eskola ($Ca_{0.5}\square_{0.5}AlSi_2O_6$) component, which is similar to the mechanism proposed for OH incorporation in omphacite (Smyth et al., 1991).

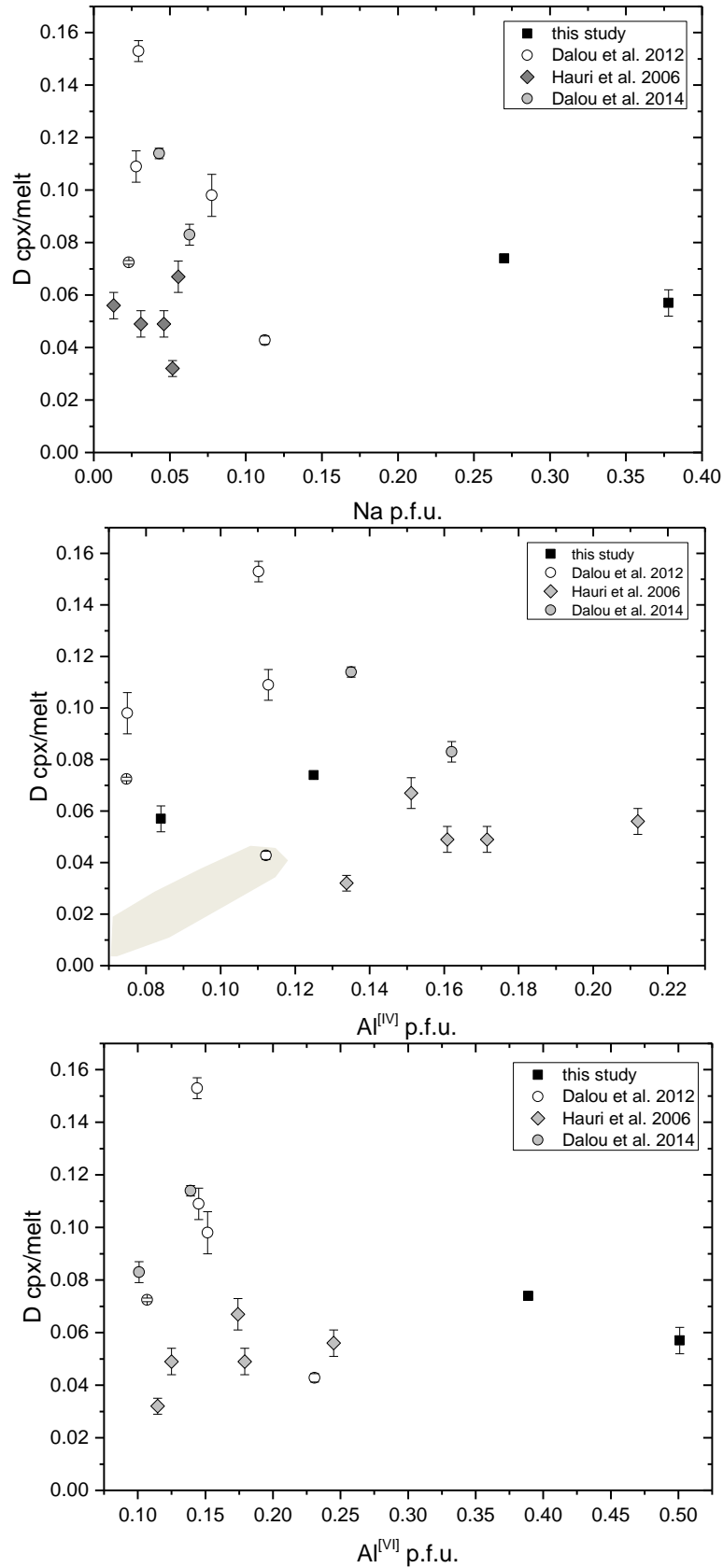


Fig. 7.5.2 a) D_F vs. Na in cpx **b)** D_F vs. octahedral Al in cpx. The grey area represents $\text{H}_2\text{O}/\text{melt}$ partitioning coefficients (Hauri et al. 2006) **c)** D_F vs. tetrahedral Al in cpx. No distinct correlation with the jadeite component is obvious. The partitioning is basically independent of the bulk mineral composition. Errors are given as the 1σ error as denoted in Table 7.5.1.

If vacancies would be the major substitution mechanism, clinopyroxenes from silica-undersaturated systems would be essentially F-free, however, because they contain no Ca-Eskola component. In these experiments run H3601 contains no Ca-Eskola whereas run H3483 contains 3.8 mole% Ca-Eskola and both experiments have very similar F-concentrations of $1693 \pm 24 \mu\text{g/g}$ respectively $1916 \pm 170 \mu\text{g/g}$. It is also possible that F is incorporated by the mechanism,



operating through the replacement of cations on the M2 octahedral site, as proposed by Mosenfelder and Rossman (2013b). If this is the case then F can likely reside in clinopyroxene to even greater depths. However, eventually cpx components in eclogitic and peridotitic rocks will become completely dissolved as majorite components in the garnet structure. Although the effect of majorite components on F incorporation are not known, a potential resulting drop in the bulk partition coefficient for F may result in its release from solid phases and the enrichment of overlying rocks. This could for example occur within subducting oceanic crustal rocks as they enter the Earth's transition zone. Upon release F may become dissolved in higher pressure minerals within the overlying ultramafic mantle such as superfluorous phase B (Hazen et al., 1997), ringwoodite, and wadsleyite (Roberge et al., 2013).

More generally speaking, when reviewing the existing partitioning data (Table 7.5.2, Fig. 7.5.2a-c) it would appear that $D_F^{cpx/melt}$ is apparently independent of variations in Al-bearing cpx endmembers, e.g. jadeite, Ca-Eskola, and Ca-Tschermaks. The OH partition coefficient on the other hand has quite a strong dependence of $\text{Al}^{[IV]}$ which is therefore in contrast to F, even though both anions are similar in many ways (Fig. 7.5.2b).

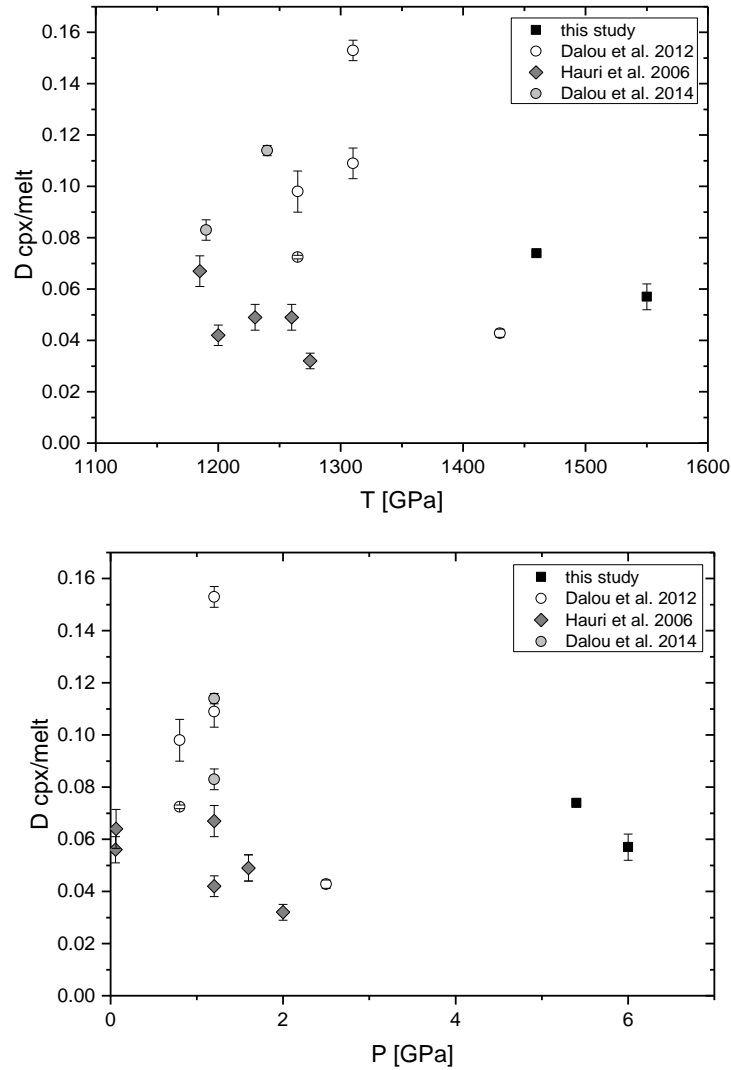


Fig. 7.5.3 a) D_F between cpx and glass vs. temperature **b)** D_F between cpx and glass vs. pressure. Cpx F-partitioning shows no systematic trends within the studied pressure/temperature range. Errors are given as the 1σ error as denoted in Table 7.5.1.

On the current sample basis a predominant incorporation mechanism cannot be identified. Either both mechanisms are simultaneously active or subsequently active which results in constant F partitioning coefficients over the analyzed range of conditions.

In a previous study it has been proposed that garnet contains basically no fluorine (Beyer et al., 2012). Recent measurements enable a correction of this assumption. Based on all available experimental data the relative partitioning of fluorine is $D_F^{cpx/melt} > D_F^{opx/melt} \gg D_F^{grt/melt} > D_F^{ol/melt}$ (Dalou et al. 2012), a relationship which stays constant over a large P-T interval as found in the Earth's upper mantle.

F partitioning between eclogitic garnet, clinopyroxene and melt at upper mantle conditions

Table 7.5.2 Compilation of fluorine partitioning data in nominally fluorine-free mantle silicates

Run#	D _F	1σ	P [GPa]	T [°C]	coexisting phases	chemical system	reference
Olivine							
NAF4-9	0.0014	3	0.001	1380	fo,gl	CMAS	Beyer et al. 2012
PC555	0.0015	1	1	1400	fo,gl	CMAS	Beyer et al. 2012
PC563	0.0033	12	1	1345	fo,opx,gl	NCMAS	Beyer et al. 2012
PC566	0.0007	7	1	1285	ol,cpx,gl	natural ankamaritic basalt	Beyer et al. 2012
CC01#8kb4	0.116	6	0.8	1265	ol,opx,cpx,plag,gl	70% basalt-30% peridotite	Dalou et al. 2012
B330	0.0031	5	1.2	1200	ol,cpx,gl	hydrous peridotite	Hauri et al. 2006
B333	0.003	n.a.	1.2	1245	ol,opx,gl	hydrous peridotite	Hauri et al. 2006
B359	0.0018	3	1.6	1260	ol,opx,cpx,gl	hydrous peridotite	Hauri et al. 2006
B366	0.0024	5	1.6	1230	ol,opx,cpx,grt,gl	hydrous peridotite	Hauri et al. 2006
B384	0.0015	2	1.2	1200	ol,opx,gl	hydrous peridotite	Hauri et al. 2006
B388	0.0028	5	1.2	1200	ol,opx,gl	hydrous peridotite	Hauri et al. 2006
B408	0.0019	n.a.	1.6	1370	ol,opx,gl	hydrous peridotite	Hauri et al. 2006
B432	0.0047	n.a.	1.2	1185	ol,opx,cpx,gl	hydrous peridotite	Hauri et al. 2006
1450	0.0021	2	0.5	1025	ol,cpx,gl	basanite	Hauri et al. 2006
CD2H3	0.002	0.1	1.2	1240	ol,cpx,opx,gl	hydrous basalt	Dalou et al. 2014
Orthopyroxene							
PC554	0.037	1	2	1410	opx,sp,gl	CMAS	Beyer et a. 2012
PC561	0.034	4	1.7	1425	opx,sp,gl	CMAS	Beyer et a. 2012
PC562	0.036	1	2.5	1445	opx,sp,gl	CMAS	Beyer et a. 2012
PC563	0.031	5	1	1345	fo,opx,gl	NCMAS	Beyer et a. 2012
F2p#2a	0.043	3	1.2	1360	ol,opx,gl	70% basalt-30% peridotite	Dalou et al. 2012
F4p#3a	0.0557	5	1.2	1360	opx,gl	70% basalt-30% peridotite	Dalou et al. 2012
F1#3b	0.0465	3	1.2	1360	opx,gl	70% basalt-30% peridotite	Dalou et al. 2012
F5#3b	0.050	3	1.2	1360	opx,gl	70% basalt-30% peridotite	Dalou et al. 2012
C8p#2b	0.050	3	1.2	1360	opx,ol,opx	70% basalt-30% peridotite	Dalou et al. 2012
CC01#8kb4	0.184	9	0.8	1265	ol,opx,cpx,plag,gl	70% basalt-30% peridotite	Dalou et al. 2012
CF1#8kb5	0.085	1	0.8	1265	ol,opx,cpx,gl	70% basalt-30% peridotite	Dalou et al. 2012
CC4#7b	0.123	4	1.2	1310	opx,cpx,gl	70% basalt-30% peridotite	Dalou et al. 2012
CF5#7c	0.088	6	1.2	1310	opx,cpx,gl	70% basalt-30% peridotite	Dalou et al. 2012
CF01#16kb1	0.098	7	1.6	1350	opx,cpx,gl	70% basalt-30% peridotite	Dalou et al. 2012
C4p#25kb	0.016	1	2.5	1430	opx,cpx,grt,gl	70% basalt-30% peridotite	Dalou et al. 2012
B451	0.026	5	1.2	1325	opx,gl	carbonated olivine tholeiite	Rosenthal et al. 2015
B452	0.030	5	1.5	1365	opx,gl	carbonated olivine tholeiite	Rosenthal et al. 2015
B396	0.028	3	1.5	1400	opx,gl	carbonated olivine tholeiite	Rosenthal et al. 2015
B398	0.020	5	1.5	1400	opx,gl	carbonated olivine tholeiite	Rosenthal et al. 2015
B453	0.025	2	1.7	1365	opx,gl	carbonated olivine tholeiite	Rosenthal et al. 2015
A965	0.036	5	2	1375	opx,gl	carbonated olivine tholeiite	Rosenthal et al. 2015
A859	0.038	3	2.2	1400	opx,cpx,gl	carbonated olivine tholeiite	Rosenthal et al. 2015
A957	0.035	3	2.5	1450	opx,gl	carbonated olivine tholeiite	Rosenthal et al. 2015
A898	0.029	4	3	1400	opx,grt,gl	carbonated olivine tholeiite	Rosenthal et al. 2015
A955	0.024	2	3	1500	opx,cpx,grt,gl	carbonated olivine tholeiite	Rosenthal et al. 2015

F partitioning between eclogitic garnet, clinopyroxene and melt at upper mantle conditions

Table 7.5.2 (continued)

Run#	D _F	1σ	P [GPa]	T [°C]	coexisting phases	chemical system	reference
A971	0.029	8	0.8	1230	ol,ox,gl	carbonated olivine tholeiite	Rosenthal et al. 2015
B479	0.029	3	0.8	1250	ol,opx,gl	carbonated olivine tholeiite	Rosenthal et al. 2015
A969	0.029	8	1	1300	ol-incl.,opx,gl	carbonated olivine tholeiite	Rosenthal et al. 2015
B467	0.026	5	1.2	1300	opx,cpx,gl	carbonated olivine tholeiite	Rosenthal et al. 2015
A972	0.022	2	1.5	1320	opx,cpx,gl	carbonated olivine tholeiite	Rosenthal et al. 2015
B478	0.020	2	2.5	1400	opx,cpx,gl	carbonated olivine tholeiite	Rosenthal et al. 2015
B480	0.028	4	2.8	1430	opx,gl	carbonated olivine tholeiite	Rosenthal et al. 2015
A974	0.030	n.a.	3	1430	opx,cpx,gl	carbonated olivine tholeiite	Rosenthal et al. 2015
A1006	0.032	2	0.8	1250	opx,gl	carbonated olivine tholeiite	Rosenthal et al. 2015
B501	0.034	2	1	1320	opx,gl	carbonated olivine tholeiite	Rosenthal et al. 2015
A1002	0.029	3	1.5	1320	opx,gl	carbonated olivine tholeiite	Rosenthal et al. 2015
A1005	0.016	n.a.	2	1350	opx,gl	carbonated olivine tholeiite	Rosenthal et al. 2015
A1003	0.0186	n.a.	2.5	1400	opx,cpx,gl	carbonated olivine tholeiite	Rosenthal et al. 2015
A1001	0.025	1	3	1400	opx,cpx,gl	carbonated olivine tholeiite	Rosenthal et al. 2015
B333	0.025	2	1.2	1245		hydrous peridotite	Hauri et al. 2006
B359	0.025	1	1.6	1260		hydrous peridotite	Hauri et al. 2006
B366	0.030	3	1.6	1230		hydrous peridotite	Hauri et al. 2006
B384	0.015	10	1.2	1200		hydrous peridotite	Hauri et al. 2006
B388	0.019	3	1.2	1200		hydrous peridotite	Hauri et al. 2006
B399	0.017	1	2	1275		hydrous peridotite	Hauri et al. 2006
B408	0.022	3	1.2	1200		hydrous peridotite	Hauri et al. 2006
B432	0.033	2	1.2	1185		hydrous peridotite	Hauri et al. 2006
1799	0.045	11	2	1080		hydrous peridotite	Hauri et al. 2006
1802	0.042	13	2	1080		hydrous tholeiite	Hauri et al. 2006
CD2H3	0.0560	3	1.2	1240	ol,cpx,opx,gl	hydrous basalt	Dalou et al. 2014
CD2H5	0.042	4	1.2	1190	opx,cpx,gl	hydrous basalt	Dalou et al. 2014
CD2H6	0.021	31	1.2	1200	opx,amph,gl	hydrous basalt	Dalou et al. 2014
Clinopyroxene							
H3601	0.074	1	5.4	1460	grt,cpx,gl	eclogite	this study
H3483	0.057	5	6	1550	grt,cpx,gl	eclogite	this study
CC01#8kb4	0.098	8	0.8	1265	ol,opx,cpx,plag,gl	70%basalt-30%peridotite	Dalou et al. 2012
CF1#8kb5	0.0725	7	0.8	1265	ol,opx,cpx,gl	70%basalt-30%peridotite	Dalou et al. 2012
CC4#7b	0.153	4	1.2	1310	opx,cpx,gl	70%basalt-30%peridotite	Dalou et al. 2012
CF5#7c	0.109	6	1.2	1310	opx,cpx,gl	70%basalt-30%peridotite	Dalou et al. 2012
C4p#25kb	0.043	2	2.5	1430	opx,cpx,grt,gl	70%basalt-30%peridotite	Dalou et al. 2012
A859	0.052	3	2.2	1400	opx,cpx,gl	carbonated olivine tholeiite	Rosenthal et al. 2015
A955	0.029	3	3	1500	opx,cpx,grt,gl	carbonated olivine tholeiite	Rosenthal et al. 2015
B467	0.05	1	1.2	1300	opx,cpx,gl	carbonated olivine tholeiite	Rosenthal et al. 2015
A972	0.042	n.a.	1.5	1320	opx,cpx,gl	carbonated olivine tholeiite	Rosenthal et al. 2015
B478	0.037	2	2.5	1400	opx,cpx,gl	carbonated olivine tholeiite	Rosenthal et al. 2015
A970	0.034	7	3	1460	cpx,grt,gl	carbonated olivine tholeiite	Rosenthal et al. 2015
A974	0.042	5	3	1430	opx,cpx,gl	carbonated olivine tholeiite	Rosenthal et al. 2015

F partitioning between eclogitic garnet, clinopyroxene and melt at upper mantle conditions

Table 7.5.2 (continued)

Run#	D_F	1σ	P [GPa]	T [°C]	coexisting phases	chemical system	run#	reference
A1001	0.038	2	3	1400	opx,cpx,gl	carbonated olivine tholeiite	Rosenthal et al. 2015	
A1003	0.035	7	2.5	1400	opx,cpx,gl	carbonated olivine tholeiite	Rosenthal et al. 2015	
B330	0.042	4	1.2	1200	ol,cpx,gl	hydrous peridotite	Hauri et al. 2006	
B359	0.049	5	1.6	1260	ol,opx,cpx,gl	hydrous peridotite	Hauri et al. 2006	
B366	0.049	5	1.6	1230	ol,opx,cpx,grt,gl	hydrous peridotite	Hauri et al. 2006	
B399	0.032	3	2	1275	opx,cpx,grt,gl	hydrous peridotite	Hauri et al. 2006	
B432	0.067	6	1.2	1185	ol,opx,cpx,gl	hydrous peridotite	Hauri et al. 2006	
1446	0.044	9	1.5	1050	cpx,amph,mica,gl	basanite	Hauri et al. 2006	
1450	0.064	7	0.5	1025	ol,cpx,gl	basanite	Hauri et al. 2006	
1802	0.056	5	2	1080	opx,cpx,gl	hydrous tholeiite	Hauri et al. 2006	
1833	0.014	2	4	1100	cpx,gl	hydrous peridotite	Hauri et al. 2006	
CD2H3	0.114	2	1.2	1240	ol,cpx,opx,gl	hydrous basalt	Dalou et al. 2014	
CD2H5	0.083	4	1.2	1190	opx,cpx,gl	hydrous basalt	Dalou et al. 2014	
Garnet								
H3601	0.017	3	5.4	1460	grt,cpx,gl	eclogite	this study	
H3522	0.020	2	5	1470	grt,gl	eclogite	this study	
H3483	0.015	2	6	1550	grt,cpx,gl	eclogite	this study	
C4p#25kb	0.0123	4	2.5	1430	opx,cpx,grt,gl	70%basalt-30%peridotite	Dalou et al. 2012	
A898	0.0047	5	3	1400	opx,grt,gl	carbonated olivine tholeiite	Rosenthal et al. 2015	
A955	0.0023	5	3	1500	opx,cpx,grt,gl	carbonated olivine tholeiite	Rosenthal et al. 2015	
A970	0.002	1	3	1460	cpx,grt,gl	carbonated olivine tholeiite	Rosenthal et al. 2015	
B366	0.0020	3	1.6	1230	ol,opx,cpx,grt,gl	hydrous peridotite	Hauri et al. 2006	
B399	0.0017	2	2	1275	opx,cpx,grt,gl	hydrous peridotite	Hauri et al. 2006	
1795	0.0039	3	3	1180	grt,gl	hydrous peridotite	Hauri et al. 2006	
1842	0.017	2	2.5	1100	grt,gl	hydrous peridotite	Hauri et al. 2006	
CD2-2.5GPa	0.166	2	2.5	1370	grt,cpx,opx,gl	hydrous basalt	Dalou et al. 2014	
Plagioclase								
CC01#8kb4	0.098	4	0.8	1265	ol,opx,cpx,plag,gl	70%basalt-30%peridotite	Dalou et al. 2012	

ol = olivine, opx = orthopyroxene, cpx = clinopyroxene, grt = garnet, plag = plagioclase, gl = glass/melt, amph = amphibole, n.a. = standard deviation not available

1σ = one standard deviation in terms of last digit

7.6. Geological implications

Clinopyroxene has a significantly higher partition coefficient than other minerals, which will affect the bulk partition coefficient for F in cpx dominated lithologies, e.g. in subducted oceanic crust. Nevertheless, given the fact that the major volume fraction of subducted slabs is represented by depleted peridotite and harzburgite, which basically consist of olivine and orthopyroxene, the bulk partition coefficient of oceanic slabs will

F partitioning between eclogitic garnet, clinopyroxene and melt at upper mantle conditions

remain constant even if subducted oceanic crust is strongly dominated by eclogitic part only.

John et al. (2011) showed that F resides in the altered harzburgitic lithosphere and is not liberated during serpentinization. Instead F is recycled into the mantle. Based on the analyses of basalts from Iceland Sigvaldason and Oskarsson (1986) found that these basalts contain several hundred $\mu\text{g/g}$ F. From this observation questions arise on the fate of F when it is not released by volatilization or melting processes in the uppermost mantle during descent into the deeper mantle and not returned entirely by ascending OIB plumes and MORBs. Several scenarios which may explain the role of fluorine in the deeper upper mantle are proposed.

The first scenario is that structurally bound fluorine in olivine, orthopyroxene, clinopyroxene, and garnet is ultimately incorporated into phases with a higher F-affinity in the transition zone (e.g. wadsleyite, ringwoodite, hydrous phase B). This would lead to an enrichment of F in the transition zone up to, as yet, undetermined saturation limits of these candidate minerals and until a steady-state is reached. This process would be analogous to the water cycle in the mantle, making the transition zone an efficient fluorine trap. If OIB plumes or kimberlites penetrate through the transition zone and form small degree partial melts, this would explain the enriched F concentration in comparison to F estimates on the MORB source.

The second scenario suggests that F is not effectively incorporated into transition zone minerals and is rather released during solid state phase transformation causing an accumulation of F in the lowermost upper mantle and on top of the transition zone which could trigger small degree partial melting by depressing the liquidus if the concentration,

potentially, in association with other volatiles such as H₂O and CO₂, reaches a certain threshold value.

An intriguing piece of evidence that might help to test these hypotheses is that ultrapotassic lamproites, which have been proposed in some studies to originate from the Earth's transition zone or lower mantle (Murphy et al., 2002), contain very high amounts of fluorine with concentrations of up to 2 wt.% (Aoki et al., 1981) and high F/H₂O ratios (i.e. Mitchell, 1995). In previous studies it has been shown that F has compatible partition coefficients greater than one, in the presence of i.e. K-hollandite, apatite, and phlogopite, therefore a melt generated from a source rock containing these phases is not sufficient to explain the high F-concentrations in lamproites (Edgar and Charbonneau, 1991). If it is assumed that the source mainly contains nominally fluorine-free minerals (NFFMs), in which F is incompatible, than the corresponding small degree partial melting could significantly contribute to the high F-concentrations in ultrapotassic rocks.

An indicator of a fluorine enriched region in the deeper upper mantle is the presences of ultrapotassic lithologies. Foley (1992) argued that a hybrid source consisting of a certain amount of alkali-enriched veins and peridotitic wall rock can form these ultrapotassic lithologies. F enriched NFFMs, in particular cpx, could significantly contribute to the bulk F-concentration in heterogeneous sources, increasing the stability of later produced F-rich phlogopite to greater depth. The approach discussed in the next paragraph may help to test this hypothesis.

Using partition coefficients of F in combination with those for H₂O, i.e. Hauri et al. (2006) is a useful way to examine the origin of the high F/H₂O ratio in lamproitic rocks. To trace the evolution of the F/H₂O ratios, a modal eclogite with a 60:40 assemblage of clinopyroxene and garnet has been assumed. $D(F) = 0.055$ was based on the data presented

in this study and $D(\text{H}_2\text{O}) = 0.014$ was based on the H_2O partitioning measurements of Hauri et al. (2006). The ratios were kept constant regardless of potential P and T effects. This a reasonable assumption based on experimental data that D_F and $D_{\text{H}_2\text{O}}$ are basically constant in clinopyroxene and garnet, showing only a mild decrease with pressure for H_2O in clinopyroxene (Hauri et al., 2006).

Initial H_2O of $574 \mu\text{g/g}$ is based on the measurements of H_2O contents of natural eclogitic mantle xenoliths (Katayama et al., 2006), whereas the initial F-content had to be inferred from previous calculations in Beyer et al. (2012), thus $\sim 12 \mu\text{g/g}$ F is assumed. The starting F/ H_2O ratio is then 0.02 for the 60:40 grt-cpx assemblage.

Small degree partial melting of $f = 1 - 2 \%$ produces F/ H_2O ratios of 0.03 to 0.04. To obtain F/ H_2O ratios within the range of assumed F/ H_2O ratios in lamproitic source lithologies, 0.07 - 0.56 (Edgar et al., 1992; Edgar and Vukadinovic, 1993) to 0.92 (Mitchell, 1995), multiple episodes of small degree partial melting are required (Fig. 7.6.1).

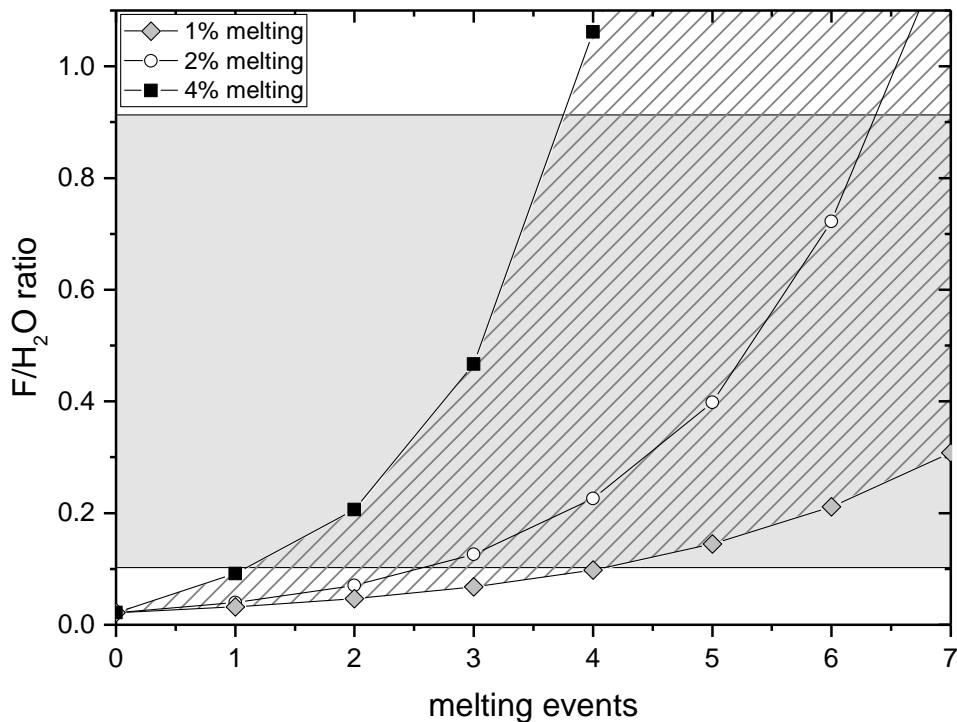


Fig. 7.6.1 The effect of small degree partial melting on the evolution of the F/ H_2O ratio. The grey area represents lamproitic F/ H_2O ratios.

For example, the first iteration of 2 % melting produces a F/H₂O ratio of 0.04, the second iteration increases the ratio to 0.07, the third iteration increases the ratio to 0.12. To reach F/H₂O ratios as suggested by Mitchell (1995) requires at least six events of small degree partial melting. Accordingly, remnants of subducted oceanic crust exposed to several events of small degree partial melting, present as heterogeneous fragments within the peridotitic mantle, could have been incorporated into the source of lamproitic source magmas. This would be compatible with the vein-plus-wall-rock hypothesis of Foley (1992) to explain the elevated F/H₂O ratios and does not need to invoke F-bearing phases in the source. The outlined process is illustrated in Fig. 7.6.2.

In a more K-rich bulk rock it can be speculated, that F is probably associated to K-rich clinopyroxene which occurs at pressures above 5 GPa as found in the Smoky Butte lamproite (Edgar and Vukadinovic, 1993). This would explain a correlation of F with K₂O without the need to invoke phlogopite. Experiments on high pressure phase relations in a K-rich system demonstrate that SiO₂-rich lamproite magmas could be primary partial melts from the deeper mantle (Edgar and Mitchell, 1997). Hence, the results of this study suggest, that besides being a dominant K-bearing phase in the deeper mantle (Edgar and Vukadinovic, 1993), cpx could be also an important reservoir for F.

Aoki et al. (1981) found that F in kimberlites from South Africa is not correlated with K₂O. Accordingly, F is not directly associated to any K-bearing phase, e.g. micas and amphiboles and could be derived from melting of cpx dominated material where cpx is the liquidus phase, subsequently, enriching the produced melt in F. Another explanation for the high F in kimberlites would be F-apatite (Aoki et al., 1981). However, it is debatable whether accessory amounts of F-apatite are sufficient to supply the majority of F in kimberlitic magmas.

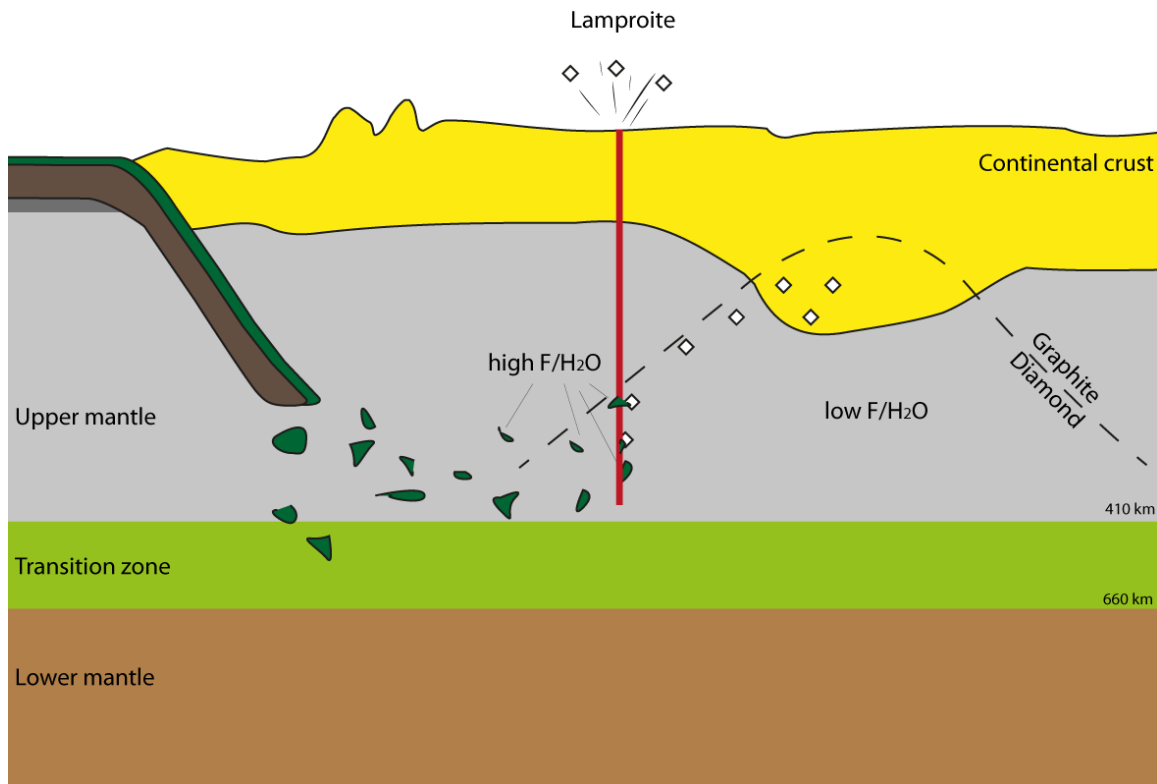


Fig. 7.6.2 Schematic of a potential incorporation of partially molten fragments of subducted oceanic crust into ascending lamproitic magmas.

Future studies should focus on the partitioning of fluorine into nominally halogen-free high pressures mantle phases, e.g. majorite, bridgmanite, and high pressure hydrous phases to understand the fate of F in the deeper Earth. In order to shed light on the role of clinopyroxenes as F-hosts in ultrapotassic lithologies, experiments at high pressures in a potassic system are required. Along with these experimental studies it is important to obtain halogen concentrations of rocks from a large variety of tectonic settings to get a more comprehensive idea of where halogens reside in the Earth and what their role in the formation of ultrapotassic magmas is. Moreover, the interplay between F and H₂O needs intensive work, because the F/H₂O ratio has a strong influence on the stability of phlogopite in the upper mantle (Foley et al., 1986).

8. Final conclusions and outlook

During the course of this thesis a thermodynamically self-consistent geobarometer for eclogites has been presented, solely based on garnet and clinopyroxene. The barometer relies on the incorporation of tetrahedrally coordinated aluminum in clinopyroxene coexisting with garnet using high pressure experiments between pressures of 3 to 7 GPa and temperatures from 1200 to 1550 °C. Careful chemical analyses along with well equilibrated experimental charges were the key aspect to set up the barometer. The model reproduces the data within analytical uncertainties despite using simplified interaction parameters. This geobarometer is applicable to eclogites equilibrated under normal or reducing conditions. Future work could focus on mixing on the octahedral to take into account the effect of ferric iron in oxidized systems. Therefore experiments with varying oxygen fugacities under controlled conditions have to be conducted to obtain pressures of last equilibration for highly oxidized lithologies.

To extend the barometer to transition zone depths, another geobarometer has been formulated that accounts for the various pressure-dependent majorite substitution mechanisms. In the subsequent chapter an empirical geobarometer for majoritic garnets based on a large set of experimental high-pressure data has been calibrated. The barometer is applicable to eclogitic and peridotitic majoritic inclusions in diamonds from the lowermost upper mantle and the transition zone. The barometer is in general agreement with the C10 barometer, but yields a higher precision and accuracy on eclogitic compositions. Moreover, the barometer of this study accounts for the secondary effect of chromium on the stability of Mj-majorite which improves the reproduction of pressures from natural high-Cr majoritic inclusions. The application of the barometer to a large set of inclusions in diamonds proves that carbonaceous fluids are present at transition zone depth

triggering the precipitation of diamonds from eclogites. Accordingly, the calculated pressures are a strong argument supporting previous findings of Stagno et al. (2013, 2015) on the formation of diamonds within different mantle lithologies.

In order to develop a standardized internally consistent pressure determination for the majority of phase assemblages in the Earth's upper mantle and transition zone a cross calibration of the barometers obtained within this study and existing barometers (i.e. grt-opx, Brey and Köhler, 1990) is extremely useful. The existing geobarometers for eclogitic and peridotitic rocks have been all calibrated against *ex-situ* calibrants using known mineral reaction boundaries, i.e. quartz-coesite and fayalite-ringwoodite and relying on the reproducibility between sample pressure and multi-anvil oil pressure. This is intrinsically unreliable and differences in the pressure calibrations between different laboratories potentially biased the obtained geobarometric calibrations. No *in-situ* pressure calibrations have been used for high pressure barometer equilibria in the past and hence there is great disparity between them. To date *in-situ* pressure determinations of this transformation are lacking. By equilibrating a series of geobarometer equilibria while simultaneously measuring pressure using *in situ* methods these barometers can be independently tested and the different geobarometers compared.

The third project dealt with the effect of composition on elasticity of aluminous garnet solid solutions. SC-XRD on room pressure static compression experiments in the DAC showed that K_{T0} is very similar for eclogitic garnets and chemical effects cannot be resolved within the given analytical uncertainties. A slight variation of K'_{T0} was observable as a function of grossular content. Nevertheless, K'_{T0} for aluminous garnet solid solution is $K'_{T0} \sim 4$. The almandine rich specimen has the highest bulk modulus among aluminous garnet and has a strong effect on the solid solution's bulk modulus. High P/T experiments

showed that almandine has a strong effect on the softening with temperature under upper mantle conditions. By accounting for almandine within mantle compositions, these results may improve the interpretation of seismic profiles of the Earth's upper mantle. Recalculating experimental data with the model of Stixrude and Lithgow-Bertelloni (2011) showed that excess volumes play an important role reproducing elastic properties of complex solid solution. Neglecting these non-ideal contributions leads to a misinterpretation of the Earth's density profiles obtained by seismic measurements. In order to set-up a thermodynamic description based on interaction terms describing the excess-volumes, experiments covering a wider range of compositions have to be performed. Performing precise high-temperature experiments at conditions of the upper mantle is challenging in the DAC, therefore taking advantage of high-brilliant synchrotron beamlines might improve the quality of the data. These new data may greatly enhance the understanding of temperature effects on excess-volumes of garnet solid solutions. Upon revision, these data enhance the interpretation of the elasticity of garnet-bearing facies in the deeper Earth's mantle.

Clinopyroxene is also a major rock forming mineral within mafic compositions of the Earth's upper mantle, it is very important to study non-ideal elastic mixing properties of complex clinopyroxenes, too. This task is challenging because clinopyroxene forms even more extensive solid solution, incorporating vacancies (Ca-Eskola) and monovalent cations (Li, Na, K). In comparison to garnet, clinopyroxene is monoclinic and highly anisotropic in terms of compressibility, which makes an accurate determination of the compressibility even more complicated.

In the last project the first high-pressure fluorine mineral-melt partitioning data of garnet and clinopyroxene have been obtained. Neither garnet nor clinopyroxene show distinct

variations in partitioning within the investigated pressure and temperature range. The results suggest that clinopyroxene is the major host for fluorine in Earth's upper mantle and is able to transport fluorine to greater depth, where the clinopyroxene dominated subducted oceanic crust might be exposed to small degree partial melting. These melting events could be responsible for an increase of the F/H₂O ratio of the residual material. If the residuum is incorporated into the source of ultrapotassic rocks (i.e. lamproites) they might be the reason for the increased F/H₂O ratio of these rocks. Experiments within ultrapotassic compositions focused on the F-concentrations in NFFMs might help to confine the proposed mechanism. To improve the interpretations, more high pressure experiments are required to investigate potential effects of F on partial melting under conditions where ultrapotassic magmas might originate.

Appendix 1 Results of microprobe analyses. Numbers in parentheses are number of analyses per sample.

Sample:	A571	H3543	H3540	H3639	H3483	H3602	H3510	H3605x
Conditions (P[GPa]/T [°C])	3/1430	4/1460	6/1480	5/1445	56/1549	6/1518	6/1380	7/1480
Garnet	(10)	(9)	(17)	(23)	(13)	(6)	(11)	(20)
SiO ₂	40.0 (2)	39.9 (3)	40.0 (3)	41.1 (2)	40.6 (5)	40.5 (3)	39.7 (6)	40.1 (2)
TiO ₂	0.4 (1)	0.45 (4)	0.4 (1)	0.35 (8)	0.34 (4)	0.52 (9)	0.6 (1)	0.52 (7)
Al ₂ O ₃	22.3 (3)	21.8 (2)	21.4 (3)	22.9 (3)	22.1 (2)	21.5 (2)	21.0 (2)	21.6 (1)
FeO*	11.3 (6)	14.2 (4)	12.2 (4)	9.2 (9)	11.6 (2)	13.4 (5)	14.3 (3)	14.1 (2)
MgO	12.8 (2)	10.7 (3)	11.0 (5)	12.8 (6)	11.7 (2)	10.4 (7)	9.6 (2)	9.9 (2)
MnO	0.29 (4)	0.19 (3)	0.25 (3)	0.28 (3)	0.24 (2)	0.26 (2)	0.25 (3)	0.25 (3)
CaO	11.0 (8)	10.8 (2)	12.7 (4)	13.0 (5)	12.1 (2)	11.8 (6)	12.3 (2)	12.0 (2)
Na ₂ O	0.12 (2)	0.17 (2)	0.28 (3)	0.20 (3)	0.29 (4)	0.27 (3)	0.28 (3)	0.29 (4)
IrO ₂ **	0.2 (2)	0.2 (2)	0.2 (2)	0.1 (2)	0.1 (1)	n.m.	0.2 (2)	0.2 (2)
total	98.6	98.3	98.4	99.9	99.0	98.5	98.1	98.9
Cations per 12 oxygens								
Si	2.977	3.008	3.020	2.995	3.013	3.042	3.025	3.017
Ti	0.023	0.026	0.020	0.019	0.019	0.029	0.034	0.029
Al	1.961	1.936	1.909	1.968	1.934	1.901	1.879	1.919
Fe	0.668	0.849	0.731	0.532	0.585	0.795	0.861	0.839
Mg	1.421	1.207	1.237	1.396	1.293	1.163	1.089	1.111
Mn	0.018	0.012	0.016	0.017	0.015	0.017	0.016	0.016
Ca	0.881	0.872	1.024	1.013	0.966	0.046	0.999	0.968
Na	0.017	0.025	0.041	0.028	0.042	0.039	0.047	0.042
Cation sum	7.961	7.931	7.998	7.966	7.962	7.931	7.947	7.939
Clinopyroxene								
	(8) core	(12)	(16)	(25)	(11)	(8)	(6)	(21)
SiO ₂	49.0 (8)	51.8 (3)	53.9 (3)	53.8 (7)	53.4 (2)	53.7 (5)	54.5 (6)	54.9 (2)
TiO ₂	0.37 (7)	0.36 (8)	0.16 (3)	0.23 (7)	0.19 (4)	0.5 (4)	0.35 (4)	0.30 (4)
Al ₂ O ₃	13 (1)	13.5 (3)	12.4 (2)	12.8 (6)	13.8 (2)	12.7 (4)	12.9 (1)	12.8 (2)
FeO	5.3 (1)	5.9 (2)	4.6 (1)	3.4 (5)	4.4 (1)	5.1 (4)	5.0 (2)	5.0 (1)
MgO	10.8 (4)	8.8 (3)	8.7 (2)	9.9 (6)	8.7 (1)	8.2 (7)	8.2 (1)	8.2 (1)
MnO	0.10 (1)	0.07 (3)	0.05 (2)	0.06 (3)	0.06 (3)	0.05 (1)	0.06 (2)	0.06 (2)
CaO	17.3 (3)	14.4 (2)	13.0 (2)	15.0 (3)	12.8 (1)	13.2 (3)	12.9 (1)	12.8 (2)
Na ₂ O	2.45 (9)	3.9 (1)	5.6 (1)	4.6 (2)	5.4 (2)	4.9 (2)	5.2 (1)	5.0 (1)
IrO ₂ **	n.m.	0.2 (2)	0.1 (1)	0.2 (2)	0.3 (3)	0.2 (3)	0.2 (2)	n.m.
total	98.9	98.9	98.5	100.0	99.0	99.16	99.0	99.2
Cations per 6 oxygens								
T								
Si	1.791	1.874	1.942	1.908	1.916	1.930	1.948	1.958
Al ^{IV}	0.209	0.126	0.058	0.092	0.084	0.070	0.052	0.042
M2								
Fe ²⁺	0.023	0.026	0.015	0.010	0.021	0.016	0.019	0.019
Mg	0.105	0.087	0.062	0.065	0.079	0.057	0.071	0.069
Mn	0.003	0.002	0.002	0.002	0.002	0.002	0.002	0.002
Ca	0.677	0.557	0.502	0.571	0.492	0.529	0.493	0.488
Na	0.174	0.276	0.392	0.316	0.378	0.341	0.356	0.348
M1								
Al ^{VI}	0.366	0.451	0.470	0.444	0.501	0.467	0.476	0.495
Ti	0.010	0.010	0.004	0.008	0.005	0.013	0.010	0.008
Fe ³⁺ (+)	0.032	0.035	0.009 [†]	0.020	0.024	0.030	0.030	0.029
Fe ²⁺	0.107	0.116	0.095	0.071	0.103	0.107	0.102	0.101
Mg	0.484	0.388	0.403	0.457	0.385	0.382	0.382	0.367
Cation sum	3.982	3.948	3.972	3.964	3.973	3.944	3.941	3.925

Appendix 1 continued

Sample:	V772-2	V772-3	V772-4	V772-5	V780-1	V780-2	V780-3	V780-4	V780-5	V792-4	V792-5
Conditions (P[Gpa]/T [°C])	4/1200	4/1200	4/1200	4/1200	6/1200	6/1200	6/1200	6/1200	6/1200	4/1050	4/1050
Garnet	(6)	(7)	(8)	(7)	(7)	(10)	(9)	(10)	(10)	(5)	(5)
SiO ₂	38.0 (3)	38.8 (1)	40.2 (4)	42.4 (4)	38.3 (2)	38.8 (2)	39.4 (2)	41.0 (6)	41.4 (2)	40.3 (2)	41.2 (4)
TiO ₂	n.m.										
Al ₂ O ₃	20.4 (4)	21.3 (1)	21.7 (3)	22.8 (6)	19.9 (4)	20.4 (4)	21.1 (2)	21.7 (6)	22.2 (2)	21.6 (3)	21.7 (5)
FeO*	34.4 (5)	30.2 (3)	25.0 (9)	14.9 (6)	35.4 (3)	34.0 (3)	29.6 (2)	22.5 (3)	19.0 (8)	25 (1)	17.8 (2)
MgO	2.9 (1)	6.0 (1)	9.7 (4)	16.9 (9)	3.3 (1)	4.01 (8)	7.2 (1)	12.2 (4)	14.6 (4)	9.7 (8)	15.2 (2)
MnO	n.m.										
CaO	4.9 (4)	4.2 (2)	4.3 (4)	3.8 (7)	3.9 (1)	3.8 (1)	3.7 (3)	3.7 (4)	3.3 (3)	4.9 (8)	4.6 (2)
Na ₂ O	0.06 (3)	0.06 (3)	0.07 (5)	0.09 (8)	0.16 (2)	0.14 (2)	0.12 (3)	0.15 (7)	0.11 (1)	0.08 (5)	0.3 (1)
IrO ₂ **	n.m.										
total	100.7	100.6	100.9	100.8	100.9	101.1	101.1	101.3	100.6	101.6	100.8
Cations per 12 oxygens											
Si	3.015	3.008	3.023	3.040	3.055	3.055	3.035	3.047	3.042	3.031	3.022
Ti											
Al	1.905	1.942	1.925	1.930	1.867	1.893	1.918	1.902	1.922	1.912	1.879
Fe	2.280	1.956	1.573	0.893	2.356	2.244	1.908	1.399	1.169	1.582	1.093
Mg	0.343	0.696	1.090	1.903	0.387	0.471	0.828	1.351	1.595	1.089	1.663
Mn											
Ca	0.405	0.347	0.345	0.291	0.333	0.324	0.308	0.294	0.262	0.393	0.360
Na	0.011	0.009	0.010	0.013	0.025	0.021	0.018	0.022	0.016	0.012	0.040
Cation sum	7.959	7.958	7.966	7.970	8.024	8.009	8.015	8.013	8.005	8.019	8.058
Clinopyroxene											
	(12)	(12)	(11)	(11)	(16)	(18)	(22)	(14)	(19)	(5)	(3)
SiO ₂	50.4 (2)	51.9 (2)	53.4 (2)	55.5 (2)	50.8 (2)	51.3 (3)	52.5 (2)	54.4 (2)	55.0 (3)	51.6 (6)	53.7 (3)
TiO ₂	n.m.										
Al ₂ O ₃	4.3 (3)	4.5 (4)	5.3 (2)	5.4 (4)	4.0 (4)	4.2 (5)	4.8 (3)	7.6 (8)	7.7 (2)	7 (1)	6.4 (2)
FeO	31.0 (9)	24.3 (5)	18.1 (4)	9.3 (8)	31 (2)	29 (1)	22 (1)	16 (1)	12.3 (6)	17.9 (4)	10.0 (3)
MgO	5.0 (1)	9.6 (2)	13.2 (2)	18.2 (6)	5.3 (2)	6.8 (5)	10.1 (4)	15.0 (6)	17.9 (5)	12.8 (6)	15.8 (4)
MnO	n.m.										
CaO	7.2 (4)	7.3 (3)	7.6 (2)	8.9 (8)	7.3 (6)	7.3 (7)	7.8 (5)	7.6 (8)	7.7 (2)	8.5 (4)	10.4 (6)
Na ₂ O	2.5 (1)	2.3 (2)	2.5 (1)	2.8 (2)	2.6 (3)	2.7 (3)	2.9 (2)	2.7 (3)	2.62 (9)	2.9 (2)	3.6 (1)
IrO ₂ **	n.m.										
total	100.4	100.1	100.0	100.1	100.9	100.7	100.4	100.8	100.3	100.2	99.9
Cations per 6 oxygens											
T											
Si	1.979	1.977	1.976	1.972	1.997	1.995	1.989	1.988	1.985	1.803	1.771
Al ^{IV}	0.021	0.023	0.024	0.028	0.003	0.005	0.011	0.012	0.015	0.197	0.229
M2											
Fe ²⁺	0.368	0.289	0.205	0.091	0.388	0.355	0.267	0.195	0.146	0.228	0.115
Mg	0.116	0.219	0.291	0.344	0.118	0.151	0.216	0.319	0.378	0.289	0.325
Mn											
Ca	0.302	0.296	0.300	0.375	0.306	0.303	0.317	0.297	0.297	0.319	0.366
Na	0.191	0.172	0.180	0.191	0.199	0.200	0.209	0.192	0.183	0.194	0.228
M1											
Al ^{VI}	0.179	0.181	0.207	0.196	0.181	0.186	0.202	0.199	0.189	0.329	0.387
Ti											
Fe ³⁺ (+)	0.080 [‡]	0.061 [‡]	0.044 [‡]	0.022 [‡]	0.080 [‡]	0.073 [‡]	0.056 [‡]	0.039 [‡]	0.029 [‡]	0.073 [‡]	0.080 [‡]
Fe ²⁺	0.564	0.430	0.310	0.163	0.628	0.572	0.442	0.303	0.226	0.295	0.160
Mg	0.177	0.327	0.440	0.620	0.191	0.186	0.202	0.199	0.189	0.375	0.453
Cation sum	3.977	3.976	3.977	4.001	4.011	4.009	4.009	4.002	4.005	40.31	4.035

* All Fe is given as FeO. ** Ir-nuggets present as small inclusions (<1 μm), (+) according to Fe³⁺/ΣFe ratios from EELS measurements in the two representative samples. (‡)Fe³⁺/ΣFe for cpx equals 0.06, for all other cpx it is 0.19. n.m. - not measured; number in brackets reflects the standard deviation in terms of last digit.

Appendix 2 Compositions of samples used in the empirical majorite barometer

	Z1113#2	Z1138#4	H3955#2	H3953#4	This study JB-1			Z1132#4	V868#4rim
					H3967#4	H3966#4	V860#2		
P [GPa]	16	14	12	10	12	10	8	16	10
T [°C]	1400	1400	1400	1400	1200	1200	1200	1200	1000
SiO ₂	42.34	41	41.99	41.6	41.8	41.2	41.3	42.3	41.5
TiO ₂	1.2	1.1	0.55	0.8	1.1	0.8	0.62	1.3	0.9
Al ₂ O ₃	19.1	21.1	20.3	21.1	20.5	21.2	22.2	19.2	21.3
Cr ₂ O ₃									
FeO	10.08	10.6	11.3	12.4	11.2	12.7	9.5	10.4	11.2
MnO	2.46	2.8	2.74	3	2.1	2.2	3.6	1.9	2.5
MgO	10.63	10.4	10.86	10.7	10.2	10.2	11.8	10.4	11.3
CaO	12.69	11.7	11.29	10.6	11.9	11.1	11.4	12.1	11.7
Na ₂ O	1.29	0.9	0.71	0.5	0.8	0.4	0.24	1.3	0.3
K ₂ O	0.03	0.01	0.01	0	0	0	0	0.1	0
Total	99.81	99.7	99.74	100.6	99.5	99.8	100.6	99	100.7
cations per 12 oxygens									
Si	3.143	3.054	3.121	3.074	3.108	3.070	3.025	3.161	3.052
Ti	0.067	0.062	0.031	0.044	0.062	0.045	0.034	0.073	0.050
Al	1.671	1.852	1.778	1.837	1.797	1.862	1.917	1.691	1.846
Cr	0.000	0.000	0.000	0.000	0.000	0.000	0.000	0.000	0.000
Fe	0.590	0.660	0.702	0.766	0.697	0.791	0.582	0.650	0.689
Mn	0.155	0.177	0.172	0.188	0.132	0.139	0.223	0.120	0.156
Mg	1.176	1.155	1.203	1.179	1.131	1.133	1.289	1.158	1.239
Ca	1.009	0.934	0.899	0.839	0.948	0.886	0.895	0.969	0.922
Na	0.186	0.130	0.102	0.072	0.115	0.058	0.034	0.188	0.043
K	0.003	0.001	0.001	0.000	0.000	0.000	0.000	0.010	0.000
total	8.032	8.024	8.011	7.999	7.989	7.983	7.999	8.020	7.996
P this study [GPa]	15.5	13.1	12.9	10.8	13.0	10.1	8.1	15.7	9.3
P C10 [GPa]	12.9	10.2	10.3	9.1	10.6	8.6	7.4	13.2	8.3

Appendix 2 continued

	This study NMORB4										
	Z1113#4	Z1138#2	H3955#4	H3953#2	H3966#2	Z1132#2	H3967#2	V860#4 core	V860#4rim	V868#2	Z1136#2
P [GPa]	16	14	12	10	10	16	12	8	8	10	16
T [°C]	1400	1400	1400	1400	1200	1200	1200	1200	1200	1000	1000
SiO ₂	41.82	40.5	41.77	41.1	41.1	42	41.2	40.7	40.8	40.8	42.4
TiO ₂	1.17	1.7	0.7	1.2	0.8	1.3	1.5	0.8	0.7	1.2	1.4
Al ₂ O ₃	19.49	21.3	20.75	20.9	21.2	19.7	20.8	21.7	21.9	20.5	19.1
Cr ₂ O ₃											
FeO	12.52	13	13.75	15.1	14.9	12.7	12.3	17.2	15.5	16.1	13.5
MnO	0.04	0.06	0.05	0.1	0	0	0	0.23	0.19	0.03	0
MgO	10.01	9.6	9.98	9.7	9.8	9.9	9.3	10.2	10.7	8.6	10.8
CaO	13.94	12.6	12.31	11.6	12.2	12.8	14.1	9.9	10.6	13.4	12.4
Na ₂ O	1.2	1	0.77	0.5	0.4	1.1	0.8	0.27	0.3	0.2	1.2
K ₂ O	0.02	0.01	0	0	0	0.02	0	0	0	0.005	0.01
Total	100.21	99.8	100.08	100.1	100.4	99.67	100	100.9	100.7	100.79	100.8
cations per 12 oxygens											
Si	3.109	3.020	3.101	3.063	3.056	3.131	3.062	3.022	3.020	3.050	3.131
Ti	0.065	0.095	0.039	0.067	0.045	0.073	0.084	0.045	0.039	0.067	0.078
Al	1.708	1.872	1.816	1.835	1.858	1.731	1.822	1.899	1.911	1.806	1.662
Cr	0.000	0.000	0.000	0.000	0.000	0.000	0.000	0.000	0.000	0.000	0.000
Fe	0.779	0.811	0.854	0.941	0.926	0.792	0.765	1.068	0.960	1.007	0.834
Mn	0.003	0.004	0.003	0.006	0.000	0.000	0.000	0.014	0.012	0.002	0.000
Mg	1.110	1.067	1.105	1.078	1.086	1.100	1.030	1.129	1.181	0.958	1.189
Ca	1.111	1.007	0.979	0.926	0.972	1.022	1.123	0.788	0.841	1.073	0.981
Na	0.173	0.145	0.111	0.072	0.058	0.159	0.115	0.039	0.043	0.029	0.172
K	0.002	0.001	0.000	0.000	0.000	0.002	0.000	0.000	0.000	0.000	0.001
total	8.059	8.021	8.007	7.989	8.000	8.011	8.001	8.003	8.007	7.994	8.047
P this study [GPa]	15.0	12.6	13.0	10.6	9.8	14.6	12.2	8.6	8.6	9.4	14.8
P C10 [GPa]	12.3	10.4	10.2	9.2	8.5	12.1	10.3	7.6	7.6	8.3	12.7

Appendix 2 continued

	This study OC1/2									
	Z1113#3	Z1138#3	H3953#3	H3955#3	H3966#3	H3967#3	V860#3	Z1132#3	V868#3	Z1136#3
P [GPa]	16	14	10	12	10	12	8	16	10	16
T [°C]	1400	1400	1400	1400	1200	1200	1200	1200	1000	1000
SiO ₂	42.11	40.8	41.3	41.99	40.8	41.2	41.2	42.1	39.9	41.1
TiO ₂	0.79	0.65	0.4	0.48	0.6	1.2	0.3	0.8	0.71	1.4
Al ₂ O ₃	18.98	21.1	21.5	20.71	21.1	20.8	22.5	18.7	21.5	18.8
Cr ₂ O ₃										
FeO	10.98	11.3	12.7	11.75	13.5	12	10.3	10.9	15.1	11.4
MnO	0.19	0.21	0.2	0.23	0	0	0.5	0	0.24	0.18
MgO	9.96	9.9	10.4	10.24	9.6	9.4	11.6	9.5	7.8	8.9
CaO	14.74	14	12.8	13.21	13.1	14.2	13.3	14.8	13.9	15.7
Na ₂ O	1.17	0.8	0.4	0.6	0.4	0.8	0.21	1.1	0.3	1.2
K ₂ O	0	0.01	0	0	0	0	0	0	0	0
Total	98.92	98.8	99.7	99.22	99	99.6	99.9	98.03	99.4	98.7
cations per 12 oxygens										
Si	3.157	3.059	3.067	3.123	3.063	3.070	3.025	3.184	3.020	3.112
Ti	0.045	0.037	0.022	0.027	0.034	0.067	0.017	0.046	0.040	0.080
Al	1.677	1.865	1.882	1.815	1.867	1.827	1.947	1.667	1.918	1.678
Cr	0.000	0.000	0.000	0.000	0.000	0.000	0.000	0.000	0.000	0.000
Fe	0.688	0.709	0.789	0.731	0.848	0.748	0.633	0.689	0.956	0.722
Mn	0.012	0.013	0.013	0.014	0.000	0.000	0.031	0.000	0.015	0.012
Mg	1.113	1.107	1.151	1.135	1.074	1.044	1.270	1.071	0.880	1.005
Ca	1.184	1.125	1.018	1.053	1.054	1.134	1.046	1.199	1.127	1.274
Na	0.170	0.116	0.058	0.087	0.058	0.116	0.030	0.161	0.044	0.176
K	0.000	0.001	0.000	0.000	0.000	0.000	0.000	0.000	0.000	0.000
total	8.045	8.031	7.999	7.986	7.998	8.007	7.999	8.018	8.002	8.057
P this study [GPa]	15.8	12.8	10.0	12.3	10.0	12.6	7.7	15.8	8.7	14.7
P C10 [GPa]	12.6	9.7	8.3	9.8	8.5	10.2	7.0	12.7	7.6	12.6

Appendix 2 continued

	This study Mix1G						
	Z1113#1	H3955#1	H3953#5	H3967#5	H3966#5	V860#1	V868#5
P [GPa]	16	12	10	12	10	8	10
T [°C]	1400	1400	1400	1200	1200	1200	1000
SiO ₂	44.01	43.74	42.7	43.8	42.6	42.6	42.5
TiO ₂	0.86	0.78	0.8	0.9	1	0.5	1
Al ₂ O ₃	16.05	19.28	20.1	20	19.6	22.7	19.4
Cr ₂ O ₃							
FeO	8.2	7.97	2.8	7.5	8.6	6	9.2
MnO	0.22	0.38	0.2	0	0	0.5	0.24
MgO	17.36	17.19	16	18.1	17.9	19.4	17.5
CaO	11.58	10.43	16.7	9.8	9.7	8.2	10.2
Na ₂ O	0.91	0.49	0.2	0.4	0.4	0.14	0.26
K ₂ O	0.01	0	0	0	0	0	0.01
Total	99.19	100.26	99.4	100.5	99.7	100.1	100.1
cations per 12 oxygens							
Si	3.217	3.143	3.076	3.120	3.079	3.018	3.073
Ti	0.047	0.042	0.043	0.048	0.054	0.027	0.054
Al	1.383	1.633	1.706	1.679	1.670	1.896	1.653
Cr	0.000	0.000	0.000	0.000	0.000	0.000	0.000
Fe	0.452	0.479	0.169	0.447	0.520	0.356	0.556
Mn	0.014	0.023	0.012	0.000	0.000	0.030	0.015
Mg	1.892	1.841	1.718	1.922	1.929	2.049	1.886
Ca	0.907	0.803	1.289	0.748	0.751	0.623	0.790
Na	0.129	0.068	0.028	0.055	0.056	0.019	0.036
K	0.001	0.000	0.000	0.000	0.000	0.000	0.001
total	8.087	8.033	8.042	8.020	8.059	8.017	8.065
P this study [GPa]	15.0	11.8	9.3	10.9	10.2	7.3	9.7
P C10 [GPa]	13.5	10.5	8.8	9.9	9.7	7.1	9.3

Appendix 2 continued

	Okamoto & Maruyama (2004) MORB							Ono & Yasuda (1996) MORB			
	Table 1 S867	Table 1 S873	Table 1 S905	S1004	S1002	S904	S991	Table 4 GW39	Table 4 GW14	GE7	GW9
P [GPa]	12	14	16	18	19	16	19	7	12	13.3	16.7
T [°C]	900	900	900	900	1000	1100	1100	1400	1400	1600	1600
SiO ₂	41.16	41.79	44.64	46.46	45.23	44.36	46.09	40.94	41.61	43.25	44.15
TiO ₂	1.81	1.7	1.59	1.6	1.47	1.67	1.32	1.49	1.5	2.17	1.86
Al ₂ O ₃	18.45	18.24	17.29	17.34	17.42	17.78	17.06	22.56	21.56	20.2	19.61
Cr ₂ O ₃											
FeO	16.56	16.29	10.9	8.66	10.09	11.25	9.48	12.29	11.79	8.98	10.75
MnO											
MgO	7.91	8.47	9.19	9.78	9.28	9.33	9.53	9.96	9.07	9.75	8.42
CaO	13.95	13.48	14.61	13.38	14.08	13.25	13.02	12.46	13.65	13.84	12.96
Na ₂ O	0.51	0.57	2.02	1.97	2.23	2.27	2.91	0.27	0.92	1.65	2.47
K ₂ O		0.01	0.01	0.01	0.01	0.01					
Total	100.35	100.55	100.25	99.2	99.8	99.9	99.4	99.97	100.1	99.8	100.2
cations per 12 oxygens											
Si	3.111	3.141	3.293	3.398	3.330	3.278	3.388	3.019	3.073	3.166	3.239
Ti	0.103	0.096	0.088	0.088	0.081	0.093	0.073	0.083	0.083	0.119	0.103
Al	1.644	1.616	1.503	1.495	1.512	1.549	1.478	1.961	1.877	1.743	1.695
Cr	0.000	0.000	0.000	0.000	0.000	0.000	0.000	0.000	0.000	0.000	0.000
Fe	1.047	1.024	0.672	0.530	0.621	0.695	0.583	0.758	0.728	0.550	0.659
Mn	0.000	0.000	0.000	0.000	0.000	0.000	0.000	0.000	0.000	0.000	0.000
Mg	0.891	0.949	1.011	1.066	1.019	1.028	1.044	1.095	0.999	1.064	0.921
Ca	1.130	1.086	1.155	1.049	1.111	1.049	1.026	0.984	1.080	1.085	1.019
Na	0.075	0.083	0.289	0.279	0.318	0.325	0.415	0.039	0.132	0.234	0.351
K	0.000	0.001	0.001	0.001	0.001	0.001	0.000	0.000	0.000	0.000	0.000
total	8.001	7.997	8.012	7.906	7.993	8.018	8.007	7.938	7.971	7.961	7.987
P this study [GPa]	11.4	12.0	17.7	17.8	18.3	17.3	18.5	9.4	12.9	14.8	16.1
P C10 [GPa]	10.9	11.4	17.4	18.2	18.3	17.9	20.9	7.7	10.5	14.4	17.5

Appendix 2 continued

	Yasuda et al. (1994) MORB					Herzberg & Zhang (1996) Peridotite							
	MP23	MP8	TY01	TY6	TY11	Table 1 9.7 Gt3	Table 1 9.7 Gt2	Table 1 15.5 Gt1	Table 1 15.5 Gt2	Table 1 18 Gt1	Table 1 18 Gt3	Table 1 20 Gt3	Table 1 20 Gt3
P [GPa]	7.5	7.5	14	14	20	9.7	9.7	15.5	15.5	18	18	20	20
T [°C]	1700	1775	1600	2100	2200	1900	1950	2150	2050	2150	2050	2150	2200
SiO ₂	40.92	41.26	42.13	42.75	45.07	46.12	46.98	51.2	50.22	51.79	52.86	55.27	54.24
TiO ₂	0.76	0.86	1.4	0.51	0.45	0.28	0.05	0.04	0.04	0.05	0.09	0.09	0.12
Al ₂ O ₃	21.82	22.19	19.57	20.83	19.69	16.34	17.58	11.47	12.53	9.64	6.74	5.09	5.02
Cr ₂ O ₃						1.2	1.1	0.73	0.69	0.61	0.49	0.43	0.41
FeO	13.29	11.73	12.33	8.94	8.04	7.08	4	3.15	2.94	3.14	4.02	4.07	4.55
MnO						0.15	0.08	0.08	0.08	0.06	0.09	0.12	0.11
MgO	11.83	12.75	9.23	12.28	11.43	24.52	27.5	31.57	31.63	32.46	31.85	32.18	31.87
CaO	10.6	10.48	12.89	12.54	12.35	4.5	2.6	1.77	1.46	1.93	3.13	2.67	3.65
Na ₂ O	0.24	0.26	1.07	1.08	2.11	0.12	0.02	0.05	0.05	0.06	0.1	0.12	0.21
K ₂ O													
Total	99.5	99.5	98.6	98.9	99.1	100.31	99.91	100.06	99.64	99.74	99.37	100.04	100.18
cations per 12 oxygens													
Si	3.033	3.031	3.162	3.140	3.284	3.246	3.247	3.505	3.448	3.559	3.673	3.798	3.751
Ti	0.042	0.048	0.079	0.028	0.025	0.015	0.003	0.002	0.002	0.003	0.005	0.005	0.006
Al	1.906	1.921	1.731	1.803	1.691	1.355	1.432	0.925	1.014	0.781	0.552	0.412	0.409
Cr	0.000	0.000	0.000	0.000	0.000	0.067	0.060	0.040	0.037	0.033	0.027	0.023	0.022
Fe	0.824	0.721	0.774	0.549	0.490	0.417	0.231	0.180	0.169	0.180	0.234	0.234	0.263
Mn	0.000	0.000	0.000	0.000	0.000	0.009	0.005	0.005	0.005	0.003	0.005	0.007	0.006
Mg	1.307	1.396	1.033	1.345	1.242	2.573	2.833	3.221	3.238	3.326	3.299	3.296	3.285
Ca	0.842	0.825	1.037	0.987	0.964	0.339	0.193	0.130	0.107	0.142	0.233	0.197	0.270
Na	0.034	0.037	0.156	0.154	0.298	0.016	0.003	0.007	0.007	0.008	0.013	0.016	0.028
K	0.000	0.000	0.000	0.000	0.000	0.000	0.000	0.000	0.000	0.000	0.000	0.000	0.000
total	7.989	7.979	7.971	8.007	7.994	8.037	8.006	8.014	8.027	8.035	8.040	7.988	8.042
P this study [GPa]	8.5	8.8	14.7	15.3	20.5	11.2	10.5	15.4	14.5	16.3	18.0	19.4	19.2
P C10 [GPa]	7.6	7.6	12.4	11.4	16.1	11.1	10.4	15.3	14.3	16.5	18.7	20.6	20.4

Appendix 2 continued

	Wang & Takahashi (2000) Peridotite				Walter (1998) Pyrolite								
	Table 3 S857	Table 3 S858	Table 6 60.02	Table 6 60.04	Table 6 60.01	Table 6 60.07	Table 6 60.05	Table 6 70.01	Table 6 70.07	Table 6 70.02	Table 6 70.05	Table 6 70.09	Table 6 70.08
P [GPa]	18.7	17.1	6	6	6	6	6	7	7	7	7	7	7
T [°C]	1500	2100	1670	1670	1710	1740	1755	1740	1790	1810	1820	1835	1850
SiO ₂	50.61	53.33	42.15	42.89	43.41	43.44	42.83	42.88	43.91	43.3	43.89	43.57	44.32
TiO ₂	0.09	0.01	0.55	0.4	0.35	0.26	0.18	0.51	0.33	0.17	0.28	0.11	0.09
Al ₂ O ₃	7.35	9.84	21.68	21.98	21.96	21.96	22.11	20.93	21.14	21.22	21.65	21.36	21.19
Cr ₂ O ₃	0.61	0.69	1.77	1.01	1.39	1.26	1.28	1.54	1.21	1.41	1.04	1.43	1.36
FeO	5.18	3.46	6.52	5.83	5.8	5.1	4.83	6.37	5.43	4.88	4.55	4.2	3.7
MnO	0.15	0.1	0.19	0.18	0.17	0.16	0.15	0.19	0.16	0.15	0.16	0.12	0.12
MgO	28.47	30.75	22.4	22.96	23.36	24.22	24.23	23.14	24.21	24.69	24.44	25.8	26.73
CaO	4.06	2.03	4.44	4.58	4.04	3.88	3.9	4.3	4	3.64	3.85	2.98	2.24
Na ₂ O	0.3	0.07	0.04	0.04	0.02	0.03	0.02	0.05	0.04	0.03	0.03	0.03	0.02
K ₂ O	0.02	0.09											
Total	96.84	100.37	99.74	99.87	100.5	100.31	99.53	99.91	100.43	99.49	99.89	99.6	99.77
cations per 12 oxygens													
Si	3.645	3.636	2.987	3.016	3.029	3.026	3.005	3.027	3.060	3.039	3.058	3.039	3.069
Ti	0.005	0.001	0.029	0.021	0.018	0.014	0.010	0.027	0.017	0.009	0.015	0.006	0.005
Al	0.624	0.791	1.810	1.822	1.806	1.803	1.828	1.741	1.736	1.755	1.778	1.756	1.729
Cr	0.035	0.037	0.099	0.056	0.077	0.069	0.071	0.086	0.067	0.078	0.057	0.079	0.074
Fe	0.312	0.197	0.386	0.343	0.338	0.297	0.283	0.376	0.316	0.286	0.265	0.245	0.214
Mn	0.009	0.006	0.011	0.011	0.010	0.009	0.009	0.011	0.009	0.009	0.009	0.007	0.007
Mg	3.057	3.125	2.366	2.407	2.430	2.515	2.534	2.435	2.515	2.583	2.538	2.682	2.759
Ca	0.313	0.148	0.337	0.345	0.302	0.290	0.293	0.325	0.299	0.274	0.287	0.223	0.166
Na	0.042	0.009	0.005	0.005	0.003	0.004	0.003	0.007	0.005	0.004	0.004	0.004	0.003
K	0.002	0.008	0.000	0.000	0.000	0.000	0.000	0.000	0.000	0.000	0.000	0.000	0.000
total	8.043	7.958	8.032	8.026	8.013	8.027	8.037	8.036	8.024	8.038	8.012	8.040	8.026
P this study [GPa]	18.5	17.5	6.3	6.5	6.5	6.2	5.4	6.9	7.2	6.1	7.1	5.9	6.6
P C10 [GPa]	18.7	17.1	6.4	6.8	6.8	6.8	6.4	7.2	7.5	7.1	7.3	7.0	7.4

Appendix 2 continued

	Nishihara and Takahashi (2001) Al-depleted komatiite									
	Table 3 S785	Table 3 S786	Table 3 S801	Table 3 S837	Table 3 S793	Table 3	Table 3 S955	Table 3 S810	Table 3 S816	Table 3 S799
P [GPa]	7	9	11	12.5	13	14	15	16	17	19
T [°C]	1100	1200	1300	1400	1450	1450	1450	1500	1500	1550
SiO ₂	41.47	42.4	43.56	43.67	45.11	45.28	47.12	51.25	49.47	52.18
TiO ₂	0.37	0.57	0.56	0.63	0.47	0.61	0.26	0.33	0.44	0.12
Al ₂ O ₃	20.95	18.68	15.17	13.62	13.45	12.38	12.04	8.17	8.12	7.36
Cr ₂ O ₃										
FeO	12.78	13.12	13.02	13.26	10.75	11.27	9.33	8	9.27	6.34
MnO	0.25	0.37	0.31	0.34	0.3	0.27	0.15	0.24	0.31	0.12
MgO	17.31	17.92	19.58	19.06	21.33	20.59	22.24	25.29	23.36	25.71
CaO	6.07	6.05	5.97	6.86	6.42	6.9	6.46	6.52	7.93	7.39
Na ₂ O	0.05	0.11	0.21	0.12	0.18	0.16	0.13	0.24	0.44	0.3
K ₂ O										
Total	99.25	99.22	98.38	97.56	98.01	97.46	97.73	100.04	99.34	99.52
cations per 12 oxygens										
Si	3.038	3.116	3.232	3.283	3.325	3.369	3.447	3.634	3.582	3.694
Ti	0.020	0.032	0.031	0.036	0.026	0.034	0.014	0.018	0.024	0.006
Al	1.809	1.618	1.327	1.207	1.168	1.086	1.038	0.683	0.693	0.614
Cr	0.000	0.000	0.000	0.000	0.000	0.000	0.000	0.000	0.000	0.000
Fe	0.783	0.806	0.808	0.834	0.663	0.701	0.571	0.474	0.561	0.375
Mn	0.016	0.023	0.019	0.022	0.019	0.017	0.009	0.014	0.019	0.007
Mg	1.891	1.963	2.166	2.136	2.344	2.284	2.425	2.673	2.522	2.714
Ca	0.476	0.476	0.475	0.553	0.507	0.550	0.506	0.495	0.615	0.561
Na	0.007	0.016	0.030	0.017	0.026	0.023	0.018	0.033	0.062	0.041
K	0.000	0.000	0.000	0.000	0.000	0.000	0.000	0.000	0.000	0.000
total	8.040	8.051	8.088	8.087	8.078	8.065	8.029	8.024	8.078	8.013
P this study [GPa]	7.3	9.5	11.8	12.5	13.2	14.0	15.0	17.9	17.9	19.0
P C10 [GPa]	7.3	9.2	11.9	12.7	13.3	14.1	14.7	18.4	18.5	19.3

Appendix 2 continued

	Ulmer & Sweeney (2002) Group 2 Kimberlite						
	Table 3 653	Table 3 642	Table 3 MA22	Table 3 652	Table 3 524	Table 3 525	Table 3 MA25
P [GPa]	9.5	8	7.5	9.5	7.5	6	7.5
T [°C]	1400	1200	1280	1200	1450	1400	1200
SiO ₂	41.82	41.52	42.51	42.09	43.62	42.39	40.52
TiO ₂	1.6	1.77	0.78	0.84	1.07	0.82	1.4
Al ₂ O ₃	17.44	18.5	20.28	19.76	19.72	20.71	20.12
Cr ₂ O ₃	2.88	2.02	1.98	0.9	2.31	3	1.78
FeO	8.66	10.93	7.53	10.95	5.76	6.07	10.33
MnO	0.32	0.35	0.29	0.36	0.24	0.27	0.47
MgO	20.91	19.61	21.85	20.68	23.39	22.02	18.72
CaO	5.91	5.48	5.15	4.74	5.05	5.54	6.22
Na ₂ O	0.09	0.11	0.04	0.13	0.09	0.04	0.05
K ₂ O	0.03	0.01	0.07	0.12	0.13	0.09	0.02
Total	99.66	100.3	100.48	100.57	101.38	100.95	99.63
cations per 12 oxygens							
Si	3.034	3.011	3.016	3.024	3.045	2.986	2.956
Ti	0.087	0.097	0.042	0.045	0.056	0.043	0.077
Al	1.491	1.581	1.696	1.673	1.622	1.719	1.730
Cr	0.165	0.116	0.111	0.051	0.127	0.167	0.103
Fe	0.525	0.663	0.447	0.658	0.336	0.358	0.630
Mn	0.020	0.022	0.017	0.022	0.014	0.016	0.029
Mg	2.261	2.120	2.311	2.215	2.434	2.312	2.036
Ca	0.459	0.426	0.392	0.365	0.378	0.418	0.486
Na	0.013	0.015	0.006	0.018	0.012	0.005	0.007
K	0.003	0.001	0.006	0.011	0.012	0.008	0.002
total	8.059	8.052	8.044	8.083	8.036	8.034	8.055
P this study [GPa]	8.7	8.6	7.2	8.0	8.3	6.6	7.7
P C10 [GPa]	8.7	8.5	7.3	8.0	8.1	6.7	7.0

Appendix 2 Clinopyroxene analyses given as wt.% oxides measured by microprobe.

	V867#4	H3951#2	V860#2	V868#4	H3966#4	H3953#4	H3967#4	H3955#2	Z1132#4	Z1138#4	Z1113#2
P[GPa]	6	6	8	10	10	10	12	12	12	14	16
T [°C]	1000	1400	1200	1000	1200	1400	1200	1400	1600	1400	1400
Bulk materials	JB-1	JB-1	JB-1	JB-1	JB-1	JB-1	JB-1	JB-1	JB-1	JB-1	JB-1
SiO ₂	55.5	54.5	56.6	57.2	57.1	57.5	57.5	56.8	57.4	55.7	57.52
TiO ₂	0.5	1.2	0.44	0.28	0.4	0	0.6	0.44	0.4	0.44	0.31
Al ₂ O ₃	11.9	12.4	12.8	12.5	12	12.4	12.5	12.23	12.7	14	13.99
FeO	4.8	2.5	2.6	3.7	3.7	3.5	2.8	3.45	5.2	2.9	5.9
MnO	0.2	0.9	0.6	0.34	0.2	0.5	0.1	0.47	0	0.39	0.25
MgO	8.5	10.5	8.9	7.9	8.2	8.4	8.2	8.22	6.1	7.5	5.08
CaO	12.8	14.1	12.4	11.3	11.4	11.4	10.8	10.68	7.6	9.7	6.25
Na ₂ O	5.6	4.7	6.2	7.4	7.2	6.9	7.9	7.38	9.6	8.3	10.48
K ₂ O	0.1	0.1	0.07	0.34	0.4	0.19	0.3	0.42	0.5	0.41	0.46
Total	99.8	100.8	100.6	100.9	100.6	100.8	100.6	100.09	99.5	99.5	100.24

	V867#5	V868#5	H3966#5	H3953#5	H3967#5	Z1138#	Z1132#5	H3955#1	Z1113#1
P[GPa]	6	10	10	10	12	14	16	12	16
T [°C]	1000	1000	1200	1400	1200	1400	1200	1400	1400
Bulk materials	Mix-1G	Mix-1G	Mix-1G	Mix-1G	Mix-1G	Mix-1G	Mix-1G	Mix-1G	Mix-1G
SiO ₂	53.4	56.2	55.9	54.2	56.2	54.8	55.7	55.61	55.99
TiO ₂	0.5	0.2	0.2	0.4	0.2	0.16	0.13	0.12	0.19
Al ₂ O ₃	5.2	4.1	4.1	4.6	4.1	4.9	3.9	4.92	5.45
FeO	5.2	2.7	4.3	1.1	2.7	3.2	4.3	3.41	4.96
MnO	0	0	0	0.1	0	0.05	0	0.08	0.06
MgO	14.5	15.5	14.9	17.1	15.5	14.7	14.3	14.56	12.78
CaO	18.4	19.1	17.6	21.6	19.1	17.9	17.4	17.5	15.23
Na ₂ O	3	3.1	3.6	1.3	3.1	3.5	4.1	3.56	5.1
K ₂ O	0.02	0	0	0	0	0.04	0	0.06	0.11
Total	100.1	100.8	100.6	100.4	100.8	99.2	99.8	99.83	99.87

Appendix 2 continued

	V860#4	V868#2	H3966#2	H3953#2	H3967#2	Z1138#2	Z1132#2	H3955#4	Z1113#4
P[GPa]	8	10	10	10	12	14	16	12	16
T [°C]	1200	1000	1200	1400	1200	1400	1200	1400	1400
Bulk materials	NMORB4	NMORB4	NMORB4	NMORB4	NMORB4	NMORB4	NMORB4	NMORB4	NMORB4
SiO ₂	56.05	57.3	57.28	57.3	57.6	56.3	58.3	57.59	57.38
TiO ₂	0.64	0.3	0.37	0.7	0.53	0.5	0.3	0.37	0.29
Al ₂ O ₃	11.35	14.2	13.22	15.7	13.5	17.6	15.7	16.25	15.54
FeO	5.61	4.3	3.94	3.2	2.7	3	5.7	3.12	5.55
MnO	0.06	0.01	0	0	0	0.01	0	0.01	0.02
MgO	8.59	6.4	7.17	6.2	7.4	4.9	3.8	5.56	4.35
CaO	12.5	10	10.5	9.1	10.1	6.5	4.9	7.66	5.51
Na ₂ O	6.02	8.6	8.03	8.3	8.5	10.7	11.6	9.65	11.38
K ₂ O	0.02	0.03	0.07	0.02	0.03	0.04	0.04	0.04	0.08
Total	100.84	101	100.58	100.5	100.4	99.4	100.21	100.25	100.1

	V867#3	H3951#3	V860#3cpx1	V860#3cpx2	V868#3	H3966#3	H3953#3	H3967#3	H3955#3	Z1113#3	Z1138#3	Z1132#3
P[GPa]	6	6	8	8	10	10	10	12	12	16	14	16
T [°C]	1000	1400	1200	1200	1000	1200	1400	1200	1400	1400	1400	1200
Bulk materials	OC1/2	OC1/2	OC1/2	OC1/2	OC1/2	OC1/2	OC1/2	OC1/2	OC1/2	OC1/2	OC1/2	OC1/2
SiO ₂	57.51	53.6	56.5	54	57.6	57.09	57.1	57.3	57.57	57.46	56	56.9
TiO ₂	0.58	1.5	0.2	2.1	0.24	0.22	0.2	0.4	0.51	0.18	0.2	0.3
Al ₂ O ₃	14.31	15.3	13.2	12.5	11.9	12.09	12.6	13.2	13.67	14.57	14.5	13.1
FeO	1.64	1.9	3	5.5	3.7	3.96	3.2	2.8	3.25	5.28	2.9	4.8
MnO	0	0.1	0.1	0.2	0.02	0	0.03	0	0.03	0.02	0.03	0
MgO	7.33	8.1	8.7	6.6	8.2	7.87	8.3	7.6	7.32	5.09	7.2	5.9
CaO	9.53	15.3	13	13.7	12	11.67	12	10.6	10.18	6.66	9.8	7.9
Na ₂ O	9.72	4.1	5.6	3.9	6.9	6.88	6.7	8.3	7.76	10.44	8.4	9.5
K ₂ O	0	0	0	0	0	0.01	0	0	0.01	0.01	0.01	0
Total	100.62	99.9	100.4	98.6	100.6	99.78	100.3	100.2	100.32	99.71	99.04	98.5

Appendix 3 Compositions of eclogitic majorite inclusions in diamonds

Sample	H-5	MG25A	105A1	105A2	R4-1b	R3-1b	J1-3	J8-1	J9-1	J9-2	J9-3
Location	Arkhangelsk	Brazil	Buffalo hills	Buffalo hills	Jagersfontein	Jagersfontein	Juina	Juina	Juina	Juina	Juina
SiO ₂	40.5	40.5	42.2	41.5	42.2	45.2	41.35	41.88	42.31	41.59	40.94
TiO ₂	0.34	0.86	1.28	1.33	0.24	0.13	1.35	0.22	1.06	0.95	1.2
Al ₂ O ₃	21.2	19.6	19.5	19.6	19.5	15.4	21.64	22.22	21.45	21.1	21.36
Cr ₂ O ₃	0.06	0.2	0.07	0	0.11	0.21	0.05	0.03	0.07	0.06	0.06
FeO	17.9	16	14.49	14.44	13.8	13.5	10.51	16.64	14.9	14.86	13.54
MnO	0.32	0.34	0.31	0.28	0	0	0.3	0.41	0.3	0.28	0.23
MgO	10.7	13.1	9.54	9.63	16.2	19.7	9.03	9.45	10.05	10.58	9.51
CaO	7.6	8.39	10.66	10.82	7.91	5.74	15.63	8.21	9.48	8.68	11.57
Na ₂ O	0.23	0	1.55	1.53	0.33	0.42	0.59	0.98	0.85	0.92	0.78
K ₂ O											
Total	98.81	98.99	99.7	99.2	100.29	100.3	100.45	100.04	100.48	99.02	99.19
Cations based on 12 oxygens											
Si ⁴⁺	3.064	3.05	3.157	3.124	3.091	3.282	3.046	3.112	3.117	3.107	3.063
Ti ⁴⁺	0.019	0.049	0.072	0.075	0.013	0.007	0.075	0.012	0.059	0.053	0.068
Al ³⁺	1.891	1.739	1.72	1.74	1.683	1.318	1.88	1.946	1.863	1.858	1.884
Cr ³⁺	0.004	0.012	0.004	0	0.006	0.012	0.003	0.002	0.004	0.004	0.004
Fe ²⁺	1.132	1.008	0.907	0.909	0.845	0.82	0.648	1.034	0.918	0.928	0.847
Mn ²⁺	0.021	0.022	0.02	0.018	0	0	0.019	0.026	0.019	0.018	0.015
Mg ²⁺	1.206	1.47	1.064	1.08	1.768	2.132	0.991	1.046	1.103	1.178	1.06
Ca ²⁺	0.616	0.677	0.854	0.873	0.621	0.447	1.234	0.654	0.748	0.695	0.928
Na ⁺	0.034	0	0.225	0.223	0.047	0.059	0.084	0.141	0.121	0.133	0.113
K ⁺											
Total	7.987	8.026	8.022	8.042	8.075	8.076	7.98	7.973	7.952	7.975	7.982
P this study	8.6	8.3	16.5	16.0	9.8	13.9	11.1	14.6	13.6	13.9	12.5
P C10	7.7	7.8	13.7	13.4	9.1	12.7	9.1	10.0	10.5	10.6	9.8

Appendix 3 continued

Sample	5-108b	5-108c	5-108a	KK-1a	KK-61c	KK-5	KK81a	D27-28	A4-05	B10-01	A4-03
Location	Juina, Brasil	Juina, Brasil	Junia, Brasil	Kankan	Kankan	Kankan	Kankan	Lac De Gras	Monastery	Monastery	Monastery
SiO ₂	41.46	40.98	42.46	42.43	43.12	44.26	45.05	42.73	41.76	41.7	42.08
TiO ₂	1.95	2.36	1.83	1.48	1.37	0.06	1.16	0.79	0.72	1.14	1.21
Al ₂ O ₃	18.82	18.03	17.22	17.19	18.23	21.13	16.64	19.31	22.45	18.3	18.32
Cr ₂ O ₃	0.12	0.07	0.1	0.04	0.14	0.05	0.08	0.07	0.29	0.06	0.01
FeO	13.37	14.2	12.68	12.78	12.62	12.18	10.32	14.16	9.29	14.72	14.74
MnO	0.3	0.25	0.23	0.25	0.36	0.35	0.26	0.29	0.23	0.25	0.27
MgO	12.46	11.88	12.3	10.92	17.22	16.64	15.18	9.87	20.6	10.33	10.31
CaO	10.7	11.12	12.18	14.67	6.35	4.53	9.89	13.05	4.31	13.15	11.89
Na ₂ O	0.67	0.61	0.88	0.69	0.59	1.41	1.37	0.11	0.08	0.76	1.08
K ₂ O	0	0	0	0.01	0.01	0	0.01	0	0	0	0
Total	99.85	99.5	99.88	100.46	100.01	100.61	99.96	100.38	99.73	100.41	99.91
Cations based on 12 oxygens											
Si ⁴⁺	3.083	3.078	3.159	3.161	3.144	3.17	3.281	3.17	2.983	3.122	3.154
Ti ⁴⁺	0.109	0.133	0.102	0.083	0.075	0.003	0.064	0.044	0.039	0.064	0.068
Al ³⁺	1.649	1.596	1.51	1.509	1.566	1.784	1.428	1.688	1.89	1.615	1.618
Cr ³⁺	0.007	0.004	0.006	0.002	0.008	0.003	0.005	0.004	0.016	0.004	0.001
Fe ²⁺	0.831	0.892	0.789	0.796	0.769	0.73	0.629	0.878	0.555	0.922	0.924
Mn ²⁺	0.019	0.016	0.014	0.016	0.022	0.021	0.016	0.018	0.014	0.016	0.017
Mg ²⁺	1.381	1.33	1.364	1.212	1.871	1.777	1.648	1.091	2.193	1.153	1.152
Ca ²⁺	0.852	0.895	0.971	1.171	0.496	0.348	0.772	1.037	0.33	1.055	0.955
Na ⁺	0.097	0.089	0.127	0.1	0.083	0.196	0.193	0.016	0.011	0.11	0.157
K ⁺	0	0	0	0.001	0.001	0	0.001	0	0	0	0
Total	8.028	8.033	8.044	8.051	8.036	8.031	8.036	7.948	8.031	8.06	8.047
P this study	11.7	10.8	13.6	13.2	12.5	17.5	17.4	10.7	7.1	13.2	15.1
P C10	11.1	11.4	13.0	12.3	11.4	12.3	15.5	9.5	6.6	11.5	12.8

Appendix 3 continued

Sample	A1-23	A4-08	B9-17	A2-01	A5-13	AI-20-17	AL-24	B9-23	MW52-78	#5	#6
Location	Monastery	Monastery	Monastery	Monastery	Monastery	Monastery	Monastery	Monastery	Mwadui	Premier	Premier
SiO ₂	42.65	42.73	43.45	44.25	45.39	45.43	47.43	41.97	41.14	40.7	41.3
TiO ₂	0.89	0.24	1.15	0.57	0.78	0.81	0.78	0.13	1.93	0.25	0.31
Al ₂ O ₃	17.46	18.91	16.3	15.87	14.97	14.82	11.29	21.35	17.82	22.2	22.4
Cr ₂ O ₃	0	0.07	0.06	0.11	0.18	0.06	0.2	0.1	0.14	0.05	0.11
FeO	15.63	15.85	12.99	11.56	12.92	9.77	10.51	16.39	15.75	13.3	14.7
MnO	0.3	0.32	0.27	0.29	0.25	0.29	0.19	0.41	0.29	0	0
MgO	12.89	12.76	13.48	17.86	18.68	18.2	22.05	13.59	12.39	11.2	13.5
CaO	10.18	7.83	11.93	8.77	5.8	9.27	7.11	5.89	9.57	11.5	7.35
Na ₂ O	0.69	1	0.64	0.35	0.53	0.58	0.33	0.93	0.75	0.23	0.35
K ₂ O	0	0	0	0	0	0	0		0	0.01	0
Total	100.69	99.71	100.27	99.63	99.5	99.23	99.89	100.76	99.78	99.44	100.02
Cations based on 12 oxygens											
Si ⁴⁺	3.167	3.18	3.216	3.241	3.317	3.316	3.429	3.08	3.091	3.025	3.033
Ti ⁴⁺	0.05	0.013	0.064	0.031	0.043	0.044	0.042	0.007	0.109	0.014	0.017
Al ³⁺	1.528	1.659	1.422	1.37	1.289	1.275	0.962	1.847	1.578	1.945	1.938
Cr ³⁺	0	0.004	0.004	0.006	0.01	0.003	0.011	0.006	0.008	0.003	0.006
Fe ²⁺	0.971	0.987	0.804	0.708	0.79	0.596	0.635	1.006	0.99	0.827	0.903
Mn ²⁺	0.019	0.02	0.017	0.018	0.015	0.018	0.012	0.025	0.018	0	0
Mg ²⁺	1.427	1.415	1.487	1.95	2.035	1.98	2.376	1.486	1.388	1.241	1.478
Ca ²⁺	0.81	0.624	0.946	0.688	0.454	0.725	0.551	0.463	0.77	0.916	0.578
Na ⁺	0.099	0.144	0.092	0.05	0.075	0.082	0.046	0.132	0.109	0.033	0.05
K ⁺	0	0	0	0	0	0	0		0	0.001	0
Total	8.069	8.047	8.053	8.064	8.028	8.041	8.065	8.053	8.061	8.004	8.003
P this study	13.6	15.6	13.9	12.9	14.9	15.1	15.5	13.8	12.2	7.7	8.9
P C10	11.9	12.0	12.8	12.1	13.8	14.0	15.7	10.0	11.7	7.0	7.5

Appendix 3 continued

Compositions of pyroxenitic majorite inclusions in diamonds

Sample	#13	#6	SI5-6	odd1-24	JF-01	JF-09	JF-37	JF-50	JF-58	JF-44	
Location	Premier	Premier	Slave	Jagersfontein							
SiO ₂	41.7	42.3	42.1	47.91	45.73	42.6	42.4	42.4	42.5	43.5	44.1
TiO ₂	0.86	0.25	0.44	0.68	0.28	0.14	0.09	0.18	0.09	0.28	0.32
Al ₂ O ₃	20.6	22.2	21.7	9.01	15.31	20	21	20.7	21	18.3	17.9
Cr ₂ O ₃	0.29	0.21	0.07	0.53	0.29	0.24	0.08	0.13	0.15	0.18	0.31
FeO	12.3	14.3	15.5	13.22	12.48	12.6	14.1	12.9	13.2	14.7	11.8
MnO	0	0	0.34	0.3	0.31	0.42	0.4	0.38	0.36	0.41	0.3
MgO	18.6	16.8	16.6	22.04	18.84	17.6	16.2	16.9	17.7	18.3	17.7
CaO	4.66	4.14	3.03	5.32	6.38	6.14	6.11	6.43	4.87	4.62	7.97
Na ₂ O	0.13	0.03	0.33	0.55	0.37	0.15	0.2	0.14	0.19	0.27	0.18
K ₂ O	0	0									
Total	99.14	100.23	100.1	99.56	99.99	99.9	100.59	100.16	100.06	100.56	100.58
Cations based on 12 oxygens											
Si ⁴⁺	3.04	3.059	3.064	3.51	3.32	3.1	3.08	3.081	3.08	3.161	3.19
Ti ⁴⁺	0.047	0.014	0.024	0.037	0.015	0.008	0.005	0.01	0.005	0.015	0.017
Al ³⁺	1.77	1.892	1.862	0.778	1.311	1.716	1.799	1.773	1.794	1.568	1.526
Cr ³⁺	0.017	0.012	0.004	0.031	0.017	0.014	0.005	0.007	0.009	0.01	0.018
Fe ²⁺	0.75	0.865	0.943	0.81	0.758	0.767	0.857	0.784	0.8	0.893	0.714
Mn ²⁺	0	0	0.021	0.019	0.019	0.026	0.025	0.023	0.022	0.025	0.018
Mg ²⁺	2.021	1.811	1.801	2.406	2.039	1.909	1.754	1.83	1.912	1.982	1.908
Ca ²⁺	0.364	0.321	0.236	0.418	0.496	0.479	0.476	0.501	0.378	0.36	0.618
Na ⁺	0.018	0.004	0.047	0.078	0.052	0.021	0.028	0.02	0.027	0.038	0.025
K ⁺	0	0									
Total	8.028	7.977	8.002	8.087	8.027	8.038	8.027	8.029	8.027	8.053	8.034
P this study	8.5	7.1	9.3	17.4	14.3	8.5	8.4	8.1	8.3	10.8	10.8
P C10	7.9	7.0	8.2	17.8	13.0	8.4	8.0	8.0	8.0	10.1	10.3

Appendix 3 continued

Sample	JF-84	JF-39	JF-42	JF-48	JF-22	bz7-3	bz22-1	BZ43, maj	BZ19, maj	BZ19, bulk	BZ43, bulk
Location	Jagersfontein	Jagersfontein	Jagersfontein	Jagersfontein	Jagersfontein	Juina, Sao Luiz	Juina, Sao Luiz	Juina, Sao Luiz	Juina, Sao Luiz	Juina, Sao Luiz	Juina, Sao Luiz
SiO ₂	44.3	45.2	43.4	41.8	48.7	45.7	42.3	43.33	43.72	45.03	45.98
TiO ₂	0.41	0.31	0.54	0.19	0.5	2.31	1.99	1.48	1.59	1.49	1.42
Al ₂ O ₃	17.3	15	17.4	21.6	9.65	12.71	17.82	15.95	16.66	14.91	14.21
Cr ₂ O ₃	0.3	0.24	0.03	0.11	0.22	0.27	0.08	0.15	0.12	0.12	0.13
FeO	11.7	10.8	12.9	13.8	11.7	11.57	12.12	12.13	11.18	10.4	10.99
MnO	0.31	0.24	0.36	0.4	0.36	0.21	0.24	0.25	0.22	0.2	0.21
MgO	18.8	20.3	13.4	16.2	21.7	21.91	10.33	13.92	14.29	13.99	13.59
CaO	6.36	5.67	11.16	5.89	5.73	4.77	14.08	11.72	11.73	12.19	11.29
Na ₂ O	0.3	0.37	0.54	0.13	0.65	0.58	1.15	0.97	0.9	1.49	2.16
K ₂ O											
Total	99.78	98.13	99.7	100.12	99.4	100.11	100.32	99.9	100.58	100	100
Cations based on 12 oxygens											
Si ⁴⁺	3.215	3.315	3.216	3.046	3.549	3.307	3.15	3.215	3.2	3.316	3.383
Ti ⁴⁺	0.022	0.017	0.03	0.01	0.027	0.126	0.111	0.083	0.088	0.083	0.079
Al ³⁺	1.48	1.297	1.52	1.856	0.829	1.084	1.565	1.395	1.437	1.295	1.233
Cr ³⁺	0.017	0.014	0.002	0.006	0.013	0.015	0.005	0.003	0.002	0.002	0.003
Fe ²⁺	0.71	0.663	0.799	0.841	0.713	0.7	0.755	0.753	0.684	0.641	0.676
Mn ²⁺	0.019	0.015	0.023	0.025	0.022	0.013	0.015	0.016	0.014	0.012	0.013
Mg ²⁺	2.034	2.219	1.48	1.759	2.357	2.363	1.146	1.539	1.559	1.536	1.49
Ca ²⁺	0.495	0.446	0.886	0.46	0.447	0.37	1.124	0.932	0.92	0.962	0.89
Na ⁺	0.042	0.053	0.078	0.018	0.092	0.081	0.166	0.14	0.128	0.213	0.308
K ⁺											
Total	8.035	8.038	8.032	8.022	8.049	8.059	8.037	8.074	8.041	8.059	8.075
P this study	12.1	14.3	13.6	7.2	18.4	12.5	14.1	15.0	14.4	17.3	18.6
P C10	11.1	13.0	11.8	7.3	18.2	15.5	13.5	14.1	13.6	17.0	19.8

Appendix 3 continued

Sample	S-6	A2-01	A1-23	A1-32	A2-05	A4-04	A6-01	A1-14	A4-14	A4-10
Location	Monastery									
SiO ₂	46.11	44.25	42.65	41.83	42.85	41.82	42.12	42.34	42.7	42.53
TiO ₂	0.46	0.57	0.89	0.7	1.08	1.13	0.79	1.27	1.1	1.41
Al ₂ O ₃	15.64	15.87	17.46	18.61	19.01	18.05	17.41	17.05	17.42	16.51
Cr ₂ O ₃	0.43	0.11	0	0.01	0.18	0.09	0.06	0.11	0.07	0.06
FeO	8.04	11.56	15.63	16.7	14.82	13.48	13.98	13.33	12.65	14.04
MnO	0	0.29	0.3	0.28	0.29	0.27	0.3	0.3	0.26	0.28
MgO	20.88	17.86	12.89	8.54	17.64	10.23	12.58	13.38	12.15	13.31
CaO	8.16	8.77	10.18	12.89	4.37	13.23	11.73	11.27	13.09	11.34
Na ₂ O	0	0.35	0.69	0.95	0.23	0.66	0.56	0.55	0.65	0.6
K ₂ O										
Total	99.72	99.63	100.69	100.54	100.56	99.61	99.53	99.6	100.09	100.08
Cations based on 12 oxygens										
Si ⁴⁺	3.3	3.241	3.167	3.151	3.117	3.158	3.157	3.159	3.173	3.17
Ti ⁴⁺	0.025	0.031	0.05	0.04	0.059	0.064	0.045	0.071	0.061	0.079
Al ³⁺	1.32	1.371	1.528	1.653	1.63	1.607	1.538	1.5	1.526	1.451
Cr ³⁺	0.024	0.006	0	0.001	0.01	0.005	0.004	0.006	0.004	0.004
Fe ²⁺	0.481	0.708	0.971	1.052	0.901	0.851	0.876	0.832	0.786	0.875
Mn ²⁺	0	0.018	0.019	0.018	0.018	0.017	0.019	0.019	0.016	0.018
Mg ²⁺	2.227	1.95	1.426	0.959	1.912	1.151	1.405	1.488	1.345	1.479
Ca ²⁺	0.626	0.688	0.81	1.04	0.341	1.07	0.942	0.901	1.042	0.906
Na ⁺	0	0.05	0.099	0.139	0.032	0.097	0.081	0.08	0.094	0.087
K ⁺										
Total	8.003	8.064	8.069	8.052	8.02	8.02	8.068	8.056	8.048	8.067
P this study	12.2	12.9	13.6	14.8	10.5	13.2	12.7	12.6	13.4	12.6
P C10	11.7	12.1	11.9	11.9	9.7	11.6	11.4	11.8	12.0	12.3

Appendix 3 continued

Compositions of peridotitic majorite inclusions in diamonds

Sample	A4-06	A2-06	A2-01	B9-15	B9-07	G204-206	#2/13	Po-99
Location	Monastery	Monastery	Monastery	Monastery	Monastery	Birim	Arkhangelsk	Arkhangelsk
SiO ₂	42.43	43.62	44.25	45.31	45.94	41.93	43.2	44.9
TiO ₂	1.02	1.57	0.57	0.49	0.89	0.61	0.02	0.71
Al ₂ O ₃	17.08	16.33	15.87	15.32	13.59	19.52	20.4	16.6
Cr ₂ O ₃	0.01	0.37	0.11	0.15	0.25	1.9	3	1.23
FeO	14.93	12.73	11.56	11.17	11.34	11.8	5.8	8.65
MnO	0.27	0.28	0.29	0.25	0.26	0.27	0.23	0.21
MgO	11.94	20.49	17.86	17.18	18.76	19.5	24.1	23.5
CaO	11.64	4.07	8.77	10.23	7.66	3.91	2.94	3.77
Na ₂ O	0.48	0.28	0.35	0.5	0.4	0	0.05	0.25
K ₂ O								
Total	99.8	99.74	99.35	100.6	100.09	99.44	99.74	99.82
Cations based on 12 oxygens								
Si ⁴⁺	3.181	3.173	3.241	3.291	3.365	3.051	3.046	3.2
Ti ⁴⁺	0.058	0.086	0.031	0.027	0.049	0.033	0.001	0.038
Al ³⁺	1.51	1.4	1.371	1.312	1.174	1.675	1.695	1.394
Cr ³⁺	0.001	0.021	0.006	0.009	0.014	0.109	0.167	0.069
Fe ²⁺	0.936	0.774	0.708	0.678	0.695	0.718	0.342	0.516
Mn ²⁺	0.017	0.017	0.018	0.015	0.016	0.017	0.014	0.013
Mg ²⁺	1.334	2.221	1.95	1.86	2.048	2.115	2.532	2.496
Ca ²⁺	0.935	0.317	0.688	0.796	0.601	0.305	0.222	0.288
Na ⁺	0.07	0.039	0.05	0.07	0.057	0	0.007	0.035
K ⁺								
Total	8.041	8.05	8.064	8.058	8.02	8.023	8.026	8.048
P this study	12.6	11.4	12.9	14.5	14.9	7.7	6.3	11.6
P C10	11.6	11.6	12.1	13.2	14.4	7.5	7.0	11.1

Appendix 3 continued

Sample	G303-305h	L08	L09	L10	L16	S02	S04-2	S04-3	S5(1)	S06-1	S10(1)
Location	Birim	China, pipe No 50	China, pipe No 50	China, pipe No 50	China, pipe No 50	China, Shengli 1					
SiO ₂	40.8	42.44	42.95	42.42	41.69	41.43	41.8	42.16	41.69	42.09	42.33
TiO ₂	0.02	0.02	0	0.03	0.02	0.04	0.07	0.07	0.19	0.08	0.05
Al ₂ O ₃	7	14.76	18.82	17.69	13.33	11.18	15.74	15.34	13.75	17.48	13.85
Cr ₂ O ₃	20.56	11.3	5.96	6.73	12.85	15.35	9.49	10.3	11.88	7.82	12.27
FeO	6.73	5.83	5.63	6.37	6.63	6.85	6.7	7.1	7	6.15	5.08
MnO	0.29	0.33	0.27	0.33	0.4	0.5	0.42	0.49	0.44	0.39	0.29
MgO	22.7	22.75	23.94	20.37	19.43	20.69	19.58	19.97	20.26	19.2	24.26
CaO	1.57	2.35	1.66	5.77	5.39	4.52	5.49	5.42	4.78	6.65	1.7
Na ₂ O	0.11	0.01	0	0.01	0.03	0.03	0	0	0.02	0.04	0.02
K ₂ O											
Total	99.78	99.8	99.23	99.77	99.79	100.63	99.29	100.85	100.02	99.92	99.88
Cations based on 12 oxygens											
Si ⁴⁺	3.062	3.068	3.056	3.061	3.072	3.055	3.062	3.053	3.057	3.047	3.055
Ti ⁴⁺	0.001	0.001	0	0.002	0.001	0.002	0.004	0.004	0.01	0.004	0.003
Al ³⁺	0.619	1.258	1.579	1.505	1.158	0.972	1.359	1.31	1.189	1.492	1.178
Cr ³⁺	1.22	0.646	0.335	0.384	0.749	0.895	0.55	0.59	0.689	0.448	0.7
Fe ²⁺	0.422	0.352	0.335	0.384	0.409	0.422	0.41	0.43	0.429	0.372	0.307
Mn ²⁺	0.018	0.02	0.016	0.02	0.025	0.031	0.026	0.03	0.027	0.024	0.018
Mg ²⁺	2.539	2.451	2.539	2.19	2.134	2.273	2.138	2.155	2.214	2.072	2.609
Ca ²⁺	0.126	0.182	0.127	0.446	0.426	0.357	0.431	0.421	0.376	0.516	0.131
Na ⁺	0.016	0.001	0	0.001	0.004	0.004	0	0	0.003	0.006	0.003
K ⁺											
Total	8.025	7.98	7.987	7.994	7.976	8.012	7.98	7.993	7.995	7.981	8.004
P this study	6.9	6.2	6.0	6.3	6.5	6.1	6.3	6.1	6.6	6.3	6.1
P C10	7.4	6.9	6.7	6.9	7.0	7.0	6.8	6.8	7.0	6.6	6.9

Appendix 3 continued

Sample	S24(1)	S30(2)-1	Xiyu-1	#9	#10	B5-1	W2-1	Al-15
Location	China, Shengli 1	China, Shengli 1	China, Shengli 1	Droujba	Droujba	Jagersfontein	Jagersfontein	Monastery
SiO ₂	42.7	42.26	41.71	43.2	44	41.3	40.3	46.3
TiO ₂	0	0.04	0.01	0.69	0.34	0.71	0.59	1.05
Al ₂ O ₃	15.92	15.19	11.67	19.9	21.3	19.4	17.5	13.6
Cr ₂ O ₃	9.57	8.92	14.13	2.18	0.83	1.27	1.93	1.2
FeO	5.91	5.81	6.45	8.11	7.62	12.8	15.5	9.07
MnO	0.31	0.28	0.39	0.24	0.38	0	0	0.23
MgO	24.04	22.73	21.99	22.7	21.3	18.2	16.8	23.6
CaO	1.73	3.35	3.23	4.37	4.12	5.28	5.42	5.16
Na ₂ O	0	0.03	0	0.06	0.12	0.07	0	0.14
K ₂ O								
Total	100.2	98.64	99.57	101.45	100.01	99.03	98.04	
Si ⁴⁺	3.054	3.081	3.075	3.036	3.103	3.04	3.05	3.302
Ti ⁴⁺	0	0.002	0.001	0.036	0.018	0.039	0.034	0.056
Al ³⁺	1.342	1.305	1.014	1.648	1.771	1.683	1.562	1.143
Cr ³⁺	0.541	0.514	0.824	0.121	0.046	0.074	0.116	0.068
Fe ²⁺	0.353	0.354	0.398	0.477	0.449	0.788	0.981	0.541
Mn ²⁺	0.019	0.017	0.024	0.014	0.023	0	0	0.014
Mg ²⁺	2.562	2.469	2.416	2.378	2.239	1.997	1.895	2.509
Ca ²⁺	0.133	0.262	0.255	0.329	0.311	0.416	0.44	0.394
Na ⁺	0	0.004	0	0.008	0.016	0.01	0	0.019
K ⁺								
Total	8.004	8.009	8.006	8.047	7.978	8.047	8.077	8.046
P this study	5.9	6.8	6.3	7.7	8.6	8.0	7.8	12.8
P C10	6.8	7.4	7.2	7.7	8.0	7.8	8.0	13.0

Appendix 3 continued

Sample	A3-01	12	P-98	P-50	#2	#7	SI3-31	SI3-30	
Location	Monastery	Mwadui	Premier	Premier	Premier	Premier	Slave	Slave	
SiO ₂	43.77	41.9	41.8	44	42.6	43.1	42.2	42.3	
TiO ₂	0.51	0.03	0.11	0.07	0.07	0.3	0.19	0.06	
Al ₂ O ₃	16.19	16.1	15.5	19.23	15.2	17.2	12.3	9.46	
Cr ₂ O ₃	5.34	8.06	10.2	2.75	9.59	6.53	11.8	12.8	
FeO	7.23	5.36	5.7	5.63	5.34	5.81	6.52	7.64	
MnO	0.27	0	0.28	0.21	0	0	0.32	0.33	
MgO	22.86	22.8	22.5	24.9	23	21.8	21.1	21.2	
CaO	3.66	4.14	3.26	1.9	3.85	5.3	4.68	5.11	
Na ₂ O	0.07	0.75	0	0	0.09	0.08	0.03	0.01	
K ₂ O									
Total	99.9	99.14	99.35	98.69	99.74	100.12	99.1	99	
Cations based on 12 oxygens									
Si ⁴⁺	3.134	3.038	3.035	3.117	3.07	3.08	3.114	3.166	
Ti ⁴⁺	0.027	0.002	0.006	0.004	0.004	0.016	0.011	0.003	
Al ³⁺	1.367	1.376	1.326	1.605	1.291	1.449	1.07	0.835	
Cr ³⁺	0.302	0.462	0.585	0.154	0.546	0.369	0.688	0.757	
Fe ²⁺	0.433	0.325	0.346	0.334	0.322	0.347	0.402	0.478	
Mn ²⁺	0.016	0	0.017	0.013	0	0	0.02	0.021	
Mg ²⁺	2.439	2.464	2.435	2.629	2.47	2.322	2.32	2.364	
Ca ²⁺	0.281	0.322	0.254	0.144	0.297	0.406	0.37	0.41	
Na ⁺	0.01	0.105	0	0	0.013	0.011	0.004	0.001	
K ⁺									
Total	8.009	8.094	8.004	8	8.014	8	7.999	8.036	
P this study	9.3	11.9	5.9	7.7	7.1	7.7	7.8	8.1	
P C10	9.0	9.0	6.6	8.0	7.5	7.7	8.1	9.2	

References

- Akaogi, M., Akimoto, S.-i., 1977. Pyroxene-garnet solid-solution equilibria in the systems Mg₄Si₄O₁₂ • Mg₃Al₂Si₃O₁₂ and Fe₄Si₄O₁₂ • Fe₃Al₂Si₃O₁₂ at high pressures and temperatures. *Phys. Earth Planet. Inter.* 15, 90-106.
- Anderson, D.L., 1979. Chemical Stratification of the Mantle. *J. Geophys. Res.* 84, 6297-6298.
- Anderson, O.L., Isaak, D.G., 1995. Elastic constants of mantle minerals at high temperature. *Mineral Physics & Crystallography: A Handbook of Physical Constants*, 64-97.
- Angel, R.J., 2000. Equations of state. *Reviews in mineralogy and geochemistry* 41, 35-59.
- Angel, R.J., Alvaro, M., Gonzalez-Platas, J., 2014. EosFit7c and a Fortran module (library) for equation of state calculations, *Zeitschrift für Kristallographie - Crystalline Materials*, p. 405.
- Angel, R.J., Finger, L.W., 2011. SINGLE: a program to control single-crystal diffractometers. *Journal of Applied Crystallography* 44, 247-251.
- Aoki, I., Takahashi, E., 2004. Density of MORB eclogite in the upper mantle. *Phys. Earth Planet. Inter.* 143, 129-143.
- Aoki, K.-I., Kanisawa, S., 1979. Fluorine contents of some hydrous minerals derived from upper mantle and lower crust. *Lithos* 12, 167-171.
- Aoki, K., Ishiwaka, K., Kanisawa, S., 1981. Fluorine geochemistry of basaltic rocks from continental and oceanic regions and petrogenetic application. *Contrib. Mineral. Petrol.* 76, 53-59.
- Ashchepkov, I.V., Pokhilenko, N.P., Vladykin, N.V., Logvinova, A.M., Afanasiev, V.P., Pokhilenko, L.N., Kuligin, S.S., Malygina, E.V., Alymova, N.A., Kostrovitsky, S.I., 2010. Structure and evolution of the lithospheric mantle beneath Siberian craton, thermobarometric study. *Tectonophysics* 485, 17-41.
- Babuška, V., Fiala, J., Kumazawa, M., Ohno, I., Sumino, Y., 1978. Elastic properties of garnet solid-solution series. *Phys. Earth Planet. Inter.* 16, 157-176.
- Bailey, J.C., 1977. Fluorine in granitic rocks and melts: A review. *Chemical Geology* 19, 1-42.
- Bass, J.D., 1989. Elasticity of grossular and spessartite garnets by Brillouin spectroscopy. *Journal of Geophysical Research: Solid Earth* 94, 7621-7628.
- Bass, J.D., Liebermann, R.C., Weidner, D.J., Finch, S.J., 1981. Elastic properties from acoustic and volume compression experiments. *Phys. Earth Planet. Inter.* 25, 140-158.
- Beard, B., Fraracci, K.N., Clayton, R.A., Mayeda, T.K., Snyder, G., Sobolev, N., Taylor, L., 1996. Petrography and geochemistry of eclogites from the Mir kimberlite, Yakutia, Russia. *Contrib. Mineral. Petrol.* 125, 293-310.
- Berman, R.G., 1990. Mixing properties of Ca-Mg-Fe-Mn garnets. *Am. Miner.* 75, 328-344.
- Berman, R.G., Koziol, A.M., 1991. Ternary excess properties of grossular - pyrope - almandine garnet and their influence in geothermobarometry. *Am. Miner.* 76, 1223-1231.
- Bernini, D., Wiedenbeck, M., Dolejš, D., Keppler, H., 2013. Partitioning of halogens between mantle minerals and aqueous fluids: implications for the fluid flow regime in subduction zones. *Contrib. Mineral. Petrol.* 165, 117-128.
- Beyer, C., Frost, D.J., Miyajima, N., 2015. Experimental calibration of a garnet-clinopyroxene geobarometer for mantle eclogites. *Contrib. Mineral. Petrol.* 169, 1-21.

- Beyer, C., Klemme, S., Wiedenbeck, M., Stracke, A., Vollmer, C., 2012. Fluorine in nominally fluorine-free mantle minerals: Experimental partitioning of F between olivine, orthopyroxene and silicate melts with implications for magmatic processes. *Earth and Planetary Science Letters* 337–338, 1-9.
- Bina, C.R., Helffrich, G., 2014. 3.2 - Geophysical Constraints on Mantle Composition, in: Turekian, H.D.H.K. (Ed.), *Treatise on Geochemistry (Second Edition)*. Elsevier, Oxford, pp. 41-65.
- Birch, F., 1947. Finite elastic strain of cubic crystals. *Physical Review* 71, 809.
- Birch, F., 1986. Equation of state and thermodynamic parameters of NaCl to 300 kbar in the high-temperature domain. *Journal of Geophysical Research: Solid Earth (1978–2012)* 91, 4949-4954.
- Boehler, R., De Hantsetters, K., 2004. New anvil designs in diamond-cells. *High Pressure Research* 24, 391-396.
- Boyd, F.R., England, J.L., 1960. Apparatus for phase-equilibrium measurements at pressures up to 50 kilobars and temperatures up to 1750 degrees C. *Journal of Geophysical Research* 65, 741-748.
- Brey, G., Köhler, T., 1990. Geothermobarometry in four-phase lherzolites II. New thermobarometers, and practical assessment of existing thermobarometers. *Journal of Petrology* 31, 1353-1378.
- Brey, G., Nickel, K., Kogarko, L., 1986. Garnet-pyroxene equilibria in the system CaO-MgO-Al₂O₃-SiO₂ (CMAS): prospects for simplified ('T-independent') lherzolite barometry and an eclogite-barometer. *Contrib. Mineral. Petrol.* 92, 448-455.
- Brey, G.P., Köhler, T., Nickel, K.G., 1990. Geothermobarometry in Four-phase Lherzolites I. Experimental Results from 10 to 60 kb. *Journal of Petrology* 31, 1313-1352.
- Bromiley, D.W., Kohn, S.C., 2007. Comparisons between fluoride and hydroxide incorporation in nominally anhydrous and fluorine-free mantle minerals. *Geochimica et Cosmochimica Acta* 71, A124.
- Bulanova, G.P., Walter, M.J., Smith, C.B., Kohn, S.C., Armstrong, L.S., Blundy, J., Gobbo, L., 2010. Mineral inclusions in sublithospheric diamonds from Collier 4 kimberlite pipe, Juina, Brazil: subducted protoliths, carbonated melts and primary kimberlite magmatism. *Contrib. Mineral. Petrol.* 160, 489-510.
- Bundy, F., 1962. General principles of high pressure apparatus design. *Modern Very High Pressure Techniques*, 1-24.
- Carmichael, R.S., 1989. *Practical handbook of physical properties of rocks and minerals*. CRC press.
- Carswell, D., Dawson, J., Gibb, F., 1981. Equilibration conditions of upper-mantle eclogites: implications for kyanite-bearing and diamondiferous varieties. *Mineral. Mag.* 44, 79-89.
- Cartigny, P., 2005. Stable Isotopes and the Origin of Diamond. *Elements* 1, 79-84.
- Chai, M., Brown, J.M., Slutsky, L.J., 1997. The elastic constants of a pyrope-grossular-almandine garnet to 20 Gpa. *Geophysical Research Letters* 24, 523-526.
- Chen, G., Miletich, R., Mueller, K., Spetzler, H.A., 1997. Shear and compressional mode measurements with GHz ultrasonic interferometry and velocity-composition systematics for the pyrope-almandine solid solution series. *Phys. Earth Planet. Inter.* 99, 273-287.
- Cheng, W., Ganguly, J., 1994. Some aspects of multicomponent excess free energy models with subregular binaries. *Geochimica et Cosmochimica Acta* 58, 3763-3767.
- Coleman, R.G., Lee, D.E., Beatty, L.B., Brannock, W.W., 1965. Eclogites and Eclogites: Their Differences and Similarities. *Geological Society of America Bulletin* 76, 483-508.
- Collerson, K.D., Hapugoda, S., Kamber, B.S., Williams, Q., 2000. Rocks from the mantle transition zone: majorite-bearing xenoliths from Malaita, Southwest Pacific. *Science* 288, 1215-1223.

- Collerson, K.D., Williams, Q., Kamber, B.S., Omori, S., Arai, H., Ohtani, E., 2010. Majoritic garnet: A new approach to pressure estimation of shock events in meteorites and the encapsulation of sub-lithospheric inclusions in diamond. *Geochimica et Cosmochimica Acta* 74, 5939-5957.
- Connolly, J., Kerrick, D., 2002. Metamorphic controls on seismic velocity of subducted oceanic crust at 100–250 km depth. *Earth and Planetary Science Letters* 204, 61-74.
- Conrad, P.G., Zha, C.S., Mao, H.K., Hemley, R.J., 1999. The high-pressure, single-crystal elasticity of pyrope, grossular, and andradite. *Am. Miner.* 84, 374-383.
- Cordier, P., Rubie, D.C., 2001. Plastic deformation of minerals under extreme pressure using a multi-anvil apparatus. *Materials Science and Engineering: A* 309, 38-43.
- Cosca, M.A., Peacor, D.R., 1987. Chemistry and structure of esseneite (CaFe (super 3+) AlSiO 6), a new pyroxene produced by pyrometamorphism. *Am. Miner.* 72, 148-156.
- Crépeisson, C., Blanchard, M., Bureau, H., Sanloup, C., Withers, A.C., Khodja, H., Surblé, S., Raepsaet, C., Béneut, K., Leroy, C., 2014. Clumped fluoride-hydroxyl defects in forsterite: Implications for the upper-mantle. *Earth and Planetary Science Letters* 390, 287-295.
- Dalou, C., Koga, K., Le Voyer, M., Shimizu, N., 2014. Contrasting partition behavior of F and Cl during hydrous mantle melting: implications for Cl/F signature in arc magmas. *Prog. in Earth and Planet. Sci.* 1, 1-17.
- Dalou, C., Koga, K., Shimizu, N., Boulon, J., Devidal, J.-L., 2012. Experimental determination of F and Cl partitioning between lherzolite and basaltic melt. *Contrib. Mineral. Petrol.* 163, 591-609.
- Dasgupta, R., Hirschmann, M.M., Withers, A.C., 2004. Deep global cycling of carbon constrained by the solidus of anhydrous, carbonated eclogite under upper mantle conditions. *Earth and Planetary Science Letters* 227, 73-85.
- Davies, R., Pearson, N., O'reilly, S., Griffin, W., Andrew, A., Doyle, B., 2000. Diamonds from the deep: pipe DO-27, Slave Craton, Canada, Research Report 1995-2000.
- Davies, R.M., Griffin, W.L., O'Reilly, S.Y., McCandless, T.E., 2004. Inclusions in diamonds from the K14 and K10 kimberlites, Buffalo Hills, Alberta, Canada: diamond growth in a plume? *Lithos* 77, 99-111.
- Dawson, J., Carswell, D., 1990. High temperature and ultra-high pressure eclogites. *Eclogite Facies Rocks*, 314-349.
- Debye, P., 1912. On the theory of specific heats. *The Collected Papers of Peter JW Debye*, 650-696.
- Du, W., Clark, S.M., Walker, D., 2015. Thermo-compression of pyrope-grossular garnet solid solutions: Non-linear compositional dependence. *Am. Miner.* 100, 215-222.
- Duba, A., Olinger, B., 1972. Compression of garnet to 100 kilobars. *Journal of Geophysical Research* 77, 2496-2499.
- Dubrovinsky, L., Dubrovinskaia, N., Prakapenka, V.B., Abakumov, A.M., 2012. Implementation of micro-ball nanodiamond anvils for high-pressure studies above 6[thinsp]Mbar. *Nat Commun* 3, 1163.
- Edgar, A., Charbonneau, H., 1991. Fluorine-bearing phases in lamproites. *Mineral. Petrol.* 44, 125-149.
- Edgar, A., Charbonneau, H., Mitchell, R., 1992. Phase relations of an armalcolite-phlogopite lamproite from Smoky Butte, Montana: applications to lamproite genesis. *Journal of Petrology* 33, 505-520.
- Edgar, A., Pizzolato, L., 1995. An experimental study of partitioning of fluorine between K-richrichterite, apatite, phlogopite, and melt at 20 kbar. *Contrib. Mineral. Petrol.* 121, 247-257.

- Edgar, A.D., Lloyd, F.E., Vukadinovic, D., 1994. The role of fluorine in the evolution of ultrapotassic magmas. *Mineral. Petrol.* 51, 173-193.
- Edgar, A.D., Mitchell, R.H., 1997. Ultra high pressure–temperature melting experiments on an SiO₂-rich lamproite from Smoky Butte, Montana: derivation of siliceous lamproite magmas from enriched sources deep in the continental mantle. *Journal of Petrology* 38, 457-477.
- Edgar, A.D., Vukadinovic, D., 1993. Potassium-rich clinopyroxene in the mantle: An experimental investigation of a K-rich lamproite up to 60 kbar. *Geochimica et Cosmochimica Acta* 57, 5063-5072.
- Ellis, D.J., Green, D.H., 1979. An experimental study of the effect of Ca upon garnet-clinopyroxene Fe-Mg exchange equilibria. *Contrib. Mineral. Petrol.* 71, 13-22.
- Fabrizio, A., Stalder, R., Hametner, K., Günther, D., 2013a. Experimental chlorine partitioning between forsterite, enstatite and aqueous fluid at upper mantle conditions. *Geochimica et Cosmochimica Acta* 121, 684-700.
- Fabrizio, A., Stalder, R., Hametner, K., Günther, D., Marquardt, K., 2013b. Experimental partitioning of halogens and other trace elements between olivine, pyroxenes, amphibole and aqueous fluid at 2 GPa and 900–1,300 C. *Contrib. Mineral. Petrol.* 166, 639-653.
- Fabrichnaya, O., Seifert, H.J., Ludwig, T., Aldinger, F., Navrotsky, A., 2001. The assessment of thermodynamic parameters in the Al₂O₃-Y₂O₃ system and phase relations in the Y-Al-O system. *Scandinavian journal of metallurgy* 30, 175-183.
- Fan, D.W., Zhou, W.G., Liu, C.Q., Liu, Y.G., Wan, F., Xing, Y.S., Liu, J., Bai, L.G., Xie, H.S., 2009. The thermal equation of state of (Fe_{0.86}Mg_{0.07}Mn_{0.07})₃Al₂Si₃O₁₂ almandine. *Mineral. Mag.* 73, 95-102.
- Filiberto, J., Wood, J., Dasgupta, R., Shimizu, N., Le, L., Treiman, A.H., 2012. Effect of fluorine on near-liquidus phase equilibria of an Fe–Mg rich basalt. *Chemical Geology* 312–313, 118-126.
- Flesch, L.M., Li, B., Liebermann, R.C., 1998. Sound velocities of polycrystalline MgSiO₃-orthopyroxene to 10 GPa at room temperature. *Am. Miner.* 83, 444-450.
- Foley, S., 1991. High-pressure stability of the fluor- and hydroxy-endmembers of pargasite and K-richterite. *Geochimica et Cosmochimica Acta* 55, 2689-2694.
- Foley, S., 1992. Vein-plus-wall-rock melting mechanisms in the lithosphere and the origin of potassic alkaline magmas. *Lithos* 28, 435-453.
- Foley, S., Taylor, W., Green, D., 1986. The effect of fluorine on phase relationships in the system KAlSiO₄-Mg₂SiO₄-SiO₂ at 28 kbar and the solution mechanism of fluorine in silicate melts. *Contrib. Mineral. Petrol.* 93, 46-55.
- Frost, D.J., Dolejš, D., 2007. Experimental determination of the effect of H₂O on the 410-km seismic discontinuity. *Earth and Planetary Science Letters* 256, 182-195.
- Frost, D.J., Poe, B.T., Trønnes, R.G., Liebske, C., Duba, A., Rubie, D.C., 2004. A new large-volume multianvil system. *Phys. Earth Planet. Inter.* 143–144, 507-514.
- Fukao, Y., Obayashi, M., Inoue, H., Nenbai, M., 1992. Subducting slabs stagnant in the mantle transition zone. *Journal of Geophysical Research: Solid Earth* 97, 4809-4822.
- Fukao, Y., Obayashi, M., Nakakuki, T., 2009. Stagnant Slab: A Review. *Annu. Rev. Earth Planet. Sci.* 37, 19-46.
- Ganguly, J., 2008. *Thermodynamics in earth and planetary sciences*. Springer.

- Ganguly, J., Cheng, W.J., Oneill, H.S., 1993. Syntheses, volume, and structural changes of garnets in the pyrope-grossular join - implications for stability and mixing properties. *Am. Miner.* 78, 583-593.
- Ganguly, J., Cheng, W.J., Tirone, M., 1996. Thermodynamics of aluminosilicate garnet solid solution: New experimental data, an optimized model, and thermometric applications. *Contrib. Mineral. Petrol.* 126, 137-151.
- Ganguly, J., Saxena, S.K., 1984. Mixing properties of aluminosilicate garnets - constraints from natural and experimental data, and applications to geothermobarometry. *Am. Miner.* 69, 88-97.
- Gasparik, T., 1989. Transformation of enstatite - diopside - jadeite pyroxenes to garnet. *Contrib. Mineral. Petrol.* 102, 389-405.
- Gasparik, T., 1996. Diopside-jadeite join at 16–22 GPa. *Phys. Chem. Miner.* 23, 476-486.
- Gasparik, T., Tripathi, A., Parise, J.B., 2000. Structure of a new Al-rich phase, $[K, Na]_{0.9} [Mg, Fe]_2 [Mg, Fe, Al, Si]_{6O12}$, synthesized at 24 GPa. *Am. Miner.* 85, 613-618.
- Geiger, C.A., 1999. Thermodynamics of $(Fe^{2+}, Mn^{2+}, Mg, Ca)_3-Al_2Si_3O_{12}$ garnet: a review and analysis. *Mineral. Petrol.* 66, 271-299.
- Geiger, C.A., 2000. Volumes of mixing in aluminosilicate garnets: Solid solution and strain behavior. *Am. Miner.* 85, 893-897.
- Geiger, C.A., Feenstra, A., 1997. Molar volumes of mixing of almandine-pyrope and almandine-spessartine garnets and the crystal chemistry and thermodynamic-mixing properties of the aluminosilicate garnets. *Am. Miner.* 82, 571-581.
- Green, D.H., Ringwood, A.E., 1967. An experimental investigation of the gabbro to eclogite transformation and its petrological applications. *Geochimica et Cosmochimica Acta* 31, 767-833.
- Green, T.H., Blundy, J.D., Adam, J., Yaxley, G.M., 2000. SIMS determination of trace element partition coefficients between garnet, clinopyroxene and hydrous basaltic liquids at 2–7.5 GPa and 1080–1200°C. *Lithos* 53, 165-187.
- Griffin, W.L., O'Reilly, S.Y., Abe, N., Aulbach, S., Davies, R.M., Pearson, N.J., Doyle, B.J., Kivi, K., 2003. The origin and evolution of Archean lithospheric mantle. *Precambrian Research* 127, 19-41.
- Gwanmesia, G.D., Liu, J., Chen, G., Kesson, S., Rigden, S.M., Liebermann, R.C., 2000. Elasticity of the pyrope ($Mg_3Al_2Si_3O_{12}$)-majorite ($MgSiO_3$) garnets solid solution. *Phys. Chem. Miner.* 27, 445-452.
- Gwanmesia, G.D., Zhang, J.Z., Darling, K., Kung, J., Li, B.S., Wang, L.P., Neuville, D., Liebermann, R.C., 2006. Elasticity of polycrystalline pyrope ($Mg_3Al_2Si_3O_{12}$) to 9 GPa and 1000 degrees C. *Phys. Earth Planet. Inter.* 155, 179-190.
- Hacker, B.R., 1996. Eclogite formation and the Rheology, Buoyancy, Seismicity, and H₂O Content of Oceanic Crust, Subduction Top to Bottom. American Geophysical Union, pp. 337-346.
- Haggerty, S.E., 1986. Diamond genesis in a multiply-constrained model.
- Haggerty, S.E., Sautter, V., 1990. Ultradeep (Greater Than 300 Kilometers), Ultramafic Upper Mantle Xenoliths. *Science* 248, 993-996.
- Hall, H.T., 1958. Some High-Pressure, High-Temperature Apparatus Design Considerations: Equipment for Use at 100,000 Atmospheres and 3000°C. *The Review of Scientific Instruments* 29, 267-275.
- Hall, H.T., 1960. Ultra-High-Pressure, High-Temperature Apparatus: the "Belt". *Review of Scientific Instruments* 31, 125-131.

- Hammouda, T., Moine, B., Devidal, J.-L., Vincent, C., 2009. Trace element partitioning during partial melting of carbonated eclogites. *Phys. Earth Planet. Inter.* 174, 60-69.
- Harte, B., 2010. Diamond formation in the deep mantle: the record of mineral inclusions and their distribution in relation to mantle dehydration zones. *Mineral. Mag.* 74, 189-215.
- Harte, B., Cayzer, N., 2007. Decompression and unmixing of crystals included in diamonds from the mantle transition zone. *Phys. Chem. Miner.* 34, 647-656.
- Hatton, C., Gurney, J., 1987. Roberts Victor eclogites and their relation to the mantle. *Mantle Xenoliths*, 453-463.
- Hatton, C.J., Gurney, J.J., 1979. A Diamond-Graphite Eclogite from the Roberts Victor Mine, The Mantle Sample: Inclusion in Kimberlites and Other Volcanics. American Geophysical Union, pp. 29-36.
- Hauri, E., 2002. SIMS analysis of volatiles in silicate glasses, 2: isotopes and abundances in Hawaiian melt inclusions. *Chemical Geology* 183, 115-141.
- Hauri, E.H., Gaetani, G.A., Green, T.H., 2006. Partitioning of water during melting of the Earth's upper mantle at H₂O-undersaturated conditions. *Earth and Planetary Science Letters* 248, 715-734.
- Hazen, R.M., Downs, R.T., Conrad, P.G., Finger, L.W., Gasparik, T., 1994. Comparative compressibilities of majorite-type garnets. *Phys. Chem. Miner.* 21, 344-349.
- Hazen, R.M., Yang, H., Prewitt, C.T., Gasparik, T., 1997. Crystal chemistry of superfluorous phase B (Mg~1~0Si~3O~1~4F~4): Implications for the role of fluorine in the mantle. *Am. Miner.* 82, 647-650.
- Heinz, D.L., Jeanloz, R., 1984. The equation of state of the gold calibration standard. *Journal of applied physics* 55, 885-893.
- Helffrich, G.R., Stein, S., Wood, B.J., 1989. Subduction zone thermal structure and mineralogy and their relationship to seismic wave reflections and conversions at the slab/mantle interface. *Journal of Geophysical Research: Solid Earth* (1978–2012) 94, 753-763.
- Helmstaedt, H., Doig, R., 1975. Eclogite nodules from kimberlite pipes of the Colorado Plateau—samples of subducted Franciscan-type oceanic lithosphere. *Physics and Chemistry of the Earth* 9, 95-111.
- Herzberg, C., Zhang, J., 1996. Melting experiments on anhydrous peridotite KLB-1: Compositions of magmas in the upper mantle and transition zone. *Journal of Geophysical Research: Solid Earth* (1978–2012) 101, 8271-8295.
- Herzberg, C.T., 1978. Pyroxene geothermometry and geobarometry: experimental and thermodynamic evaluation of some subsolidus phase relations involving pyroxenes in the system CaO-MgO-Al₂O₃-SiO₂. *Geochimica et Cosmochimica Acta* 42, 945-957.
- Hirose, K., Fei, Y.W., Ma, Y.Z., Mao, H.K., 1999. The fate of subducted basaltic crust in the Earth's lower mantle. *Nature* 397, 53-56.
- Hirose, K., Takafuji, N., Sata, N., Ohishi, Y., 2005. Phase transition and density of subducted MORB crust in the lower mantle. *Earth and Planetary Science Letters* 237, 239-251.
- Hirschmann, M.M., Kogiso, T., Baker, M.B., Stolper, E.M., 2003. Alkalic magmas generated by partial melting of garnet pyroxenite. *Geology* 31, 481-484.
- Hofmann, A.W., White, W.M., 1982. Mantle plumes from ancient oceanic crust. *Earth and Planetary Science Letters* 57, 421-436.

- Holland, T., Powell, R., 2011. An improved and extended internally consistent thermodynamic dataset for phases of petrological interest, involving a new equation of state for solids. *Journal of Metamorphic Geology* 29, 333-383.
- Huang, S., Chen, J., 2014. Equation of state of pyrope–almandine solid solution measured using a diamond anvil cell and in situ synchrotron X-ray diffraction. *Phys. Earth Planet. Inter.* 228, 88-91.
- Irifune, T., 1987. An experimental investigation of the pyroxene-garnet transformation in a pyrolite composition and its bearing on the constitution of the mantle. *Phys. Earth Planet. Inter.* 45, 324-336.
- Irifune, T., 1993. Phase transformations in the earth's mantle and subducting slabs: Implications for their compositions, seismic velocity and density structures and dynamics. *Island Arc* 2, 55-71.
- Irifune, T., Higo, Y., Inoue, T., Kono, Y., Ohfuji, H., Funakoshi, K., 2008. Sound velocities of majorite garnet and the composition of the mantle transition region. *Nature* 451, 814-817.
- Irifune, T., Ringwood, A.E., 1987. Phase transformations in a harzburgite composition to 26 GPa: implications for dynamical behaviour of the subducting slab. *Earth and Planetary Science Letters* 86, 365-376.
- Irifune, T., Ringwood, A.E., 1993. Phase transformations in subducted oceanic crust and buoyancy relationships at depths of 600–800 km in the mantle. *Earth and Planetary Science Letters* 117, 101-110.
- Irifune, T., Sekine, T., Ringwood, A.E., Hibberson, W.O., 1986. The eclogite-garnetite transformation at high pressure and some geophysical implications. *Earth and Planetary Science Letters* 77, 245-256.
- Isaak, D.G., Anderson, O.L., Oda, H., 1992. High-temperature thermal expansion and elasticity of calcium-rich garnets. *Phys. Chem. Miner.* 19, 106-120.
- Isaak, D.G., Graham, E.K., 1976. The elastic properties of an almandine-spessartine garnet and elasticity in the garnet solid solution series. *Journal of Geophysical Research* 81, 2483-2489.
- Ito, E., Harris, D.M., Anderson, A.T., 1983. Alteration of oceanic-crust and geologic cycling of chlorine and water. *Geochimica et Cosmochimica Acta* 47, 1613-1624.
- Ito, E., Katsura, T., Aizawa, Y., Kawabe, K., Yokoshi, S., Kubo, A., Nozawa, A., Funakoshi, K.-i., Chen, J., Wang, Y., 2005. High-pressure generation in the Kawai-type apparatus equipped with sintered diamond anvils: application to the wurtzite–rocksalt transformation in GaN. *Advances in High-Pressure Techniques for Geophysical Applications*, 451-460.
- Jackson, I., Rigden, S.M., 1996. Analysis of PVT data: constraints on the thermoelastic properties of high-pressure minerals. *Phys. Earth Planet. Inter.* 96, 85-112.
- Jacob, D., Jagoutz, E., Lowry, D., Matthey, D., Kudrjavitseva, G., 1994. Diamondiferous eclogites from Siberia: remnants of Archean oceanic crust. *Geochimica et Cosmochimica Acta* 58, 5191-5207.
- Jacob, D.E., 2004. Nature and origin of eclogite xenoliths from kimberlites. *Lithos* 77, 295-316.
- Jacobsen, S.D., Holl, C.M., Adams, K.A., Fischer, R.A., Martin, E.S., Bina, C.R., Lin, J.-F., Prakapenka, V.B., Kubo, A., Dera, P., 2008. Compression of single-crystal magnesium oxide to 118 GPa and a ruby pressure gauge for helium pressure media. *Am. Miner.* 93, 1823-1828.
- Jiang, F.M., Speziale, S., Duffy, T.S., 2004. Single-crystal elasticity of grossular- and almandine-rich garnets to 11 GPa by Brillouin scattering. *Journal of Geophysical Research-Solid Earth* 109.
- John, T., Scambelluri, M., Frische, M., Barnes, J.D., Bach, W., 2011. Dehydration of subducting serpentinite: Implications for halogen mobility in subduction zones and the deep halogen cycle. *Earth and Planetary Science Letters* 308, 65-76.

- Kaminsky, F., Zakharchenko, O., Davies, R., Griffin, W., Khachatryan-Blinova, G., Shiryaev, A., 2001. Superdeep diamonds from the Juina area, Mato Grosso State, Brazil. *Contrib. Mineral. Petrol.* 140, 734-753.
- Kantor, I., Prakapenka, V., Kantor, A., Dera, P., Kurnosov, A., Sinogeikin, S., Dubrovinskaia, N., Dubrovinsky, L., 2012. BX90: A new diamond anvil cell design for X-ray diffraction and optical measurements. *Review of Scientific Instruments* 83, 125102.
- Katayama, I., Nakashima, S., Yurimoto, H., 2006. Water content in natural eclogite and implication for water transport into the deep upper mantle. *Lithos* 86, 245-259.
- Kawai, N., Endo, S., 1970. The generation of ultrahigh hydrostatic pressures by a split sphere apparatus. *Review of Scientific Instruments* 41, 1178-1181.
- Kendrick, M.A., Jackson, M.G., Kent, A.J., Hauri, E.H., Wallace, P.J., Woodhead, J., 2014. Contrasting behaviours of CO₂, S, H₂O and halogens (F, Cl, Br, and I) in enriched-mantle melts from Pitcairn and Society seamounts. *Chemical Geology* 370, 69-81.
- Kennedy, C.S., Kennedy, G.C., 1976. The equilibrium boundary between graphite and diamond. *Journal of Geophysical Research* 81, 2467-2470.
- Keppler, H., Frost, D.J., 2005. Introduction to minerals under extreme conditions. *Mineral Behaviour at Extreme Conditions*, EMU Notes Mineral 7, 1-30.
- Kessel, R., Ulmer, P., Pettke, T., Schmidt, M., Thompson, A., 2005. The water–basalt system at 4 to 6 GPa: phase relations and second critical endpoint in a K-free eclogite at 700 to 1400 C. *Earth and Planetary Science Letters* 237, 873-892.
- Kesson, S.E., Fitz Gerald, J.D., Shelley, J.M.G., 1994. Mineral chemistry and density of subducted basaltic crust at lower-mantle pressures. *Nature* 372, 767-769.
- King, H., Finger, L., 1979. Diffracted beam crystal centering and its application to high-pressure crystallography. *Journal of Applied Crystallography* 12, 374-378.
- Kiseeva, E.S., Yaxley, G.M., Hermann, J., Litasov, K.D., Rosenthal, A., Kamenetsky, V.S., 2012. An experimental study of carbonated eclogite at 3–5–5 GPa—implications for silicate and carbonate metasomatism in the cratonic mantle. *Journal of Petrology* 53, 727-759.
- Kiseeva, E.S., Yaxley, G.M., Stepanov, A.S., Tkalčić, H., Litasov, K.D., Kamenetsky, V.S., 2013. Metapyroxenite in the mantle transition zone revealed from majorite inclusions in diamonds. *Geology* 41, 883-886.
- Klemme, S., 2004. Evidence for Fluoride melts in Earth's mantle formed by liquid immiscibility. *Geology* 32, 441-444.
- Klemme, S., Blundy, J.D., Wood, B.J., 2002. Experimental constraints on major and trace element partitioning during partial melting of eclogite. *Geochimica et Cosmochimica Acta* 66, 3109-3123.
- Klotz, S., Chervin, J.C., Munsch, P., Marchand, G.L., 2009. Hydrostatic limits of 11 pressure transmitting media. *Journal of Physics D: Applied Physics* 42, 075413.
- Knapp, N., Woodland, A.B., Klimm, K., 2013. Experimental constraints in the CMAS system on the Ca-Eskola content of eclogitic clinopyroxene. *Eur. J. Mineral.* 25, 579-596.
- Koch-Müller, M., Matsyuk, S.S., Wirth, R., 2004. Hydroxyl in omphacites and omphacitic clinopyroxenes of upper mantle to lower crustal origin beneath the Siberian platform. *Am. Miner.* 89, 921-931.

- Kogiso, T., Hirschmann, M.M., 2006. Partial melting experiments of bimineralec eclogite and the role of recycled mafic oceanic crust in the genesis of ocean island basalts. *Earth and Planetary Science Letters* 249, 188-199.
- Konzett, J., Frost, D.J., Proyer, A., Ulmer, P., 2008. The Ca-Eskola component in eclogitic clinopyroxene as a function of pressure, temperature and bulk composition: an experimental study to 15 GPa with possible implications for the formation of oriented SiO₂-inclusions in omphacite. *Contrib. Mineral. Petrol.* 155, 215-228.
- Koons, P.O., 1984. Implications to garnet-clinopyroxene geothermometry of non-ideal solid solution in jadeitic pyroxenes. *Contrib. Mineral. Petrol.* 88, 340-347.
- Krogh, E.J., 1988. The garnet-clinopyroxene Fe-Mg geothermometer—a reinterpretation of existing experimental data. *Contrib. Mineral. Petrol.* 99, 44-48.
- Kroll, H., Kirfel, A., Heinemann, R., Barbier, B., 2012. Volume thermal expansion and related thermophysical parameters in the Mg, Fe olivine solid-solution series. *Eur. J. Mineral.* 24, 935-956.
- Kurnosov, A., Kantor, I., Boffa-Ballaran, T., Lindhardt, S., Dubrovinsky, L., Kuznetsov, A., Zehnder, B.H., 2008. A novel gas-loading system for mechanically closing of various types of diamond anvil cells. *Review of Scientific Instruments* 79, 045110.
- Kuskov, O.L., Kronrod, V.A., Prokof'ev, A.A., 2011. Thermal structure and thickness of the lithospheric mantle underlying the Siberian Craton from the kraton and kimberlit superlong seismic profiles. *Izv., Phys. Solid Earth* 47, 155-175.
- Lager, G., Armbruster, T., Faber, J., 1987. Neutron and X-ray diffraction study of hydrogarnet Ca₃Al₂(O₄H₄)₃. *Am. Miner.* 72, 756-765.
- Le Voyer, M., Asimow, P.D., Mosenfelder, J.L., Guan, Y., Wallace, P.J., Schiano, P., Stolper, E.M., Eiler, J.M., 2014. Zonation of H₂O and F Concentrations around Melt Inclusions in Olivines. *Journal of Petrology* 55, 685-707.
- Lehnert, K., Su, Y., Langmuir, C.H., Sarbas, B., Nohl, U., 2000. A global geochemical database structure for rocks. *Geochem. Geophys. Geosyst.* 1, 1-14.
- Lin-Gun, L., 1980. The mineralogy of an eclogitic earth mantle. *Phys. Earth Planet. Inter.* 23, 262-267.
- Liou, J.G., Ernst, W.G., Zhang, R.Y., Tsujimori, T., Jahn, B.M., 2009. Ultrahigh-pressure minerals and metamorphic terranes – The view from China. *Journal of Asian Earth Sciences* 35, 199-231.
- Liu, Y., Taylor, L.A., Sarbadhikari, A.B., Valley, J.W., Ushikubo, T., Spicuzza, M.J., Kita, N., Ketcham, R.A., Carlson, W., Shatsky, V., 2009. Metasomatic origin of diamonds in the world's largest diamondiferous eclogite. *Lithos* 112, 1014-1024.
- Luth, R., Canil, D., 1993. Ferric iron in mantle-derived pyroxenes and a new oxybarometer for the mantle. *Contrib. Mineral. Petrol.* 113, 236-248.
- Luth, R., Virgo, D., Boyd, F., Wood, B., 1990. Ferric iron in mantle-derived garnets. *Contrib. Mineral. Petrol.* 104, 56-72.
- Luth, R.W., 1988. Effects of F on phase-equilibria and liquid structure in the system NaAlSiO₄-CaMgSi₂O₆-SiO₂. *Am. Miner.* 73, 306-312.
- MacGregor, I.D., Manton, W.I., 1986. Roberts victor eclogites: Ancient oceanic crust. *Journal of Geophysical Research: Solid Earth* 91, 14063-14079.

- Mao, H., Xu, J.-A., Bell, P., 1986. Calibration of the ruby pressure gauge to 800 kbar under quasi-hydrostatic conditions. *Journal of Geophysical Research: Solid Earth* (1978–2012) 91, 4673-4676.
- Mao, H.K., Mao, W.L., 2007. 2.09 - Theory and Practice – Diamond-Anvil Cells and Probes for High P–T Mineral Physics Studies, in: Schubert, G. (Ed.), *Treatise on Geophysics*. Elsevier, Amsterdam, pp. 231-267.
- Maruyama, S., Okamoto, K., 2007. Water transportation from the subducting slab into the mantle transition zone. *Gondwana Research* 11, 148-165.
- McCormick, T.C., Hazen, R.M., Angel, R.J., 1989. Compressibility of omphacite to 60 kbar; role of vacancies. *Am. Miner.* 74, 1287-1292.
- Meyer, H., Mahin, R., 1986. The kimberlites of Guinea, West Africa, 4th Int. Kimberlite Conf., Geol. Soc. Australia Abstr., pp. 66-67.
- Meyer, H.O., Svisero, D.P., 1975. Mineral inclusions in Brazilian diamonds. *Physics and Chemistry of the Earth* 9, 785-795.
- Mitchell, R.H., 1995. Melting experiments on a sanidine phlogopite lamproite at 4–7 GPa and their bearing on the sources of lamproitic magmas. *Journal of Petrology* 36, 1455-1474.
- Miura, H., Hamada, Y., Suzuki, T., Akaogi, M., Miyajima, N., Fujino, K., 2000. Crystal structure of CaMg₂Al₆O₁₂, a new Al-rich high pressure form. *Am. Miner.* 85, 1799-1803.
- Miyajima, N., Yagi, T., Hirose, K., Kondo, T., Fujino, K., Miura, H., 2001. Potential host phase of aluminum and potassium in the Earth's lower mantle. *Am. Miner.* 86, 740-746.
- Moore, R., Gurney, J., 1989. Mineral inclusions in diamond from the Monastery kimberlite, South Africa. *Kimberlites and related rocks* 2, 1029-1041.
- Moore, R.O., Gurney, J.J., 1985. Pyroxene solid solution in garnets included in diamond.
- Moore, R.O., Gurney, J.J., Griffin, W.L., Shimizu, N., 1991. Ultra-high pressure garnet inclusions in Monastery diamonds: trace element abundance patterns and conditions of origin. *Eur. J. Mineral.*, 213-230.
- Mosenfelder, J.L., Rossman, G.R., 2013a. Analysis of hydrogen and fluorine in pyroxenes: I. Orthopyroxene. *Am. Miner.* 98, 1026-1041.
- Mosenfelder, J.L., Rossman, G.R., 2013b. Analysis of hydrogen and fluorine in pyroxenes: II. Clinopyroxene. *Am. Miner.* 98, 1042-1054.
- Mukhopadhyay, B., 1991. Garnet-Clinopyroxene Geobarometry - The Problems, a Prospect, and an Approximate Solution with some Applications. *Am. Miner.* 76, 512-529.
- Mukhopadhyay, B., Basu, S., Holdaway, M.J., 1993. A discussion of margules-type formulations for multicomponent solutions with a generalized approach. *Geochimica et Cosmochimica Acta* 57, 277-283.
- Murphy, D.T., Collerson, K.D., Kamber, B.S., 2002. Lamproites from Gaussberg, Antarctica: Possible Transition Zone Melts of Archaean Subducted Sediments. *Journal of Petrology* 43, 981-1001.
- Nakamura, D., 2009. A new formulation of garnet–clinopyroxene geothermometer based on accumulation and statistical analysis of a large experimental data set. *Journal of Metamorphic Geology* 27, 495-508.
- Newton, R., 1986. Metamorphic temperatures and pressures of Group B and C eclogites. *Geol Soc Am Mem* 164, 17-30.
- Newton, R., Perkins, D., 1982. Thermodynamic calibration of geobarometers based on the assemblages garnet-plagioclase-orthopyroxene (clinopyroxene)-quartz. *Am. Miner.* 67, 203-222.
- Nickel, K., Green, D., 1985. Empirical geothermobarometry for garnet peridotites and implications for the nature of the lithosphere, kimberlites and diamonds. *Earth and Planetary Science Letters* 73, 158-170.

- Nikitina, L., 2000. Garnet–Orthopyroxene and Garnet–Clinopyroxene Thermobarometers for Mantle Xenoliths. *Capricious Earth: models and modelling of geologic processes and objects*. Eds. Glebovitsky VA, Dech VN. *Theophrastus contributions to advanced studies in geology* 3, 44-53.
- Nimis, P., Taylor, W.R., 2000. Single clinopyroxene thermobarometry for garnet peridotites. Part I. Calibration and testing of a Cr-in-Cpx barometer and an enstatite-in-Cpx thermometer. *Contrib. Mineral. Petrol.* 139, 541-554.
- Nimis, P., Ulmer, P., 1998. Clinopyroxene geobarometry of magmatic rocks Part 1: An expanded structural geobarometer for anhydrous and hydrous, basic and ultrabasic systems. *Contrib. Mineral. Petrol.* 133, 122-135.
- Nishihara, Y., Takahashi, E., 2001. Phase relation and physical properties of an Al-depleted komatiite to 23 GPa. *Earth and Planetary Science Letters* 190, 65-77.
- Nishihara, Y., Takahashi, E., Matsukage, K., Kikegawa, T., 2003. Thermal equation of state of omphacite. *Am. Miner.* 88, 80-86.
- O'Hara, M.J., 1969. The origin of eclogite and ariégite nodules in basalt. *Geological Magazine* 106, 322-330.
- O'Hara, M.J., Saunders, M.J., Mercy, E.L.P., 1975. Garnet-peridotite, primary ultrabasic magma and eclogite; Interpretation of upper mantle processes in kimberlite. *Physics and Chemistry of the Earth* 9, 571-604.
- O'Neill, B., Bass, J.D., Smyth, J.R., Vaughan, M.T., 1989. Elasticity of a grossular-pyrope-almandine garnet. *Journal of Geophysical Research: Solid Earth* 94, 17819-17824.
- O'Reilly, S.Y., Griffin, W., 1995. Trace-element partitioning between garnet and clinopyroxene in mantle-derived pyroxenites and eclogites: P- T-X controls. *Chemical geology* 121, 105-130.
- O'Reilly, S.Y., Griffin, W.L., 2000. Apatite in the mantle: implications for metasomatic processes and high heat production in Phanerozoic mantle. *Lithos* 53, 217-232.
- Ohtani, E., Kagawa, N., Shimomura, O., Togaya, M., Suito, K., Onodera, A., Sawamoto, H., Yoneda, M., Tanaka, S., Utsumi, W., 1989. High-pressure generation by a multiple anvil system with sintered diamond anvils. *Review of Scientific Instruments* 60, 922-925.
- Okamoto, K., Maruyama, S., 1998. Multi-anvil re-equilibration experiments of a Dabie Shan ultrahigh-pressure eclogite within the diamond-stability fields. *Island Arc* 7, 52-69.
- Okamoto, K., Maruyama, S., 2004. The eclogite-gametite transformation in the MORB+H₂O system. *Phys. Earth Planet. Inter.* 146, 283-296.
- Olijnyk, H., Paris, E., Geiger, C., Lager, G., 1991. Compressional study of katoite [Ca₃Al₂(O₄H₄)₃] and grossular garnet. *Journal of Geophysical Research: Solid Earth (1978–2012)* 96, 14313-14318.
- Ono, S., Ito, E., Katsura, T., 2001. Mineralogy of subducted basaltic crust (MORB) from 25 to 37 GPa, and chemical heterogeneity of the lower mantle. *Earth and Planetary Science Letters* 190, 57-63.
- Ono, S., Yasuda, A., 1996. Compositional change of majoritic garnet in a MORB composition from 7 to 17 GPa and 1400 to 1600 degrees C. *Phys. Earth Planet. Inter.* 96, 171-179.
- Palme, H., O'Neill, H.S.C., 2003. Cosmochemical estimates of mantle composition. *Treatise on geochemistry* 2, 1-38.
- Pavese, A., Bocchio, R., Ivaldi, G., 2000. High temperature single crystal X-ray diffraction study of a natural omphacite. *Mineral. Mag.* 64, 983-993.

- Pavese, A., Diella, V., Pischedda, V., Merli, M., Bocchio, R., Mezouar, M., 2001a. Pressure-volume-temperature equation of state of andradite and grossular, by high-pressure and -temperature powder diffraction. *Phys. Chem. Miner.* 28, 242-248.
- Pavese, A., Levy, D., Pischedda, V., 2001b. Elastic properties of andradite and grossular, by synchrotron X-ray diffraction at high pressure conditions. *Eur. J. Mineral.* 13, 929-937.
- Pearson, D.G., Brenker, F.E., Nestola, F., McNeill, J., Nasdala, L., Hutchison, M.T., Matveev, S., Mather, K., Silversmit, G., Schmitz, S., Vekemans, B., Vincze, L., 2014. Hydrous mantle transition zone indicated by ringwoodite included within diamond. *Nature* 507, 221-224.
- Perrillat, J.-P., Ricolleau, A., Daniel, I., Fiquet, G., Mezouar, M., Guignot, N., Cardon, H., 2006. Phase transformations of subducted basaltic crust in the upmost lower mantle. *Phys. Earth Planet. Inter.* 157, 139-149.
- Pertermann, M., Hirschmann, M.M., 2003. Anhydrous partial melting experiments on MORB-like eclogite: Phase relations, phase compositions and mineral-melt partitioning of major elements at 2-3 GPa. *Journal of Petrology* 44, 2173-2201.
- Pokhilenko, N., Sobolev, N., Reutsky, V., Hall, A., Taylor, L., 2004. Crystalline inclusions and C isotope ratios in diamonds from the Snap Lake/King Lake kimberlite dyke system: evidence of ultradeep and enriched lithospheric mantle. *Lithos* 77, 57-67.
- Pollack, H.N., Chapman, D.S., 1977. On the regional variation of heat flow, geotherms, and lithospheric thickness. *Tectonophysics* 38, 279-296.
- Purwin, H., Lauterbach, S., Brey, G.P., Woodland, A.B., Kleebe, H.-J., 2013. An experimental study of the Fe oxidation states in garnet and clinopyroxene as a function of temperature in the system CaO–FeO–Fe₂O₃–MgO–Al₂O₃–SiO₂: implications for garnet–clinopyroxene geothermometry. *Contrib. Mineral. Petrol.*, 1-17.
- Rapp, R.P., Shimizu, N., Norman, M.D., 2003. Growth of early continental crust by partial melting of eclogite. *Nature* 425, 605-609.
- Rapp, R.P., Watson, E.B., Miller, C.F., 1991. Partial melting of amphibolite/eclogite and the origin of Archean trondhjemites and tonalites. *Precambrian Research* 51, 1-25.
- Reed, S.J.B., 2005. *Electron microprobe analysis and scanning electron microscopy in geology*. Cambridge University Press.
- Ringwood, A., Lovering, J., 1970. Significance of pyroxene-ilmenite intergrowths among kimberlite xenoliths. *Earth and Planetary Science Letters* 7, 371-375.
- Ringwood, A., Major, A., 1971. Synthesis of majorite and other high pressure garnets and perovskites. *Earth and Planetary Science Letters* 12, 411-418.
- Roberge, M., Bureau, H., Bolfan-Casanova, N., FROST, D., Raepsaet, C., Surblé, S., Khodja, H., Fiquet, G., 2013. F and Cl solubilities in wadsleyite and ringwoodite. *Mineral. Mag.* 77, 2068.
- Robinson, D.N., 1979. Diamond and graphite in eclogite xenoliths from kimberlite. *The Mantle Sample: Inclusion in Kimberlites and Other Volcanics*, 50-58.
- Rosenthal, A., Hauri, E.H., Hirschmann, M.M., 2015. Experimental determination of C, F and H partitioning between mantle minerals and carbonated basalt, CO₂/Ba and CO₂/Nb systematics of partial melting, and the CO₂ contents of basaltic source regions. *Earth and Planetary Science Letters* in press.
- Rubie, D.C., 1999. Characterising the sample environment in multianvil high-pressure experiments. *Phase Transitions* 68, 431-451.

- Rudnick, R.L., Gao, S., 2003. The Composition of the Continental Crust, in: Rudnick, R.L. (Ed.), *Treatise on Geochemistry Vol 3. - The Crust*. Elsevier-Pergamon, Oxford, pp. 1-64.
- Ruoff, A.L., Xia, H., Luo, H., Vohra, Y.K., 1990. Miniaturization techniques for obtaining static pressures comparable to the pressure at the center of the earth: X-ray diffraction at 416 GPa. *Review of Scientific Instruments* 61, 3830-3833.
- Sand, K.K., Waight, T.E., Pearson, D.G., Nielsen, T.F., Makovicky, E., Hutchison, M.T., 2009. The lithospheric mantle below southern West Greenland: A geothermobarometric approach to diamond potential and mantle stratigraphy. *Lithos* 112, 1155-1166.
- Schilling, J.G., Bergeron, M.B., Evans, R., 1980. Halogenes in the mantle beneath the North-Atlantic. *Philos. Trans. R. Soc. Lond. Ser. A-Math. Phys. Eng. Sci.* 297, 147-178.
- Schmickler, B., Jacob, D., Foley, S., 2004. Eclogite xenoliths from the Kuruman kimberlites, South Africa: geochemical fingerprinting of deep subduction and cumulate processes. *Lithos* 75, 173-207.
- Schulze, D.J., 1989. Constraints on the abundance of eclogite in the upper mantle. *Journal of Geophysical Research: Solid Earth* 94, 4205-4212.
- Sekine, T., Irifune, T., Ringwood, A.E., Hibberson, W.O., 1986. High-pressure transformation of eclogite to garnetite in subducted oceanic crust. *Nature* 319, 584-586.
- Shannon, R.D., 1976. Revised effective ionic-radii and systematic studies of interatomic distances in halides and chalcogenides. *Acta Crystallogr. Sect. A* 32, 751-767.
- Shee, S., Bristow, J., Bell, D., Smith, C., Allsopp, H., Shee, P., 1989. The petrology of kimberlites, related rocks and associated mantle xenoliths from the Kuruman Province, South Africa. *Geol. Soc. Aust. Spec. Publ* 14, 60-81.
- Shirey, S.B., Carlson, R.W., Richardson, S.H., Menzies, A., Gurney, J.J., Pearson, D.G., Harris, J.W., Wiechert, U., 2001. Archean emplacement of eclogitic components into the lithospheric mantle during formation of the Kaapvaal Craton. *Geophysical Research Letters* 28, 2509-2512.
- Sigvaldason, G.E., Oskarsson, N., 1986. Fluorine in basalts from Iceland. *Contrib. Mineral. Petrol.* 94, 263-271.
- Simakov, S.K., 2008. Garnet-clinopyroxene and clinopyroxene geothermobarometry of deep mantle and crust eclogites and peridotites. *Lithos* 106, 125-136.
- Simakov, S.K., Taylor, L.A., 2000. Geobarometry for mantle eclogites: Solubility of Ca-Tschermaks in clinopyroxene. *Int. Geol. Rev.* 42, 534-544.
- Sirotkina, E.A., Bobrov, A.V., Bindi, L., Irifune, T., 2015. Phase relations and formation of chromium-rich phases in the system $Mg_4Si_4O_{12}$ - $Mg_3Cr_2Si_3O_{12}$ at 10-24 GPa and 1,600 °C. *Contrib. Mineral. Petrol.* 169, 1-14.
- Smart, K.A., Heaman, L.M., Chacko, T., Simonetti, A., Kopylova, M., Mah, D., Daniels, D., 2009. The origin of high-MgO diamond eclogites from the Jericho Kimberlite, Canada. *Earth and Planetary Science Letters* 284, 527-537.
- Smith, J.V., 1981. Halogen and phosphorus storage in the Earth. *Nature* 289, 762-765.
- Smith, J.V., Delaney, J.S., Hervig, R.L., Dawson, J.B., 1981. Storage of F and Cl in the upper mantle: geochemical implications. *Lithos* 14, 133-147.
- Smyth, J., Bell, D., Rossman, G., 1991. Incorporation of hydroxyl in upper-mantle clinopyroxenes.

- Smyth, J.R., Caporuscio, F.A., McCormick, T.C., 1989. Mantle eclogites: evidence of igneous fractionation in the mantle. *Earth and Planetary Science Letters* 93, 133-141.
- Smyth, J.R., Madel, R.E., McCormick, T.C., Munoz, J.L., Rossman, G.R., 1990. Crystal-structure refinement of a F-bearing spessartine garnet. *Am. Miner.* 75, 314-318.
- Sobolev, A.V., Hofmann, A.W., Sobolev, S.V., Nikogosian, I.K., 2005. An olivine-free mantle source of Hawaiian shield basalts. *Nature* 434, 590-597.
- Sobolev, N., Kaminsky, F., Griffin, W., Yefimova, E., Win, T., Ryan, C., Botkunov, A., 1997. Mineral inclusions in diamonds from the Sputnik kimberlite pipe, Yakutia. *Lithos* 39, 135-157.
- Sobolev, N.V., 1977. Deep-Seated Inclusions in Kimberlites and the Problem of the Composition of the Upper Mantle. American Geophysical Union.
- Sobolev, N.V., Jr., Lavrent'ev, J.G., 1971. Isomorphic sodium admixture in garnets formed at high pressures. *Contrib. Mineral. Petrol.* 31, 1-12.
- Spandler, C., Yaxley, G., Green, D.H., Rosenthal, A., 2008. Phase relations and melting of anhydrous K-bearing eclogite from 1200 to 1600 C and 3 to 5 GPa. *Journal of Petrology* 49, 771-795.
- Stachel, T., Aulbach, S., Brey, G.P., Harris, J.W., Leost, I., Tappert, R., Viljoen, K.S., 2004. The trace element composition of silicate inclusions in diamonds: a review. *Lithos* 77, 1-19.
- Stachel, T., Brey, G.P., Harris, J.W., 2000. Kankan diamonds (Guinea) I: from the lithosphere down to the transition zone. *Contrib. Mineral. Petrol.* 140, 1-15.
- Stachel, T., Brey, G.P., Harris, J.W., 2005. Inclusions in sublithospheric diamonds: glimpses of deep Earth. *Elements* 1, 73-78.
- Stachel, T., Harris, J.W., 1997. Syngenetic inclusions in diamond from the Birim field (Ghana)—a deep peridotitic profile with a history of depletion and re-enrichment. *Contrib. Mineral. Petrol.* 127, 336-352.
- Stachel, T., Harris, J.W., 2008. The origin of cratonic diamonds — Constraints from mineral inclusions. *Ore Geology Reviews* 34, 5-32.
- Stachel, T., Harris, J.W., 2009. Formation of diamond in the Earth's mantle. *Journal of Physics: Condensed Matter* 21, 364206.
- Stagno, V., Frost, D.J., McCammon, C.A., Mohseni, H., Fei, Y., 2015. The oxygen fugacity at which graphite or diamond forms from carbonate-bearing melts in eclogitic rocks. *Contrib. Mineral. Petrol.* 169, 1-18.
- Stagno, V., Ojwang, D.O., McCammon, C.A., Frost, D.J., 2013. The oxidation state of the mantle and the extraction of carbon from Earth's interior. *Nature* 493, 84-88.
- Stalder, R., Ulmer, P., 2001. Phase relations of a serpentine composition between 5 and 14 GPa: significance of clinohumite and phase E as water carriers into the transition zone. *Contrib. Mineral. Petrol.* 140, 670-679.
- Stixrude, L., Lithgow-Bertelloni, C., 2005. Thermodynamics of mantle minerals—I. Physical properties. *Geophys. J. Int.* 162, 610-632.
- Stixrude, L., Lithgow-Bertelloni, C., 2011. Thermodynamics of mantle minerals - II. Phase equilibria. *Geophys. J. Int.* 184, 1180-1213.
- Stracke, A., Bizimis, M., Salters, V.J.M., 2003. Recycling of oceanic crust: quantitative constraints. *Geochemistry Geophysics Geosystems* 4, Q8003.

- Straub, S.M., Layne, G.D., 2003. The systematics of chlorine, fluorine, and water in Izu arc front volcanic rocks: Implications for volatile recycling in subduction zones. *Geochimica et Cosmochimica Acta* 67, 4179-4203.
- Sumino, Y., Nishizawa, O., 1978. Temperature variation of elastic constants of pyrope-almandine garnets. *Journal of Physics of the Earth* 26, 239-252.
- Suzuki, I., Anderson, O.L., 1983. Elasticity and thermal expansion of a natural garnet up to 1,000 K. *Journal of Physics of the Earth* 31, 125-138.
- Takahashi, T., Liu, L.G., 1970. Compression of ferromagnesian garnets and the effect of solid solutions on the bulk modulus. *Journal of Geophysical Research* 75, 5757-5766.
- Tange, Y., Irifune, T., Funakoshi, K.-I., 2008. Pressure generation to 80 GPa using multianvil apparatus with sintered diamond anvils. *High Pressure Research* 28, 245-254.
- Tappe, S., Smart, K.A., Pearson, D.G., Steenfelt, A., Simonetti, A., 2011. Craton formation in Late Archean subduction zones revealed by first Greenland eclogites. *Geology* 39, 1103-1106.
- Tateno, S., Hirose, K., Ohishi, Y., Tatsumi, Y., 2010. The Structure of Iron in Earth's Inner Core. *Science* 330, 359-361.
- Taylor, L.A., Neal, C.R., 1989. Eclogites with Oceanic Crustal and Mantle Signatures from the Bellsbank Kimberlite, South Africa, Part I: Mineralogy, Petrography, and Whole Rock Chemistry. *The Journal of Geology* 97, 551-567.
- Terashima, S., Taniguchi, M., Mikoshiba, M., Imai, N., 1998. Preparation of Two New GSJ Geochemical Reference Materials: Basalt JB-1b and Coal Fly Ash JCFA-1. *Geostandards Newsletter* 22, 113-117.
- Trots, D., Kurnosov, A., Vasylechko, L., Berkowski, M., Boffa Ballaran, T., Frost, D., 2011. Elasticity and equation of state of Li₂B₄O₇. *Phys. Chem. Miner.* 38, 561-567.
- Trots, D.M., Kurnosov, A., Ballaran, T.B., Tkachev, S., Zhuravlev, K., Prakapenka, V., Berkowski, M., Frost, D.J., 2013. The Sm:YAG primary fluorescence pressure scale. *Journal of Geophysical Research: Solid Earth* 118, 2013JB010519.
- Tsai, H.M., Meyer, H.O., Moreau, J., Milledge, H.J., 1979. Mineral inclusions in diamond: premier, Jagersfontein and Finsch kimberlites, South Africa, and Williamson mine, Tanzania. *Kimberlites, Diatremes, and Diamonds: Their Geology, Petrology, and Geochemistry*, 16-26.
- Tsuno, K., Dasgupta, R., 2011. Melting phase relation of nominally anhydrous, carbonated pelitic-eclogite at 2.5–3.0 GPa and deep cycling of sedimentary carbon. *Contrib. Mineral. Petrol.* 161, 743-763.
- Ulmer, P., Sweeney, R.J., 2002. Generation and differentiation of group II kimberlites: constraints from a high-pressure experimental study to 10 GPa. *Geochimica et Cosmochimica Acta* 66, 2139-2153.
- van Aken, P.A., Liebscher, B., 2002. Quantification of ferrous/ferric ratios in minerals: new evaluation schemes of Fe L 2,3 electron energy-loss near-edge spectra. *Phys. Chem. Miner.* 29, 188-200.
- van Aken, P.A., Liebscher, B., Styrsa, V.J., 1998. Quantitative determination of iron oxidation states in minerals using Fe L 2,3 -edge electron energy-loss near-edge structure spectroscopy. *Phys. Chem. Miner.* 25, 323-327.
- van der Hilst, R., Engdahl, R., Spakman, W., Nolet, G., 1991. Tomographic imaging of subducted lithosphere below northwest Pacific island arcs. *Nature* 353, 37-43.
- van der Hilst, R., Seno, T., 1993. Effects of relative plate motion on the deep structure and penetration depth of slabs below the Izu-Bonin and Mariana island arcs. *Earth and Planetary Science Letters* 120, 395-407.

- Verma, R.K., 1960. Elasticity of some high-density crystals. *Journal of Geophysical Research* 65, 757-766.
- Viljoen, F., Dobbe, R., Harris, J., Smit, B., 2010. Trace element chemistry of mineral inclusions in eclogitic diamonds from the Premier (Cullinan) and Finsch kimberlites, South Africa: Implications for the evolution of their mantle source. *Lithos* 118, 156-168.
- Viljoen, K., Schulze, D., Quadling, A., 2005. Contrasting group I and Group II eclogite xenolith petrogenesis: petrological, trace element and isotopic evidence from eclogite, garnet-websterite and alkremite xenoliths in the Kaalvallei kimberlite, South Africa. *Journal of Petrology* 46, 2059-2090.
- Walker, D., Carpenter, M., Hitch, C., 1990. Some simplifications to multianvil devices for high pressure experiments. *Am. Miner.* 75, 1020-1028.
- Walter, M.J., 1998. Melting of Garnet Peridotite and the Origin of Komatiite and Depleted Lithosphere. *Journal of Petrology* 39, 29-60.
- Wang, H., Huang, K., 1975. ELASTIC-CONSTANTS OF NATURAL PYROPE, TRANSACTIONS-AMERICAN GEOPHYSICAL UNION. AMER GEOPHYSICAL UNION 2000 FLORIDA AVE NW, WASHINGTON, DC 20009, pp. 601-601.
- Wang, H., Simmons, G., 1974. Elasticity of some mantle crystal structures 3. Spessartite-almantine garnet. *Journal of Geophysical Research* 79, 2607-2613.
- Wang, W., Sueno, S., Takahashi, E., Yurimoto, H., Gasparik, T., 2000. Enrichment processes at the base of the Archean lithospheric mantle: observations from trace element characteristics of pyropic garnet inclusions in diamonds. *Contrib. Mineral. Petrol.* 139, 720-733.
- Wang, W., Takahashi, E., 2000. Subsolidus and melting experiments of K-doped peridotite KLB-1 to 27 GPa: Its geophysical and geochemical implications. *Journal of Geophysical Research: Solid Earth* (1978–2012) 105, 2855-2868.
- Wang, Z.C., Ji, S.C., 2001. Elasticity of six polycrystalline silicate garnets at pressure up to 3.0 GPa. *Am. Miner.* 86, 1209-1218.
- Weaver, J.S., Takahashi, T., Bass, J., 1976. Isothermal compression of grossular garnets to 250 kbar and the effect of calcium on the bulk modulus. *Journal of Geophysical Research* 81, 2475-2482.
- Webb, S.L., 1989. The elasticity of the upper mantle orthosilicates olivine and garnet to 3 GPa. *Phys. Chem. Miner.* 16, 684-692.
- Weir, C., Lippincott, E., Van Valkenburg, A., Bunting, E., 1959. Infrared studies in the 1-to 15-micron region to 30,000 atmospheres. *J. Res. Natl. Bur. Stand. A* 63, 55-62.
- Wilding, M.C., 1990. A study of diamonds with syngenetic inclusions.
- Williams, Q., Revenaugh, J., 2005. Ancient subduction, mantle eclogite, and the 300 km seismic discontinuity. *Geology* 33, 1-4.
- Witter, J.B., Kuehner, S.M., 2004. A simple empirical method for high-quality electron microprobe analysis of fluorine at trace levels in Fe-bearing minerals and glasses. *Am. Miner.* 89, 57-63.
- Wood, B.J., Banno, S., 1973. Garnet-orthopyroxene and orthopyroxene-clinopyroxene relationships in simple and complex systems. *Contrib. Mineral. Petrol.* 42, 109-124.
- Wood, B.J., Fraser, D.G., 1978. *Elementary thermodynamics for geologists*. Oxford University Press Oxford UK.
- Wood, B.J., Nicholls, J., 1978. The thermodynamic properties of reciprocal solid solutions. *Contrib. Mineral. Petrol.* 66, 389-400.

- Woodland, A., Knapp, N., Klimm, K., 2013. Is the X-discontinuity really related to the presence of eclogite bodies in the mantle?, EGU General Assembly Conference Abstracts, p. 10299.
- Woodland, A.B., O'Neill, H.S., 1997. Thermodynamic data for Fe-bearing phases obtained using noble metal alloys as redox sensors. *Geochimica et Cosmochimica Acta* 61, 4359-4366.
- Wu, J., Koga, K.T., 2013. Fluorine partitioning between hydrous minerals and aqueous fluid at 1GPa and 770–947° C: A new constraint on slab flux. *Geochimica et Cosmochimica Acta* 119, 77-92.
- Yasuda, A., Fujii, T., Kurita, K., 1994. Melting phase relations of an anhydrous mid-ocean ridge basalt from 3 to 20 GPa: Implications for the behavior of subducted oceanic crust in the mantle. *Journal of Geophysical Research: Solid Earth* 99, 9401-9414.
- Yaxley, G.M., Brey, G.P., 2004. Phase relations of carbonate-bearing eclogite assemblages from 2.5 to 5.5 GPa: implications for petrogenesis of carbonatites. *Contrib. Mineral. Petrol.* 146, 606-619.
- Zha, C.-s., Duffy, T.S., Downs, R.T., Mao, H.-k., Hemley, R.J., 1998. Brillouin scattering and X-ray diffraction of San Carlos olivine: direct pressure determination to 32 GPa. *Earth and Planetary Science Letters* 159, 25-33.
- Zhang, L., Ahsbahs, H., Kutoglu, A., 1998. Hydrostatic compression and crystal structure of pyrope to 33 GPa. *Phys. Chem. Miner.* 25, 301-307.
- Zhang, L., Ahsbahs, H., Kutoglu, A., Geiger, C., 1999. Single-crystal hydrostatic compression of synthetic pyrope, almandine, spessartine, grossular and andradite garnets at high pressures. *Phys. Chem. Miner.* 27, 52-58.
- Zhao, S., Nee, P., Green, H.W., Dobrzhinetskaya, L.F., 2011. Ca-Eskola component in clinopyroxene: Experimental studies at high pressures and high temperatures in multianvil apparatus. *Earth and Planetary Science Letters* 307, 517-524.
- Zou, Y., Gréaux, S., Irifune, T., Whitaker, M., Shinmei, T., Higo, Y., 2012. Thermal equation of state of Mg₃Al₂Si₃O₁₂ pyrope garnet up to 19 GPa and 1,700 K. *Phys. Chem. Miner.* 39, 589-598.
- Zou, Y., Irifune, T., 2012. Phase relations in Mg₃Cr₂Si₃O₁₂ and formation of majoritic knorringite garnet at high pressure and high temperature. *Journal of Mineralogical and Petrological Sciences* 107, 197-205.

(Eidesstattliche) Versicherungen und Erklärungen

(§ 8 S. 2 Nr. 6 PromO)

Hiermit erkläre ich mich damit einverstanden, dass die elektronische Fassung meiner Dissertation unter Wahrung meiner Urheberrechte und des Datenschutzes einer gesonderten Überprüfung hinsichtlich der eigenständigen Anfertigung der Dissertation unterzogen werden kann.

(§ 8 S. 2 Nr. 8 PromO)

Hiermit erkläre ich eidesstattlich, dass ich die Dissertation selbständig verfasst und keine anderen als die von mir angegebenen Quellen und Hilfsmittel benutzt habe.

(§ 8 S. 2 Nr. 9 PromO)

Ich habe die Dissertation nicht bereits zur Erlangung eines akademischen Grades anderweitig eingereicht und habe auch nicht bereits diese oder eine gleichartige Doktorprüfung endgültig nicht bestanden.

(§ 8 S. 2 Nr. 10 PromO)

Hiermit erkläre ich, dass ich keine Hilfe von gewerblichen Promotionsberatern bzw. -vermittlern in Anspruch genommen habe und auch künftig nicht nehmen werde.

.....

Ort, Datum, Unterschrift